Crustal Movements in Colombia based on GPS Space Geodesy with the GeoRED Network

MORA PÁEZ Héctor

A dissertation for the degree of Doctor of Science

Department of Earth and Environmental Sciences,
Graduate School of Environmental Studies,
Nagoya University

2020

Abstract

The northwestern corner of South America, the southeastern of Central America and the Caribbean plate correspond to a wide plate convergence boundary. The tectonic and volcanic activity in this zone is a result of the interaction of the oceanic Cocos, Nazca and Caribbean plates, and the continental South American plate as well as the North Andean, Maracaibo, Chocó and Panamá blocks wedged in between, as was exposed by various studies. This highly complex tectono-dynamic situation of intense intraplate deformation is observed in a high density of faults, most of which are considered active or potentially active over northwestern South America and southeastern Central America. Also, the seismicity is spread over a broad area across the wide plate boundary in northwestern South America, Central America, and southwestern Caribbean, whose complexity was referred as a "Wide Plate Margin". This, coupled with a potential of large magnitude megathrust and tsunami events related to the Pacific subduction zone, means that a high percentage of Colombia's population lives under a constant threat of unannounced large magnitude earthquakes and tsunamis, with a potential of inflicting great damage in terms of loss of lives and destruction of infrastructure.

Given the tectonic complexity in the mentioned region and the high possibility of occurrence of large earthquakes and tsunamis as well as volcanic eruptions among other hazards of geological origin, systematic studies to establish a monitoring system for the current situation of crustal deformation using space geodesy techniques is of great importance. In Colombia, the establishment of an adequate network of GPS stations covering the entire Colombian territory, named GeoRED project, has begun to contribute to the understanding of the crustal dynamic processes. During the last decade, the main focus and efforts have been directed to the design and installation of the network. Generation of a steadily increasing stream of data has permitted, until to date, to construct a sufficiently detailed velocity field that is capable of registering the process of tectonic escape of the North Andean Block.

Using data from 60 permanent GPS stations from Colombia, Ecuador, Panama, Costa Rica and Venezuela, located on the Nazca, South American, Cocos and Caribbean plates, a new velocity field was estimated in ITRF2008.

By combining the velocity data obtained in this study and those in Ecuador, a new comprehensive model of the North Andean Block (NAB) was estimated, with a motion estimate of 8.6 ± 1.0 mm/yr with respect to the South American plate (SOAM) in the N60°E direction. This NAB velocity can be resolved into a margin-parallel component of 8.1 ± 0.7 mm/yr and a margin-normal component of 4.3 ± 0.6 mm/yr, assuming an average trend of N35°E of the NAB-SOAM margin based on the general direction of the eastern edge of the Eastern Cordillera in Colombia between latitudes 1° and 7° N. Various mechanisms responsible for the tectonic escape of the NAB are considered such as the collision of the Carnegie ridge, the rapid oblique convergence of the Nazca plate along the Colombia-Ecuador trench, and the high coupling at the Nazca-NAB subduction plate interface. Among them, the last two are clearly demonstrated with GPS results.

The GPS velocity field allows to observe the oblique subduction of the Nazca plate at a rate of 54.1 ± 0.4 mm/yr in N87°E direction with respect to the South American plate, based on two GPS stations. Given the limited number of GPS stations located on the Nazca plate, a GPS station of the GeoRED network on the Malpelo Island (Colombia), the only island in the northern part of the Nazca plate, allows refining the motion of the Nazca plate. Velocity vectors at stations located on the Pacific coast of Colombia reflect clear evidence of strain accumulation on the Nazca subduction zone.

The oblique convergence of the Caribbean plate with respect to the South America plate is represented by the velocity of stations installed in Colombian islands located on the Caribbean plate. The velocities of those stations are 17.6 ± 0.6 mm/yr in the S100°E direction with respect to the South American plate. This plate motion is probably absorbed at the South Caribbean Deformed Belt, which is a submarine prism that was formed at the interface between oceanic material that is subducting in the basins of Colombia and Venezuela, and arc terranes along the northern edge of the South American plate.

There is geodetic evidence of the active collision between the Panama block and NAB. Although the Atrato-Uraba Fault Zone is a candidate location of the boundary, the collision boundary is diffused over a wide area in the range of 200 to 300 km. This feature is reflected in the east components of the velocities with respect to NAB. In order to distinguish the effect of the Nazca plate or the Panama block, an analysis was performed

using a velocity diagram, finding a combined effect of the subduction of the Nazca plate and the collision of Panama at BASO station (6.203°N, 77.393°W). But it is not possible to distinguish which of the two effects is more representative.

In southwestern Colombia, GPS velocities obtained from GeoRED network were significantly different from those observed in 1990's. Postseismic deformation associated with the M_w 8.2 earthquake on December 12, 1979 is considered to be a candidate mechanism for this difference and a viscoelastic relaxation effect due to this earthquake was evaluated for 40 years after the occurrence of the earthquake using the viscoelastic-gravitational dislocation theory. It is concluded that the postseismic effect was significant in 1990's when the first space geodetic measurements were conducted in Colombia while the effect has faded out in 2010's, resulting in a significant velocity changes in southwestern Colombia. The consistency between the observation and the model implies that the mantle viscosity along the Nazca subduction is around 10^{19} Pa・s, consistent with other major subduction zones.

From the velocity field obtained in this dissertation, a margin-normal shortening across the Eastern Cordillera of Colombia is estimated less than 4.1 mm/yr. This observation is not consistent with paleobotanical studies of the uplift history of the Eastern Cordillera that suggest a rapid uplift (7 km) and shortening (120 km) during the last 10 Ma. As an alternative scenario regarding mountain building and shortening in the Eastern Cordillera of Colombia due to the collision of the Panama block, a "broken indenter" model for the Panama-Choco arc is proposed. The model considers that the Choco arc has been recently (1-2 Ma) accreted to the NAB and the shortening as well as the uplift rate at the Eastern Cordillera drastically decreased.

Acknowledgements

To God, for enlightening and tracing the right path of my life and granting me the privilege of having great satisfactions and joys.

My deepest gratitude to Professor Takeshi Sagiya, who has patiently supported this research with his experience and knowledge, allowing me, with his advice and permanent encouragement, to advance in the understanding and analysis of space geodetic information, and thus contribute to the progress in geodetic applications to gain knowledge about the dynamics of the earth's crust in Colombia.

To Professor Takeo Ito for his support in this task, as well as to Professor Hiroyuki Kumagai for supporting this scientific growth.

I am grateful to the Government of Japan, which has given me the opportunity to reach this honorable academic degree thanks to JICA's support through the SATREPS project performed in Colombia. This project has allowed overcoming the existing limitations in terms of the proper analysis and interpretation of GPS results. Thus, important achievements have been obtained, based on the exchange and transfer of knowledge by the aforementioned professors.

To the Colombian Geological Survey, and especially its General Director, Dr. Oscar Paredes Zapata, who, by strengthening the Space Geodetic Research Group in 2011, facilitated the realization of a personal dream of 1994, that was approved as a project in 2006 after several attempts. This technological and scientific incursion has allowed not only the institutional strengthening of the Colombian Geological Survey through the creation of the National Network of GNSS permanent stations for geodynamics purposes, known as GeoRED network, widely recognized in the Latin American context, but also the construction of institutional capacities, and training personnel for the execution of the

various activities inherent to the project, ranging from the stage of site selection and stations installation following procedures that guarantee high quality data, to the scientific processing of GNSS data, under my direct supervision.

To my collaborators of the Space Geodetic Research Group, who have contributed during these years to the development of the GeoRED project. My special gratitude to Leidy, Yuli, Fredy, Karime and Jair for their support.

I must also acknowledge the valuable contribution to the GeoRED project of researchers from the Universities of South Carolina, Alaska and Colorado, and UNAVCO in the United States, and from SEGAL of the University of Interior Beira of Portugal. I must highlight the support of professors James Kellogg, Peter Molnar, Jeff Freymueller, Rui Fernandes. Also, Dave Mencin and Karl Feaux from UNAVCO. Thanks a lot.

Finally, with all my love to my family, Héctor Andrés, María Paula, Alexandra as well as Diana for her words of encouragement to complete this challenge.

To Janeth, my partner in this life, for her infinite patience and permanent encouragement. Thanks forever. I do not have enough words to express my gratitude.

Table of contents

List of Figures

List of Tables

Glossary of abbreviations

BINEX	Binary Exchange Format
CGS	Colombian Geological Survey
CORS	Continuously Operating Reference Station
CIDA	Canadian International Development Agency
EFS	Eastern Fault System
FLINN	Fiducial Laboratories for an International Natural science Network Global Network
GeoRED	GNSS Project for Geodynamics Studies in Colombia, South America
GIPSY-OASIS	GNSS-Inferred Positioning System and Orbit Analysis Simulation Software
GNSS	Global Navigation Satellite System
GPS	Global Positioning System
IERS	International Earth Rotation and Reference Systems Service
IGS	International GPS service
INGEOMINAS	Former Institute of Geosciences, Mining and Chemical Research of Colombia
ITRF	International Terrestrial Reference Frame
NA	North Amerian Plate
NAB	North Andean Block
NAS	North Andes Silver
NEIC	National Earthquake Information Center, USGC
NGS	National Geodetic Survey, USA
NSZ	Nazca Subduction Zone
PNUD	United Nations Development Program
PPP	Precise Point Positioning
RINEX	Receiver Independent Exchange Format
SGRG	Space Geodesy Research Group of the Colombian Geological Survey
SOAM	South America plate
TMB	Triangulated Maracaibo Block
TELECOM	Former Colombian Telecommunications Company
TEQC	A GNSS tool developed by UNAVCO for translating, editing and quality checking GNSS files
UNAVCO	University NAVSTAR Consortium - A non-profit, membership-governed university consortium facilitating geoscience research and education using geodesy
USGS	United States Geological Survey

CHAPTER 1

INTRODUCTION

1. Tectonic frame and seismicity in the study area

Tectonic and volcanic activities are intimately related to the interaction of different lithospheric plates and crustal blocks. The tectonic setting of South America is unique: in no other part of the world does a major oceanic plate subduct beneath a large continental plate along an almost 6,000 kilometers long trench (Assumpcao, 1992). In this region, the tectonics and volcanic activity is directly related to the interaction of the South America, Nazca, Cocos and Caribbean plates, with the smaller North Andean, Maracaibo, Choco and Panama blocks wedged in between, as is shown in Figure 1 (e.g., Case et al., 1971; Dewey, 1972; Pennington, 1981; Kellogg and Bonini, 1982; Freymueller et al., 1993; Ego et al., 1993; van der Hilst and Mann, 1994; Kellogg and Vega, 1995; Pindell et al. 1998; Taboada et al., 2000; Trenkamp et al., 2002; Cediel et al., 2003; Audemard and Audemard, 2002; Audemard, 2014; Romero et al., 2017).

This highly complex tectono-dynamic situation of intense intraplate deformation is manifested in a high density of faults, most of which are considered active or potentially active over northwestern South America and southeastern Central America. In addition, seismicity is spread over a broad area across the wide plate boundary in northwestern South America, Central America, and southwestern Caribbean. This complexity was referred by Trenkamp et al. (2002) as a “Wide Plate Margin”. This, coupled with a potential of large magnitude megathrust and tsunami events related to the Pacific subduction zone, means that a high percentage of Colombia’s population lives under a constant threat of unannounced large magnitude earthquakes and tsunamis, with a potential of inflicting great damage in terms of loss of lives and destruction of infrastructure (Hermelin, 2005). Additionally, another threat is posed by the many active volcanoes located on the North Andean region that have a potential for devastating eruptions as shown in the Armero disaster of November 13, 1985, the second worst volcanic disaster in the last century,

caused by the eruption of the Nevado del Ruiz volcano, Colombia (Herd, 1986; Banks et al, 1990; Thouret, 1990).

Figure 1 shows the main tectonic plates that converge in the study region, main geological faults located in Venezuela, Colombia and Ecuador, and volcanoes on the Colombian and Ecuadorean territories. Figure 2 corresponds to a map showing the regions and the political boundaries between the continental countries located in the study region.

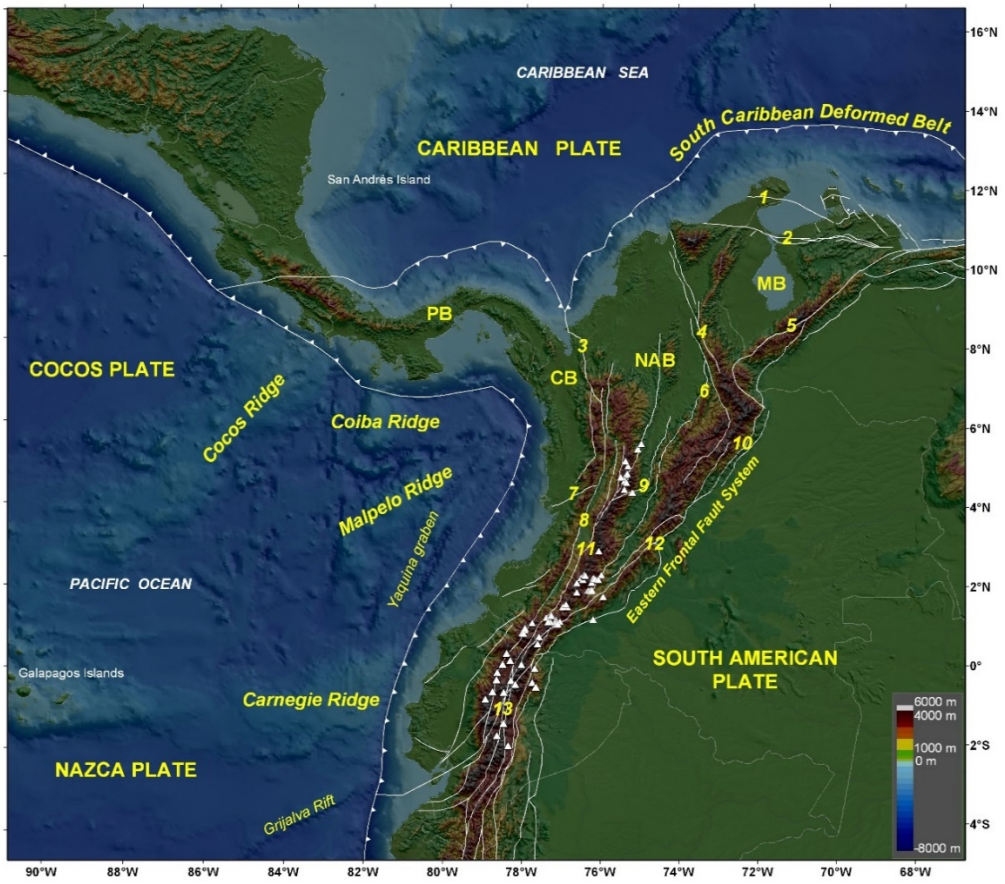

Figure 1. North Andes Region Tectonic Framework.
Blocks: MB (Maracaibo B.), NAB (North Andean B.), PB (Panama B.), CB (Choco B.). **Faults:** 1 (Cuisa F., 2 (Oca F.), 3 (Uramita F.), 4 (Bucaramanga-Santa Marta F.), 5 (Boconó F.), 6 (Suarez F.), 7 (Garrapatas F.), 8 (Cauca-Patía F.), 9 (Ibagué F.), 10 (Guaicáramo F.), 11 (Romeral F. System), 12 (Algeciras F.), 13 (Pallatanga F.). **Volcanoes:** white triangles. Modified from Mora-Páez et al., 2018.

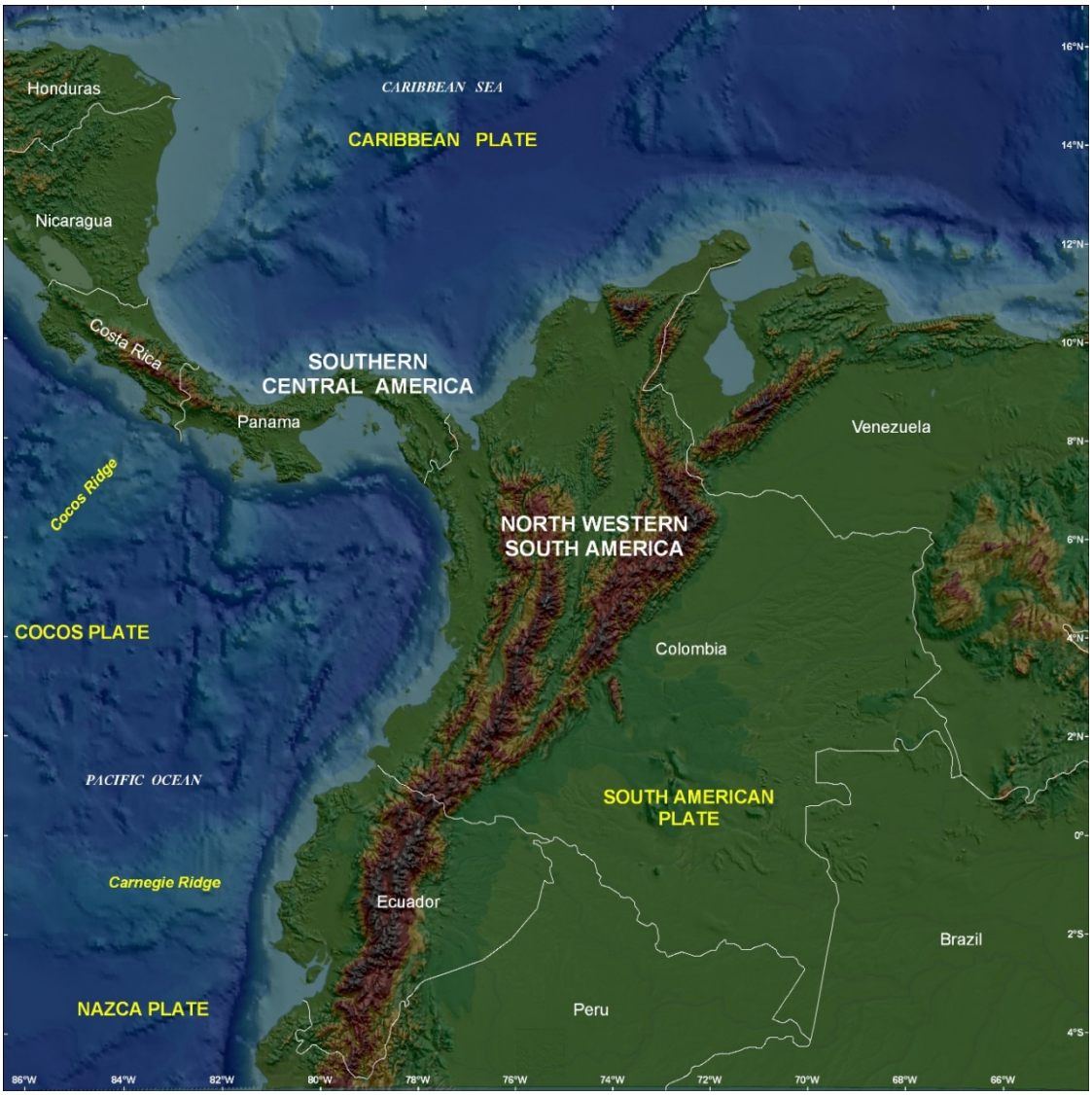

Figure 2. Regions and political boundaries on the study zone.

1.1. Tectonic frame of Northwestern South America

Northwestern South America is a broad ocean-continent convergent plate boundary zone with a clear expression of major plate tectonic features such as active seismicity, active volcanism, subduction and on-going arc-continent collision. Active seismicity occurs continuously along the western edge of South America. The oceanic Nazca Plate is being subducted eastward under the continent along a well-defined Wadati-Benioff zone. The Andes of Colombia, Venezuela and Ecuador represents the northern termination of the Andean belt, which extends along the western margin of South America. The most tectonically notable feature of the South American Plate is the Andean Mountains, which share a common tectonic pattern from Colombia in the north to southern Chile. The major

physiographic features of the Andes are the result of the subduction of the Pacific lithosphere beneath the South American continent. The Nazca-Andean margin is characterized by a marine trench, a row of active volcanoes, longitudinal mountain ranges, and shallow to deep seismicity (Hall and Wood, 1985). The bending of the Nazca plate and its interaction with the South America plate is indicated by the concentration of epicenters to the east of the Colombian-Ecuadorian trench. The boundary between these two plates in the region of Ecuador and southwestern Colombia is one of the few plate-boundary segments that have produced major earthquakes more than once during the period of instrumental seismology (Mendoza and Dewey, 1984).

Three distinct tectonic regimes characterize the Nazca plate oceanward of Colombia and Ecuador. Between latitudes 1°N and 7°N, the ocean bottom topography is nearly flat. Its age varies progressively from 10 to 26 million years toward the north (Lonsdale and Klitgard, 1978). Its subduction to the east, under Colombia, coincides with a row of active strato-volcanoes. Between latitudes 2°S and 4°S, the ocean bottom in front of the Ecuadorian trench is a 230 km wide fractured and complex zone. In between these two tectonic regimes, between latitude 1°N and 2°S, a submarine mountain range called the Carnegie Ridge, which was generated by the Galapagos mantle plume, collides against the South American continent. Where the subduction of the Carnegie Ridge takes place, the trench is shallow, the coastal region is uplifted, and extensive and chemical diverse volcanism occurs in the Andes (Londsale and Klitgard, 1978). West of the Ecuadorian Trench, there is a fractured and complex zone. This region is cut by several oceanic fracture zones trending in the NE direction (Yepes et al., 2016); the northern one of them, the Grijalva fracture is showed in the Figure 1. As this region is subducted under the South American plate, it may behave as a separate microplate independent of the adjacent plates (Pennington, 1981; Hall and Wood, 1985).

With the advent of instrumental seismology, several earthquakes during the last century of Ms>7.5 have been located in the Colombia-Ecuador subduction zone, the most powerful being in 1906. This great earthquake (Ms 8.7) of January 31, 1906, (Mw 8.8 according to Gutscher et al, 1999) ruptured the Ecuador-Colombian subduction interface over ~500 km in length (Kelleher,1972). The same area broke again in sequence from south to north in the earthquakes of May 14, 1942 (Ms 7.9), January 19, 1958 (Ms 7.8) and

December 12, 1979 (Ms 7.7) (Herd et al. 1981; Kanamori and McNally, 1982) (Figure 3). Nishenko (1989) estimated a 60-90% time-dependent probability for the recurrence of either a large (7.0 < Ms < 7.7) or great (Ms > 7.7) shallow-plate boundary earthquake during the 10-year period 1989-1999, and Papadimitriou (1993) considered a 68% time-dependent probability for a large (Ms > 7.5) in the same area for a period of time between 1992-2002.

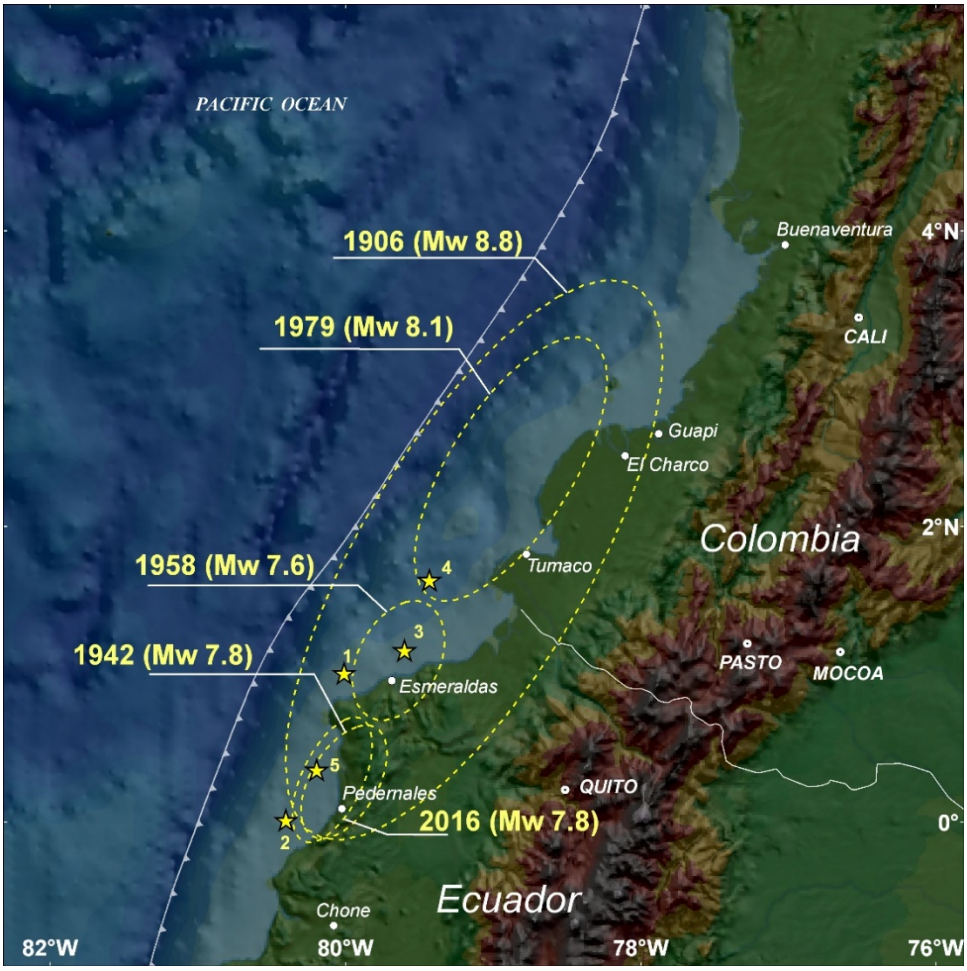

Figure 3. Main earthquakes that have occurred along the Colombia-Ecuador trench. Earthquakes: 1) January 31, 1906; 2) May 14, 1942; 3) January 19, 1958; 4) December 12, 1979; 5) April 16, 2016 (Modified from Adriano et al., 2017, and Nocquet et al., 2016)

The most recent large seismic event in the North Andean region occurred on April 16, 2016, when a Mw 7.8 earthquake struck the coast of Ecuador, and was also felt in Colombia and Peru. This earthquake took place at the southern segment of the Nazca subduction zone along the pacific coast of Colombia-Ecuador, and was almost a repeat of the Ms 7.9 1942 earthquake, the first one of the sequence of three seismic events after the

great 1906 Mw 8.8 earthquake (Nocquet et al, 2017). Mothes et al. (2018) estimated, from near-field GPS stations, horizontal surface displacements up to 80 cm and High-Rate GPS (HRGPS) recorded dynamic displacements reaching 2 m, confirming the strong SW-S directivity of the earthquake.

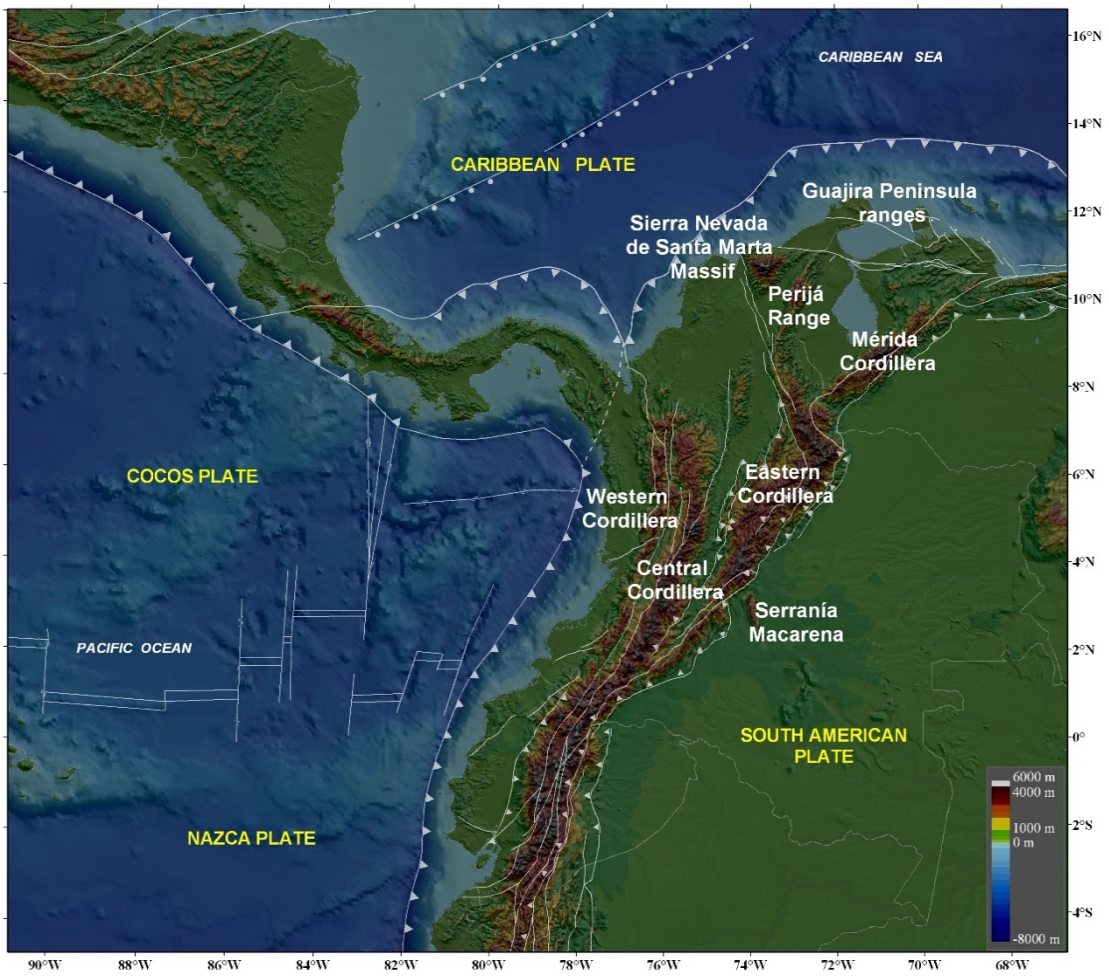

Figure 4. Main physiographic features located in Colombia.

In Colombia, the structure of the crust is very complex because of the diverse tectonic features in the country. In the west, the subduction zone of the Nazca plate has its expression in shallow seismicity that becomes deeper to the east. The dominant physiographic feature in Colombia is the Northern Andes Mountain System, which is divided into three great cordilleras between 1°N and 8°N of latitude: Occidental (Western), Central, and Oriental (Eastern). Other ranges include the Sierra Nevada de Santa Marta (Santa Marta massif), Guajira Peninsula ranges, and physiographic extensions of the Eastern Cordillera northeast into Venezuela, including the Sierra de Perijá and the Mérida Cordillera (Venezuelan Andes) (Figure 4). Figure 5 corresponds to a map of geological

faults in Colombia (SGC, 2015), which indicates the intense tectonic deformation in the country, with faults mainly in the general south-north direction, but also in the west-east direction.

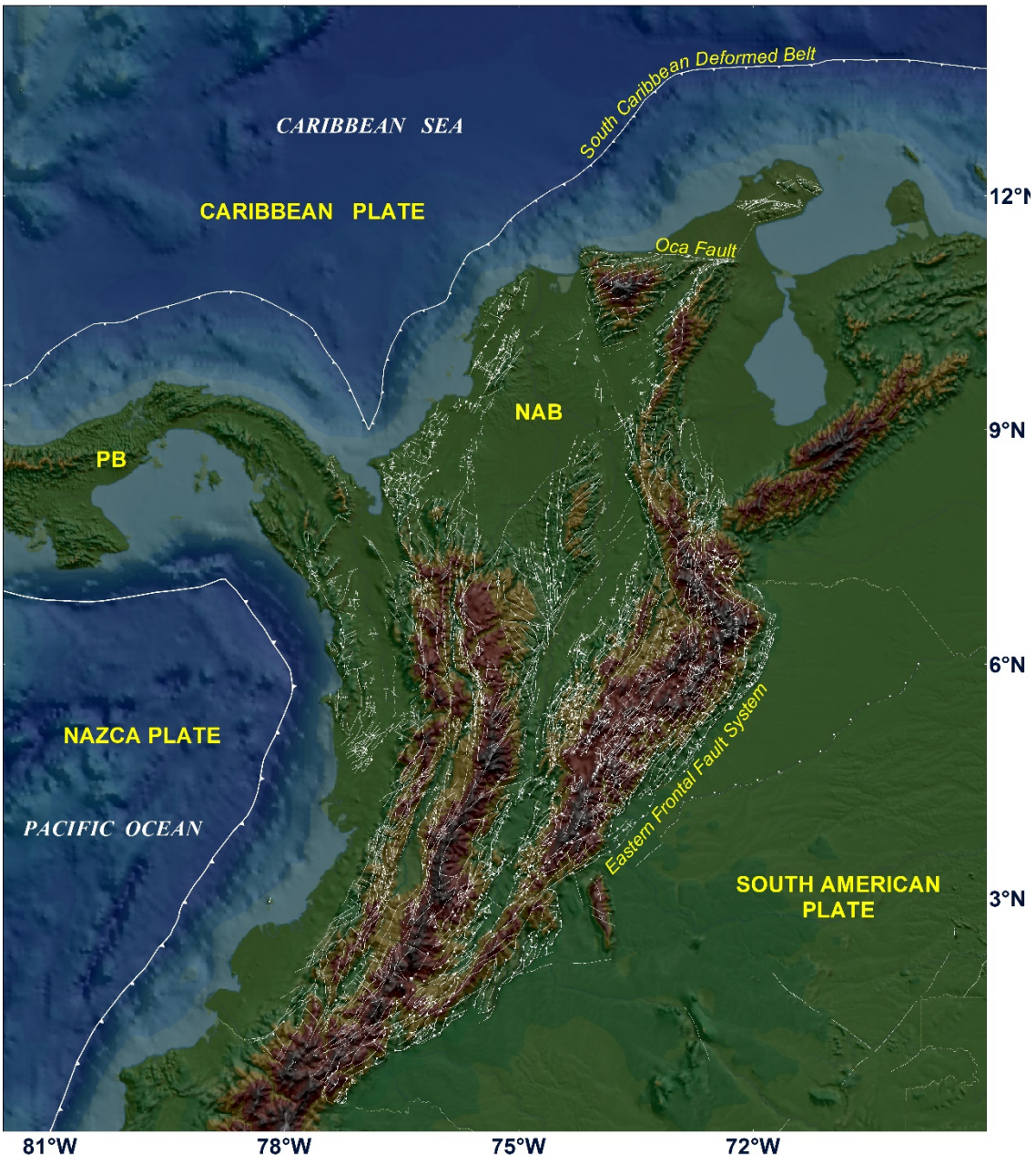

Figure 5. Geological fault maps of Colombia (SGC, 2015).

There is a volcanic chain along the Central Cordillera, and zones of normal and reverse faulting, as well as shallow and deep seismicity. The Nariño Project, a refraction experiment permitted to obtain the velocity structure of the crust and confirmed the great complexity of the crustal structure (Meyer et al., 1976; Ramírez and Aldrich, 1977).

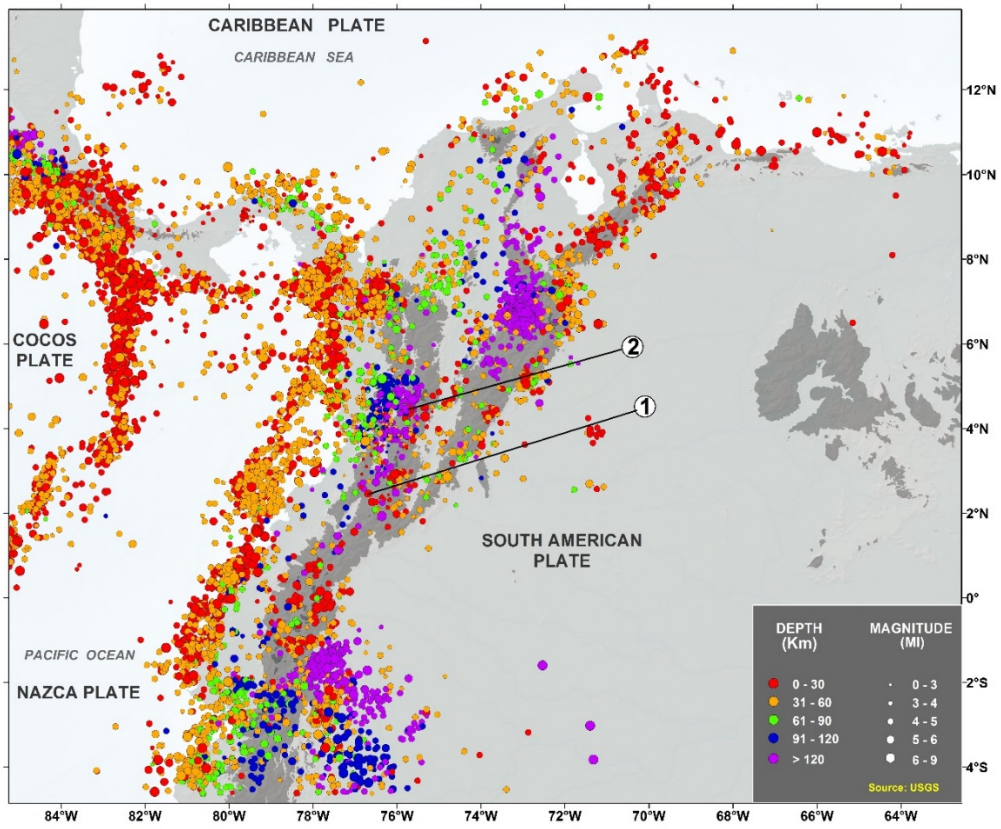

Figure 6. Earthquake epicenters in Colombia and surrounding areas obtained from NEIC and the National Seismological Network of Colombia (1993-2017).
Seismic events: 1, 1983 Popayan earthquake; 2, Quindio Earthquake

Colombia is a seismically active country and has several areas of high seismic risk due to the complex tectonics described above. Figure 6 shows earthquake epicenters obtained from NEIC and also from the National Seismological Network of Colombia from June, 1993 until December, 2017. Two recent intraplate earthquakes are important in the history of disasters in Colombia: the 1983 Popayán earthquake and the 1999 Quindío Earthquake. The first one, on March 31, 1983, a shallow earthquake Mw 5.7, (2.45ºN, 76.67ºW, depth 12 km) destroyed Popayán, a small city located in southwestern Colombia. There were more than 200 deaths and about 1500 injured; some 30,000 people were left homeless (Lomnitz and Hashizume, 1985; INGEOMINAS, 1986). This earthquake is of great scientific importance for the country because it allowed to start considering the necessity to establish in Colombia a national seismological network. The second one, on January 25th, 1999, an earthquake affected the Coffee Growers Region in central Colombia, (4.432 ºN, -75.703 ºW, depth 18 km, Mw 6.2, 18:19:16 UTC); it

was the most important recent intraplate earthquake that caused extensive damage and the death of 1,185 people and injuries to approximately 8,500 (PNUD-CEPAL, 1999). The main shock ruptured along a left-lateral strike slip with a normal faulting component. This faulting was located at a shallow depth in the continental crust. Its rupture length was 11.7 km and 10.6 km width; this yields a total rupture area of 124 km^2 (Monsalve and Vargas, 2002). Because of this seismicity, the Colombian Geological Survey, the local authorities of the Armenia city and the Quindío Department, as well as the academic participation of the Universidad del Quindío, decided to establish the Quindío Seismological Observatory for monitoring the seismicity generated on the region (Vargas et al. 2018). Appendix A provides an overview of some of the major earthquakes that have affected the Colombian territory.

1.2. Tectonic frame of Southern Central America

Southern Central America is defined as the combined land areas of the countries of Costa Rica and Panama and their adjacent offshore areas in the Pacific Ocean and Caribbean Sea (Mann, 1995). Molnar and Sykes (1969) first placed southern Central America into a plate tectonic framework by pointing out that the region forms a tectonically active junction between four major lithospheric plates: Caribbean, South America, Cocos and Nazca. This recent plate tectonic activity has imposed a confusing overprint of late faults, large-scale rotations and uplift. The southern Central American convergent margin is created by subduction of the Cocos and Nazca plates underneath the Caribbean plate. The upper plate in this region contains the moving Panama block that is detached from the Caribbean plate by a diffuse boundary of deformation to the west, a back-arc thrust belt to the northwest and by a deformed accretionary prism sequence offshore central Panama to the northeast (Morell, 2016). The tectonics and kinematics of the Panama block have been described by several models ranging from internal deformation of the isthmus along isthmus-cutting strike-slip faults (Silver et al., 1990) to the interaction of small tectonic blocks (Adamek et al., 1988; Trenkamp et al., 2002; Rockwell et al., 2010). Thus, the Isthmus of Panamá, which acts as a separate Panamá or Chocó-Panamá microplate (Adamek et al., 1988; Kellogg and Vega, 1995; Lundgren et al., 1999; Taboada et al., 2000; Trenkamp et al., 2002) provides an additional complexity to this area. The Panamá block is considered as a broad zone of deformation (Pennington, 1981) with diffuse boundaries.

Offshore southern Panamá, the boundary between the Panamá microplate and the Nazca plate is delimited by the Southern Panamá fault zone or Southern Panamá deformed belt, a diffuse left-lateral fault zone that accommodates the eastward motion of the Nazca plate, and north-south convergence (Jordan, 1975; Hey, 1977; Adamek et al., 1988; Silver et al., 1990; Mann and Kolarsky, 1995; Westbrook et al., 1995). Thus, it is possible to say that Costa Rica and Panama, the easternmost countries of Central America, are immersed between the sinuos east-west trend of the North Panama Deformed Belt the South Panama Deformed Belt; both belts are mainly located offshore and are seismically active (Bird, 2003).

1.3. Tectonic framework of South Caribbean

The southern limit of the Caribbean plate at the region of Colombia, Panama and Venezuela is characterized by a broad zone of internal deformation (Pennington, 1981). The southern boundary of the Caribbean Sea is a transpressive plate boundary between the Lesser Antilles and western South America subduction zones (Molnar and Sykes, 1969). Schubert (1984) said that the existence of large strike-slip fault zones in northern Venezuela supports this interpretation. In northern Colombia and Venezuela, deformation and shallow seismicity is diffused, and the Andean mountains are two to three times wider than the southern Colombia and Ecuador (van der Hilst and Mann, 1994). They also confirmed that the North Andean Block and Maracaibo blocl are converging with the Caribbean plate by showing a high-seismic velocity slab of the subducted Caribbean lithosphere which dips in a direction of 150° at an angle of 17° to a depth of 275 km.

1.4. The North Andean Block

Colombia is located in the northwestern corner of South America, and a large part of its territory is located in the Northern Andean Block, an area characterized by existing deformation, evidenced by different physiographic features previously mentioned. However, it is important to know the meaning of the Northern Block of the Andes.

Pennington (1981) considered that the concept of plate tectonics was difficult to be applied to north of the equator along the margin of the Andes, the south of the Caribbean

as well as in Panama region. In this part of the world, the Cocos, Nazca, South American and Caribbean plates interact, but there is no complete agreement regarding the boundaries between such plates. Thus, based on instrumental seismicity, he proposed the existence of a crustal block separated from the rest of South America by the Eastern Front Fault. This block is compressed in an E-W direction by the South American and Nazca tectonic plates, and moves NNE with respect to the rest of South America, as a consequence of the collision of the Carnegie ridge in the Colombia-Ecuador trench; this block is currently known as the North Andean Block. Freymueller et al. (1993) mentioned that the North Andes Block is limited by the Colombia-Ecuador trench to the west, the South Caribbean Deformed Belt to the north, and the Boconó and the Eastern Frontal fault zones to the east.

To the south, the boundary between the North Andean Block and the South America plate is located on the Dolores-Guayaquil megathrust, that is apparently reactivated in an oblique dextra-normal direction (Collot et al., 2002). To the northeast, the boundary continues along the East Andean Frontal Fault system along the eastern mountain range of Colombia to the Andes of Merida in Venezuela. According to Audemard and Audemard (2002), this fault system is a partitioned slip zone on sub-parallel and/or en-echelon dextral and thrust faults, including the Pallatacanga fault in Ecuador; Algeciras, Guicáramo and Yopal faults in Colombia, and Boconó fault in Venezuela, (Taboada et al., 2000; Audemard and Audemard, 2002). The northern boundary of the North Andean Block is the subduction zone, which it overthursts the Caribbean plate. This area extends westward from the Gulf of Darién in Colombia where the Caribbean-Panama-North Andean Block triple junction is located (Bird, 2003). This author considers that the North Andean Block includes the Maracaibo block, and the southwest and north limits of that block, which are the Bucaramanga-Santa Marta and Oca-Ancón faults respectively, which are not considered as block boundaries.

The physiographic scheme of Colombian territory allows to distinguish at least two main domains. The first, to the west, corresponding to a mountainous region characterized by the presence of the Andes mountain range, formed by three mountain ranges separated by depressions and wide valleys, that corresponds to the North Andean Block; and the second, to the east, constituted by extensive plains that make up the regions known as Orinoquía and Amazonía, located on the “stable” South America plate.

This dissertation deals with the following problems in this area of high complexity based on GPS results.

a) The complex horizontal motion in the northwestern corner of South America.
b) The motion of the North Andean Block and the determination of the Euler pole
c) The subduction rate of the Nazca plate beneath South America
d) The velocity in the collision zone of the Panama block with the North Andean Block

2. Importance of GNSS Space Geodesy for crustal deformation studies

Given the tectonic complexity in the study region and the high possibility of occurrence of large earthquakes and tsunamis as well as volcanic eruptions among other hazards of geological origin, it is required to carry out systematic and detailed studies to establish the current situation of the deformation of the earth's crust, using various techniques and methods, such as those provided by the space geodesy developments. Earth scientists from a variety of countries in South America, engaged in tectonic and geophysical research, have approached the complexities of crustal deformation and the consequences of living in active tectonic regions. Amongst them, there is a growing awareness of the potential contribution that space geodesy can make to the detailed observation, analysis and understanding of crustal kinematics in the tectonically most dynamic regions of the continent. In fact, space geodetic studies are now the primary method of studying the kinematics of plate boundary zones on land. Because space geodetic measurements are conducted in a global reference frame, they can be used to measure motions within the boundary zones as well as relative global motions of plate interiors (Stein and Sella, 2002).

The expansion of local and regional space geodesy networks is greatly improving our ability to investigate Earth system processes such as the driving forces of tectonic plates (Ghosh and Holt, 2012). Integrated regional GPS/GNSS networks provide a framework for studying solid earth as well as atmospheric processes at the continental scale. GPS/GNSS station positions can be integrated to produce velocity fields used to constrain kinematic block models of plate boundary zone deformation (Davis et al., 2012; Herring et al. 2016). In spite of the spatial limitations posed by incomplete coverage of national

GNSS/GPS networks, those networks in South America have already contributed to systematic research in estimating the magnitude and spatial variability of interplate coupling, as well as, episodic and aseismic release of energy related to faults (Mora-Páez, 2013). Such observations lead to better understanding of the mechanical processes that govern the behavior of fault systems. Permanent and real time GNSS/GPS networks have the potential to provide data on the motion of individual faults that, together with neotectonic and paleoseismologic field data, constitute a vital input to the evaluation of the seismogenic potential of these faults, as was mentioned by many authors (e.g., Barka and Reilinger, 1997; Blewitt, 2009; Meilano et al., 2012; Symithe et al., 2015; Mukul et al., 2018).

There are also many studies that have demonstrated the utility of regional GPS networks to study the collisional margins and the kinematics of the upper-plate deformation such as those carried out by Sagiya et al. (2002, 2004) in Japan, Wallace et al. (2005, 2009, 2012) in New Zealand.

There has been a long-lasting discussion regarding the best way to describe the deformation of the continents. Some researchers prefer to consider relative movements of rigid blocks while others consider the continuous deformation (Elliot et al., 2016). These two points of view have been the object of study and analysis by different authors. In the first case, known as "microplate or block model", it is assumed that the deformation is active in the continents and can be divided into small rigid blocks separated by important fault zones that can even cut the earth's crust (e. g., Thatcher, 1995, 2009). In this case, each block follows basic principles of the kinematics of plate tectonics, (McKenzie and Parker, 1967, Zheng, 2017). The velocities at any point of the block can be described as rotations around the Euler pole, with strain in the limits of said blocks (Zheng, 2017). In the second case, continuous deformation, it is considered that deformation is treated as continuous in a viscous medium (e. g., England and McKenzie, 1982, King et al., 1994). This form of analyzing the deformation, known as "continuum model", takes into account physical laws to establish the velocities of the surface of a deformed region, assuming that the lithosphere deforms under the consideration of a viscous fluid (Zheng, 2017).

Given the controversies over whether continental deformation is best described as relative movements of rigid blocks or continuous deformation, whether mountain building rates can be compared to convergent boundary processes, and how slip is partitioned at complex convergent plate boundaries, northwestern South America offers a good field laboratory because it includes an active arc-continent collision, margin-parallel slip, and active "flat-slab" and "normal" subduction. In the case of Colombia, the active deformation includes a range of processes and tectonic settings found in few countries, if any, and more commonly spread out over a wider extent than the territory of Colombia. The processes include subduction of oceanic lithosphere, one of the fundamental elements of plate tectonics; moreover, subduction occurs at both relatively high and low rates, at the Nazca plate beneath the west coast of Colombia and at the Caribbean plate beneath northwestern Colombia, respectively.

Thus, the complex interaction and deformation that occurs on the northwestern South America and southeastern Central America can be studied by integrating geodetic networks from Ecuador, Colombia, Venezuela, Panama, and Costa Rica taking into consideration the major tectonic plates that converge in this zone. In addition, GPS/GNSS networks can be used to constrain the magnitude and spatial variability in plate boundary coupling along the principal plate boundary fault systems. This provides the ability for earth scientists to know potentially where and how big a future earthquake may be (Dixon et al., 2011).

In Colombia, the establishment of an adequate network of GNSS stations covering the entire Colombian territory has begun to contribute to the understanding of the crustal dynamic processes that result from interaction of the tectonic plates in northwestern South America, the monitoring of elastic deformation of the crust, the modelling of processes of interseismic plate coupling along the subduction interface, and the estimation of strain accumulation along crustal faults, (Mora-Páez et al., 2013). During the last ten years, the main focus and efforts have been directed to the design and installation of the network, but the generation of a steadily increasing stream of data has permitted, until to date, to construct a sufficiently detailed velocity field that is capable of registering the process of tectonic escape of the North Andean Block (Mora-Páez et al., 2018). It is important to mention that, since the decade of the 1980´s of the last century, Colombia began the

deployment of geophysical instruments to build networks aimed to understand the dynamics of the earth's crust in Colombia. Thus, there are several networks of different types of instruments, at national and local levels (Vargas et al. 2018); the youngest one, the GPS National Network for Geodynamics started being deployed and operation in 2007 (Mora-Páez, 2006; Mora-Páez et al., 2018).

3. Dissertation content

This dissertation presents the work carried out by myself during more than 30 years in geodetic applications for studying the geodynamics in Colombian territory. I started working on volcano deformation in 1987 at the Volcanological and Seismological branch in Manizales city, and one year later, I began to receive information about the development of space geodesy techniques and its applications in geodynamics, that permitted me since then, to be involved in three stages: first, to be involved in the Central And South America (CASA) Project (1988-1998); second, to be part of the Survey of Geodynamics Information of the Colombian Territory Project (1998-2006), that included a GPS componente carried out by myself; and third, to propose the deployment of a National GPS Network for Geodynamics (Mora-Páez, 2006), a personal dream that permitted me since 2007 to conduct and to lead the development of the GeoRED Project. Technical issues about GPS and its fundamentals and explanations about the routine analysis of processing are not considered in this dissertation.

This dissertation is composed of seven chapters including this introductory chapter. A complete bibliography is presented as well as five appendixes at the end.

Chapter 1, Introduction, presents a brief description of the tectonic framework of the northwestern corner of South America and southeastern Central America, which corresponds to the tectonic convergence between the Nazca, South America, Caribbean and Cocos tectonic plates. Also, a general description of the main earthquakes that have occurred in the Northern Andean Block and the general seismicity in the study region is shown. The importance of GNSS spatial geodesy for crustal deformation studies in this part of the world is also pointed out.

Chapter 2, Overview of GPS for Geodynamics studies in Colombia, describes the introduction of the scientific use of GPS for geodynamic studies in the northwestern corner of South America, southeastern Central America and the Caribbean region based on four sequential components over time.

Chapter 3, The GNSS GeoRED Project, presents a general description of the GeoRED project, which corresponds to the GNSS infrastructure implemented in Colombia in order to carry out geodynamic studies, consisting of permanent geodetic stations of continuous operation as well as field stations of episodic occupation under field campaigns style.

Chapter 4, GPS Data and Analysis for Velocity Estimation, indicates the GPS data that are being processed at the Regional Data Processing Center in Colombia, software used, time series generation and as well as the estimation of geodetic velocities based on stations located in Colombia and also in neighboring countries.

Chapter 5, Results, presents the new velocity field for the northwestern of South America, southeastern of Central America and the southwestern Caribbean derived from GPS stations that belong to the GeoRED continuous GPS network in Colombia, and other continuously operating reference sites (CORS) located in Costa Rica, Panama, Ecuador and Venezuela countries. It is also presented a comparison with the results of previous studies. A comprehensive model of the North Andean block (NAB) motion is also presented.

Chapter 6, Discussion, presents the analysis and discussion of the main results obtained using space geodetic technology in Colombia.

Chapter 7 presents a discussion based on GPS results regarding the collision of the Isthmus of Panama, uplift of the Eastern mountain range of Colombia, and scenarios associated with mountain building.

Chapter 8, Conclusions shows the main conclusions of the geodetic work carried out until now, as well as the challenges that Colombia will have to face to advance to gain understanding the tectonic complexity of the northwestern corner of South America through the application of geodetic methods.

CHAPTER 2

OVERVIEW OF GPS FOR GEODYNAMICS STUDIES IN COLOMBIA

The introduction of the scientific use of GPS in the northwestern corner of South America, southeastern of Central America, the Caribbean region, and especially in Colombia focused on the study of the geodynamics of the region has four main time-components namely:

1. The Central And South America (CASA) GPS Project
2. Survey of Geodynamics Information of the Colombian Territory Project
3. The GNSS GeoRED Project
4. The COCONet Project

2.1. The Central and South America (CASA) GPS Project

The CASA Project dates back to early 1988, when scientists from more than 25 organizations and 13 different countries cooperated in the largest GPS project in the world at that time, using 43 receivers to obtain daily information from 59 stations (Kellogg and Dixon, 1990). The CASA Project was planned with the following initial scientific objectives for the first decade, 1988-1998 (Kellogg and Dixon, 1990):

- To obtain baseline measurements between several Pacific islands located on the Nazca and Cocos Plates, and sites in Colombia, Ecuador, Costa Rica, and Panamá, that, when compared with future observations, will monitor subduction rates across the trenches and spreading rates across the Galapagos Rise.
- To establish a GPS network across the South Caribbean Deformed Belt that will demonstrate whether the Caribbean crust is subducting amagmatically beneath the northern Andes.

- To acquire baseline measurements across the Romeral, Santa Marta, and Boconó–East Andean fault systems that would eventually determine strain distribution across the North Andean continental margin.
- To obtain elevation measurements that would determine whether the northern Andes are still rising, as suggested by uplifted terraces of Pliocene-Quaternary age.
- To co-locate GPS and Doppler stations to improve the transformation between the WGS72 and WGS84 reference systems in this region.

A fundamental aspect in the development of the CASA Project was the support provided by the deployment of a first civil global tracking network (Neilan et al, 1989), in order to reduce errors in the satellite ephemeris as well as the uncertainties in the accuracy of the baselines. It was an important step in the development of a global network of permanent GPS stations (Freymueller et al., 1990). Figure 7 shows the stations that were used as reference network for the CASA Project observations.

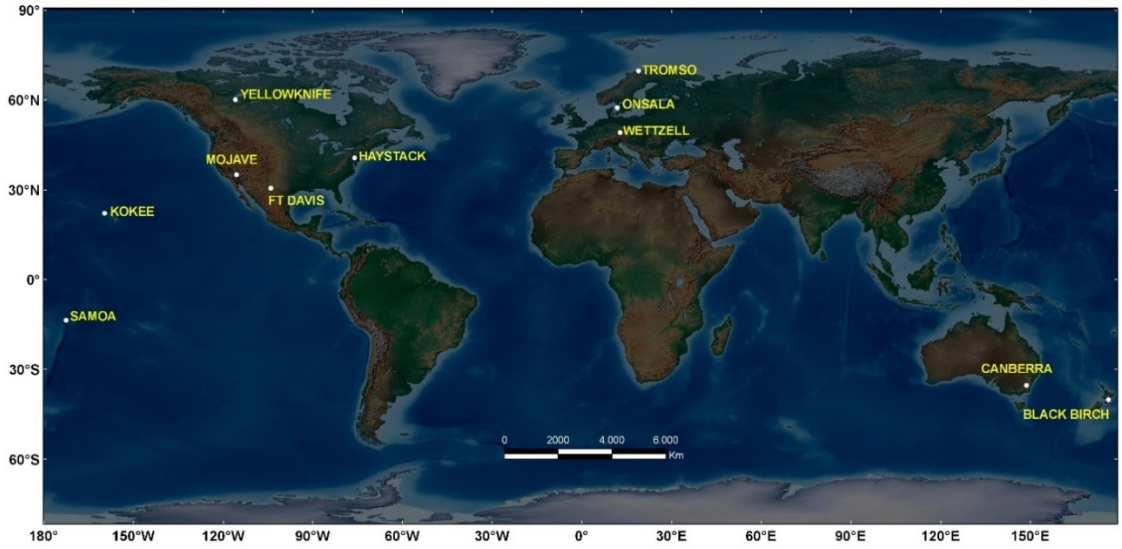

Figure 7. Tracking network that supported the CASA Project observations.

CASA Project was sponsored by NASA and NSF from USA together with institutions from each of the participant countries. Colombia was the center of the North Andean field campaigns, and the enthusiastic participation of INGEOMINAS (now the Colombian Geological Survey) with logistics, training, and personnel was a key to the success of CASA.

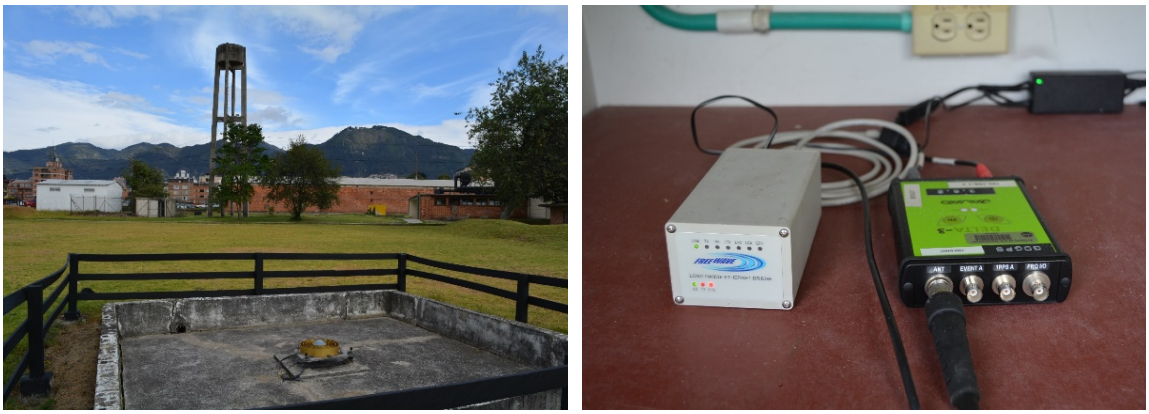

Figure 8. Current BOGT IGS station.

An important date for the development of a GPS network in Colombia was November 4, 1994. With the support of NASA and under an agreement, the first permanent GPS station was installed in Bogotá, Colombia, as part of the Fiducial Laboratories for an International Natural science Network (FLINN) Global Network, (NASA, 1991) and named BOGT. Figure 8 shows the instruments that are currently installed in this station.

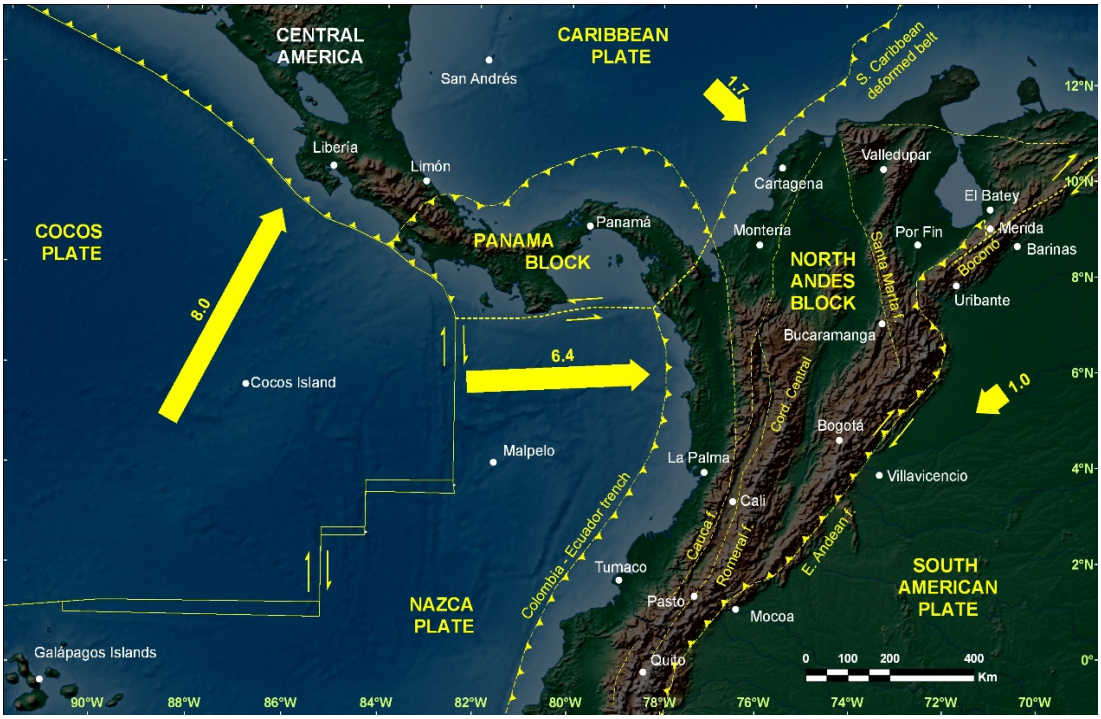

Figure 9. CASA UNO sites, tectonic framework of the northwestern corner of South America and southeastern of Central America. Present-day plate motions (bold arrows) relative to the NAB (Cocos plate motion relative to Caribbean). Adapted from Kellogg and Dixon (1990).

Figure 9 shows the CASA UNO sites, the tectonic framework of the northwestern corner of South America and southeastern Central America, and the present plate motions relative to the NAB (Cocos plate velocity is expressed with respect to the Caribbean plate); showing average slip rates (cm/yr) during the last 5 to 10 m.y. (Kellogg and Dixon, 1990), prior to the use of space geodesy technology. Those models were tested with GPS measurements of relative plate motion in the northwest corner of South America.

Although the primary purpose of the GPS CASA project, the most extensive GPS experiment in the world at that time, was to make measurements in areas of significant crustal deformation, it also allowed obtaining various scientific results based on the execution of the field campaigns. For example, the named CASA UNO experiment, which corresponds to the analysis of data acquired in the 1988 campaign using TI-4100 receivers during three five-day sessions, allowed to face the challenge of having baselines greater than 100 km and even 1000 km, which generated an increase in GPS errors because of the length of the baselines and the uncertainties in the ephemeris of the GPS satellites at the time of the observations. Usually, this effect was handled by collecting GPS data at some sites whose positions were well known using an independent technique such as a VLBI (Very Long Baseline Interferometry), Dixon et al. (1985). These fiducial sites thus defined the frame of reference for the observations carried out. In several previous GPS experiments, VLBI stations established in the United States were sufficient for this purpose, even for some experiments that were conducted outside the continental United States, for example, in the northern Caribbean (Dixon et al. 1991a) and also in the Gulf of California, Mexico (Dixon et al. 1990b). However, the accuracies of satellite ephemerides based on a fiducial network in the US degrades over South America. The analysis carried out in CASA UNO experiment allowed to suggest a significant improvement in the accuracy of the GPS orbits and baselines using an extended tracking network (Schutz et al, 1990) as in fact it was done by implementing a network of GPS receivers in several sites of the world, Figure 6. In this way, significant improvements were achieved by having a global tracking network (Kellogg and Dixon, 1990), which became the first step of what is now known as the global network of permanent tracking stations. The large number of cycle slips in the CASA UNO experiment data set made it clear that manual intervention in data analysis should be minimized, for which an algorithm for the automatic edition of GPS data was developed and tested (Blewitt, 1990). The baseline solutions established the first set of measurements

for the monitoring of crustal deformation in the northern Andes (Kellogg et al., 1990). Some calibration tests of the wet troposphere were also carried out to minimize errors (Dixon and Wolf, 1990).

With respect to the application of GPS in geodynamics in the northwestern corner of South America, the results of the GPS measurements of the CASA project can be summarized in the following aspects: a) estimation of the rapid oblique subduction of the Nazca plate occurring along the Colombia-Ecuador trench; b) estimation of the convergence rates along the Colombia-Ecuador trench and the transferred motion to the North Andes block that supports its tectonics escape to the northeast; c) demonstration of the active collision of Panama with Colombia and ongoing deformation up to 550 km from the suture zone; d) estimation of the convergence rate of an island in the Caribbean with respect to South America (Trenkamp et al., 2002).

2.2. Survey of Geodynamics Information of the Colombian Territory Project

After the CASA Project, continuation of a densification of GPS stations and field campaigns to occupy them were considered as a very important way to improve our knowledge related to crustal deformation in Colombia. Thus, in 1998, the formerly INGEOMINAS, now Colombian Geological Survey, started the project called "Survey of Geodynamics Information of the Colombian territory", (Pre-GeoRED stage), that corresponds to the systematic process of building field stations in order to increase the number of the GPS field stations network. Coverage was expanded, including volcanic areas such as Nevado del Ruiz and Galeras volcanoes. The primary purpose of this activity was to measure the stress field in Colombian crust using GPS techniques, following the main considerations proposed by Mora-Páez (1994).

In 2003, a subset of 36 sites previously occupied was chosen for a geological and geophysical project to understand the stresses and neotectonic deformation within the central region of the Cauca river valley and the city of Cali, the largest urban center in southwestern Colombia. As part of this study to assess the earthquake hazard potential near Cali city and areas adjacent to the Cauca valley, a field campaigns were performed (Figure 10). Data were collected using the three GPS Trimble receivers and the choke-ring

antennas mentioned before. Site occupations consisted of a minimum of three 8-hour observation days and were continuous over 3 days when security conditions permitted (Trenkamp et al., 2004).

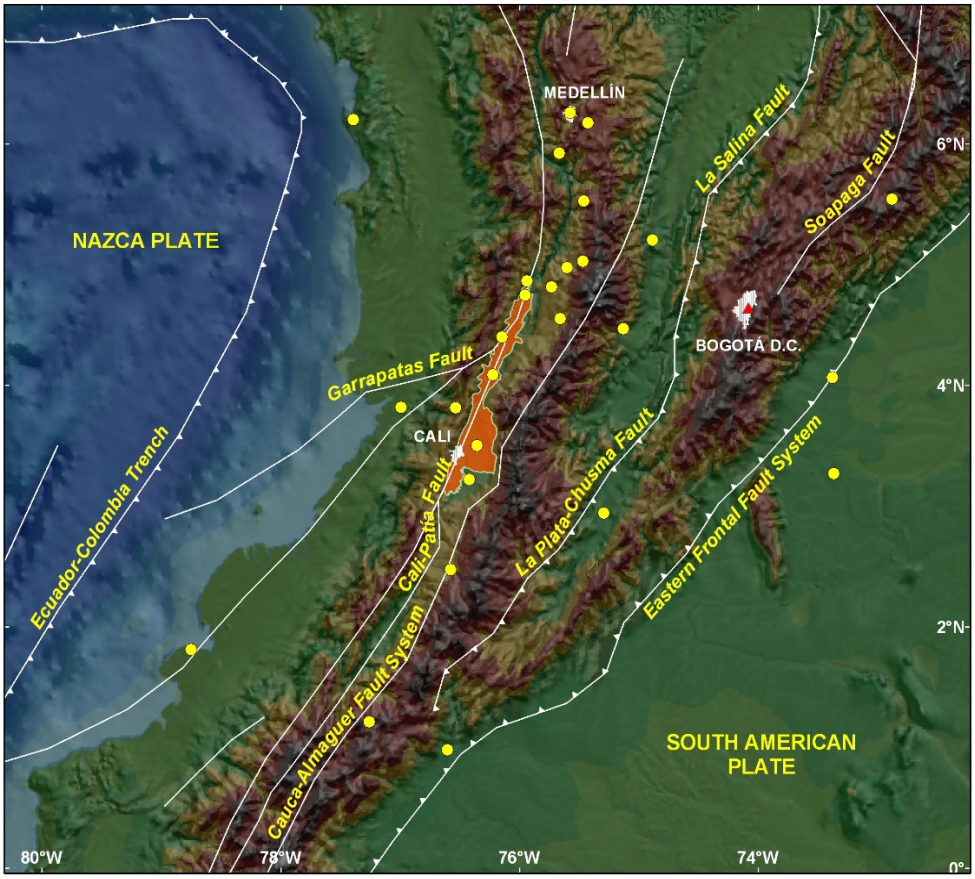

Figure 10. Cauca Valley region and GPS field sites (yellow balls) and BOGT (red triangle) as permanent station. Orange area corresponds to the central region of the Cauca river valley.

2.3. The GNSS GeoRED Project

The GNSS GeoRED Project, a research project performed in Colombia, is the main aspect considered for this dissertation; further illustration of the project will be presented in the following chapters.

2.4. The COCONet Project

On January 12, 2010, a magnitude 7.0 earthquake affected the Republic of Haiti, causing more than 316,000 people dead or missing, 300,000 injured, and over 1.3 million homeless (DesRoches et al., 2011). This earthquake focused world's attention with its solemn reminder of the devastating power that natural hazards can unleash. The proximity of circum-Caribbean nations with burgeoning populations to the active plate boundaries that circumscribe the Caribbean plate gives rise to escalating regional exposure.

For that reason, in order to advance the understanding the geodynamics of the Caribbean plate and to support the regional capacity for hazards identification and risk mitigation, the National Science Foundation funded the Continuously Operating Caribbean GPS Observational Network (COCONet) project, conceived as a way to strengthen and complement existing large-scale, state-of-the-art geodetic and meteorological infrastructure in the Caribbean. The infrastructure will also serve as a platform for international partnerships for science and societal applications, (Dixon et al, 2011; Braun et al., 2012). Under the frame of this project, four new stations were installed in Colombian territory, and integrated to the GeoRED network, and the SAN0 station, located on the San Andres Island, was upgraded.

CHAPTER 3

THE GNSS GeoRED PROJECT

GeoRED is a research and development project based on space geodesy technology that takes a multifaceted approach to cataloging and defining the geodynamics of northwestern South America. GeoRED is a spanish acronym for "**Geo**desia: **R**ed de **E**studios de **D**eformación", (Geodesy: Deformation Studies Network). The general purpose of the GeoRED Project is to "Improve the technical, scientific and operational capabilities in Colombia for analysis, interpretation and policy formulation regarding phenomena related to crustal deformation in Colombia, using GNSS satellite technology" (Mora-Páez, 2006). The GNSS GeoRED project is being executed under the operations framework of the Space Geodesy Research Group (SGRG) of the Geohazards Directorate of the Colombian Geological Survey, and is responsible, among other actions, for geodetic research with geodynamic purposes.

Current endeavors are focused on the acquisition of high quality GPS/GNSS data to be shared by intergovernmental institutions and university research centers within Colombia as well as collaborative international research efforts including reciprocal data sharing between the neighboring countries of Panama, Venezuela, Brazil, Peru and Ecuador.

GeoRED is also designed to meet the following specific objectives (Mora-Páez, 2006):

- To implement a National GNSS Permanent Network for geodynamics with data transmission to an information-gathering center.
- To create GNSS mobile teams for campaign style data acquisition (active fault studies, post-seismic assistance, volcanic crisis assistance, mass movement monitoring, etc).
- To generate information about horizontal and vertical displacements for studies of crustal deformation.
- To establish a high precision geodetic reference frame for multipurpose activities within the Colombian Geological Survey (CGS).

- To provide information within CGS as well as to other government institutions toward the execution of research and development projects using GNSS data

For geohazard decision making in Colombia, especially related to seismic and volcanic hazards, it is of great importance to enhance the technical and scientific capacity to capture, process, analyze, and display crustal deformation in near real time. To increase our knowledge of geodynamic phenomena, especially seismic and volcanic, and help to reduce the risks associated with these disasters, instrumental networks are needed: seismometers, accelerometers, and GPS receivers for geodynamic studies, among others, with good spatial coverage, long term functioning, high data quality, and timely information retrieval. These integrated information networks will allow us to better formulate local, departmental, regional and national development and disaster management plans.

3.1. Sites selection based on working hypothesis

Beginning in 2007, discussions within the GeoRED group led to a master plan for the potential distribution of the GPS permanent stations array and specific areas of interest for campaign site construction. A working hypothesis adopted by the working group in 2010 proposed a division of the Colombian territory into geological blocks. These blocks are bounded by geological faults, whose traces and descriptions were obtained from the existing literature. The region of the Northern Andes in Colombia was temporarily divided into 20 blocks, and the GPS site selection was conducted with this block segmentation into mind, which allows to have, at least, three stations per block (Figure 11).

Several criteria have been used for choosing the most appropriate sites for the installation of the GPS stations, which can be summarized in geological and geodetic conditions, security analysis, potential communication systems, access and logistics. The interdisciplinary work in the field (geodesy, geology) takes those criteria into account for site selection, and is focused in two statements: a) that it is required to ensure the stability of the antenna, which depends on the site of location, type of monument and antenna mounting system, and (b) that this will allow to obtain reliable continuous time series of

station coordinates at each station, which will in turn make it possible to characterize transient signals that may be or not be of tectonic origin (Blewitt et al, 2009).

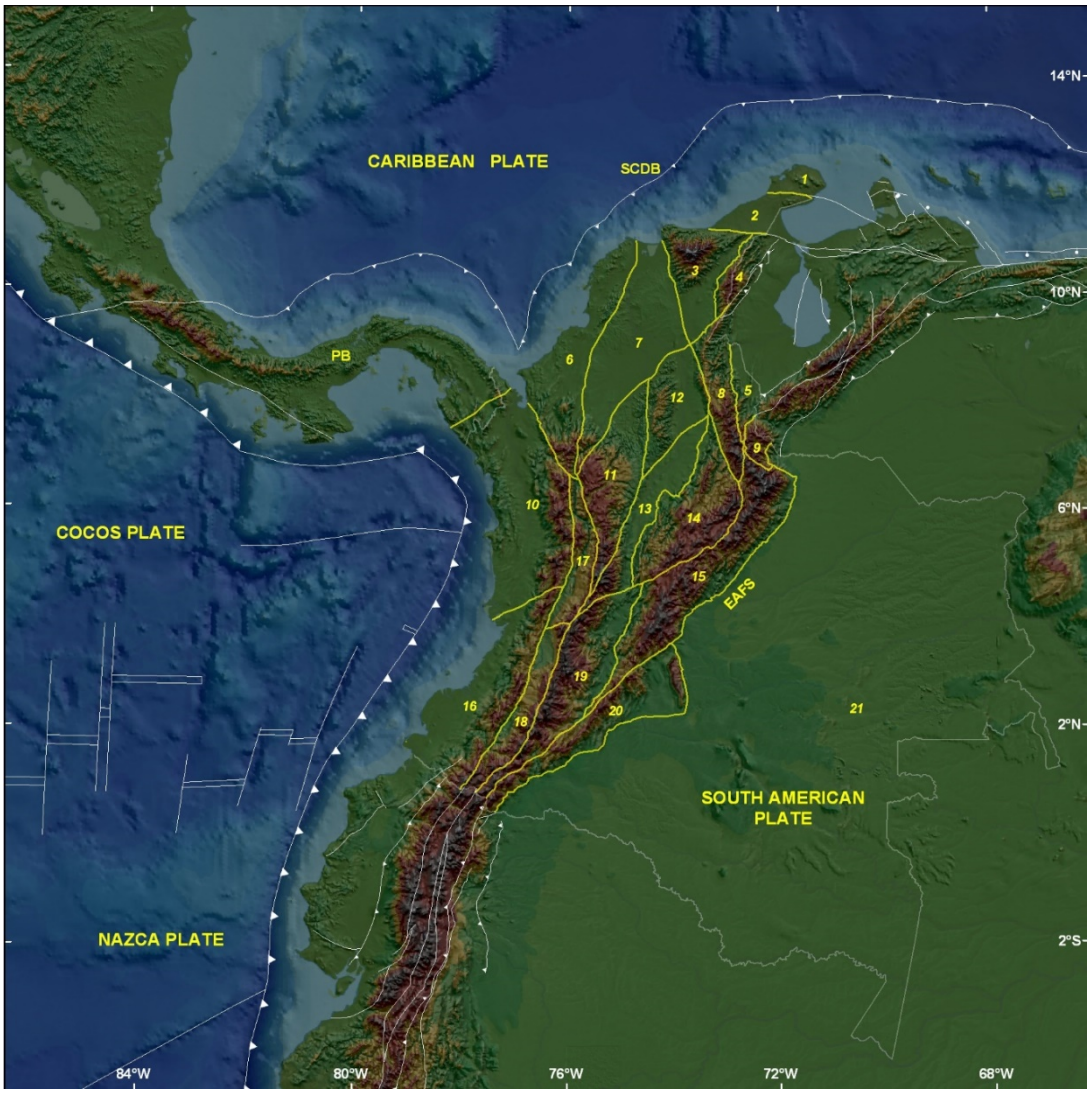

Figure 11. Tectonic segmentation of the Colombian territory as a working hypothesis.

Before performing the field work, some potential zones for selecting sites were identified, according to the distribution of geological blocks and existing surrounding stations in order to increase the spatial coverage of the network. Geological maps and access roads are checked. In the field, we sought for exposed bedrock free from geological faults and possibilities of landslides. When there is no bedrock, consolidated soil is chosen for the installation of the station.

At the potential site for the installation of the GPS station, the sky view is checked in such a way that it is possible to have a good visibility above the horizon, preferably 0° or at least 10° degrees of elevation mask. Sometimes higher values of elevation mask are considered when the safety conditions for the protection of the equipment regarding vandalism in the area are optimal. It is also required to be clear of reflective surfaces as well as the external electromagnetic sources and high voltage power lines that can affect the GPS signals. (IGS, 2017).

Another essential aspect in site selection is security conditions, that minimize or avoid the possible actions of vandalism. Also, the access, both for the installation of the stations or for maintenance are critical issue, with the permissions requirements; this is an important aspect to choose the monumentation type, either shallow-drilled braced or deep-drilled braced monuments. During the reconnaissance trip, it is also analyzed the existing communications and how it is possible to take advantage of the installed communications infrastructure, if exists.

3.2. Site monumentation

Monumentation of the geodetic stations is probably the most important issue to be considered in the implementation of a geodetic network for geodynamics (e.g. Langbein et al., 1995; Blewitt et al, 2009). It is directly related to the data quality; the performance of a permanent geodetic site is dependent on the quality of the signals received by the geodetic antenna. Several institutions such as IGS, UNAVCO, and NGS have analyzed the GPS data quality and have provided general directions about monumentation (e.g. Langbein et al., 1995; Combrinck and Schmidt, 1998; Blewitt et al, 2009; Blume at al., 2013; Bartel, 2014; ICSM, 2014; UNAVCO, 2016; IGS, 2017). In order to achieve a good stability at each site, different monument types and antenna mounts have been used by the Space Geodesy Research Group for both long-term continuous sites and field campaigns.

So, for CORS stations, the following ground-based monuments have been used for the installation of the geodetic antennas: reinforced concrete pillar, shallow-drilled braced, shallow braced (non-drilled), and deep-drilled braced monuments.

The first monuments used for the GPS network were reinforced concrete pillars (CPM), 0.8 m x 0.8 m x 2 m high, sticking out 1 meter above the ground surface (Figure 12). A central steel bar of 3 m length was embedded in the monument; the antenna mounting system was placed on this steel bar. When the monument was setup on consolidated soil, four 1" diameter, 2 m steel rods were hammered to help stabilize the pillar against tilting. When the monument was placed on bedrock, four ¾" diameter steel bar reinforcing rods were set with epoxy into holes drilled about 15 cm into the rock. This type of monument construction was abandoned in 2011 after attending several scientific meetings organized by UNAVCO in the United States as well as participating in the joint installation with UNAVCO staff of COCONet stations in Colombia. It was concluded that the new way of construction of the monument would allow to obtain better results. These new types of installation are as follows.

Figure 12. Reinforced concrete pillar (ALPA station).

The shallow-drilled braced monument (SDBM), or the SCIGN Short Drilled-Braced Geodetic Monument (Mini-Monument), consists of a 1" diameter stainless rod buried about 2.4 m and three 1" diameter stainless steel legs buried about 2 m each in a tripod configuration (quad pod); everything is welded together at the top (Dockert et al, 2018). A combihammer tool is used with active vibration reduction and active torque control for heavy-duty drilling on bedrock (Figure 13).

The shallow braced (non-drilled) monument consists of a 1" diameter stainless rod buried about 4-5 m and three 1" diameter stainless steel legs buried about 2.5 m each one

in a tripod configuration; everything is welded together at the top. A heavy-duty hammer drill is used on consolidated soils.

Figure 13. Shallow-drilled braced monument (ANCH station).

The deep-drilled braced monument (DDBM) corresponds to several 3 m pieces welded in-situ of 1" diameter stainless rod buried 12 meters or more, sometimes more than 20 meters, and three 1" diameter stainless steel legs buried about 3 m each one in a tripod configuration; everything is welded together at the top. A rotary drill is used for the installation. (Figure 14).

Figure 14. Deep-drilled braced monument (AEDO station).

The selection of the monumentation type at each site depends essentially on the access to the chosen site. The shallow-drilled monument is performed using handy-tools, easy to be moved, while the deep-drilled monuments requires the use of heavy rotary drills, which must be transported in four-wheel vehicles. There are some stations that have more

than 2.4 m of drilling and less than 12 meters, that are called intermediate-drilled braced monument (IDBM).

For the campaign stations, two types of monuments have been built, the first one on consolidated soils, and the second one on bedrock. In both cases, a 1” diameter stainless steel rod is used. In the first case, a squared or circular concrete monument of 0.4 x 0.4 m x 1.2 m depth is built; the 3 m steel bar is buried on the soil with a hammer, and it is embedded in the concrete monument. For the second case, a 2.4 m steel bar is introduced into the ground after making a hole using a heavy-duty hammer drill (Figure 15).

Figure 15. Field station installed on bedrock.

3.2.1. Antenna mount adapter

Figure 16. Antenna mount adapters used by the GeoRED Project.
On the left, SECO adapter; on the right, SCIGN adapter.

For the antenna installation, two types of antenna mount adapter have been used by the GeoRED Project. Most of the antennas have been installed using the SECO 2072-series stainless steel adjustable tilt monument adapter, and few of them using the SCIGN mount, that was developed for use in the Southern California Integrated GPS Network (Figure 16).

3.2.2. Geodetic instrumentation

So far, the GeoRED CORS network operates four types of geodetic instruments: the Trimble NetRS and NetR9 geodetic receivers with Trimble choke-ring or Zephyr-2 geodetic antennas; the Topcon Net-G5 receivers with TPS-G5_A1 choke-ring antenna; and the Leica GR-10 receiver with LEIAR20 antenna. The BOGT station operates with a Javad TRE_3 DELTA receiver and also a Javad RingAnt-DM choke-ring antenna. When choke-ring antennas were installed in permanent stations, in order to keep antennas as clean as possible, antenna protective covers known as radomes, developed under the framework of the SCIGN project, have been used (Hudnut et al., 2002).

For the field stations campaigns, Topcon GB-1000 receiver with CR4 choke-ring antenna, Trimble NetR9 receiver with Zephyr-2 antenna, and recently Topcon TPS NET-G5 with TPSG5_A1 antenna have been used. For data collection, the antenna is installed on the corresponding markers using a 1-meter spike-mount system. The use of a 1-meter spike-mount was adopted with the purpose of eliminating the possibilities of mistakes in the measurement of the antenna height in field operations, and also with the intention to improve solutions in each campaign that will permit to make some comparisons in the vertical component. This idea came from a similar device of 0.50 m height provided by UNAVCO though 1-meter height was chosen in order to reduce the multipath effects.

In all cases, both for the installation of permanent as well as the field stations, the orientation of the antenna is established after making the correction for the local magnetic declination. This is always done prior to the installation, and depends on the geodetic coordinates of the locality, that are obtained during the field reconnaissance. This procedure is necessary to guarantee the correct orientation of the antenna.

The tracking/logging satellites of the majority of permanent stations is 1 Hz. There is an exception in those stations that have no connection for data download; in these cases, it is configurated to every 15 seconds which guarantees the storage of data over long time periods. Until now, the receivers are configured to receive signals from the GPS and GLONASS satellites.

3.2.3. Storage of the equipment in the GPS site

For the installation of the permanent stations, two types of enclosures have been used, the first setup on the floor, and the second setup on a steel post that is buried in the ground (Figure 17).

Figure 17. Enclosures used by the GeoRED project.

The metal floor enclosure was specially designed as part of the project for the specific purpose of storage and protection of the permanent station hardware and were cemented on the ground. They are hermetic waterproof boxes with adjustable thermostats that control the activation of fans to assure the internal air circulation.

The second type on enclosures are a slight variation of the original design used by UNAVCO for the installation of the stations of the COCONet project. These enclosures, made in Colombia, are built in aluminum, both internal and external knockouts for passing wires and cables, weatherproof seals, and are designed to be mounted on a post, that is cemented into the ground and strong enough to support 2 or 4 batteries, On the top of the post, the solar panel is mounted, and sometimes meteorological sensors are also installed.

In cases where GNSS stations are located in the same place as stations that belong to the National Seismologic Network, the same physical infrastructure for equipment storage is used for the receiver and additional equipment.

3.3. Data transmission

Data acquired at the CORS stations are transmitted to the data gathering center in Bogotá through one or by the combination of two of the following ways:

a) Direct connection to Internet and/or use of the facilities of the local entities that are the proprietors of the terrain where the stations are installed.
b) Radio frequency (RF) telemetry link
c) Satellite link using the segment assigned to the Nacional Seismological Network in those cases of sharing the station sites of seismic stations.
d) Cellular modem
e) Satellite linked Internet using Ka band, restricted to the central area of the country (Figure 18) that permits to have data in the processing center in near-real time.
f) Manual data download

Figure 18. Data transmission via satellite internet link, MET sensor and enclosure at TEAT station.

The radios that are used for the radio-link data transmission are spread spectrum type (900 MHz spectrum). The satellite internet works in the Ka band connecting to the

Amazonas-3 satellite. Diameter of the antennas is 0.74 cm, and frequencies range between 26.5 to 40 GHz.

Figure 19 shows the diagram of the main components of Information and Communication Technologies that correspond to the GeoRED project.

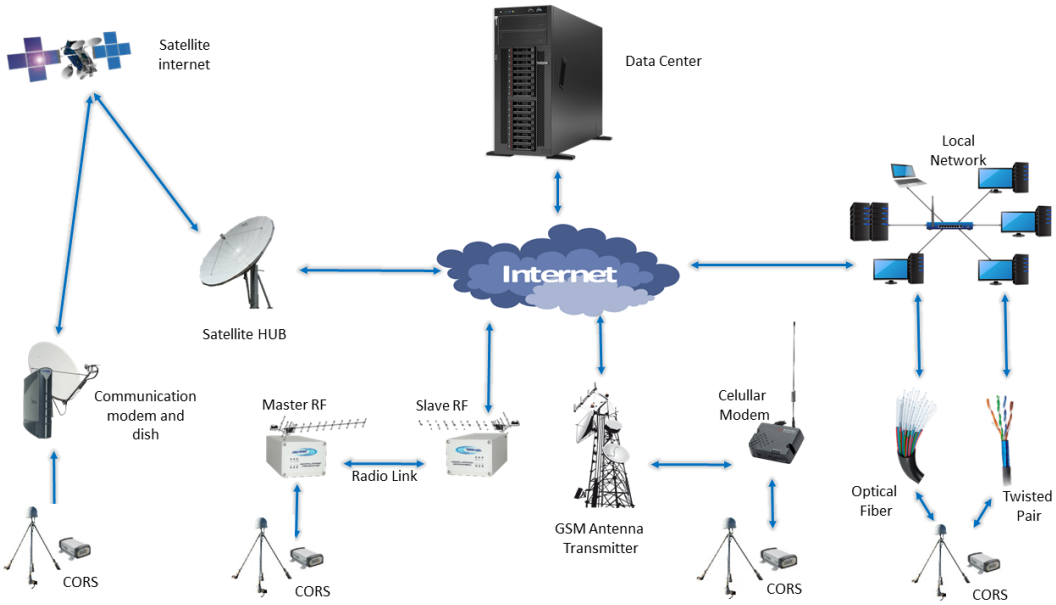

Figure 19. Diagram of ICT technologies - GeoRED Project.

Figure 20 shows the arrangement within the enclosure of two data transmission systems used by the GeoRED project, in this case, satellite linked internet and radio-modem.

Figure 20. Instruments stored inside the enclosure.
Left, internet satellite link; right, radio-modem

3.4. Power supply

Given the conditions that most permanent GNSS stations are installed in remote locations, it is necessary to think about both power supply and data transmission.

The power source of the permanent stations are photovoltaic cells and batteries that guarantee the functional autonomy of the system, using solar panels of 150 W. Solar panels are wired in parallel and connected to the back panel via a solar isolation block, which incorporates a lightning protection device, Delta LA302-DC lightning arrestor, installed on the external part of the enclosure, that protects the power system from surges due to atmospheric static discharge via the solar panels. All stations are also protected against electrical discharges by means of the Hidrosolta system of ground-connection. Solar regulator, additional electrical protection like breaker and steel bar as well as ozone capsules of Huhber-Suhner type for safeguarding the antenna-receiver connection are being employed in all permanent stations. The batteries are sealed, AGM (absorbent glass mat), free of maintenance, 12 V, 110 Ah. These types of batteries are less prone to sulfation and provide good electrical reliability. The batteries are wired in parallel and connected to the back panel.

The daily power consumption of the GPS receiver is approximately 5 W. Data transmission consumes approximately 5.2 to 29 W depending on the system. Thus, the total power consumption is calculated as 10.2 to 34 W. The number of solar panels and batteries are determined based on the data transmission system. Each site is equipped with 1 to 4 monocrustalline solar panels (150 W for each) and 2 to 4 batteries connected in parallel. The criteria for designing the solar array is based on the current hours of sunlight. Since the estimated annual average of hours of sunlight per day for Colombia is 4 hours, it is designed the power system configuration taking into account this value.

Figure 21 corresponds to the diagram of the electrical configuration for powering the GNSS permanent stations using photovoltaic systems used in the GeoRED project. Under this configuration, the autonomy time in each station without recharging batteries due to absence of sunlight is evaluated as follows.

- No data transmission system: 9-10 days

- Radio-link: 6-8 days.
- National Seismic Network satellite link: 6-8 days.
- Satellite linked internet: 2 days

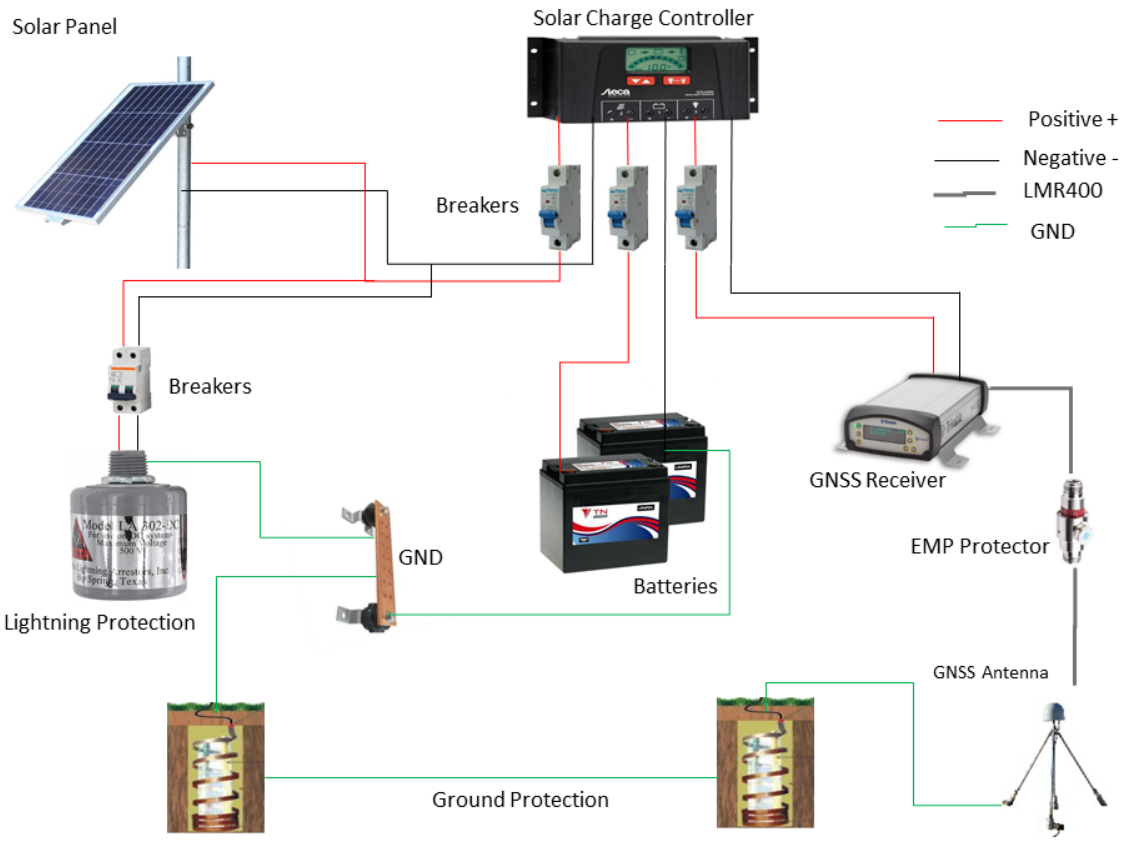

Figure 21. Electrical configuration of GNSS permanent stations.

These estimated times of autonomy could be increased twice whether other two batteries are installed in parallel. However, it is possible that solar panel does not have the capacity to charge the batteries, especially if the batteries are below 50% of charge. This would imply that necessarily, in these cases, it would be required to increase the solar panels array. However, given the conditions of location of the stations near the equator, it is very difficult to get this extreme situation.

3.5. The GNSS GeoRED network

Currently, the GeoRED Network is composed of two sub-networks: the first one is the permanent GNSS CORS (Continuously Operating Reference Station) network, and the second one consisting of campaign style field stations.

3.5.1. GeoRED CORS stations network

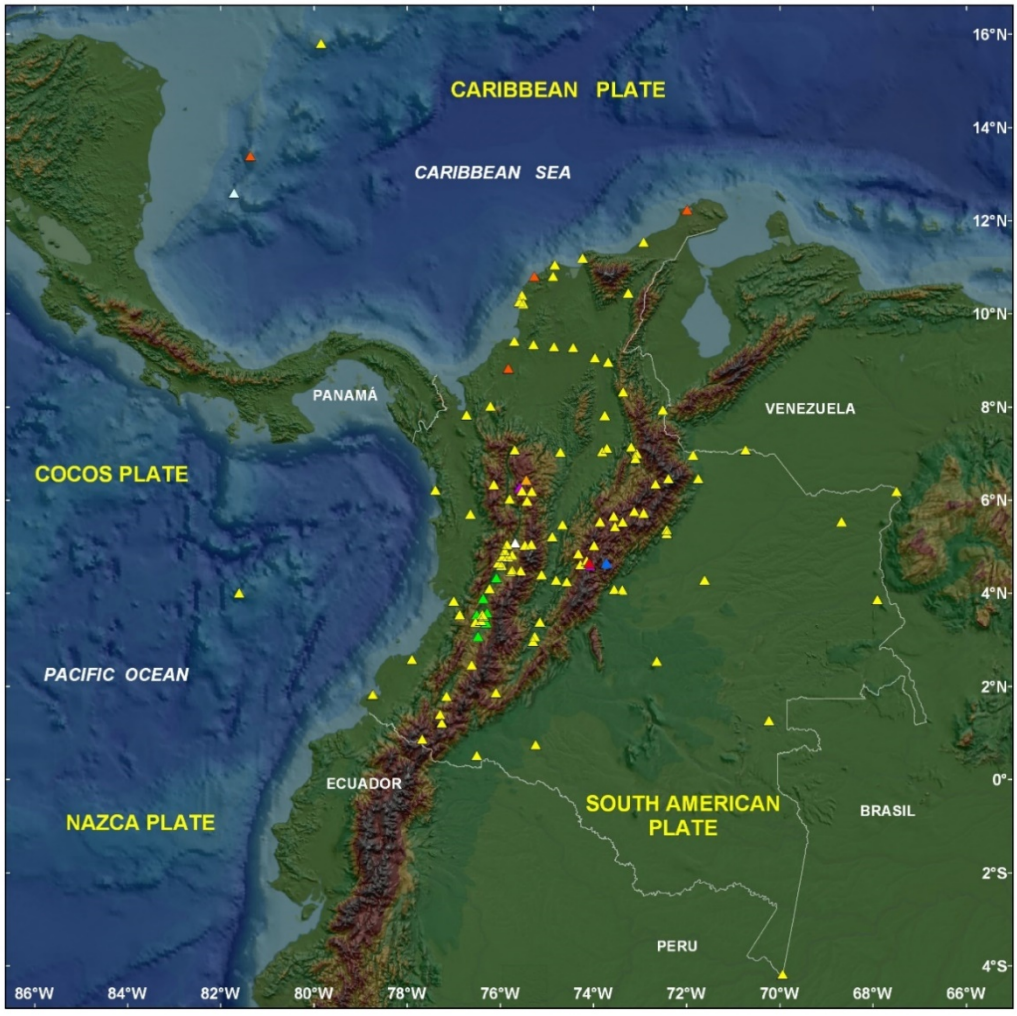

Figure 22. GeoRED permanent stations network.

The CORS network has 117 stations installed as of June 2018 (Figure 22). Among these stations, 101 are GeoRED GNSS stations (yellow triangles); 5 GNSS stations as a part of the COCONet (Continuously Operating Caribbean GPS Observational Network) Project run by UNAVCO (dark orange triangles); the Bogotá IGS GNSS station (BOGT, red triangle); and 10 stations installed under a collaborative partnership with local

Colombian institutions, such as CENICAÑA (Sugar Cane Research Institute) (green triangles); National University of Colombia, (purple triangles), Aburrá Valley Metropolitan Office (light orange triangle); and the Bogota City Water Supply Company (light blue triangle).

Table 1 shows the list of the 117 stations installed until June 2018. It contains the type of monument for the antenna installation, data transmission system and receiver and antenna currently in operation.

Table 1. Geodetic stations installed in Colombia.

No.	ID	LAT	LON	MONUMENT	DATA TX	GEODETIC EQUIPMENT	
						Receiver	Antenna
1	AEBS	2.956	-75.292	IDBM	5	Trimble Net-R9	TRM-57971.00
2	AECT	4.766	-75.954	DDBM	6	TPS Net-G5	TPS-G5_A1
3	AEDO	4.688	-74.139	DDBM	4	Trimble Net-R9	TRM-57971.00
4	AEMO	9.263	-74.436	DDBM	6	Trimble Net-R9	TRM-57971.00
5	AEMT	4.813	-75.742	DDBM	1	Trimble Net-R9	TRM-57971.00
6	AEPA	3.533	-76.382	DDBM	6	TPS Net-G5	TPS-G5_A1
7	AGTU	5.520	-73.374	IDBM	5	Trimble Net-R9	TRM-57971.00
8	AJCM	5.210	-74.885	IDBM	5	Trimble Net-R9	TRM-57971.00
9	ALPA	11.528	-72.918	CPM	1	Trimble Net-R9	TRM-57971.00
10	ANCH	3.535	-76.870	SDBM	6	Trimble Net-R9	TRM-57971.00
11	ASVI	4.272	-74.796	IDBM	5	Trimble Net-R9	TRM-57971.00
12	BA3E	0.742	-75.234	DDBM	6	Trimble Net-R9	TRM-57971.00
13	BAAP	4.072	-73.554	SDBM	4	Trimble Net-R9	TRM-29659.00
14	BACO	9.402	-75.692	IDBM	4	Trimble Net-R9	TRM-57971.00
15	BAMA	5.534	-68.673	DDBM	6	Trimble Net-R9	TRM-57971.00
16	BAME	4.236	-74.565	CPM	4	Trimble Net-R9	TRM-57971.00
17	BAPA	5.466	-74.658	CPM	4	Trimble Net-R9	TRM-57971.00
18	BARU	10.258	-75.590	IDBM	4	Trimble Net-R9	TRM-57971.00
19	BASO	6.203	-77.393	CPM	5	Trimble Net-R9	TRM-29659.00
20	BOBG	8.312	-73.358	IDBM	1	Trimble Net-R9	TRM-57971.00
21	BOGT	4.640	-74.081	CM	1	Javad Delta-3	Jav. RingAnt-DM
22	BP01	4.641	-74.080	SBR	5	Trimble Net-R9	TRM-29659.00
23	BUGT	3.826	-76.996	CPM	1	Trimble Net-R9	TRM-57971.00
24	CAPI	5.351	-72.428	CPM	4	Trimble Net-R9	TRM-57971.00

25	CAYS	15.795	-79.846	CPM	6	Trimble Net-R9	TRM-57971.00
26	CCAN	3.360	-76.300	IDBM	1	Trimble Net-R9	TRM-57971.00
27	CCAY	3.531	-76.502	DDBM	1	Trimble Net-R9	TRM-57971.00
28	CCCP	1.820	-78.729	SBR	1	Trimble Net-R9	TRM-57971.00
29	CCPA	4.325	-76.085	IDBM	1	Trimble Net-R9	TRM-57971.00
30	CCPM	3.574	-76.278	IDBM	1	Trimble Net-R9	TRM-57971.00
31	CCSQ	3.063	-76.474	DDBM	1	Trimble Net-R9	TRM-57971.00
32	CCYO	3.882	-76.369	DDBM	1	Trimble Net-R9	TRM-57971.00
33	CIA1	3.505	-76.357	CPM	1	Trimble Net-R9	TRM-57971.00
34	CIOH	10.391	-75.534	DDBM	4	Trimble Net-R9	TRM-57971.00
35	CN35	13.375	-81.363	SDBM	4	Trimble Net-R9	TRM-59800.00
36	CN36	8.820	-75.821	SDBM	4	Trimble Net-R9	TRM-59800.00
37	CN37	10.793	-75.263	SDBM	4	Trimble Net-R9	TRM-59800.00
38	CN38	12.222	-71.988	SDBM	4	Trimble Net-R9	TRM-59800.00
39	CORO	9.328	-75.288	CPM	4	Trimble Net-R9	TRM-29659.00
40	CPAS	4.472	-75.555	IDBM	5	Trimble Net-R9	TRM-57971.00
41	CUC1	7.932	-72.513	CPM	1	Trimble Net-R9	TRM-29659.00
42	GUAP	2.574	-77.895	CPM	4	Trimble Net-R9	TRM-57971.00
43	HITU	7.070	-75.689	SDBM	1	Trimble Net-R9	TRM-57971.00
44	INOB	4.595	-75.968	DDBM	5	Trimble Net-R9	TRM-57971.00
45	INRI	4.909	-75.897	DDBM	1	Trimble Net-R9	TRM-57971.00
46	INSJ	5.032	-75,854	IDBM	5	Trimble Net-R9	TRM-57971.00
47	INTO	4.642	-76.043	IDBM	5	Trimble Net-R9	TRM-57971.00
48	INVE	11.188	-74.232	DDBM	1	Trimble Net-R9	TRM-57971.00
49	LABO	1.856	-76.090	DDBM	6	Trimble Net-R9	TRM-57971.00
50	MAKA	6.337	-72.662	DDBM	4	Trimble Net-R9	TRM-57971.00
51	MALO	4.003	-81.606	CPM	3	Trimble Net-R9	TRM-57971.00
52	MECE	7.107	-73.712	CPM	3	Trimble Net-R9	TRM-29659.00
53	MITU	1.261	-70.232	IDBM	1	Trimble Net-R9	TRM-57971.00
54	MORA	8.959	-73.683	DDBM	4	Trimble Net-R9	TRM-57971.00
55	MZAL	5.030	-75.471	CM	1	Trimble Net-R9	TRM-29659.00
56	OAMU	5.647	-73.558	IDBM	5	Trimble Net-R9	TRM-57971.00
57	OANA	4.596	-74.078	SBCPM	6	Trimble Net-R9	TRM-57971.00
58	OCEL	4.271	-71.616	IDBM	1	Trimble Net-R9	TRM-57971.00
59	OVSC	1.210	-77.257	DDBM	1	Trimble Net-R9	TRM-57971.00
60	PAL2	7.131	-73.184	IDBM	1	Trimble Net-R9	TRM-57971.00
61	PASI	0.513	-76.499	IDBM	1	Trimble Net-R9	TRM-57971.00
62	PATU	5.746	-73.126	DDBM	4	Trimble Net-R9	TRM-57971.00

63	PLTR	5.044	-75.332	DDBM	5	Trimble Net-R9	TRM-57971.00
64	PNPC	4.638	-73.722	IDBM	1	Leica GR-10	LEIA-R20
65	POVA	2.449	-76.615	CPM	1	Trimble Net-RS	TRM-29659.00
66	PUIN	3.851	-67.903	CPM	4	Trimble Net-R9	TRM-59800.00
67	PWIL	7.814	-73.753	DDBM	6	Trimble Net-R9	TRM-57971.00
68	QUIL	1.394	-77.291	CPM	1	Trimble Net-RS	TRM-29659.00
69	SAN0	12.580	-81.716	NO	1	Trimble Net-R9	TRM-59800.00
70	SEL1	6.191	-75.529	CPM	3	Trimble Net-R9	TRM-57971.00
71	SGCC	3.372	-76.530	SBR	1	Trimble Net-R9	TRM-57971.00
72	SGCG	6.992	-73.064	IDBM	6	Trimble Net-R9	TRM-57971.00
73	SGCN	4.640	-74.092	SBR	1	TPS Net-G5	TPS-G5_A1
74	SUAM	5.710	-72.925	DDBM	6	Trimble Net-R9	TRM-57971.00
75	SVNA	6.954	-71.860	IDBM	4	Trimble Net-R9	TRM-57971.00
76	TASA	6.424	-75.435	DDBM	1	Trimble Net-R9	TRM-57971.00
77	TCOA	3.380	-75.147	DDBM	6	Trimble Net-R9	TRM-57971.00
78	TEAT	5.422	-73.539	IDBM	5	Trimble Net-R9	TRM-57971.00
79	TICU	-4.187	-69.939	CPM	1	Trimble Net-R9	TRM-57971.00
80	TITI	6.015	-75.792	DDBM	4	Trimble Net-R9	TRM-57971.00
81	TONE	6.324	-76.139	CPM	4	Trimble Net-RS	TRM-29659.00
82	TUCO	1.815	-78.748	CPM	3	Trimble Net-R9	TRM-57971.00
83	UDAP	4.615	-74.094	DDBM	6	TPS Net-G5	TPS-G5_A1
84	UNCA	5.072	-75.673	DDBM	6	Trimble Net-RS	TRM57971.00
85	UNME	6.264	-75.577	SDBM	6	Trimble Net-R9	TRM-57971.00
86	URR0	8.012	-76.210	IDBM	1	Trimble Net-R9	TRM-57971.00
87	UWAS	6.451	-72.391	CPM	4	Trimble Net-RS	TRM-59800.00
88	VAUC	7.067	-70.733	DDBM	4	Trimble Net-R9	TRM-57971.00
89	VBAM	9.046	-73.969	DDBM	6	Trimble Net-R9	TRM-57971.00
90	VBAR	7.028	-73.806	DDBM	6	Trimble Net-R9	TRM-57971.00
91	VBUV	5.533	-73.859	CPM	5	Trimble Net-R9	TRM-29659.00
92	VCAL	3.401	-76.406	DDBM	6	TPS Net-G5	TPS-G5_A1
93	VCAR	6.183	-67.495	IDBM	4	Trimble Net-R9	TRM-57971.00
94	VCRG	5.981	-75.419	IDBM	4	Trimble Net-R9	TRM-57971.00
95	VCTG	10.209	-75.505	DDBM	4	Trimble Net-R9	TRM-57971.00
96	VDPR	10.436	-73.248	CPM	1	Trimble Net-R9	TRM-29659.00
97	VEDE	4.460	-75.765	DDBM	5	Trimble Net-R9	TRM-57971.00
98	VMAG	9.287	-74.847	CPM	4	Trimble Net-R9	TRM-29659.00
99	VMAR	6.176	-75.324	IDBM	4	Trimble Net-RS	TRM-29659.00
100	VMER	1.785	-77.153	IDBM	4	Trimble Net-R9	TRM-57971.00

101	VMES	6.883	-73.092	IDBM	4	Trimble Net-R9	TRM-57971.00
102	VNEI	3.062	-75.255	CPM	5	Trimble Net-RS	TRM-29659.00
103	VORA	7.818	-76.722	CPM	1	Trimble Net-R9	TRM-29659.00
104	VORI	0.863	-77.672	IDBM	4	Trimble Net-R9	TRM-57971.00
105	VOTU	7.019	-74.710	IDBM	4	Trimble Net-R9	TRM-57971.00
106	VPIJ	4.397	-75.107	CPM	1	Trimble Net-R9	TRM-29659.00
107	VPOL	10.794	-74.861	IDBM	4	Trimble Net-R9	TRM-57971.00
108	VPOM	4.068	-73.382	DDBM	4	Trimble Net-R9	TRM-57971.00
109	VQUI	5.692	-76.642	DDBM	4	Trimble Net-R9	TRM-57971.00
110	VROS	4.847	-74.323	CPM	5	Trimble Net-RS	TRM-29659.00
111	VSJG	2.533	-72.639	CPM	4	Trimble Net-R9	TRM-57971.00
112	VSJP	4.781	-75.836	CPM	5	Trimble Net-R9	TRM-29659.00
113	VSOA	4.603	-74.273	IDBM	5	Trimble Net-R9	TRM-57971.00
114	VTAM	6.452	-71.753	IDBM	4	Trimble Net-R9	TRM-57971.00
115	VTUL	4.092	-76.224	IDBM	5	Trimble Net-RS	TRM-29659.00
116	VYPL	5.275	-72.427	IDBM	6	Trimble Net-R9	TRM-57971.00
117	VZPQ	5.019	-73.987	IDBM	5	Trimble Net-R9	TRM-57971.00

The information contained in previous table is:

Type of monumentation

SDBM: Short-drilled braced-monument
IDBM: Intermediate-drilled braced monument
DDBM: Deep-drilled braced-monument
CM: Concrete monument
CPM: Concrete pillar monument

Data transmission system

1: Local network
2: Radio-link
3: Satellite-link
4: Cellular modem
5: Satellite-linked internet
6: Manual data download

Appendix B illustrates how the evolution of the GeoRED network has been.

3.5.2. Campaign field stations network

Under the frame of the GeoRED Project that started in 2007, it has been possible to keep a densification plan, with a goal of building at least 20 field GPS stations each year. All the monuments that are built are occupied immediately. On the other hand, as it is important to collect the data at each station, about 120-140 field stations have been

occupied every year. Stations that have more than four occupations are revisited every two years, while those with less than 4 occupations are occupied every year. In all the cases, data collection is performed during 5 days, seeking for 120 hours of continuous observation, with sample rate of 15 seconds, using one-meter spike-mount for the antenna installation.

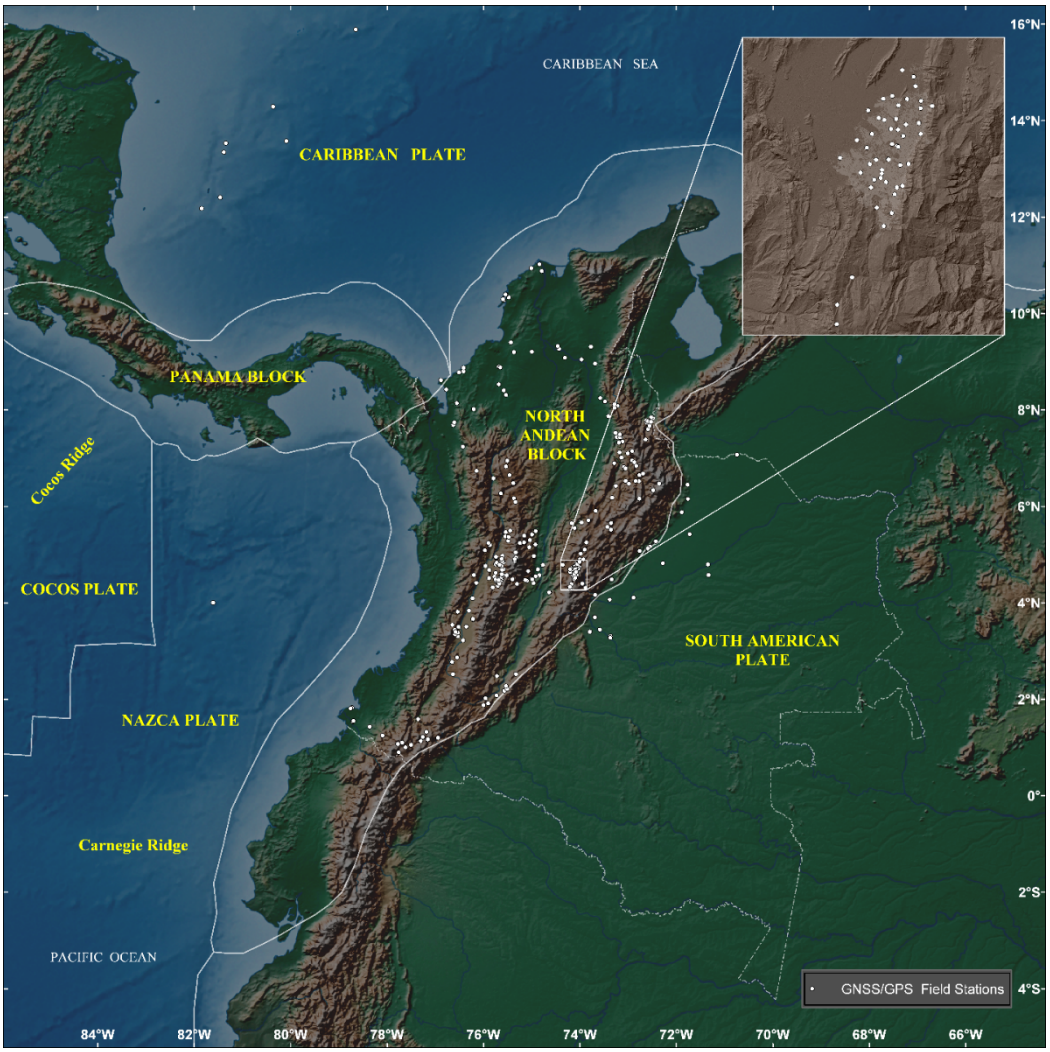

Figure 23. Location of GPS field campaign stations in Colombia.

Currently, the field stations network is composed of 382 stations as shown in Figure 23. Among them, 267 stations focus exclusively on tectonic studies; 49 stations were built under a collaborative project with the Bogotá City Land Registry Office to study land subsidence of the city; 55 stations are used to measure landslide displacements in different areas of the country; and 11 stations are for mud-diapirism analysis on the north of the country. The 267 stations for tectonic studies are occupied every one or two years. Currently a special focus is on crustal deformation around active faults such as the

Algeciras, Ibagué and Bucaramanga Faults, and the continuation in Colombia of the Boconó Fault of the Mérida Andes in Venezuela.

GeoRED has achieved, until now, an impressive densification of station coverage over the Colombian territory of both permanent and campaign GNSS stations. The geotectonic complexity of this corner of South America requires that the density of station coverage will be increased even more and its distribution be improved.

CHAPTER 4

GPS DATA AND ANALYSIS FOR VELOCITY ESTIMATION

This chapter describes general aspects regarding the GPS data used and its processing, time series generation and velocity estimation of the GPS stations located in Colombia and in neighboring countries used in this dissertation.

4.1. GPS Data

The Regional Center of GNSS Data Processing run by the Space Geodesy Research Group (SGRG) of the Colombian Geological Survey currently processes data from 181 stations located in Colombia, Ecuador, Venezuela, Panama, Costa Rica and other countries in Central America and the Caribbean region. The main purpose of the processing is the definition and maintenance of the reference frame and crustal deformation monitoring on a daily basis. The obtained results constitute a cornerstone for performing a wide range of geoscience research in the region that allow answering various scientific questions, some with direct implications in geohazards and tectonics at different scales as well as promoting the use of GNSS geodetic technology in other fields of knowledge.

The 181 stations routinely being processed are: 117 stations from the GeoRED network in Colombia as of June 2018, described in the previous chapter including the IGS BOGT station; 25 stations in Ecuador, including two IGS stations, GLPS and RIOP; 7 stations in Panama; 1 station in Costa Rica; 2 stations in Nicaragua; 2 stations in Honduras; 1 station in Guatemala; 1 station in El Salvador; 3 stations in Puerto Rico; 3 stations in Dominican Republic; 1 station in Cuba; 3 stations in Jamaica; 4 stations in Venezuela; and 11 stations distributed in others Caribbean countries. These stations are located on the South America, Nazca, Caribbean and Cocos plates (Figure 24). Twenty-five of these stations are part of the COCONet Project (Braun et al., 2012).

Figure 24. Location and countries of GPS stations that are processed at the Regional Data Center for GPS Processing.

For this dissertation, 60 permanent stations are used as shown in Figure 25. These stations are: 46 in Colombia including the BOGT IGS station; 7 stations from Ecuador including the GLPS and RIOP IGS stations; 4 stations from Panama; 1 station from Costa Rica and 2 stations from Venezuela. These stations are located on the Nazca, South America, Cocos and Caribbean plates. Nine of these stations are part of the COCONet project. There are three main reasons for the use of this number of stations: first, the study area of this dissertation is the northwestern corner of South America, with emphasis on the North Andean Block; second, the GPS data should have a minimum of 2.5 years of observations to guarantee reliable estimates of secular motion (e.g., Blewitt and Lavallee, 2002); and third, the data cover a period of time until March 31, 2016, in order to avoid any effect due to the April 16, 2016, Ecuador earthquake.

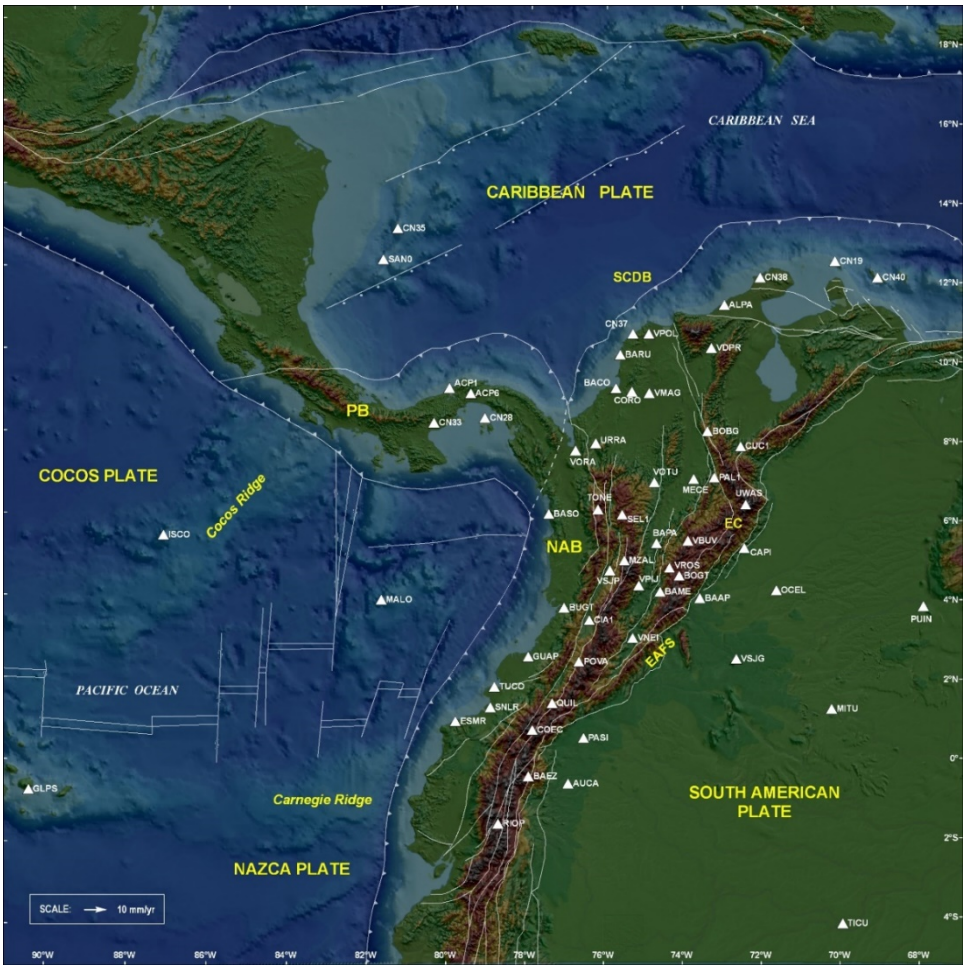

Figure 25. GPS stations used for this dissertation.

GPS data from the Colombian sites are obtained from the GeoRED project; data from Ecuadorean stations have been provided by the Geophysics Institute of the National Polytechnic University (Instituto Geofísico de la Escuela Politécnica Nacional), (Mothes et al., 2013), and data from stations located in Panama, Venezuela, Costa Rica, and Central America and Caribbean countries have been obtained from the COCONet Project (https://www.unavco.org/data/gps-gnss/gps-gnss.html) and two stations from the Panama Canal Authority. Data from IGS stations are obtained from UNAVCO at the same link mentioned before.

4.2. GPS Data Processing

4.2.1. GPS processing

All GPS data obtained in the own format of each receiver are converted to RINEX format using the TEQC (Translating. Editing. Quality Check) tool developed by UNAVCO

(Estey and Meertens, 1999). After that, GPS data are processed with GIPSY-OASIS II software v. 6.3. developed by the Jet Propulsion Laboratory (JPL) California Institute of Technology (Bertiger et al., 2010; Zumberge et al., 1997) and maintained by the Near Earth Tracking Applications and Systems groups. GIPSY/OASIS stands for "**G**NSS **I**nferred **P**ositioning **Sy**stem/**O**rbit **A**nalysis and **Si**mulation **S**oftware" and is designed for high-precision geodetic applications based on GPS data processing and GPS-aided Precise Orbit Determination. Site coordinates for each day are obtained using the Precise Point Positioning (PPP) strategy. The site coordinates are computed in the non-fiducial frame and transformed to the ITRF2008 frame (Altamimi et al., 2011, 2012).

The orbit products used for processing were JPL-NASA final orbits version 2.1 that include satellite orbits, satellite clock parameters and earth orientation parameters. The orbit products take the satellite antenna phase center offsets into account. Final orbits are obtained from ftp://sideshow.jpl.nasa.gov/pub/JPL_GPS_Products/. These products are provided in formats native to GIPSY.

Since the troposphere in the lowest ten kilometers of the atmosphere delays radio signals emitted by GNSS satellites, numerical weather models (NWM) have become an important source of atmospheric data for modeling error sources in geodetic positioning improving the accuracy of the analysis of space geodetic observations. One example in recent years is the development of the Vienna Mapping Functions (VMF1) that is an update of previous model VMF (Boehm et al., 2006) and ray-traced zenith delays derived from the European Centre for Medium-range Weather Forecasts (ECMWF) datasets (ECMWF, 2018). These products are provided on an operational basis through the Global Geodetic Observing System (GGOS) Atmosphere Project (GGOS, 2018) conducted at the research group of Advanced Geodesy of the Vienna University of Technology (Nilsson et al., 2013) to describe atmosphere angular moment (functions), atmospheric delay, gravity field coefficients for the atmosphere, and atmosphere loading corrections in a consistent as well as homogenous manner. Thus, GGOS Atmosphere Project determines the hydrostatic and wet zenith delays together with the coefficients of the VMF1 that map the zenith delays to lower elevation angles. These parameters are provided on a global grid (2.0° x 2.5° latitude-longitude) every six hours, which is the usual time resolution of the ECMWF data and also determines these parameters for selected VLBI and GNSS sites. The SGRG obtains the

tropospheric corrections as input for GPS data processing from the Vienna University of Technology at http://ggosatm.hg.tuwien.ac.at/delay.html.

Ocean loading corrections are obtained from the Onsala Space Observatory. http://holt.oso.chalmers.se/loading/tidemodels.html. Corrections are applied to remove the solid earth tide and ocean tidal loading. The amplitudes and phases of the main ocean tidal loading terms are calculated using the online program (http://holt.oso.chalmers.se/loading/) applied to the Goddard Ocean Tide (GOT4.8) model that only differs from GOT4.7 for harmonic S2. The GOT4.7 model is derived from TOPEX/Poseidon, Jason-1, ERS and GFO altimetry (Turner et al., 2013; OSO, 2018).

4.2.2. Time series and GPS velocity estimation

Space geodetic techniques are an essential tool for measuring and estimating deformations of the crustal earth. These measurements allow not only to determine the motion of tectonic plates, but to provide constraints in the rheology of the crust and mantle, to analyze the kinematics in active faults, to monitor the seismic cycle, to determine surface strain and strain rates, among several fields of geological applications (Dixon, 1991b). Thus, the geodetic velocities and their uncertainties are derived from repeated measurements of the position of the geodetic stations.

The time series of 3D coordinates can be defined as trajectories. Thus, the kinematic models that researchers use to describe geodetic or geophysical time series are essentially trajectory models (Bevis et al., 2020). Most of the researchers who use geodetic techniques to study the crustal movements routinely include cycles of annual displacements in the formulation of trajectory models for each station, as presented by Bevis and Brown (2014):

$$\boldsymbol{x}(t) = \boldsymbol{x}_R + \boldsymbol{v}\,(t - t_R) + \sum_{j=1}^{n_j} \boldsymbol{b}_j H(t - t_j) + \sum_{k=1}^{n_F} [\boldsymbol{S}_k \sin(\omega_k t) + \boldsymbol{C}_k \cos(\omega_k t)] \quad (4.1)$$

Where t_R is an arbitrary reference time, $\boldsymbol{x}_R = \boldsymbol{x}(t_R)$ is the reference position, and $\boldsymbol{v}$ is the station velocity vector. H is the Heaviside function, and $\boldsymbol{b}_j$ is a vector that represents the magnitude and direction of the jump that occurs at time t_j, n_j is the number of jumps, n_F is the number of frequencies used to model the annual displacement cycle and

$$\omega_k = \frac{2\pi}{\tau_k}, \qquad (4.2)$$

and $$\tau_1 = 1 \text{ year}; \tau_2 = \frac{1}{2} \text{year}; \tau_3 = \frac{1}{3} \text{year}, \ldots\ldots \text{ etc.}$$

In order to model jumps, the Heaviside function, commonly referred to as the unit step function, is normally used, that is defined as

$$H(t) = 0 \quad for\ t < 0$$
$$H(t) = 1 \quad for\ t \geq 0 \qquad (4.3)$$

The trajectory model, expressed in eq. 4.1, superimposes both the Heaviside jumps (eq. 4.3) and an annual cycle of constant velocity tendency, which is linear with respect to its parameters or coefficients, with the number $3 * \left(2n_F + n_j + 2\right)$ in all.

So, it is possible to say then that the main objective of trajectory models is to estimate the linear or secular trend. However, it is important to consider that the analysis of GPS time series includes detection of outliers, identification of offsets, estimation of displacements and linear as well as seasonal trends, characterization of the noise, and residual analyses among other possibilities (Andrei et al., 2018).

The analysis of the noise in the geodetic time series is essential in geodetic applications focused to study the deformation of the earth's crust. Observed geodetic coordinates are affected by various noises. These noises are statistical and their frequency dependence characterize them. Statistical characteristics of the noise are examined through analysis of data residuals with respect to a model calculation assuming appropriate physical processes such as a linear trend and a seasonal signal. Mao et al. (1999) demonstrated the importance of evaluation of noise characteristics in velocity estimation and estimated the noise in GPS time series as a sum of white (no time dependence) and colored (time-correlated) noises by the Maximum Likelihood Estimation (MLE). Most of the current analyzes of the estimation of GNSS station velocity are based on the assumption that noise in the station position can be represented by combining white noise noise and power law

noise (Zhang et al. 1997; Mao et al. 1999; Williams et al. 2004). For example, the instability of the monuments is a source of the power law behavior, while the meteorological noise due to atmospheric vapor is not a white noise.

Langbein (2004) provided a good explanation about the importance of understanding the noise model for geodetic time series. Davis et al. (2012) also studied the seasonal signals in the geodetic time series, and pointed out that it is fundamental to understand the noise as well the uncertainties in the estimated parameters of the time series in order to detect and analyze the signals of interest. They also emphasized that, by analyzing noise, it is possible to detect deficiencies in the models and the techniques used for the analysis of time series. Therefore, it is essential to find the most appropriate model. He et al. (2017) present an excellent comparative analysis of current GPS methodologies for the generation of accurate time series and their sources of error.

In this study, from the PPP processing performed with GIPSY-OASIS II software, daily positions (X, Y, Z) are obtained in an Earth-fixed, Earth-centered terrestrial reference ITRF2008, using precise models and orbits as mentioned previously. These coordinates are transformed into topocentric coordinates, that means that daily coordinate changes of each station are expressed in terms of local displacements in the North, East, North and Up components (E,N,U), with respect to a position at an initial epoch. Daily coordinates in ENU format are uploaded to HECTOR software v. 1.6 (Bos et al., 2013), a package developed at SEGAL (Space & Earth Geodetic Analysis Laboratory at the University of Beira Interior, Portugal), that is used by the SGRG for the GPS velocities estimation.

For this dissertation, GPS velocities are estimated for 60 GPS CORS with 2.5 years or longer observation time (e.g., Blewitt and Lavallee. 2002). The HECTOR software also allows the estimation of the offsets associated with the occurrence of earthquakes as well as changes in the instruments installed in the geodetic station, firmware update and reorientation of the antenna. In order to use the same reference epoch, January 1, 2010, was chosen as the reference epoch for all the estimations instead of the midpoint of each individual time series. The secular motion observed at each GPS station is computed together with periodical signals and instantaneous offsets using HECTOR software, that employs MLE, an approach that permit to compute the amount of white noise and power

law noise in the GPS time series. Seasonal signals, composed of annual and semi-annual signals, are considered in the estimation of the secular velocities in order to establish their influence on the velocity estimation. Bos et al. (2010) showed that when the time series cover periods of time exceeding 3-5 years, the remaining influence of seasonal signal for the estimation of the trend can be neglected.

Table 2 shows the estimated values of the velocity trend and its uncertainties for the three components of each GPS station, expressed in millimeters per year. The Appendix C presents the time series plot of the 60 GPS stations of this dissertation.

Table 2. Estimated values of velocity trend at the GPS stations expressed in ITRF2008.

ID	North (mm/yr)	Uncertainties (mm/yr)	East mm/yr	Uncertainties (mm/yr)	Up (mm/yr)	Uncertainties (mm/yr)
ACP1	11.4	0.3	16.7	0.3	3.0	0.7
ACP6	12.1	0.2	16.7	0.2	5.6	2.0
ALPA	13.6	0.6	8.4	0.9	-4.5	1.6
AUCA	9.9	0.2	-2.3	0.3	0.2	0.8
BAAP	9.9	0.2	-5.0	0.5	1.1	0.9
BACO	7.8	1.0	13.2	0.9	-0.7	2.4
BAEZ	10.4	0.2	2.0	0.3	2.8	0.9
BAME	14.2	0.2	1.6	0.7	3.4	1.2
BAPA	14.6	0.2	2.6	0.3	1.9	0.6
BARU	9.9	0.4	11.6	0.8	0.0	1.0
BASO	15.5	0.4	6.7	0.9	1.5	0.6
BOBG	15.1	0.3	6.7	0.5	6.3	0.7
BOGT	15.2	0.2	-0.4	0.3	-35.3	1.0
BUGT	15.0	0.2	5.0	0.3	3.6	0.5
CAPI	11.5	0.4	-3.0	0.3	1.7	0.9
CIA1	14.3	0.6	3.0	1.3	-11.5	5.9
CN19	14.1	0.6	12.8	0.7	6.3	1.8
CN28	15.1	0.5	17.3	0.7	5.0	1.4
CN33	6.3	1.8	19.9	1.8	0.0	3.9
CN35	6.6	0.4	11.0	0.6	0.3	1.1
CN37	13.8	1.6	8.5	1.1	4.4	3.6
CN38	13.8	0.3	11.3	0.5	2.8	0.8
CN40	12.9	0.7	12.2	0.7	4.1	1.6
COEC	12.5	0.4	3.0	1.0	4.7	1.1
CORO	11.4	0.3	11.7	0.3	1.2	1.3
CUC1	13.0	0.4	7.5	1.5	1.7	0.9

ESMR	16.5	0.3	17.9	0.5	2.2	1.1
GLPS	10.2	0.2	50.7	0.2	0.0	0.4
GUAP	13.4	0.4	7.9	0.5	3.0	0.9
ISCO	74.4	0.5	50.0	0.7	-2.7	1.4
MALO	13.6	0.3	48.3	0.6	-1.5	1.3
MECE	15.0	0.4	4.4	0.3	1.4	1.7
MITU	11.5	0.3	-4.7	0.4	2.6	1.8
MZAL	17.9	0.7	1.6	0.3	4.5	0.5
OCEL	11.6	0.2	-5.0	0.3	2.7	0.8
PAL1	14.7	0.4	3.5	0.4	0.6	0.8
PASI	10.3	0.4	-3.1	0.3	1.5	0.6
POVA	13.0	0.3	5.1	0.5	-2.2	0.6
PUIN	10.7	0.3	-4.6	0.5	-0.3	2.2
QUIL	14.3	0.3	5.0	0.8	0.4	0.9
RIOP	5.7	0.4	-0.5	0.6	1.0	0.5
SAN0	7.0	0.2	12.3	0.4	0.2	0.5
SEL1	14.9	0.2	4.0	0.3	1.2	0.9
SNLR	10.6	0.3	11.0	0.4	2.7	0.8
TICU	10.8	0.3	-4.2	0.3	3.5	2.0
TONE	15.5	0.2	4.2	0.5	2.6	0.6
TUCO	12.8	0.2	13.8	0.4	5.3	0.7
URRA	14.0	0.7	12.6	0.8	3.1	2.5
UWAS	13.0	0.3	0.1	0.3	2.9	0.6
VBUV	15.6	0.3	3.7	0.5	0.9	0.9
VDPR	15.2	0.2	8.5	0.2	3.1	0.9
VMAG	14.1	0.4	8.4	0.5	5.2	1.3
VNEI	13.8	0.3	-0.7	0.3	1.8	1.5
VORA	11.6	1.5	14.2	1.8	-6.6	4.8
VOTU	15.1	0.4	6.0	0.3	4.6	0.3
VPIJ	14.4	0.2	1.6	0.4	3.5	1.1
VPOL	16.6	0.2	7.6	0.5	10.3	1.7
VROS	14.5	0.3	0.1	0.5	1.1	1.1
VSJG	10.8	0.3	-4.9	0.6	1.0	1.8
VSJP	15.2	0.3	1.0	0.4	2.2	1.1

Figure 26, corresponding to the Sabana de Bogotá, where Bogotá city, the capital of the country is located, shows the position of two GPS stations, the first one located on consolidated soil (BOGT) and the second one on bedrock (VROS). These two stations allow to illustrate some general aspects related to the analysis of GPS time series.

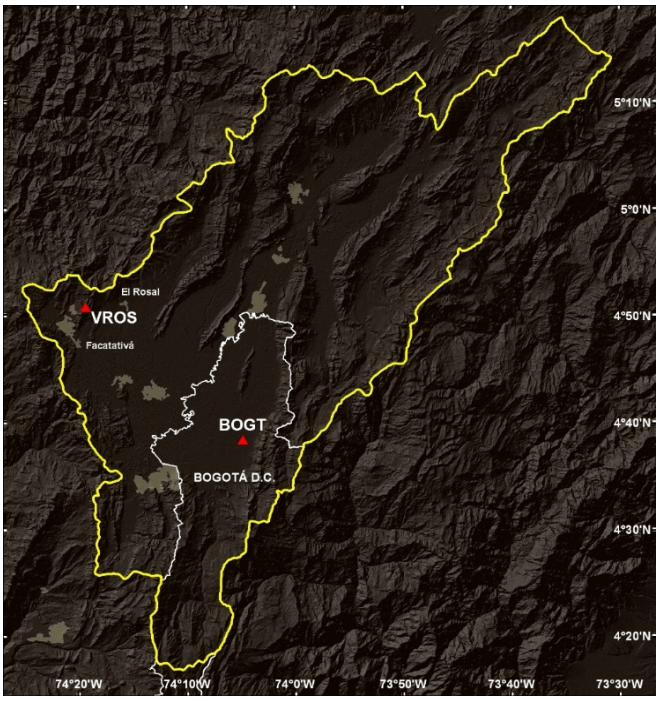

Figure 26. Map location of the BOGT and VROS permanent stations (red triangles).
Yellow line: boundary of the Sabana de Bogotá; white line: perimeter of Bogotá municipality

Figure 27 shows the time series for the above-mentioned stations. The blue lines indicate offsets associated with changes of geodetic instruments such as antenna or GPS receiver. In some cases, it can also show the reorientation of the antenna, and even, the occurrence of a representative earthquake that can generate change in the position of the antenna. The red line corresponds to the linear trend estimated by the HECTOR software. In this case, both stations show a common behavior in the northward motion while there is a big difference in their vertical components. The IGS BOGT station with a continuous observation since 1994 indicates a significant vertical velocity at a rate of ~35 ± 1.0 mm/year that is probably associated with the land subsidence in the Sabana de Bogotá. A research activity is being carried out by the SGRG deploying a new geodetic network for the capital city of Bogotá and using InSAR techniques. In turn, the VROS station, installed in 2009, is fairly stable in its behavior, 1.1 ± 1.1 mm/yr.

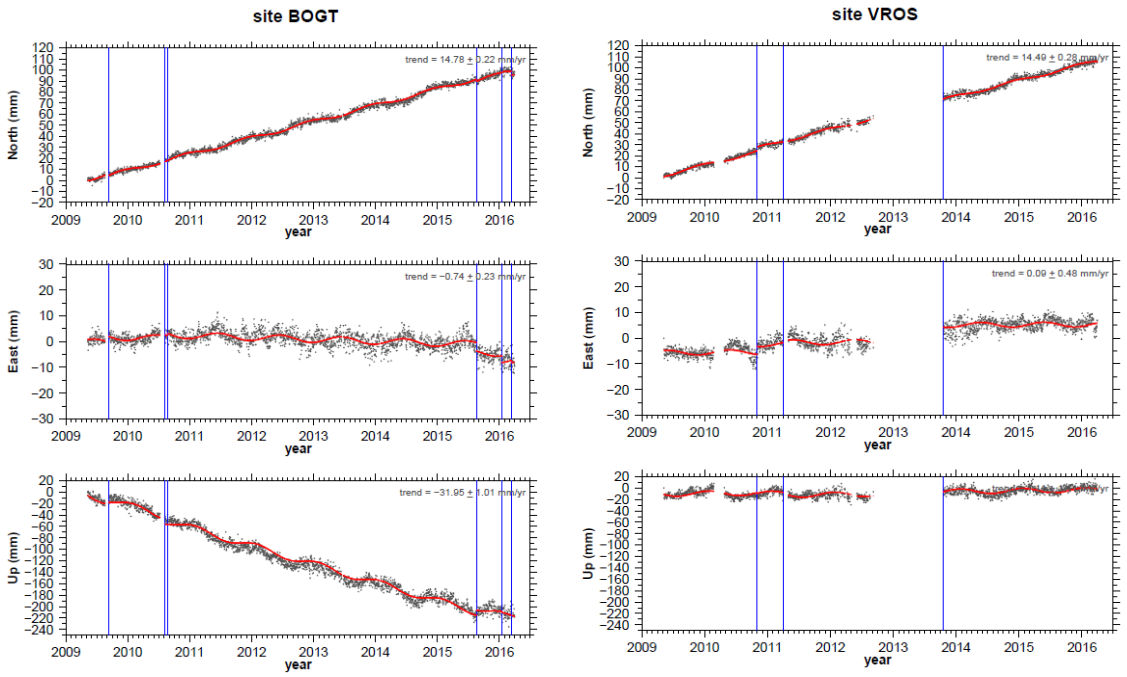

Figure 27. Time series of BOGT and VROS permanent stations located in the Sabana de Bogotá region.

As was mentioned previously, the velocities of the GPS stations were estimated using the HECTOR software. All coordinate components were analyzed with assumed power-law plus white noise model, with the purpose to estimate the velocities and their formal errors. The main objective of analyzing the noise in the GPS time series is to find an optimal model that best describes the stochastic processes generated in the time series, and the aim is to separate the deterministic part, that is, the signal, from another stochastic part, that is the noise. It is important to consider the following issues: if future values of a time series can be determined by some mathematical function, then the time series is called deterministic. If, on the contrary, the future values can only be described in terms of a probability distribution, the time series is called non-deterministic. Additionally, the statistical phenomenon that evolves over time according to probabilistic laws is called a stochastic process（Box et al. 2005).

Currently, there is a widely used combination of models to describe the noise in GNSS time series (e.g., Williams et al., 2003). It is also possible, with linear model parameters, such as those of the trajectory model previously mentioned, to be used in the maximum likelihood method for the estimation of parameters associated to the noise model.

Agnew (1992) considered that the vast majority of geophysical phenomena have time series with noise that follows the behavior of a power-law. Thus, the power-law noise, has the property that the power spectral density of the noise corresponds to a power-law curve (Bos et al. (2020), expressed in the following equation

$$P(f) = P_0 \left(\frac{f}{f_s}\right)^k , \quad (4.4)$$

where f is the spatial or temporary frequency, P_0 is a constant, f_s is the sampling frequency and the exponent k is the spectral index.

The Power Spectral Density (PSD) is expressed in decibels (dB), and corresponds to its power and distribution in the frequency of the spectrum. Depending on the PSD, it is possible to distinguish several "colors" or types of noise. This classification, based on terms of spectral density, is somewhat analogous to the classification of the visible spectrum in remote sensing, with respect to the "colors" that depend on the wavelengths. Thus, it can be said that a noise that contains a uniform distribution in its frequency of the spectrum would be a white noise, in the same way that the white color contains all the frequencies in the visible spectrum. A noise type whose spectrum is not flat is considered "colored" or autocorrelated; the term colored noise is used to refer to power-law processes other than white noise (Williams, 2003a).

Bogusz et al. (2018) points out that the power-law noise described by Agnew (1992) has the character of colored noises with a spectral index, which may or may not be an integer, and corresponds to the exponent of the frequency in the relationship between the power spectrum and the temporal frequency. White noise corresponds to the representation of phenomena temporally uncorrelated. The flicker noise, also named pink noise, encompasses all mismodelled parameters during the data processing step as well as large-scale effects. Random-walk noise is a mixture of local effects depending on the station and instability of the monument. Both flicker and random-walk noises have more power at lower frequencies. For flicker noise, the power is proportional to $\frac{1}{f}$, while for random-walk noise, the power is proportional to $\frac{1}{f^2}$. The spectral index of white noise is 1; flicker noise is -1, and random-walk noise is -2.

As previously mentioned, a power-law plus white noise model is used for the GPS time series analysis using the HECTOR software. To verify if the noise model used is the most appropriate one, a power spectra analysis is performed by HECTOR software fitting the combination of the used noise models to the computed spectrum of the GP+S observations. This analysis corresponds to the difference between the observations minus the estimated linear trend and additional offsets and periodic signal signals. The power spectral density (PSD) plots of the residuals are generated using the Welch periodogram method, that is a method for estimating power spectra dividing the time signal into successive blocks, forming the periodogram for each block, and averaging (Welch, 1967; Hayes, 1996; Stoica and Moses, 2005). For each component, the frequency is expressed in cpy (cycles per year) in the axis x, and the power spectral density in mm^2/cpy corresponding to each frequency in the axis y. As is shown in Figure 27, the fitted model is flat at high frequencies,, which is representative of the white noise; at lower frequencies the fitted model obeys a power-law with a slope of approximately one. The result permits to confirm that the assumption of the noise model is correct. In addition, this characterization allows characterizing errors for time series less than 2.5 years, which is not the case of the time series obtained in this dissertation.

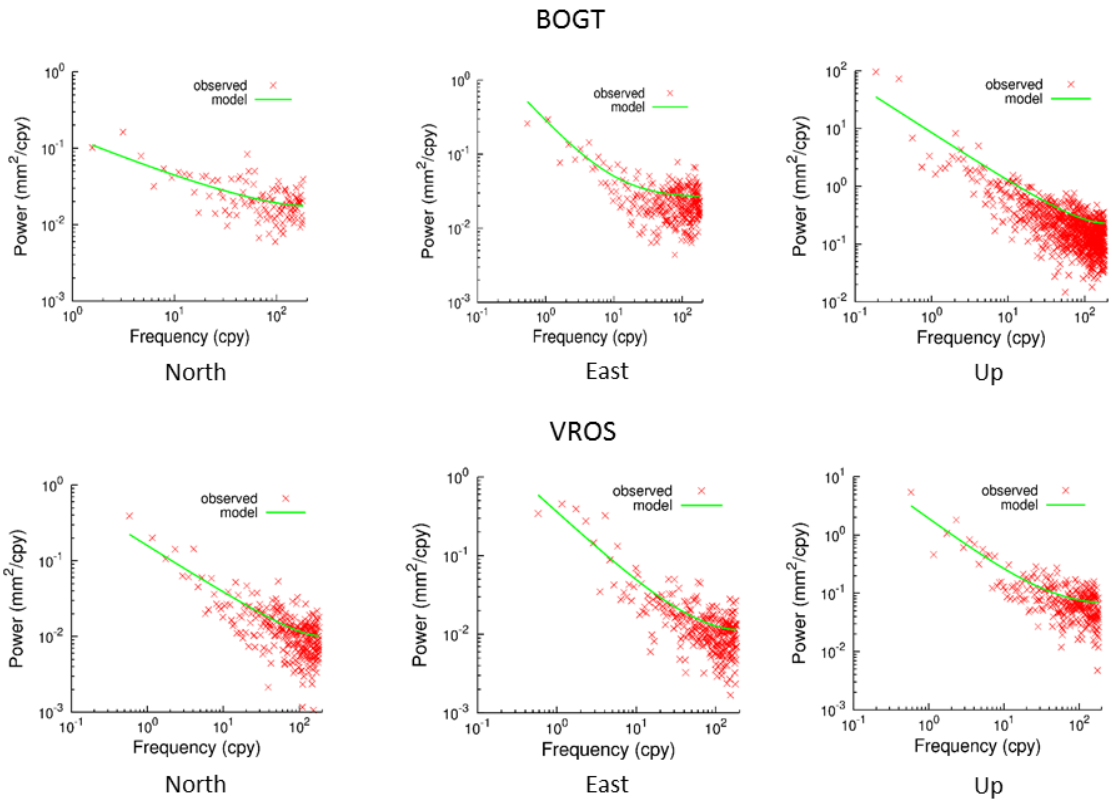

Figure 28. PSD plots for the BOGT and VROS stations.

Appendix D presents the Tables D1, D2 and D3 that contain the PSD values of the three components of the 60 stations used in this dissertation. The Figure 28 shows the PSD plots for the same GPS stations mentioned previously, BOGT and VROS. The red crosses are the computed periodogram (Welch´s method) while the solid green line is the fitted combined power-law plus white noise model. Also, it should be noted that the noise of the vertical component is larger than the horizontal ones by an order of magnitude.

For this dissertation, only horizontal velocities are used. The Figure 29 shows the GPS velocities of the 60 stations expressed with respect to ITRF2008.

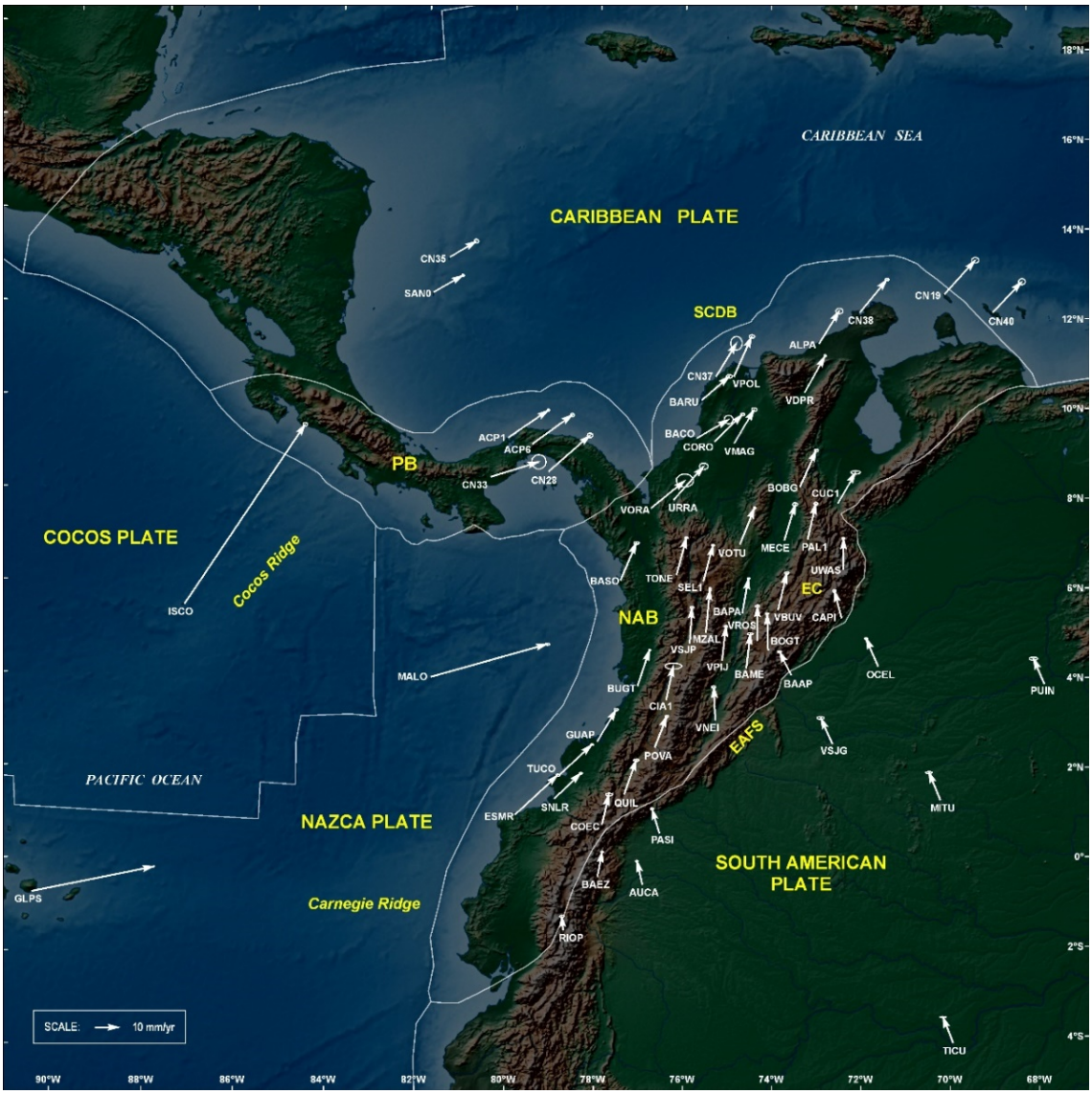

Figure 29. GPS velocities map wrt ITRF2008, Table 2.

4.2.3. South America Reference Frame

In order to estimate a good plate motion model based on geodetic data, a spatially homogeneous distribution of the GPS stations is necessary. This is one of the problems in the north of South America, because there was not a sufficient number of geodetic stations in this zone that allows the estimation of a reliable velocity model for this region of the South American plate. The GPS GeoRED stations and some stations of Brazil will surely help to improve the quality of that model.

In this dissertation, the GPS relative velocities with respect to the South American plate (SOAM) were estimated using a new Euler pole of the South American plate proposed by Rui Fernandes (pers. comm), which allows to determine the present-day movement of the South American plate from 91 stations with more than 3.5 years of observation located on the stable part of it. Some stations of the GeoRED network were used for this model. The estimated angular velocity is expressed with respect to the International Terrestrial Reference Frame ITRF2008 (Altamimi et al., 2012) as shown in Table 3.

Table 3. Euler´s pole of the SOAM plate with respect to ITRF 2008.

Plate	**Model**	**Lat** (deg)	**Lon** (deg)	**ω** (deg/Myr)	σ_{max} (deg)	σ_{min} (deg)	ζ_{max} (deg)	σ_{ω} (deg/Myr)
SOAM	Fernandes (pers comm)	-19.237	-133.603	0.1184	1.14	0.17	74.6	0.0071

where:

- Lat. Lon: geodetic position of the rotation pole
- ω: angular velocity in degrees per million of years
- σ_{max}. σ_{min}: semi-major and semi-minor axes of the 1-σ error ellipse of the rotation pole
- ζ_{max}: azimuth of the semi-major axis of the error ellipse clockwise from north.

CHAPTER 5

RESULTS

This chapter presents the results obtained in the data processing of the CORS stations located in the northwestern corner of South America, as well as the comparison with previous studies carried out in the study area.

5.1.GPS Time Series

Coordinate time series of the 60 GPS stations with a minimum observation time of 2.5 years are shown in Appendix C. In this dissertation, only horizontal components are discussed. The red line in each component indicates the fitting curve defined in eq. (4.1) of Chapter 4, and the vertical blue lines indicate the offsets due to instrumental changes that were applied for each station.

It can be seen that not all stations have presented continuity in data acquisition over time. In some of the plots, it is possible to see some jumps, whose explanation is presented later. More illustration about the impact of offsets and uncertainties is presented in the Discussion section. The GPS time series presented are the basis for the generation of the velocities in each of the stations, whose analysis is carried out later.

5.2.Example of behavior at permanent stations

The GPS time series of high precision are of vital importance in performing geodetic studies with multiple research purposes such as establishment and maintenance of reference frames at global, national or regional scales, determination of the current deformation of the earth's crust and its association with the possible occurrence of earthquakes, among others. However, it is essential to be able to establish what the behavior of the CORS stations is and to determine the true values that record the tectonic activity, which correspond to noise levels as well as the uncertainties, and which can be associated with the various types of monuments used. One way to know the behavior of the stations is to

investigate the coordinate time series of each station. Although the PAL1 and PAL2 stations are located at the Bucaramanga airport approximately 750 meters apart, they have different monumentations, one with a reinforced concrete pillar and the other with a drilled braced monument and their observation periods did not overlap, (Fig. 30)

Figure 30. Monumentation type of PAL1 station (left) and PAL2 station (right).

However, horizontal components show similar displacement patterns (Fig. 31).

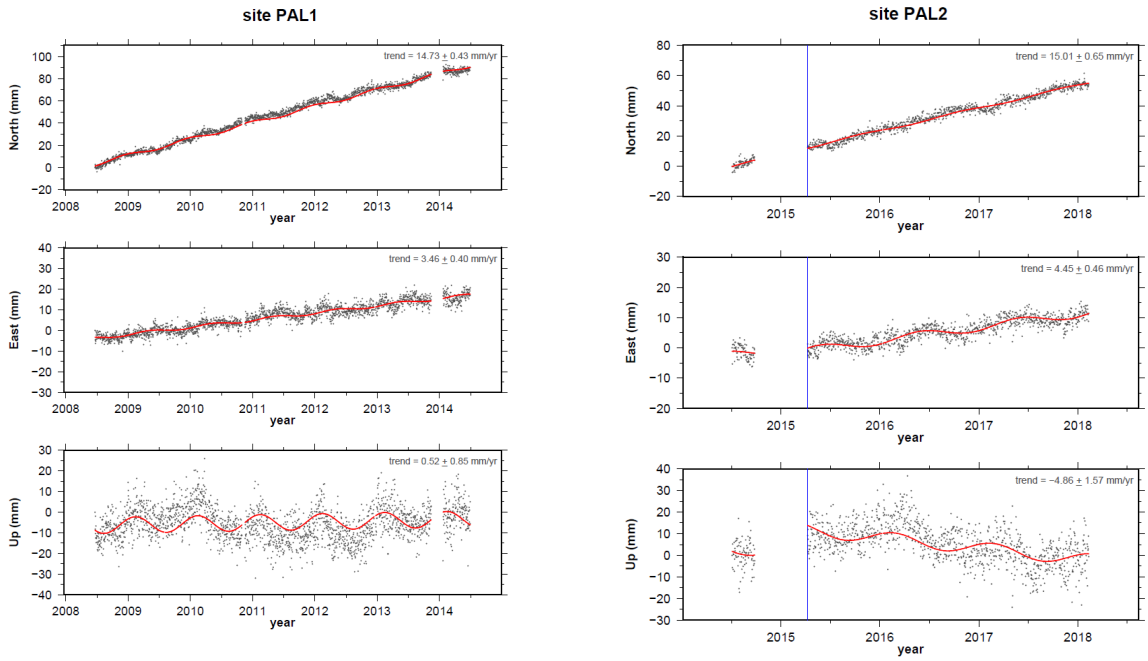

Figure 31. Time series associated to different type of monumentation.

5.3.GPS velocities

Table 4 shows the horizontal velocities with respect to the South American plate for the 60 stations located in the study area (Fig. 32), estimated following the procedure mentioned in the previous chapter.

Table 4. GPS horizontal velocities expressed wrt. South America plate (SOAM).

Sta ID	Longitude	Latitude	East Vel (mm/yr)	North Vel (mm/yr)	Sig East	Sig North
ACP1	280.050	9.371	22.2	1.7	0.3	0.3
ACP6	280.592	9.238	22.1	2.3	0.2	0.2
ALPA	287.082	11.528	13.9	3.0	0.9	0.6
AUCA	283.117	-0.641	1.9	-0.2	0.3	0.2
BAAP	286.446	4.072	-0.2	-0.6	0.5	0.2
BACO	284.308	9.402	18.6	-2.4	0.9	1.0
BAEZ	282.113	-0.459	6.2	0.5	0.3	0.2
BAME	285.435	4.236	6.4	3.9	0.7	0.2
BAPA	285.342	5.466	7.5	4.2	0.3	0.2
BARU	284.410	10.258	17.0	-0.3	0.8	0.4
BASO	282.607	6.203	11.7	5.5	0.9	0.4
BOBG	286.642	8.312	11.9	4.6	0.5	0.3
BOGT	285.919	4.640	4.4	4.7	0.3	0.2
BUGT	283.004	3.826	9.7	4.9	0.3	0.2
CAPI	287.572	5.351	1.8	0.9	0.3	0.4
CIA1	283.643	3.505	7.6	4.2	1.3	0.6
CN19	289.952	12.612	18.2	3.3	0.7	0.6
CN28	280.966	8.625	22.7	5.3	0.7	0.5
CN33	279.673	8.487	25.3	-3.3	1.8	1.8
CN35	278.637	13.375	17.0	-2.9	0.6	0.4
CN37	284.737	10.793	14.0	3.6	1.1	1.6
CN38	288.012	12.222	16.9	3.1	0.5	0.3
CN40	291.042	12.180	17.6	1.9	0.7	0.7
COEC	282.213	0.716	7.3	2.6	1.0	0.4
CORO	284.712	9.328	17.0	1.1	0.3	0.3
CUC1	287.487	7.932	12.6	2.4	1.5	0.4
ESMR	280.276	0.935	22.2	6.8	0.5	0.3
GLPS	269.696	-0.743	54.8	2.1	0.2	0.2
GUAP	282.105	2.574	12.5	3.5	0.5	0.4
ISCO	272.944	5.544	55.1	65.8	0.7	0.5
MALO	278.394	4.003	53.1	4.2	0.6	0.3
MECE	286.288	7.107	9.5	4.5	0.3	0.4
MITU	289.768	1.261	-0.4	0.7	0.4	0.3

MZAL	284.529	5.030	6.5	7.7	0.3	0.7
OCEL	288.384	4.271	-0.3	0.9	0.3	0.2
PAL1	286.811	7.136	8.5	4.2	0.4	0.4
PASI	283.501	0.513	1.2	0.2	0.3	0.4
POVA	283.385	2.449	9.7	2.8	0.5	0.3
PUIN	292.097	3.851	0.0	-0.4	0.5	0.3
QUIL	282.709	1.394	9.5	4.2	0.8	0.3
RIOP	281.349	-1.651	3.5	-4.1	0.6	0.4
SAN0	278.284	12.580	18.2	-2.4	0.4	0.2
SEL1	284.471	6.191	9.0	4.6	0.3	0.2
SNLR	281.153	1.293	15.4	0.8	0.4	0.3
TICU	290.061	-4.187	-0.4	-0.1	0.3	0.3
TONE	283.861	6.324	9.3	5.4	0.5	0.2
TUCO	281.252	1.815	18.3	3.0	0.4	0.2
URRA	283.790	8.012	17.8	3.9	0.8	0.7
UWAS	287.609	6.451	5.1	2.4	0.3	0.3
VBUV	286.141	5.533	8.6	5.1	0.5	0.3
VDPR	286.752	10.436	13.8	4.7	0.2	0.2
VMAG	285.153	9.287	13.7	3.8	0.5	0.4
VNEI	284.745	3.062	3.9	3.6	0.3	0.3
VORA	283.278	7.818	19.4	1.5	1.8	1.5
VOTU	285.290	7.019	11.1	4.8	0.3	0.4
VPIJ	284.893	4.397	6.3	4.1	0.4	0.2
VPOL	285.139	10.794	13.1	6.3	0.5	0.2
VROS	285.677	4.847	4.9	4.1	0.5	0.3
VSJG	287.361	2.533	-0.4	0.2	0.6	0.3
VSJP	284.164	4.781	5.8	5.0	0.4	0.3

The velocity field presented in Figure 32 allows to observe subduction of the Nazca plate clearly, depicted in the eastward motion of the GPS stations located on the Galapagos (Ecuador) and Malpelo (Colombia) islands at a rate of 54.8 mm/year and azimuth N87.8°E and 53.3 mm/year with an azimuth of N85.5°E, respectively, with respect to SOAM. The velocity vectors of the stations located on the coast of the Pacific Ocean show larger magnitude with respect to SOAM than most of other velocity vectors in the Colombian territory, which could be considered as a clear expression of strain accumulation on the Nazca subduction zone. In order to support this statement, ten stations are considered: five stations located on the coast and five stations located inland, selected as pairs at about the same latitude. For example, the coastal stations ESMR (23.2 mm/yr, N73.0°E), TUCU (18.5 mm/yr, N80.7°E), GUAP (13.0 mm/yr, N74.4°E), BUGT (10.9 mm/yr, N63.2°E), BASO (12.9 mm/yr, N64.8°E) show larger velocity values than the stations located inland

COEC (7.7 mm/yr, N70.4°E), QUIL (10.4 mm/yr, N66.1°E), POVA (10.1 mm/yr, N73.9°E), CIA1 (8.7 mm/yr, N61.1°E) and TONE (10.8 mm/yr, N59.9°E), implying margin-normal contraction along the Nazca subduction zone (Figure 33).

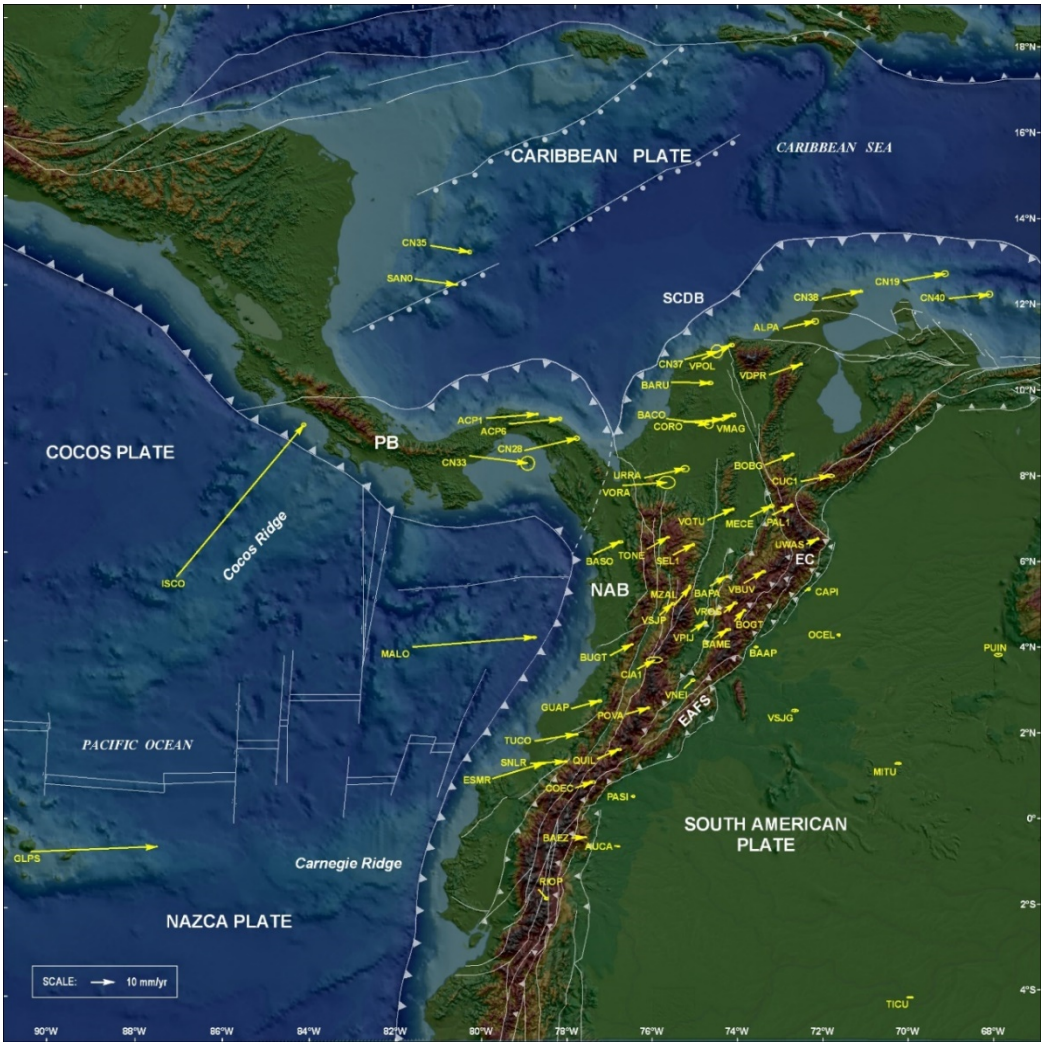

Figure 32. GPS vectors relative to stable South America, one sigma error ellipses.
North Andean Block (NAB), Eastern Cordillera (EC), East Andean fault system (EAFS), South Caribbean Deformed Belt (SCDB), Panama Block (PB)

The North Andean Block, as originally defined by Pennington (1981), is limited by the Colombia-Ecuador Trench and the Panamá Block to the west, the South Caribbean Deformed Belt (SCDB) to the north, and the Boconó fault and East Frontal fault zones to the east. The velocity vectors of the GPS stations located on the North Andean Block show, with respect to SOAM, in a general sense, a north-east direction; however, the stations located to the north of 7.5°N of latitude show a predominantly eastward trend. The velocity vectors of the stations located on the Panama Block indicate a clear collision with the North

Andean Block, and those on the islands of San Andrés and Providencia on the Caribbean plate present a general direction towards to the southeast (Figure 32).

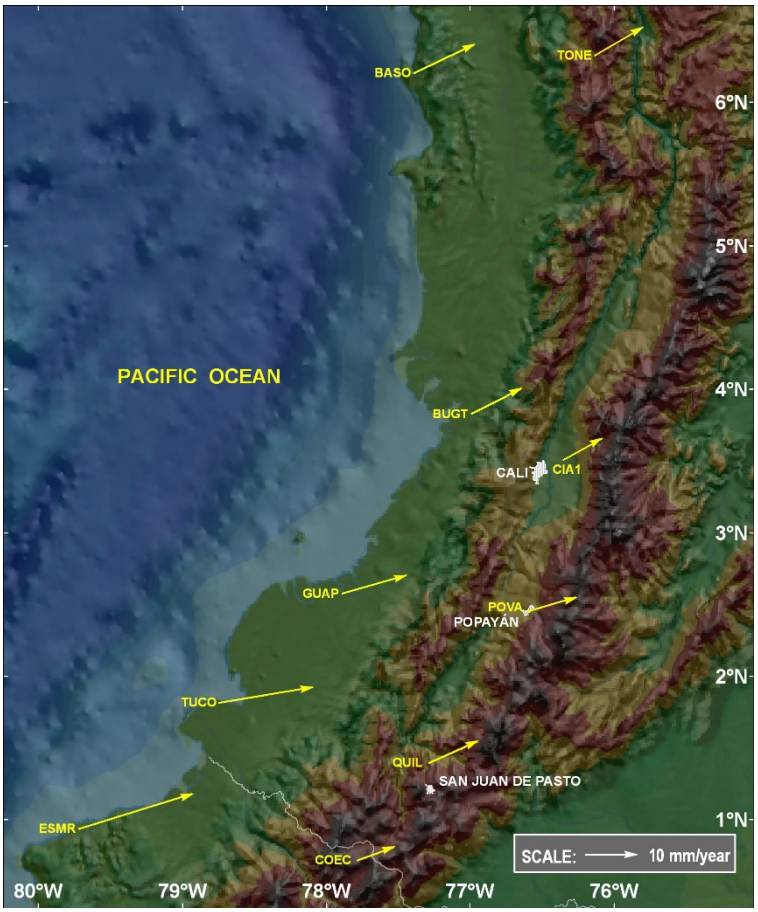

Figure 33. Velocity map of stations located on the coastal area zone and inland.

5.4.Comparison with previous studies

Previous studies conducted in the area of interest were based on episodic data collection through the field campaign measurements. In the following, I compare the velocity estimations obtained in previous studies with the results obtained in this dissertation.

Trenkamp et al. (2002) presented results from 1991 to 1998 CASA observations at 44 campaign sites to show wide plate boundary deformation and escape tectonics from the subducting Carnegie Ridge along an approximately 1400 km length of the North Andes, locking of the subducting Nazca plate, strain accumulation in the Ecuador-Colombia

forearc, collision of the Panama arc with Colombia, and Caribbean-North Andes convergence (Figure 34).

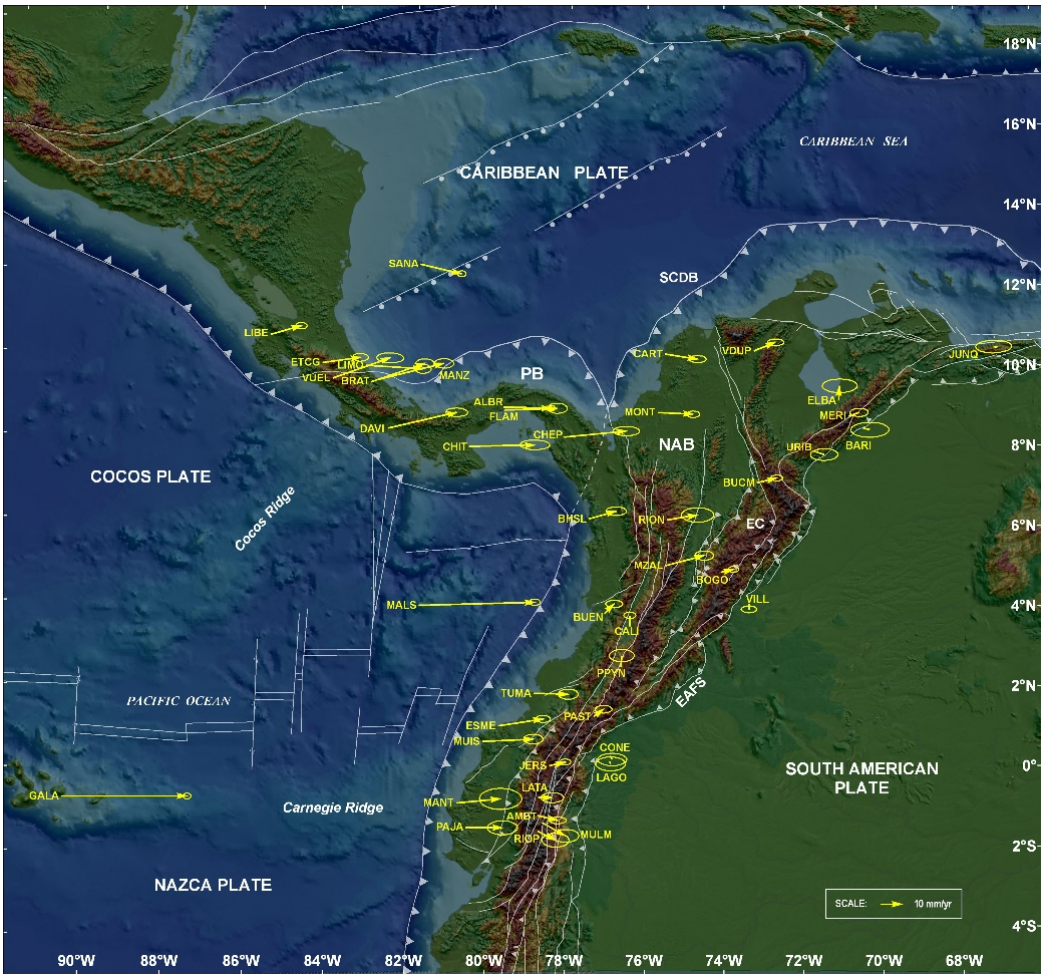

Figure 34. Velocity vectors relative to stable South America. Results from Trenkamp et al. (2002).

In order to make a comparison with previous studies, it should be noted that different sites were occupied in different solutions. Some of the GeoRED stations are located very close to the CASA field stations used by Trenkamp et al. (2002). The distance of separation between pairs of stations are in the range of hundreds of meters to a few kilometers. Given these distances of separation, it is possible to consider that the two velocities, both of Trenkamp et al. (2002) as of this study, represent the motion in the same site. It is important to point out that the velocity estimation of Trenkamp et al. (2002) is expressed with respect to ITRF96 while the velocity estimation of this dissertation is with respect to ITRF2008. The use of two different reference frames may mean some differences, which is explained later.

This study shows that MALO (Malpelo Island, Colombia) and GLPS (Galapagos Island, Ecuador) stations, located on the Nazca oceanic plate converge east to northeastward relative to stable South America at rates of 53.1 ± 0.6 mm/yr and 54.8 ± 0.2 mm/yr, respectively (Table 4). The velocity vectors estimated by Trenkamp et al. (2002) for the stations MALS (Malpelo Island) and GALA (Galapagos Island) were 53.6 ± 2.1 mm/yr and 58.2 ± 1.4 mm/yr, respectively (Figure 35).

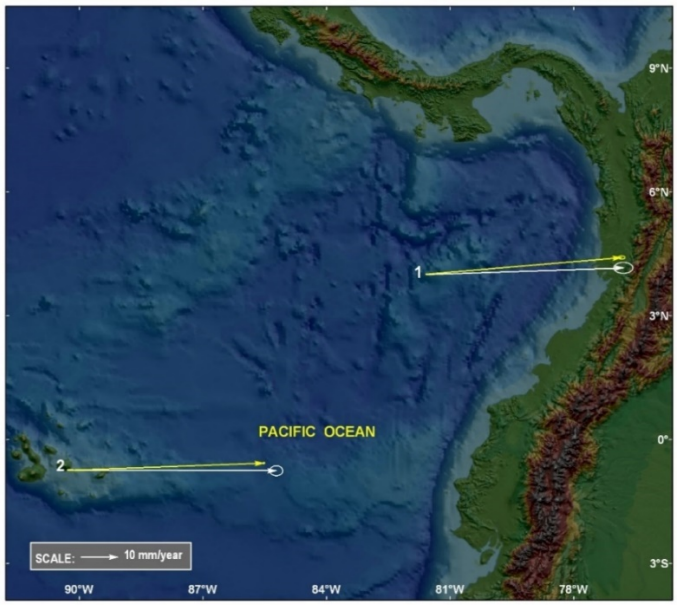

Figure 35. Comparison of velocity vectors at pairs of GPS stations (Trenkamp et al. (2002), and this dissertation) located on common places of the Nazca plate.
1: Malpelo Island; 2: Galapagos Island. White arrows: Trenkamp et al. (2002); yellow arrows: this dissertation

In Figure 35, it can be observed that the velocities of MALO and MALS stations are consistent with each other within the magnitude of their uncertainty. Although there is a small difference in the respective directions, considering the differences both in equipment and the style of the observations, the difference is not significant.

Near the Colombia-Ecuador border, coastal sites ESMR (Esmeraldas) and TUCO (TUMACO) moved rapidly east-northeastward at 22.2 ± 0.5 mm/yr and 18.3 ± 0.4 mm/yr, respectively, before the April 16, 2016, Muisne, Ecuador subduction earthquake. The velocity vectors reported in Trenkamp et al. (2002) are 20.8 ± 2.7 mm/yr for ESME and

16.1 ± 3.8 mm/yr for TUMA stations respectively (Figure 36). Considering the velocity errors in Trenkamp et al. (2003) estimation, the differences are not significant.

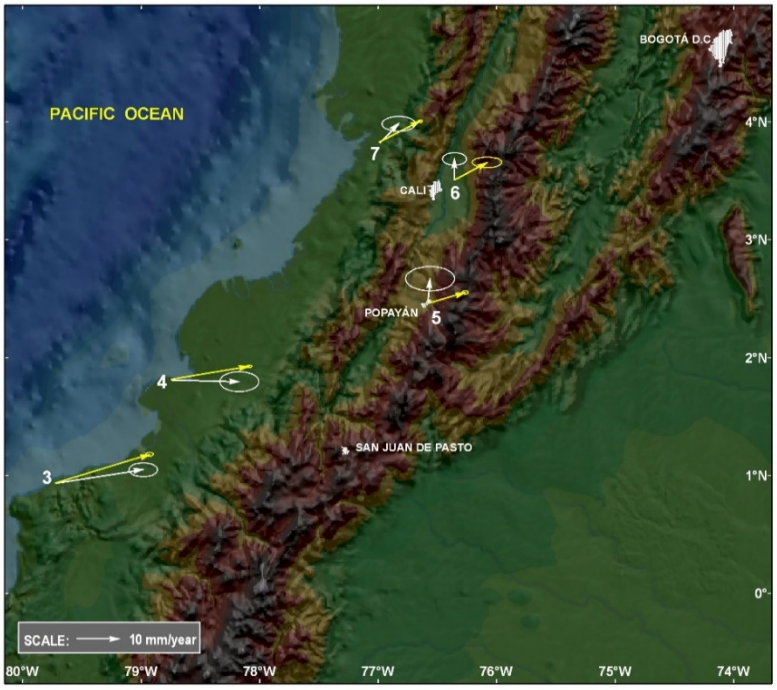

Figure 36. Comparison of velocity vectors at pairs of GPS stations (Trenkamp et al. (2002), and this dissertation) located on common places of the NAB.
Sites: 3, Esmeraldas; 4, Tumaco; 5, Popayán; 6, Palmira; 7, Buenaventura. White arrows: Trenkamp et al. (2002); yellow arrows: this dissertation

On the other hand, the new velocity vectors for several sites in southwest Colombia from 2°N to 5°N, located in sites near to the CASA sites, show an apparent increase in their eastward motion. For example, the POVA (Popayan) velocity is 9.7 ± 0.5 mm/yr to the east and the PPYN (Popayan) velocity by Trenkamp et al. (2002) was only 0.5 ± 4.7 mm/yr to the east. The velocity at CIA1 (Palmira) site is 7.6 ± 1.3 mm/yr and the CALI (Palmira) velocity was only 0.1 ± 2.3 mm/yr to the east (Trenkamp et al., 2002). These two sites are at the same location in CIAT (The International Center for Tropical Agriculture facilities). The BUGT (Buenaventura) velocity in this dissertation is 9.7 ± 0.3 mm/yr, and the nearby BUEN velocity was reported by Trenkamp et al. (2002) as 4.5 ± 3.2 mm/yr. It is noted that there are significant differences in both magnitude and the direction of the velocity vectors.

The way to obtain the data corresponds to different styles, which is probably reflected in the estimation of the velocity errors. The results of Trenkamp et al. (2002) were

obtained by field campaigns, with observation time of several days at each station and intervals between field campaigns of 2 and 3 years, while the data of this dissertation are obtained with GPS permanent stations of continuous operation. The velocity vectors of these stations indicate that the measurements and results obtained in both studies are consistent and stable for the measurement epoch, and each one corresponds to the state-of-the art in the development of the reference frame, which have been refined gradually over time. In the case of data gathering under episodic field campaigns, using wooden tripods and with different instrumental heights in each campaign and station, it is possible that different occupations in different years have some impact on the estimation of errors of the respective velocities. For the velocity vector estimation, HECTOR software uses the temporal correlations between the solutions, assuming that the daily position solutions are not independent but they are correlated.

In addition, an important aspect to take into account in this comparison is the possible impact on geodetic velocities due to the different reference frames, ITRF96 and ITRF2008. For the estimation of this impact, it is required to make the transformation of the velocities from one frame to the other. Trenkamp et al. (2002) did not include vertical velocities. Since the transformation between the reference frames includes translation, rotation and scale, it is not feasible to make the transformation from ITRF96 to ITRF2008. For this reason, the exercise was done in the opposite direction, that is, from ITRF2008 to ITRF96, for the BUGT, CIA1, ESMR, GLPS, BAD, POVA and TUCO GPS stations. The HTDP (Horizontal Time-Dependent Positioning) application (Snay et al., 2018) of the US National Geodetic Survey, was used for performing the reference frame transformation, available at https://www.ngs.noaa.gov/TOOLS/Htdp/Htdp.shtml

HTDP performs the transformation of the velocity values Vx, Vy, Vz of a station in any position expressed in the reference frame A to obtain the corresponding velocities in the reference frame B by means of the equations

$$\begin{aligned}(Vx)^B &= (Vx)^A + \dot{T}x + \dot{s}\cdot x + \dot{R}z\cdot y - \dot{R}y\cdot z \\ (Vy)^B &= (Vy)^A + \dot{T}y - \dot{R}z\cdot x + \dot{s}\cdot y + \dot{R}x\cdot z \\ (Vz)^B &= (Vz)^A + \dot{T}z + \dot{R}y\cdot x - \dot{R}x\cdot y + \dot{s}\cdot z\end{aligned} \qquad (5.1)$$

Then,

- the x, y, z values correspond to the 3D Earth-Centered Earth-Fixed (ECEF) Cartesian coordinates of the station position in the reference frame A;
- $\dot{T}x$, $\dot{T}y$, $\dot{T}z$ are the three translation rates of reference frame B relative to the reference frame A;
- $\dot{R}x$, $\dot{R}y$, $\dot{R}z$ corresponds to the three rotation rates of reference frame B with respect to the reference frame A; and,
- $\dot{s}$ is the differential scale change rate of reference frame B with respect to the reference frame A.

The transformation of the station velocities from ITRF98 to ITRF96 allowed to establish an impact of -0.3 mm/year on the annual velocity of the east component and 3.2 mm/year on the velocity of the north component. This means that the impact on the velocity estimation using ITRF96 in the east component, in which it is assumed to have larger motion due to the fact that it represents the Nazca plate subduction is negligible with respect to ITRF2008, but it has a higher impact on the north component.

Reprocessing of the campaign GPS data confirms the older results, which indicates that the differences are not related to flaws in the older GPS data analysis. It is more likely that the observed differences are due to different data spans that may reflect the time dependence of the deformation. However, the expected corrections between the two solutions are not consistent with the observed velocity differences in the Pacfic coastal region of Colombia. These differences can be attributed to a postseismic deformation effect, which will be discussed later in the Discussion chapter.

5.5.Combination with Ecuadorean Data

The GPS velocity field obtained in this dissertation for the stations located on the North Andean Block is combined with the results obtained by Nocquet et al. (2014), with the purpose of obtaining a better view of velocities in that block. Considering that the results of Nocquet et al. (2014) are based primarily on stations located in Ecuador, with only a few stations in Colombia, it is possible to demonstrate that the two data sets are mutually complementary. The model of the South America plate used in this dissertation is based on

the solution provided by Fernandes et al. (pers. comm.), which uses a different set of sites than those used by Nocquet et al. (2014) to define the South America plate model. Therefore, there is a slight difference between the two SOAM reference frames. Five overlapping sites (AUCA, ESMR, SNLR, RIOP, TUCO) between the two data sets, located in northern Ecuador and southern Colombia, are used to compute the offset between the two South America frames. Table 5 shows the velocities with respect to SOAM of the Nocquet et al. (2014) estimation and the velocities obtained in this dissertation using the Fernandes et al., (pers. comm.) estimation, for the five mentioned overlapping sites. There are small but significant differences between the two datasets.

Table 5. Nocquet´s velocities and this dissertation velocities w.r.t. SOAM of the overlapping sites.

COMMON STATIONS			Nocquet´s velocities				Velocities of this dissertation			
ID	**Lon**	**Lat**	**Vel E mm/yr**	**Vel N mm/yr**	**sig E**	**sig N**	**Vel E mm/yr**	**Vel N mm/yr**	**sig E**	**sig N**
AUCA	-76.88	-0.64	1.9	-1.9	0.5	0,5	1.9	-0.2	0.3	0.2
ESMR	-79.72	0.93	21.7	5.4	0.3	0.3	22.2	6.8	0.5	0.3
RIOP	-78.65	-1.65	4.8	-4.3	0.4	0.4	3.5	-4.1	0.6	0.4
SNLR	-78.84	1.29	16.2	-0.8	0.4	0.5	15.4	0.8	0.4	0.3
TUCO	-78.74	1.81	19.1	2.6	0.7	0.6	18.3	3.0	0.4	0.2

The estimated shift between the two sets of velocities at the overlapping sites is about -0.46 mm/yr and 1.05 mm/yr for the east and north components respectively, with a standard deviation of 0.71 mm/yr and 0.73 mm/yr for each component respectively (Table 5); this difference was added to the Nocquet et al. (2014) velocities estimation in order to obtain the combined velocity field (Figure 37). In this correction, only a translation effect was considered because the area covered by the overlapping sites is small, an unconstrained estimation of an unstable rotation could be generated. This small difference between the two reference frames allows this assumption.

It is important to mention that the overlapping sites GPH1, GYEC, CUER and TULC are Ecuadorean field stations for episodic campaigns, processed by the Geophysical Institute, and it is not possible to know if the field stations data correspond to the same period of observation of the permanent stations used for the estimation of the velocities.

Nocquet et al (2014) did not mention the sites and velocities used to define the SOAM reference frame.

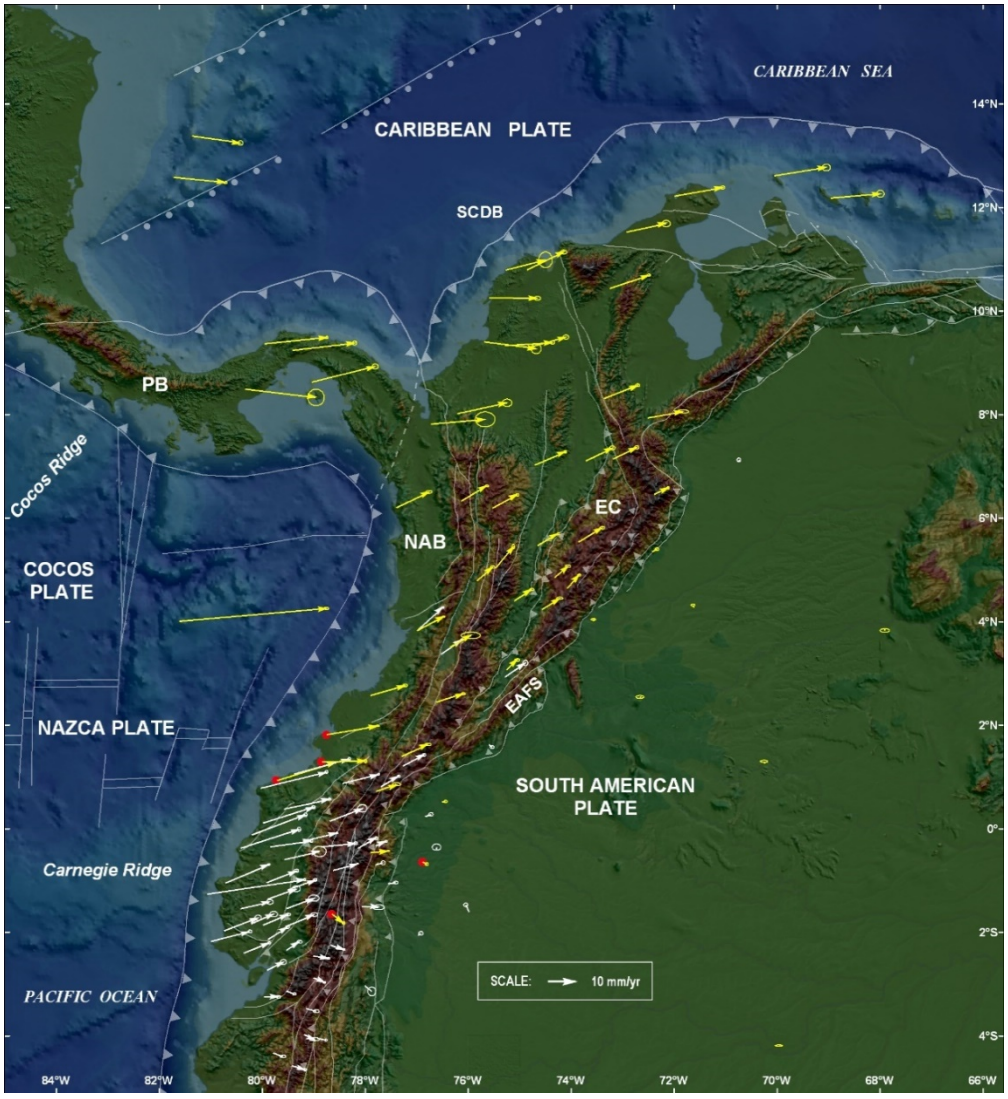

Figure 37. Combined Velocity Field relative to stable South America.
One sigma error ellipses are shown. Yellow arrows (this study); white arrows, Nocquet et al. (2014) velocities; red balls: overlapping sites. North Andean Block (NAB), Eastern Cordillera (EC), Panama Block (PB).

5.6.North Andes Block Motion

It is important to determine the relative motion of the North Andes Block (NAB) with respect to the South America plate in order to estimate accurately the slip partitioning into margin-parallel rigid body translation along the Eastern Andean Frontal Fault System (Figure 1), the accumulation of margin-normal elastic strain on the Colombia-Ecuador trench, and the permanent shortening and mountain building in the Eastern Cordillera of

Colombia. Previous studies conducted by Nocquet et al. (2014) and Chlieh et al. (2014) allowed to establish the relative motion of the North Andes Sliver (NAS) with respect to South America. But their estimates were based on data from GPS stations located in a small area. Nocquet et al. (2014) used 14 stations to estimate the Euler pole of the North Andes Sliver, with only three stations in Colombia, including the BOGT station. The number and distribution of these stations, mainly located in Ecuador, may not be appropriate to extrapolate the amount of motion farther to the north. The IGS BOGT station, which subsides at a rate of ~36 mm/yr, probably due to groundwater extraction and compaction, shows anomalous horizontal motion with respect to other stations located in the vicinity. Thus, the BOGT data may bias the estimation of the angular velocity. The exclusion of the BOGT station and the use of other more representative sites in Colombia is the main difference between the estimation of the NAB motion of this dissertation and that by Nocquet et al. (2014).

Estimation of the North Andean pole corresponds to the problem of determining the parameters of the Euler pole from the velocity vectors observed in a set of stations located in the same rigid tectonic block, which is called the inverse Euler pole problem (Nocquet, 2008; Goudarzi et al., 2014; Cannavo and Palano, 2011, 2016).

Cannavo and Palano (2011, 2016) present the methodology related to the calculation of Euler pole in the Earth-Centered Earth-Fixed (ECEF) frame. At a given position P on the surface of the earth, which is defined by its geocentric Cartesian coordinates *X, Y, Z* (expressed in meters) and the rotation of a plate defined by the rotation vector $\overline{\boldsymbol{\Omega}}$ $(\omega_x, \omega_y, \omega_z)$ (expressed in rad/year), the velocity vector in V (V_x, V_y, V_z) (in m/yr) is given by the vector product.

$$\bar{V} = \overline{\boldsymbol{\Omega}} \times \bar{P} = \begin{pmatrix} Z\omega_y - Y\omega_z \\ X\omega_z - Z\omega_x \\ Y\omega_x - X\omega_y \end{pmatrix} \qquad (5.2)$$

In equation (5.2), the resulting velocities are in the ECEF framework, so they must be transformed into the local (North, East, Up) framework. To perform the velocity conversion at the location of the corresponding station, which is defined by (φ, λ, h) (geodetic latitude,

longitude and ellipsoidal height) a combination of the three rotations is required to align the ECEF frame with the NEU frame as

$$\bar{L} = \bar{R}\bar{V} \quad (5.3)$$

where L is the velocity vector components expressed in the local frame (N, E) and R is the rotation matrix expressed as

$$R = \begin{bmatrix} -sin\lambda cos\varphi & -sin\lambda sin\varphi & cos\lambda \\ -sin\varphi & cos\varphi & 0 \end{bmatrix} \quad (5.4)$$

The inverse problem consists in computing the pole parameters from the geodetic velocities of a given number of stations. Thus, for a given station, observation equation is written in a matrix form as

$$\begin{bmatrix} V_e \\ V_n \end{bmatrix} = A\bar{\boldsymbol{\Omega}} + \varepsilon = \boldsymbol{R} \begin{bmatrix} 0 & Z & -Y \\ -Z & 0 & X \\ Y & -X & 0 \end{bmatrix} \begin{bmatrix} \omega_x \\ \omega_y \\ \omega_z \end{bmatrix} + \varepsilon \quad (5.5)$$

where A is the design matrix, and ε is the vector of measurement errors.

This problem can be solved by minimizing the weighted squared residuals by a least squares approach since the problem is over-determined with just two sites because there are three unknowns and two equations per station as follows:

$$\bar{\boldsymbol{\Omega}} = (A'WA)^{-1}A'W\boldsymbol{V} \qquad (5.6)$$

where W is the data weight matrix that is currently chosen as the inverse of the variance-covariance matrix of the measurement data, and A' is the transpose of the matrix A. The model of covariance is given by:

$$C_\Omega = (A'WA)^{-1} \qquad (5.7)$$

In order to estimate Euler pole of the North Andean Block, we need to select stations representing the rigid motion of the block. Trial and error tests were performed using different number of stations located on the NAB in order to choose the more appropriate

Euler pole that corresponds to the motion of this block. The statistical criteria play an essential role in the estimation of the Euler pole, which allows to evaluate the quality of the model, for which the following two statistical indicators were used: χ^2 (chi-square test) and F-test (Cannavó and Palano, 2011). Each trial and error test involves the analysis of statistical criteria and the elimination of stations or a combination of some of them for the next test. Initially tests are performed taking 41, 35, 28, 27, 22, 21 and 20 stations respectively, some of which are located near the Nazca subduction zone as well as the East Andean Fault System; others were located north of 7.5°N where a change in the direction of the velocity vectors with respect to SOAM is observed.

Table 6. Statistical indicators of the tests performed with different number of stations

Test	# stations	Chisqr	Redchi	F
1	41	2980.4	40.8273	39.7386
2	35	2607.5	44.1952	42.7462
3	28	527.416	11.7204	11.2216
4	27	523.2246	12.168	11.6272
5	22	386.6525	11.7167	11.0472
6	21	296.4781	9.5638	8.9842
7	20	240.9656	7.7731	7.302
8	16	200.9671	8.7371	8.0387
9	14	130.3802	5.2152	4.8289
10	14	164.8924	8.6785	7.852
11	14	108.2444	4.3298	4.0091
12	13	104.9209	4.9962	4.5618
13	13	141.5114	8.3242	7.448
14	12	65.2957	3.1093	2.8389
15	4	31.6307	6.3261	4.5187

The final site selection includes sites in southern Ecuador and across central Colombia located away from the coast where subduction-related deformation is expected to be minimal based on previously published elastic models (Trenkamp et al., 2002; Kobayashi, et al., 2014; Nocquet et al., 2014), and where neighboring sites have similar velocities indicating minimal internal strain. Sites close to major crustal fault zones are also avoided to minimize the impact of those faults. The BOGT station, used by Nocquet et al. (2014), is not used in the tests, considering the horizontal bias due to the vertical downward change presumably due to the land subsidence in the city of Bogota. The lowest values of

reduced chi-square = 3.1093 and F = 2.8389 are obtained from different tests, which is the basis for the most appropriate pole selection. Table 6 shows the statistical indicators of the trial and error tests performed, with different numbers of stations. The solution adopted corresponds to test 14. Thus, in this dissertation, the North Andean pole is re-estimated based on a set of 12 sites that span a larger part of the North Andes block (GPH1, GYEC, CUER, TULC, QUIL, BAME, VPIJ, VSJP, BAPA, VBUV, VROS, PAL1), four of them located in Ecuador and the others in Colombia (Figures 37). These sites are concentrated in southwestern Ecuador and central region of Colombia.

The Euler pole is represented by an angular rotation vector (ω_x, ω_y, ω_z), or equivalently the coordinate of the pole (ϕ, λ) and an angular velocity ω. Following relations hold between the sets of parameters.

$$\omega_x = \omega \cos\lambda \cos\phi$$

$$\omega_y = \omega \cos\lambda \sin\phi \qquad (5.8)$$

$$\omega_z = \omega \sin\lambda$$

In order to convert back to E and ω, it is required to use the following formulas:

$$\phi = \tan^{-1}(\omega_y / \omega_x)$$

$$\lambda = \tan^{-1}(\omega_z / (\omega_x^2 + \omega_y^2)^{1/2}) \qquad (5.9)$$

$$\omega = (\omega_x^2 + \omega_y^2 + \omega_z^2)^{1/2}$$

Table 7. Comparison of the estimated angular velocities for the NAB with respect to SOAM.

Plate	Model	Lat°	Lon°	ω°/Myr	σ_{max}°(a)	σ_{min}°(a)	ζ_{max}°(b)	σ_ω°/Myr
NAB	This dissertation	58.63	-174.85	0.072	22.01	1.31	80.97	0.0017
	Nocquet et al. (2014)	15.21	-83.40	0.2870	1.03	0.18	74.40	0.0180
	Symithe et al. (2015)	0.20	-71.60	0.877	N/A	N/A	N/A	N/A

(a) σ_{max}, σ_{min}: semi-major and semi-minor axes of the 1-σ error ellipse.
(b) ζ_{max}: azimuth of the semi-major axis reckoned clockwise from north.

Table 7 shows a comparison of the three estimated angular velocities for the NAB with respect to SOAM.

As the pole estimated in this dissertation is located approximately 75°- 80° from the NAB itself, the predicted motions of the NAB are almost in the same direction throughout the block, with a motion of 8.6 mm/yr with respect to the South America plate, in the N60°E direction. Chlieh et al. (2014), based on measurements at GPS stations located in Ecuador and southern Colombia, estimated a very similar motion of 8.5 ± 1.0 mm/yr, along the block that they named NAS (North Andes Sliver). In 2016, Mora-Páez et al. (2016) estimated a movement of 8.8 ± 1.7 mm/yr, but this estimation was based on data from 20 field stations and 9 permanent stations, corresponding only to a part of the NAB in the central Colombia. Recently, Pérez et al. (2018) estimate the motion of NAB with respect to South America, using data from nine GPS stations mainly from Venezuela and only four stations located in Colombia north of 7.5°N (VDPR, ALPA, CN38 and MONT). The average estimated motion of NAB with respect to South America was 15.0 ± 1.0 mm/yr with an N80°E ± 6° direction, that is estimated with respect to the Maracaibo (MARA) GPS station, located within the Maracaibo Block (MB).

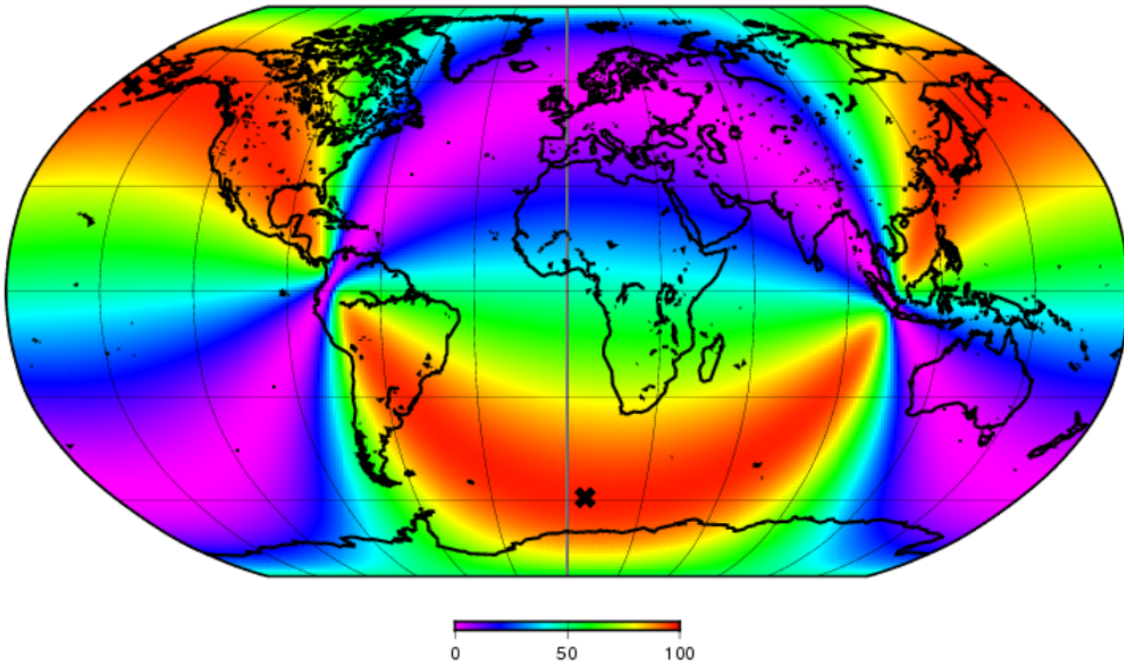

Figure 38. Variance reduction based on the Euler pole parameters obtained in this dissertation.

The estimated NAB poles by Nocquet et al. (2014) and this study appear very different. In the case of this study, the Euler pole estimation error is substantially greater than the value obtained by Nocquet et al. (2014) (Table 7). This result does not imply that the estimated pole is wrong. Since the target area for Euler pole estimation is too small, there is not significant velocity change over the whole area of interest. As a result, there is a strong correlation between the estimated pole location and the angular velocity and the pole location cannot be well resolved along the large circle. Such a characteristics can be demonstrated with a variance reduction plot for different candidate locations of the Euler pole (Figure 38). In this plot, the pole locations are tested all over the world every one degree both in latitude and longitude, and the variance reduction of the velocity data is calculated for the optimum angular velocity at each location.

The two Euler poles are indicated by thick crosses corresponding to the optimum solution. However, similar variance reduction can be achieved by Euler poles at different locations along the large circle as shown by the red region in Figure 38. Then the estimation error for the pole location becomes very large and the pole location is susceptible to small changes in the velocity data.

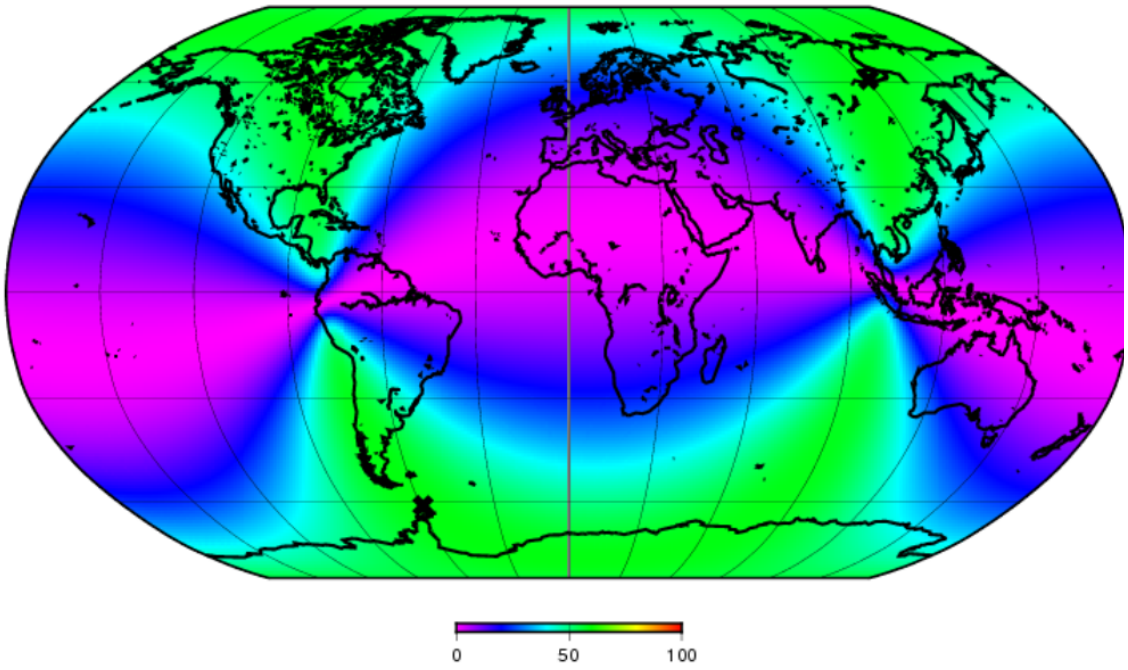

Figure 39. Variance reduction based on the Euler pole parameters obtained by Nocquet et al. (2014).

On the other hand, Figure 39 shows the plot of the variance reduction calculated for the velocity data used by Nocquet et al. (2014). The percentage of variance reduction is less than 60%, which means that data fitting with an assumption of rigid plate motion is rather poor. This is because they take many stations over a wide area into account in their Euler pole estimation. The smaller error ellipse does not necessarily imply the corresponding solution is more reliable.

Table 8 and Figure 40 show the velocities relative to the North Andes block (NAB) based on the Euler pole of NAB estimated in this study. This plot clearly shows elastic strain signals due to the Nazca plate subduction, oblique convergence across the Eastern Cordillera, and the effects of Panama arc collision and Caribbean plate subduction.

Table 8. GPS velocities (mm/yr) relative to NAB.

ID	Longitude	Latitude	Vel (E)	Vel (N)	Sig (E)	Sig (N)
ACP1	-79.950	9.371	15.3	-2.4	0.3	0.3
ACP6	-79.408	9.238	15.2	-1.8	0.2	0.2
AHUA	-77.550	-1.060	-4.3	-3.8	0.7	0.4
ALPA	-72.918	11.528	7.0	-1.1	0.9	0.6
AMAL	-79.420	-4.580	-2.3	-5.5	0.5	0.3
ARCA	-70.750	7.080	-6.8	-3.3	0.5	0.5
AUCA	-76.880	-0.640	-5.6	-5.0	0.3	0.2
AYAN	-80.750	-1.980	5.5	0.7	1.0	0.8
BAAP	-73.554	4.072	-7.3	-4.7	0.5	0.2
BACO	-75.692	9.402	11.6	-6.6	0.9	1.0
BAEZ	-77.887	-0.459	-0.8	-3.6	0.3	0.2
BALZ	-79.900	-1.360	3.4	-0.4	1.2	0.9
BAME	-74.565	4.236	-0.6	-0.3	0.7	0.2
BAPA	-74.658	5.466	0.6	0.1	0.3	0.2
BARU	-75.590	10.258	10.1	-4.4	0.8	0.4
BASO	-77.393	6.203	4.8	1.4	0.9	0.4
BOBG	-73.358	8.312	5.0	0.5	0.5	0.3
BOGT	-74.081	4.640	-2.6	0.6	0.3	0.2
BUEN	-77.010	3.882	2.3	4.1	0.4	0.2
BUGT	-76.996	3.826	2.7	0.8	0.3	0.2
CABP	-80.420	-0.380	14.2	2.7	0.5	0.6
CALI	-76.530	3.370	0.6	0.9	0.4	0.3
CAPI	-72.428	5.351	-5.2	-3.3	0.3	0.4

CHIS	-80.720	-1.050	8.8	2.5	0.4	0.3
CIA1	-76.357	3.505	0.7	0.0	1.3	0.6
CN19	-70.049	12.612	11.3	-0.8	0.7	0.6
CN28	-79.034	8.625	15.8	1.2	0.7	0.5
CN33	-80.327	8.487	18.4	-7.4	1.8	1.8
CN35	-81.363	13.375	10.3	-7.0	0.6	0.4
CN37	-75.263	10.793	7.1	-0.6	1.1	1.6
CN38	-71.988	12.222	9.9	-1.0	0.5	0.3
CN40	-68.958	12.180	10.6	-2.2	0.7	0.7
CNJO	-76.840	0.230	-4.8	-3.3	0.6	0.5
COEC	-77.787	0.716	0.4	-1.6	1.0	0.4
CORO	-75.288	9.328	10.1	-3.0	0.3	0.3
CUC1	-72.513	7.932	5.6	-1.8	1.5	0.4
CUEC	-79.000	-2.880	-3.1	-5.8	0.4	0.3
CUER	-79.530	-2.350	-2.3	-1.1	0.8	0.5
CULA	-78.690	0.140	4.8	0.6	1.3	1.1
DAUL	-79.990	-1.870	2.2	-0.2	0.7	0.4
DESV	-79.920	-1.040	3.9	0.1	0.6	0.5
ELCH	-77.800	-0.330	-3.2	-2.6	0.4	0.3
ESMR	-79.720	0.930	14.2	2.3	0.5	0.3
FLFR	-79.840	-0.350	7.9	-2.0	0.4	0.5
FLOR	-75.600	1.620	-5.7	-5.0	0.6	0.4
GPH1	-79.910	-2.730	-1.0	-1.3	0.9	0.8
GUAP	-77.895	2.574	5.5	-0.7	0.5	0.4
GYEC	-79.890	-2.140	0.1	0.3	0.5	0.4
HONA	-79.150	-3.470	-3.2	-5.2	0.9	0.4
HSPR	-78.850	-0.350	5.3	-2.9	0.5	0.4
HUAC	-77.800	-0.700	-4.2	-3.4	0.6	0.6
ISPT	-81.070	-1.260	28.4	1.0	0.4	0.3
JUJA	-79.550	-1.890	3.4	0.1	1.1	0.6
LATA	-78.620	-0.810	1.8	-1.7	0.2	0.2
LCOL	-79.200	-0.240	5.2	-1.2	0.3	0.2
LGCB	-79.570	0.380	9.3	-0.7	0.5	0.3
LIMO	-76.620	-0.400	-6.9	-3.3	1.2	0.9
LITS	-78.440	0.870	6.1	-0.8	0.3	0.3
LJEC	-79.190	-3.980	-3.1	-5.7	1.5	0.5
LORO	-75.980	-1.610	-8.2	-1.6	0.6	0.5
MACH	-79.960	-3.250	-1.9	-4.1	0.7	0.4
MALO	-81.606	4.003	46.1	0.1	0.6	0.3
MECE	-73.712	7.107	2.5	0.4	0.3	0.4
MITU	-70.232	1.261	-7.4	-3.4	0.4	0.3
MOCA	-79.500	-1.180	2.9	-0.6	0.5	0.4
MONT	-76.980	-2.060	-5.8	-3.4	0.6	0.5
MZAL	-75.471	5.030	-0.5	3.5	0.3	0.7

NARI	-79.530	-3.140	-4.0	-5.2	0.5	0.3
NEVA	-75.290	2.930	0.5	0.9	0.7	0.8
OCEL	-71.616	4.271	-7.3	-3.2	0.3	0.2
PAJA	-80.420	-1.550	3.6	-1.6	1.0	0.7
PAL1	-73.189	7.136	1.5	0.1	0.4	0.4
PAPA	-78.140	-0.380	-0.4	-0.5	0.5	0.4
PASI	-76.499	0.513	-5.8	-3.9	0.3	0.4
PDNS	-79.990	0.110	11.4	1.5	0.6	0.4
POVA	-76.615	2.449	2.7	-1.3	0.5	0.3
PPRT	-80.210	-0.120	12.6	3.1	0.5	0.5
PROG	-80.360	-2.410	2.2	-0.3	0.5	0.3
PSTO	-77.270	1.210	0.7	-0.3	0.5	0.4
PTGL	-80.030	0.780	16.9	1.7	0.5	0.4
PUEB	-79.530	-1.550	2.9	-0.3	1.6	0.9
PUIN	-67.903	3.851	-7.1	-4.5	0.5	0.3
PUYX	-78.060	-1.500	-1.0	-4.5	1.7	0.7
QUIL	-77.291	1.394	2.5	0.1	0.8	0.3
RIOP	-78.650	-1.650	-2.7	-7.4	0.6	0.4
RVRD	-79.380	1.060	13.0	1.1	0.4	0.4
SABA	-80.220	-1.840	1.3	-0.6	1.2	0.8
SALN	-80.990	-2.180	7.0	-0.5	0.6	0.4
SAN0	-81.716	12.580	11.5	-6.5	0.4	0.2
SEL1	-75.529	6.191	2.0	0.5	0.3	0.2
SNLR	-78.840	1.290	8.8	-3.9	0.4	0.3
SNTI	-78.010	-3.040	-4.4	-6.0	1.2	1.3
SOZO	-79.790	-4.330	-3.3	-5.4	0.8	0.4
SRAM	-79.560	-0.600	5.6	-1.2	2.0	1.5
TICU	-69.939	-4.187	-7.3	-4.2	0.3	0.3
TONE	-76.139	6.324	2.3	1.2	0.5	0.2
TOTO	-78.670	-2.250	-2.1	-5.7	0.3	0.2
TUCO	-78.748	1.815	11.3	-1.1	0.4	0.2
TULC	-77.700	0.810	-0.4	-0.4	0.4	0.3
URRA	-76.210	8.012	10.8	-0.3	0.8	0.7
UWAS	-72.391	6.451	-1.9	-1.8	0.3	0.3
VBUV	-73.859	5.533	1.6	1.0	0.5	0.3
VDPR	-73.248	10.436	6.9	0.6	0.2	0.2
VMAG	-74.847	9.287	6.8	-0.3	0.5	0.4
VNEI	-75.255	3.062	-3.1	-0.6	0.3	0.3
VORA	-76.722	7.818	12.4	-2.6	1.8	1.5
VOTU	-74.710	7.019	4.1	0.7	0.3	0.4
VPIJ	-75.107	4.397	-0.7	0.0	0.4	0.2
VPOL	-74.861	10.794	6.1	2.2	0.5	0.2
VROS	-74.323	4.847	-2.1	0.0	0.5	0.3
VSJG	-72.639	2.533	-7.4	-3.9	0.6	0.3

VSJP	-75.836	4.781	-1.2	0.8	0.4	0.3
ZAMO	-78.930	-4.050	-3.8	-4.8	0.3	0.3
ZHUD	-79.000	-2.460	-1.7	-5.0	0.5	0.3

The rotation pole estimated in this study is different from the rotation pole obtained by Nocquet et al. (2014), which is located in Central America, near the Caribbean coast. In Ecuador, the stations located south of the latitude 1°S show that the block motion estimated in this study is about 2.3 mm/yr more to the west, and 2.4 mm/yr more to the north, taking the results obtained by Nocquet et al. (2014) as reference. The difference in the north component is mainly due to the small difference between the two South American reference frameworks used in the two studies. The east-west component difference can be interpreted as the small east-west contraction across southern Ecuador due to a weaker coupling at the subduction zone. On the other hand, in northern Colombia, at the stations located north of latitude 7.5°N, the difference between the two Euler poles becomes larger, with a predicted motion estimate in this dissertation of the North Andean block of 3.9 mm/yr more eastward and 0.8 mm/yr more southward with respect to the predicted motion of Nocquet et al. (2014).

Taking into account the estimation of the Euler pole that was carried out as well as the values obtained in each station with respect to the NAB, it is possible to establish which stations could be in the rigid part of the North Andean Block.

The selection of the location of these stations should be based on the following considerations:

a) stations with residual values about 1 mm/year in the velocity components with respect to the NAB,
b) stations that are located away from the Pacific coast are used to avoid the subduction effect of the Nazca plate beneath South America;
c) stations that are located away from the eastern limit of the North Andean Block, corresponding to the Eastern Frontal Fault System, are used;
d) 7.5°N latitude is considered as the northern limit in order to avoid the influence of the Panama block collision as well as the Caribbean plate subduction. The current geodetic network is not dense enough to delimit the rigid part of the block clearly.

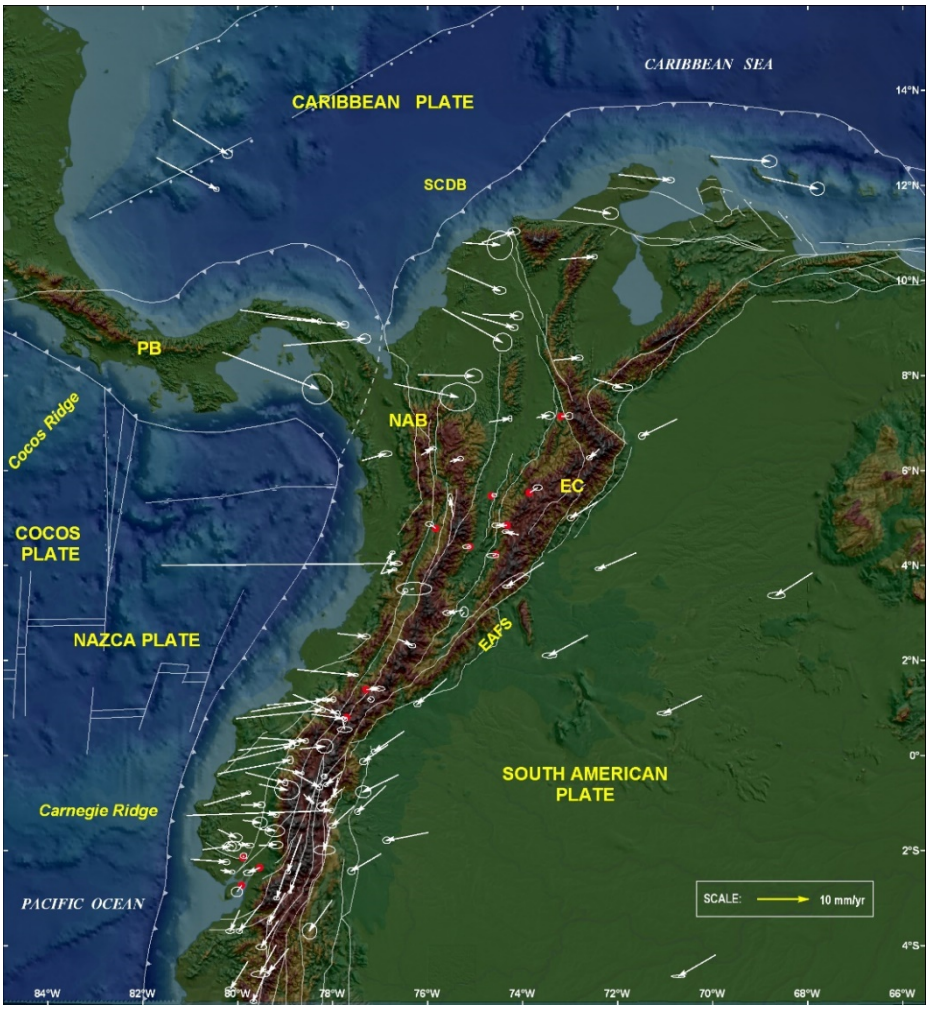

Figure 40. Velocities relative to the North Andes block (NAB), (Table 8) obtained in this dissertation. One sigma error ellipses. Red balls: sites used to re-estimate the North Andes motion

Table 9. Residuals of the Euler pole estimation for the NAB.

RESIDUALS				
Site	**R_Ve**	**R_Vn**	**S_Ve**	**S_Vn**
BAME	-0.06	-0.03	0.10	0.03
BAPA	0.06	0.01	0.04	0.03
CUER	-0.22	-0.11	0.08	0.05
GPH1	-0.09	-0.13	0.09	0.07
GYEC	0.03	0.03	0.05	0.04
PAL1	0.16	0.01	0.06	0.05
QUIL	0.26	0.01	0.09	0.04
TULC	-0.03	-0.05	0.04	0.03
VBUV	0.17	0.10	0.07	0.04
VPIJ	-0.06	-0.01	0.06	0.03
VROS	-0.20	-0.00	0.08	0.04
VSJP	-0.11	0.08	0.07	0.04

rms = 0.11 mm/yr wrms = 0.08 mm/yr

Table 9 shows the residuals obtained in the estimation of the Euler pole for NAB, from 12 stations that satisfy the conditions indicated previously. The distribution of these stations is showed in Figure 40 (red dots).

The Figure 41 corresponds to a comparison of the velocities with respect to NAB obtained in this dissertation as well as by Nocquet et al. (2014) and Symithe et al. (2015). It is observed that the velocities obtained in this study, as well as those of Nocquet et al. (2014), are very similar in central Colombia, up to around 7.5° north of latitude, although there are some minor differences in southwestern Colombia and Ecuador. Comparing these models with the model based on Symithe et al. (2015), it is possible to say that this model does not represent the central area of Colombia, and the velocities in southwestern Colombia and Ecuador are substantially different from those obtained in the other two models.

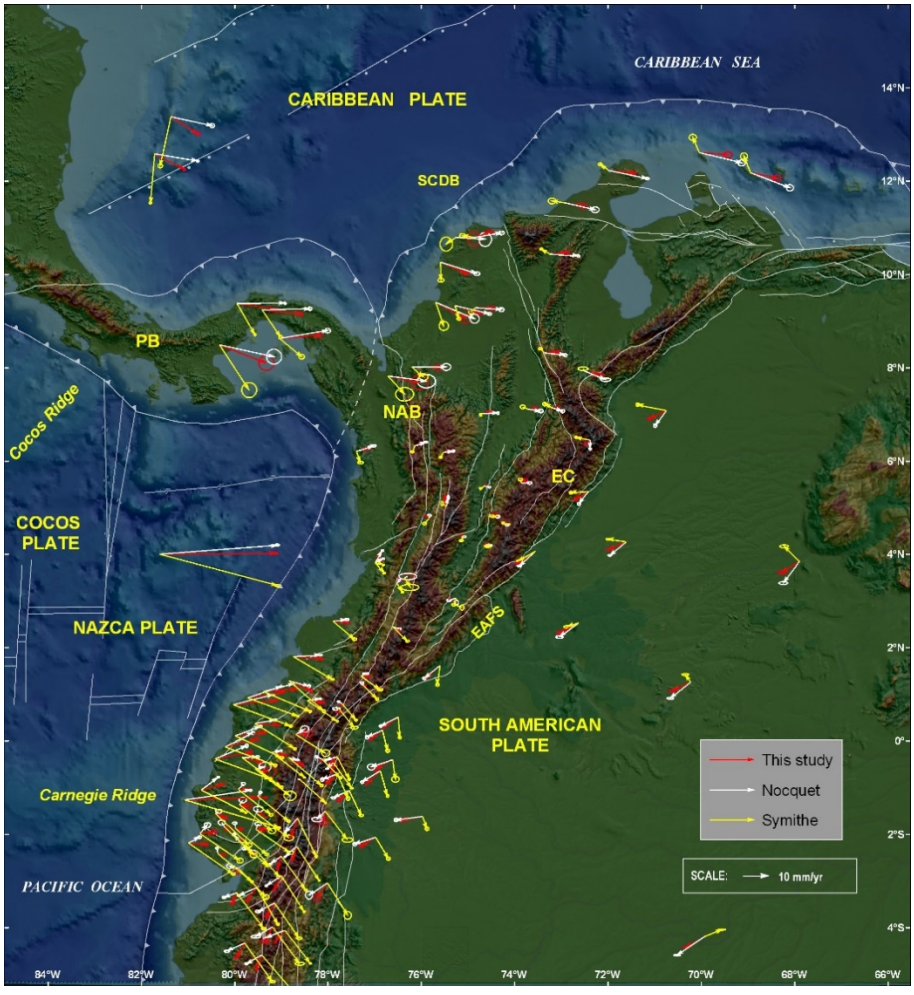

Figure 41. Comparison of the velocities relative to the North Andes block (NAB).
Obtained in this dissertation (red arrows); Nocquet et al. (2014), (white arrows); and Symithe et al. (2015), (yellow arrows).

5.7. Subduction Effects

5.7.1. Nazca Subduction.

Stations located on the Pacific coast in Colombia and Ecuador move toward inland relative to SOAM and NAB faster than those located further to the east (Figures 34 and 40). The coastal stations of ESMR (Esmeraldas, Ecuador) and TUCO (Tumaco, Colombia), located near the boundary between the two countries, moved rapidly east-northeastward at 22.2 ± 0.5 mm/yr and 18.3 ± 0.4 mm/yr with respect to SOAM respectively, and eastward relative to the NAB at 14.2 ± 0.5 mm/yr and 11.3 ± 0.4 mm/yr, respectively, before the occurrence of the April 16, 2016, Muisne, Ecuador, earthquake. The velocity values obtained in this study for these stations with respect to SOAM are slightly greater than the values reported by Trenkamp et al. (2002), 20.8 ± 2.7 mm/yr (ESME) and 16.1 ± 3.8 mm/yr (TUMA) respectively. The TUMA and TUCO stations are located in the same facilities, separated 816 m.

GUAP (Guapi) site is located 125 km from TUCO in the azimuth of N48°E (Figure 25). The eastward component of velocity of GUAP relative to SOAM is 12.5 ± 0.5 mm/yr, and 5.5 ± 0.5 mm/yr with respect to NAB. The BUGT (Buenaventura) station is located 295 km away in the N41°E direction from TUCO, and 170 km from GUAP in the N38°E direction. The direction of the trench of the Nazca subduction zone in Colombia from the border with Ecuador to Buenaventura is approximately the same direction as the location of the BUGT and GUAP stations from TUCO. This means that the distances of these stations from the trench are roughly similar. However, the velocity of the BUGT station with respect to SOAM is 9.7 ± 0.3 mm/yr towards the east, and 2.7 ± 0.3 mm/yr relative to the NAB. The increasing values of the eastward velocities from the north to the south observed at the stations BUGT, GUAP, TUCO and ESMR, suggest that the strain accumulation in the Nazca subduction zone of Nazca is increasing towards the south. The BUEN station in Trenkamp et al. (2002), located 655 m to the south of BUGT, shows an eastward velocity of 4.5 ± 3.2 mm/yr to South America, smaller than the value in this study by 8 mm/year. The GUAP station was built in 2011, so no comparisons can be made with the measurements made by Trenkamp et al. (2002) in this area. The difference observed between the results of Trenkamp et al (2002) and those obtained in this study are discussed later

Trenkamp et al. (2002) modeled the eastward motion of these coastal sites as being due to pre-earthquake 50% elastic locking above the subducting Nazca slab, down to a depth of 50 km. Such a locking depth is probably too deep, as it would be substantially deeper than the depth of slip in megathrust earthquakes observed recently (Nocquet et al., 2016; Bilek and Lay, 2018). If the locking depth is reduced, the locking fraction on the shallower part of the interface would have to increase to fit the data.

It should be noted that the BUEN station in Trenkamp et al. (2014) is a different site from the BUEN station in Nocquet et al. (2014), which is located 7.2 km to the north and run by the Geographical Institute in Colombia. The estimated eastern component of velocity in this station, as the result of the combination of the two solutions (Nocquet et al. 2014 and this dissertation), described previously, indicates a value of 9.2 ± 0.4 mm/yr with respect to SOAM, and 2.3 ± 0.4 mm/yr with respect to NAB. Both names have been retained in this dissertation for reference purposes of the respective authors.

5.7.2. Caribbean Subduction.

Caribbean plate motion around northern Colombia is represented by the motion of GPS permanent sites SANO and CN35, located on San Andres and Providencia islands. These velocities imply an east-southeastward oblique convergence with respect to SOAM at 18.2 ± 0.4 mm/yr and 17.0 ± 0.6 mm/yr, respectively (Figure 34), and southeastward with respect to NAB at 11.5 ± 0.4 mm/yr and 10.3 ± 0.6 mm/yr (Figure 40).

Slow amagmatic Caribbean subduction under the North Andes has been proposed by numerous authors based on a weakly defined Wadati-Benioff zone (e.g., Dewey, 1972; Pennington, 1981; Kellogg and Bonini, 1982; Bernal-Olaya et al., 2015), seismic tomographic evidence for a south-dipping high velocity slab (van der Hilst and Mann, 1994; van Benthem et al., 2013), seismic reflection profiles that show Caribbean acoustic basement underthrusting the deformed belt (e.g., Silver et al., 1975; Ladd et al., 1984; Bernal-Olaya et al., 2015), 3D gravity modelling defining a shallow dipping Caribbean Plate that subducts at ~5° beneath NW Colombia (Mantilla et al., 2009), and plate motion models that require a convergence (Boschman et al., 2014; Kobayashi et al., 2014).

The convergence direction of the Caribbean plate with respect to SOAM is about 100° of azimuth, (east-south motion) estimated from stations CN35 and SAN0. The South Caribbean Deformed Belt (SCDB), (Figure 32), is a submarine prism that was formed at the interface between oceanic material that is subducting in the basins of Colombia and Venezuela, and arc terranes along the northern edge of the South American plate (Kroehler et al., 2011). The SCDB represent the limit of the current convergence and transcurrent faulting between the Caribbean and South America plates, (Ladd et al., 1984).

Stations located northeast of Colombia and Venezuela move in the north-east direction; some stations (BARU, BACO, CORO) experience mainly eastward movement. Figure 42 corresponds to velocity profiles obtained at some stations from the velocities with respect to South America, estimated in the direction of convergence of azimuth 100° between the Caribbean and South America plates. The location of the CN37, BARU and BACO stations, south of 11° of latitude, indicates a general alignment perpendicular to the direction of convergence (100°) estimated from the stations SAN0 and CN35.

The motion of the Caribbean plate indicates a NW-SE contraction in the Colombian Caribbean zone. The velocities of the BACO and BARU stations show the larger magnitude with respect to SOAM of stations located in the Colombian Caribbean. These stations are perpendicular to the direction of convergence at the SCDB. These values are very similar to the velocity vectors of the SAN0 and CN35 stations located in the Caribbean, which would indicate motion transfer at the continental zone of South America, which would correspond to a larger strain accumulation associated with the subduction of the Caribbean plate. Considering the shallow dipping of the Caribbean plate subducting beneath NW Colombia obtained by 3D modeling of gravity data, (Mantilla et al., 2009), it is important to consider a possible plastic deformation that could explain the current NW-SE contraction, which could be represented in the Sinú and San Jacinto folding belts, which form a sedimentary wedge of up to 12 km thick, of low topographic slope and with the presence of mud volcanism, which has been accreted in the Cenozoic to the south american margin, Toto and Kellogg, (1992) and Kellogg et al. (2019). These authors have also considered an active shortening in these folding belts as a result of the convergence between the Caribbean plate and the northwestern margin of South America. The Block 6 of the tectonic segmentation of the Colombian territory as a working hypothesis adopted by GeoRED,

(Figure 11), corresponds essentially to the rocks of the Sinú-San Jacinto Folding Belt. BACO, BARU and CN35 stations previously mentioned are located within this block. The eastern boundary of this block is the Romeral fault zone, which is described as a paleo-suture that would be separating the rocks from the continental basement in the Paleozoic to the east, from the rocks of the oceanic basement in the Mesozoic to the west, Toto and Kellogg, (1992).

CN37 station, located further north of the other two stations experiences less value. The CN38 and ALPA stations, located in the northeast corner of Colombia, correspond to stations that reflect the oblique subduction of the Caribbean plate in the SCDB.

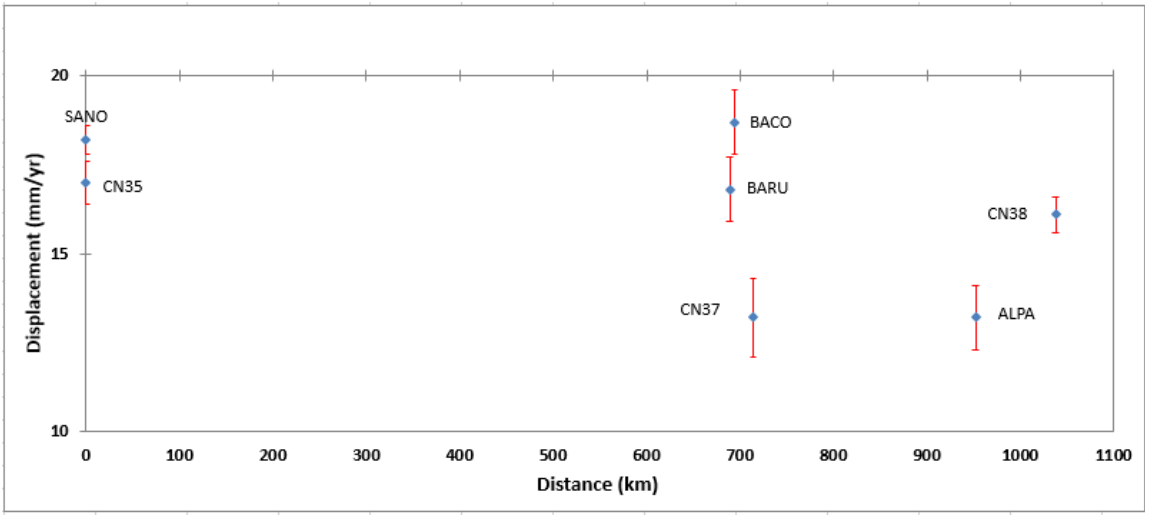

Figure 42. Velocity profiles based on velocities (east component) of permanent stations wrt SOAM used to analyze the Caribbean-South America plates convergence.

The GPS velocity vectors obtained in this dissertation suggest subduction-related deformation in the overriding North Andean block. Even though a significant eastward motion of the North Andes block relative to South America is estimated, Caribbean coastal sites still show large motions relative to the NAB. CN38 and ALPA sites are moving eastward at 9.9 ± 0.5 mm/yr and 7.0 ± 0.9 mm/yr relative to the NAB.

There is a debate regarding whether there is, or not, subduction in this plate boundary. Many authors, based on analysis and results of diverse techniques, have supported the idea of subduction of the Caribbean plate beneath the South America plate

(e.g. Duque-Caro, 1979; Case and McDonald, 1973; Kellogg and Bonini 1982; van der Hilst and Mann 1994; Taboada et al., 2000; Pindel and Kennan, 2009; Bezada, 2010; van Benthem et al., 2013, Londoño et al., 2019) among others. Audemard (2009) has named this subduction as incipient induced subduction, as a result of other geodynamic processes instead of being directed by the convection of the mantle. On the other hand, Rossello (2012) mentions that the Colombian Caribbean Margin (CMC) is the result of the oblique convergence between the Caribbean plate and the northwestern margin of South America. He pointed out that other authors, when describing the subduction of the Caribbean plate beneath South America plate, they consider sutures and other related tectonic phenomena such as the existence of an accretion prism. However, he emphasized that there is no clear surface morphological evidence such as a trench or onshore mountains that support the idea of subduction. Instead, he considered that the irregular morphology of the CMC and the different rates of sedimentation, facies distribution and sequences deposited between the Cretaceous and the present could be explained by a passive margin system, which is reaffirmed by Rossello et al. (2015) making a comparison of the Northern Borneo Margin (NBM) and the CMC.

It is important to note that the deformation that occurs in the westernmost part of Colombia, is not only caused by the motion of the Caribbean plate, but the Panama block is also responsible for such deformation. Therefore, any additional analysis should consider the two sources of deformation, responsible for this region of high tectonic complexity.

5.7.3. Panama-North Andes Collision

Geodetic evidence of active Panama-North Andes collision was reported by Mora-Páez (1995) and Kellogg and Vega (1995). Kobayashi et al. (2014) interpreted the motion of the Panama block to the east as tectonic escape from the subducting Cocos Ridge at the Middle America trench and modeled the Panama Block-NAB convergence as 12.2 mm/yr to the southeast in N124°E direction.

This collision zone is characterized by active seismicity. Two large shallow earthquakes (M_S 6.6 and 7.3) occurred in 1992 in this area (Wallace and Beck, 1993). Their focal mechanisms are consistent with compression normal to the Panamá-North Andes

suture (Freymueller et al., 1993). On September 14, 2016, another earthquake (7.37°N, 76.17°W, M_w6.0, depth=18 km) occurred in the Mutatá region, Colombia, with a focal mechanism consistent with northwest-southeast compression (USGS National Earthquake Information Center, 2017). As the convergence zone of the Panama-North Andes blocks corresponds to two thick buoyant crustal blocks of crust, consequently, the resulting deformation is similar to a collision, unlike the subduction zones in which the convergence in the overriding plate above is characterized by a recoverable elastic strain associated to the seismic cycle.

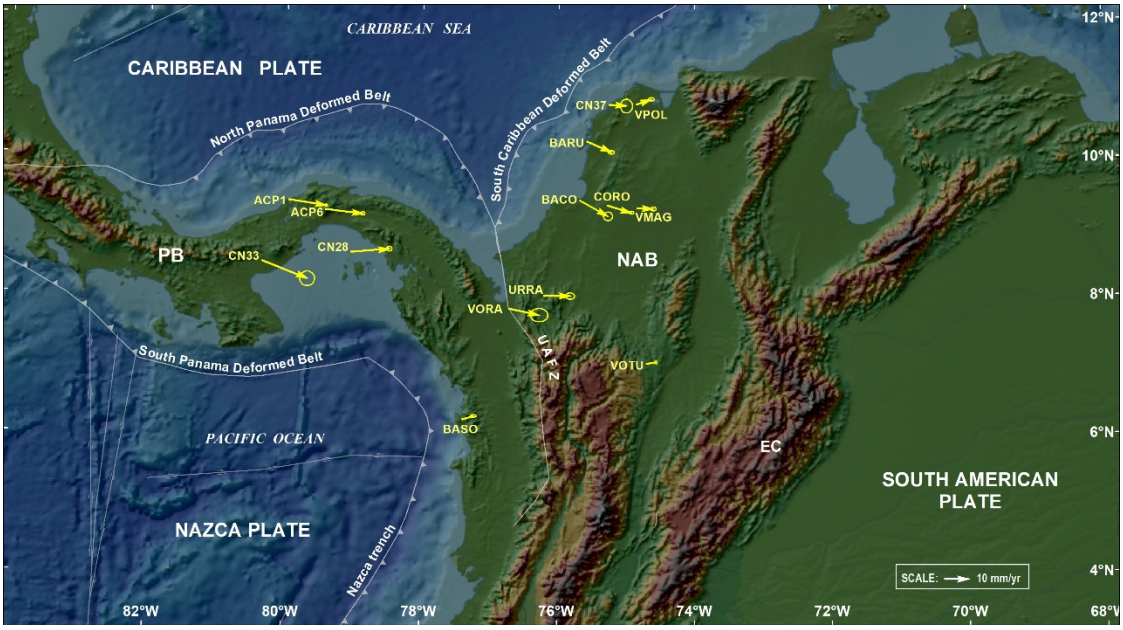

Figure 43. Station and velocities wrt NAB in the zone of Panama-NAB blocks collision.

The Panama block moves eastward with respect to SOAM at a velocity of 22.5 mm/yr and azimuth of 82.1° and 15.5 mm/yr with azimuth 93.8° with respect to NAB (Figure 43), based on the velocities obtained at ACP1, ACP2 and CN28 stations. The CN33 station has some differences with respect to the others, which can be attributed to the installation site of the station, so it is not used in these estimates. These new velocity vectors are indicating the rigid motion of that area.

Relative to the NAB, URRA site (8°N of latitude) shows an eastward velocity of 10.8 mm/yr with an azimuth of 91.6°, and VORA site (7.8°N of latitude) moves eastward at 12.7 mm/yr with an azimuth of 101.8°. These two stations represent the effect of the

collision of the Panama Block with respect to the NAB. Figure 44 shows a velocity profile of the east component at permanent stations with respect to NAB, on both sides of the mentioned reference, that has been adopted following the general direction of the Atrato-Urabá Fault Zone (AUFZ) in the Gulf of Urabá in Colombia, as proposed by Kobayashi et al. (2014). It is clearly observed that there is a decrease in the east component of the velocities of the stations as they are located more distant with respect to the reference, over a wide area of 200-300 km. This wide zone accommodates the contraction between Panama and North Andean blocks.

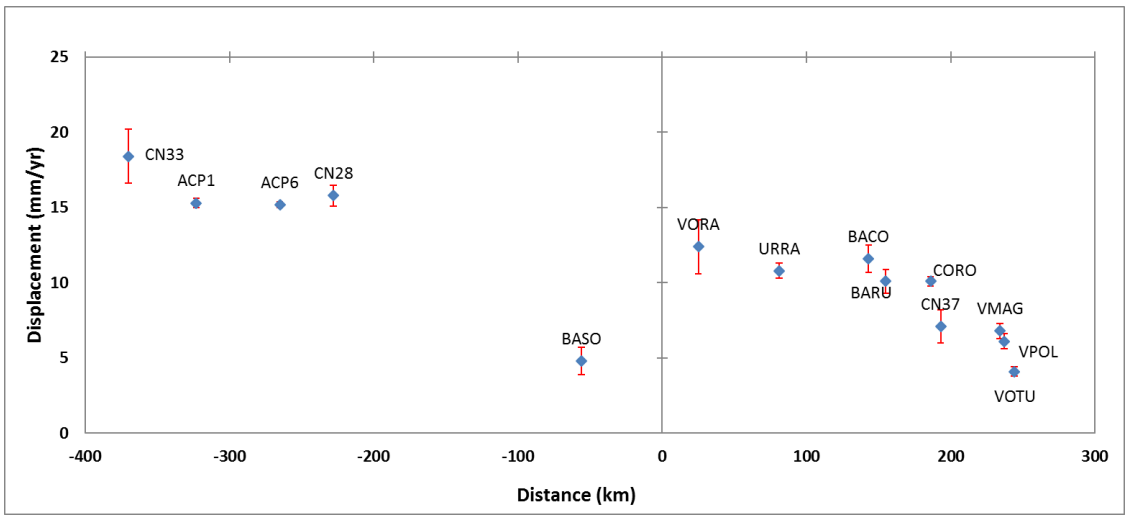

Figure 44. Velocity profiles (east component) of permanent stations with respect to NAB.

BASO site, however, about 200 km to the southwest from VORA, moves to the northeast also relative to NAB, at only 5.0 mm/yr with an azimuth of 73.7° (Figure 44). In order to evaluate the effect of the Nazca plate and the Panama block at the BASO station, the velocity of BASO is examined with a methodology by Duong et al. (2013). Observed velocity at the BASO station is compared with the rigid motions calculated from Euler poles for the Nazca plate (NP), the Panama block (PB), and the North Andean block (NAB). All the velocities are evaluated with respect to ITRF2008. For the estimation of the velocity with respect to the Nazca plate, the Euler pole parameters of Altamimi et al. (2012) are used. NAB and PB motions are calculated based on the result of this study.

As shown in Figure 45, the BASO velocity falls within a triangle composed of three rigid motions of NAB, PB, and NP. It is concluded that BASO mainly represents the North Andean Block motion, but there is a small effect related to the Nazca plate subduction

and/or the Panama collision. Although the deviation of BASO from NAB is significant, the lines indicating the contribution of Panama Block or Nazca Plate are both very close to the observed BASO velocity. Thus it is difficult to distinguish which of the two contributions is more representative. However, in any of the two possibilities, the interaction effect is quite small (the BASO deviation from NAB is less than 33% of the velocity difference between PB and NAB, or between NP and NAB).

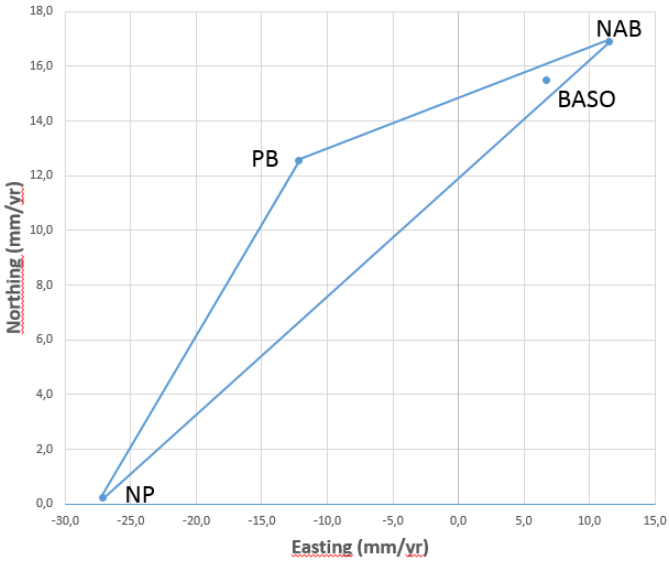

Figure 45. Velocity diagram for the BASO site with respect to different reference frames.

Finally, it is possible to say that the effect of the collision of the Panama arc is probably confined to the north of the latitude 7.5°N of the North Andean Block.

5.8.Margin-Parallel "Escape"

McCaffrey (1996) showed that about half of all modern subduction zones have mobile forearc blocks. As a consequence of the slip partitioning into margin-normal and margin-parallel components within an overriding plate in oblique subduction zones, it is common to find lithospheric blocks that are being detached from the overriding plate. The forearc blocks are driven by plate coupling and their motion is relative to the overriding plate (McCaffrey, 2002).

Figure 46 shows an average trend of N35°E of the NAB-SOAM margin, which probably represents appropriately the general direction of the eastern edge of the mountain

range, the Eastern Cordillera in Colombia, between latitudes 1° and 7° N. This value was assumed for this study. The term "margin" is used in this case as the eastern margin of the NAB, i.e., the margin of stable South America.

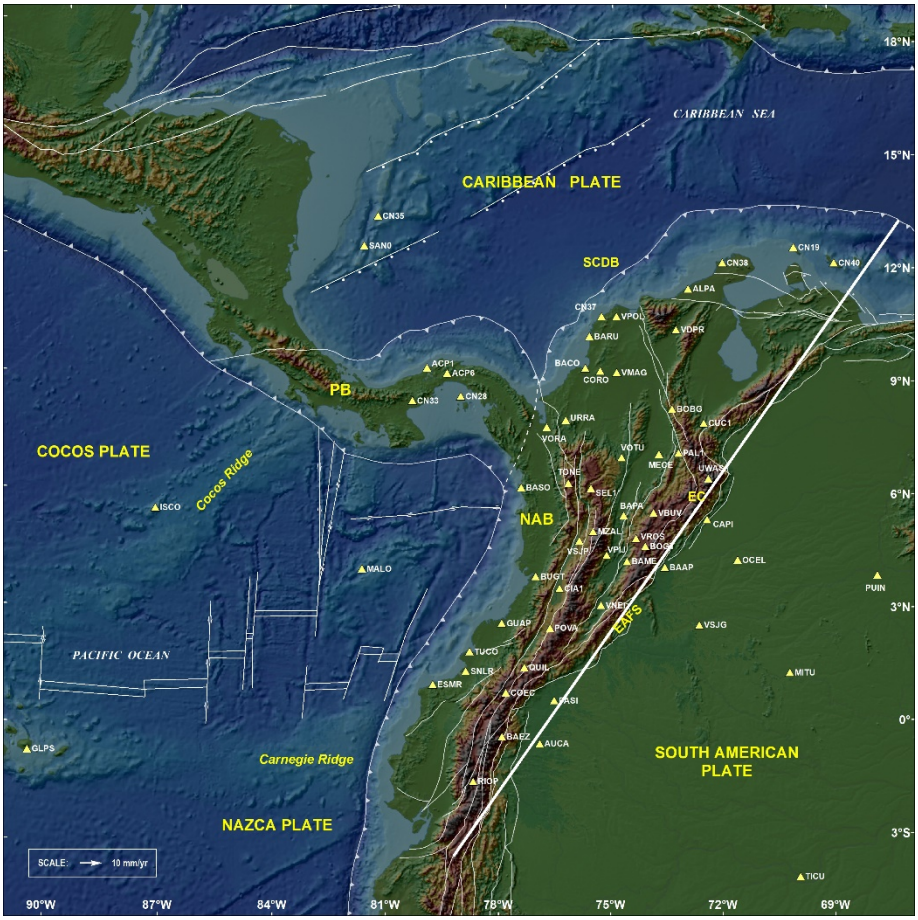

Figure 46. Regional trend N35°E (red line) and stations located on NAB for this analysis.

The velocity vectors of this dissertation with respect to SOAM can be partitioned into the components margin-parallel (35°) and normal-margin (125°), (Table 10).

Table 10. Margin-normal (125°, NW-SE), and margin-parallel (035°, NE-SW) velocities.

ID	Longitude	Latitude	Margin Normal Vel	Margin Parallel Vel	Margin Normal Sigma	Margin Parallel Sigma
ACP1	280.050	9.371	17.2	14.1	0.3	0.3
ACP6	280.592	9.238	16.8	14.6	0.2	0.2
ALPA	287.082	11.528	9.6	10.4	0.7	0.8
AUCA	283.117	-0.641	1.6	0.9	0.2	0.3
BAAP	286.446	4.072	0.2	-0.7	0.3	0.4
BACO	284.308	9.402	16.6	8.6	1.0	1.0
BAEZ	282.113	-0.459	4.8	3.9	0.2	0.2

BAME	285.435	4.236	3.0	6.8	0.4	0.6
BAPA	285.342	5.466	3.8	7.8	0.3	0.3
BARU	284.410	10.258	14.1	9.5	0.6	0.7
BASO	282.607	6.203	6.5	11.2	0.6	0.7
BOBG	286.642	8.312	7.1	10.6	0.4	0.5
BOGT	285.919	4.640	0.9	6.4	0.2	0.2
BUGT	283.004	3.826	5.1	9.6	0.2	0.3
CAPI	287.572	5.351	1.0	1.7	0.3	0.3
CIA1	283.643	3.505	3.9	7.8	0.9	1.1
CN19	289.952	12.612	13.1	13.1	0.6	0.6
CN28	280.966	8.625	15.5	17.3	0.6	0.6
CN33	279.673	8.487	22.6	11.8	1.8	1.8
CN35	278.637	13.375	15.6	7.4	0.5	0.5
CN37	284.737	10.793	9.4	11.0	1.5	1.3
CN38	288.012	12.222	12.0	12.2	0.3	0.4
CN40	291.042	12.180	13.3	11.7	0.7	0.7
COEC	282.213	0.716	4.5	6.3	0.7	0.9
CORO	284.712	9.328	13.3	10.7	0.3	0.3
CUC1	287.487	7.932	9.0	9.2	0.9	1.3
ESMR	280.276	0.935	14.3	18.3	0.4	0.5
GLPS	269.696	-0.743	43.7	33.2	0.2	0.2
GUAP	282.105	2.574	8.2	10.0	0.4	0.5
ISCO	272.944	5.544	7.4	85.5	0.6	0.6
MALO	278.394	4.003	41.1	33.9	0.4	0.5
MECE	286.288	7.107	5.2	9.1	0.4	0.3
MITU	289.768	1.261	-0.7	0.3	0.3	0.4
MZAL	284.529	5.030	0.9	10.0	0.6	0.4
OCEL	288.384	4.271	-0.8	0.6	0.2	0.3
PAL1	286.811	7.136	4.6	8.3	0.4	0.4
PASI	283.501	0.513	0.8	0.8	0.4	0.4
POVA	283.385	2.449	6.3	7.9	0.4	0.4
PUIN	292.097	3.851	0.2	-0.4	0.4	0.5
QUIL	282.709	1.394	5.3	8.9	0.5	0.7
RIOP	281.349	-1.651	5.2	-1.4	0.5	0.6
SAN0	278.284	12.580	16.3	8.5	0.3	0.3
SEL1	284.471	6.191	4.7	8.9	0.3	0.3
SNLR	281.153	1.293	12.2	9.5	0.3	0.4
TICU	290.061	-4.187	-0.3	-0.3	0.3	0.3
TONE	283.861	6.324	4.5	9.7	0.3	0.4
TUCO	281.252	1.815	13.3	13.0	0.3	0.4
URRA	283.790	8.012	12.3	13.4	0.8	0.8
UWAS	287.609	6.451	2.8	4.8	0.3	0.3
VBUV	286.141	5.533	4.1	9.1	0.4	0.4
VDPR	286.752	10.436	8.7	11.8	0.2	0.2

VMAG	285.153	9.287	9.0	11.0	0.5	0.5
VNEI	284.745	3.062	1.1	5.1	0.3	0.3
VORA	283.278	7.818	15.0	12.3	1.6	1.7
VOTU	285.290	7.019	6.3	10.3	0.4	0.3
VPIJ	284.893	4.397	2.9	7.0	0.3	0.3
VPOL	285.139	10.794	7.1	12.6	0.3	0.4
VROS	285.677	4.847	1.7	6.2	0.4	0.4
VSJG	287.361	2.533	-0.4	-0.1	0.4	0.5
VSJP	284.164	4.781	1.9	7.4	0.3	0.3

The predicted motion of the North Andean Block is 8.6 ± 1.0 mm/yr. This NAB velocity vector can be resolved into a margin-parallel component of 8.1 ± 0.7 mm/yr and a margin-normal component of 4.3 ± 0.6 mm/yr.

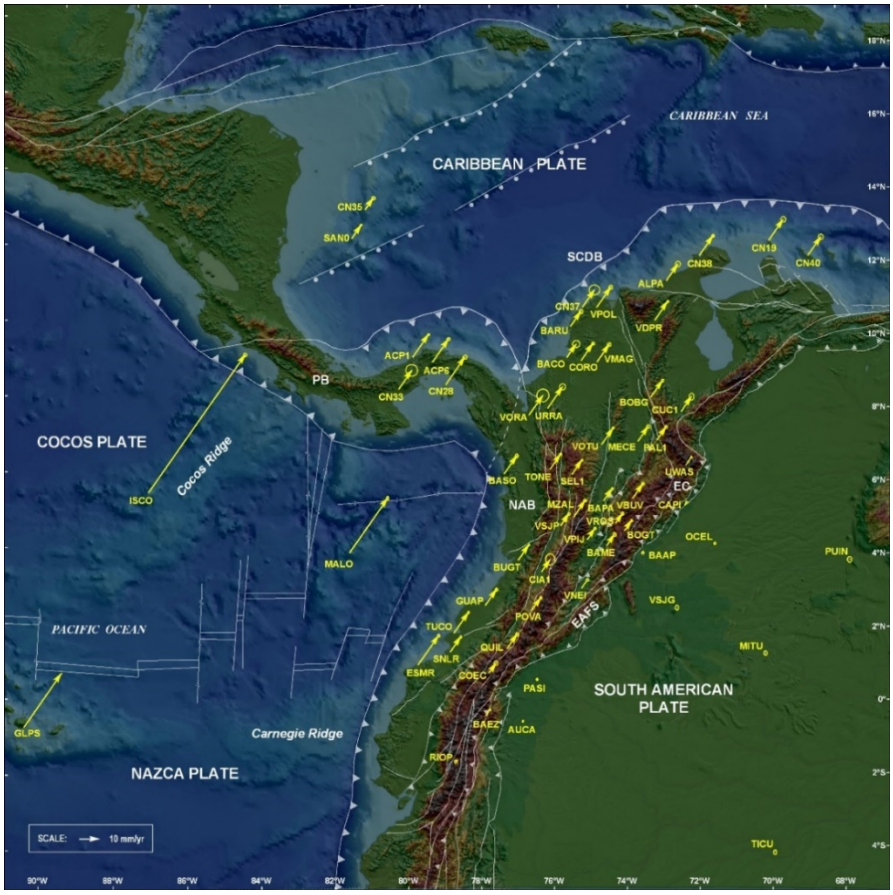

Figure 47. GPS margin parallel velocities (035°), Table 10. North Andean Block (NAB), Panama Block (PB).

Figure 47 shows the velocity vectors of the margin-parallel components obtained in this study. Most of the northeastward motion is accommodated along the broad East Andean Fault System (EAFS). Near Panamá and north of 7° N latitude the margin-parallel

rates increase up to 10.4 mm/yr (CORO, VMAG, VORA, VPOL), probably due to the Panamá arc–North Andes collision.

5.9.Margin-Normal Mountain Building

The Eastern Cordillera of Colombia is a NE-trending fold belt bounded by the Llanos foreland basin to the east and the Magdalena Valley basins to the west. The general structure of the chain is that of a raised block between the Magdalena Valley and Los Llanos of eastern Colombia. Tilting, differential uplift, and faulting produced differences in height on the order of 10,000 m in the upper surface of the basement (Jullivert, 1970). The faults in the basement are reverse faults, often high-angle reverse faults, some of which have been active until Quaternary times. It is also possible that strike-slip occurred along some faults, as has been suggested for the Santa Marta-Bucaramanga fault and for many faults in the Caribbean area (Jullivert, 1970). A rather narrow strip in the central part of the chain, between the two massifs shows a more tightly folded structure (Julivert, 1970; Colletta et al., 1990; Dengo and Covey, 1993; Cooper et al., 1995). The Eastern Cordillera is the widest and most extensive of the three branches of the Colombian Andes, and represents the leading edge of deformation in the northern Andes (Corredor, 2003). The highest peak is Ritacuba Blanco at 5,410 m in the Sierra Nevada del Cocuy.

Figure 48 shows the velocity vectors of the margin-normal components obtained in this dissertation. As previously mentioned, the margin-normal component is about 4.3 ± 0.6 mm/yr. A GPS permanent station in Ecuador (COEC) and two GPS stations in Colombia (QUIL and POVA), permit to confirm a shortening rate of 4.5 to 6 mm/yr on the margin-normal (N125°E) velocity component. Trenkamp et al. (2002), based on an elastic half-space model for a cross section across Ecuador (0°), estimated 6 mm/yr of shortening, distributed as 3 mm/yr on the Inter Andean Fault and 3 mm/yr at the Eastern Frontal Fault System. To the north, the stations BAME, UWAS, VBUV and VROS, located in Colombia's Eastern Cordillera, indicate that the shortening rates are less than 4.1 mm/yr.

Margin-parallel vectors are dominated by northeastward rigid NAB translation while margin-normal vectors are dominated by the subduction earthquake cycle and permanent mountain building. However, in the case of margin-normal vectors, it is

important to consider some additional aspects. The effect of elastic deformation due to the interplate locking is limited to the Nazca subduction zone underneath the South America plate. The oblique subduction towards the east of the Nazca plate beneath the South America plate in the Colombia-Ecuador zone can be expressed in two ways: first, when strong earthquakes occur, such as those presented in 1906, 1942, 1958, 1979 and 2016, the plate boundary is being ruptured partially, and second, between the occurrence of seismic events, there is accumulation of elastic strain that is going to be released in the next seismic event. The stress accumulated through the geological time scale is responsible for the mountain building and also for a wide distribution of normal contraction to the margin.

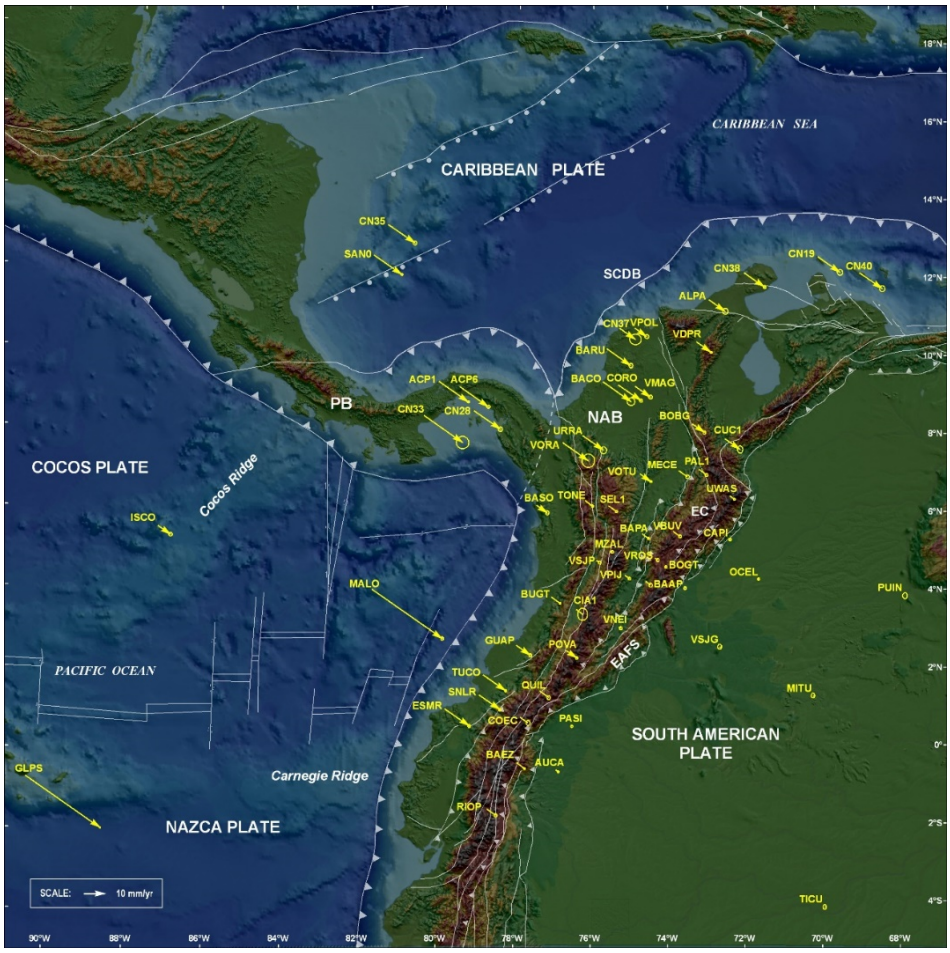

Figure 48. GPS margin normal velocities (125°). North Andean Block (NAB), Panama Block (PB).

Previously, Mora-Páez et al. (2016) performed a similar analysis of normal and perpendicular velocity components to the NAB-SOAM margin. They carried out jointly processing by the SGRG of the Colombian Geological Survey and the University of Colorado using the GIPSY-OASIS II 6.3 software (Bertiger et al., 2010; Zumberge et al.,

1997). The data, obtained by the GeoRED Project, correspond to data collected from 1996 to 2015, at nine permanent stations with more than 2.5 years of observation time, and twenty field stations occupied under several campaigns style. The GPS stations used for this analysis are mainly distributed in a region of the central area of Colombia, which includes part of the eastern mountain range, as indicated in the yellow box on the location map in the upper left of Figure 49.

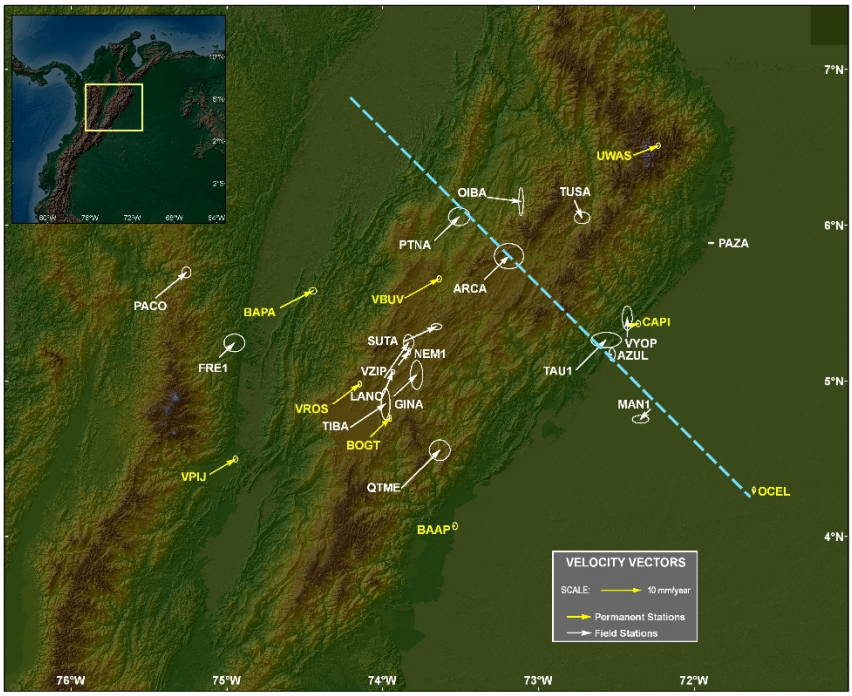

Figure 49. GPS velocities wtr SOAM.
Yellow arrows correspond to permanent stations; white arrows to field stations. Blue line is a reference line for a elevation profile in the next figure.

In Figure 49, the GPS permanent (yellow arrows) and campaign (white arrows) velocities with respect to South American reference frame are plotted with one sigma of uncertaintities. Figure 50a corresponds to a topographic elevation profile that crosses the Eastern mountain range in the NW-SE direction, perpendicular to a range trend of N45°E, between the latitudes 4°N and 6.5°N, as shown in Figure 50 with the blue reference line. The components of velocity perpendicular to the regional trend of the cordillera represent shortening (Figure 50b), while the components of velocity parallel to the range, in the direction of the regional trend correspond to simple shear (Figure 50b). The distances of the stations in the figures 50b and 50c are relative to a site of coordinates of latitude 5.17°

and longitude -72.55°. Mora-Páez et al. (2016) estimated oblique convergence at 8.8 ± 1.7 mm/yr, consisting of 8.0 ± 1.7 mm/yr of right-lateral strike-slip shear along the mountain range and 3.7 ± 0.3 mm/yr of northwest southeast horizontal shortening. The spatial resolution of the nine permanent GPS stations used by Mora-Páez et al. (2016) prevents assigning shortening or dextral movement to any localized zone. Velocities obtained from the field campaign data generally also support the conclusions above, but they were not strong evidence because of the large residuals associated with the annual signals.

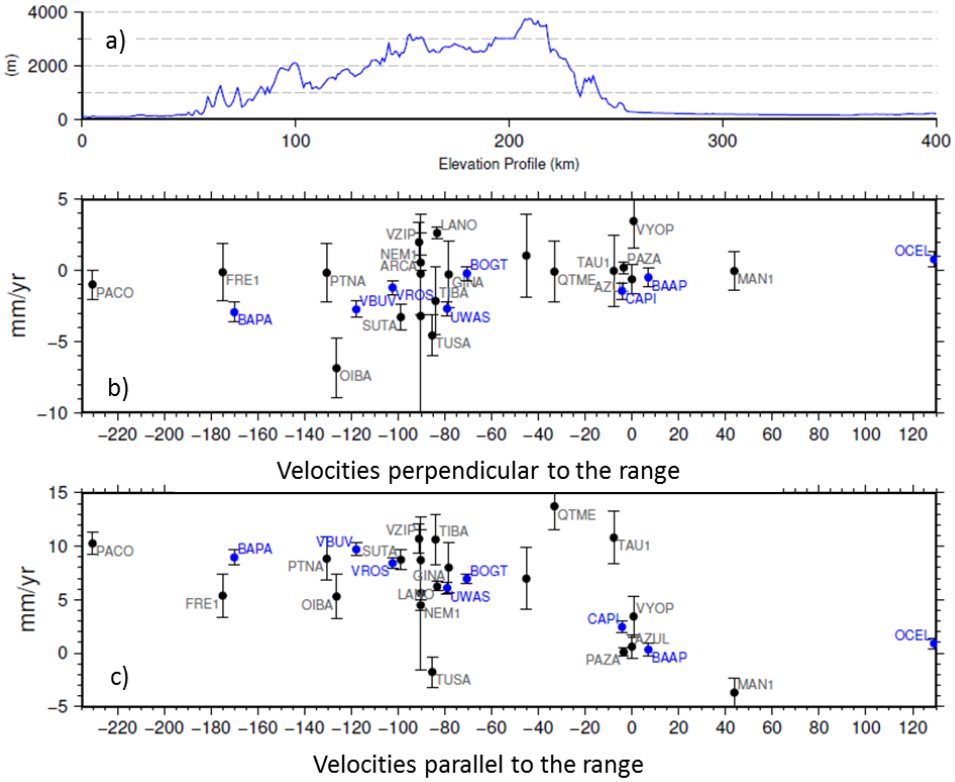

Figure 50. Elevation profile and velocities perpendicular and parallel to the range.
a) Elevation profile along blue line in previous figure. b) Components of velocity perpendicular to the range. C) Components of velocity parallel to the range. Blue dots correspond to permanent stations, and black dots to campaign stations.

It is important to note that the results obtained in the two studies, corresponding to this dissertation and those obtained by Mora-Páez et al. (2016) are very similar. The difference is that the data from this dissertation correspond to permanent stations throughout the national territory, while the data from Mora-Páez et al. (2016) correspond to nine permanent stations, located in a central region of Colombia; the results of the field stations were not used for the final inferences, for reasons mentioned previously. It can also be established that the values used in the two studies of the mountain range trend, N35° for

this dissertation and N45° E by Mora-Páez et al. (2016) are not significant in velocity estimates.

5.10. Conclusions

For this study, 60 permanent stations were used, and the respective time series were obtained. The results obtained in this study were compared with those obtained by Trenkamp et al. (2002) regarding the motion of the Nazca plate and the behavior of the geodetic stations located on the Pacific coast. The differences were analyzed and the causes of these differences were identified. The obtained velocity field allows identifiying the subduction of the Nazca plate beneath South America plate, and also to observe that some velocity vectors of stations located on the Pacific coast reflect clear evidence of strain accumulation on the Nazca subduction zone.

A new Euler pole for the NAB is estimated and compared to existing ones. Since this new Euler pole presented an error in the pole estimation compared with the obtained by Nocquet et al. (2014), the respective analysis was performed and a satisfactory explanation of this determination was obtained under the concept of variance reduction of velocity data.

Subduction analysis of the Caribbean plate was performed, establishing that the contraction due to the convergent motion of the Caribbean plate is probably absorbed by the South Caribbean Deformed Belt. It is mentioned the debate that exists regarding the existence or not of subduction of the Caribbean.

There is geodetic evidence of the active collision of the Panama and NAB blocks, the first moving eastward with respect to the second. Although the boundary of this collision is diffuse, the Atrato Uraba Fault Zone was adopted as proposed by Kobayashi et al. (2014).

Using the NAB-SOAM margin trend represented by the N45°E Colombian eastern mountain range trend, a predicted NAB motion of 8.6 ± 1.0 mm/yr was established. Thus, the NAB velocity vector can be resolved into a margin-parallel component of 8.1 mm/yr and a margin-normal component of 4.3 mm/yr.

CHAPTER 6

DISCUSSION

This chapter presents a general discussion related to the main results obtained in this dissertation.

6.1. The velocity field in the northwestern corner of South America and GPS time series

For a reliable estimation of geodetic velocities, two essential aspects were considered in the analysis of the GPS time series: the impact of offsets and the estimation of uncertainties

6.1.1. Impact of steps in the GPS time series due to external conditions that affect the velocity estimation

The interpretation of time series data is a fundamental aspect in GNSS studies for geodynamics. The geodetic time series are composed of a set of coordinates acquired in different periods of time. These observations are not perfect because they are affected by various offsets and noises with natural or artificial origins. Those noises can be either random or systematic (Williams, 2003b).

Thus, the estimation of the velocities at each GPS station from the respective time series can have biases due to the presence of offsets. Offsets with natural origin can appear due to geodynamic phenomena that produce movement in the station. For example, a large earthquake can generate a change in the 3D position of geodetic stations; therefore, the offset associated with the earthquake must be taken into account for the estimation of the velocity of the GPS station after the occurrence of the event. On the other hand, offsets with non-tectonic origin frequently appear in the time series. They are due to various factors such as environmental changes, human intervention, or instrumental issues such as receiver change, firmware update, antenna change, antenna reorientation and radome setup, among others. These offsets can dominate the uncertainties in the estimation of the velocity.

Table 11. ID Stations, dates, offset type and estimated offset in each component.

ID Sta	Date	Offset	North (mm)	East (mm)	Up (mm)
BASO	Feb 20, 2015	Change of receiver	-0.70 ± 0.86	-1.33 ± 1.16	3.22 ± 2.11
BACO	March 7, 2013	Firmware update	1.41 ± 1.17	0.33 ± 1.07	-1.29 ± 2.90
TONE	Nov. 26, 2011	Antenna reorientation	1.35 ± 0.64	1.14 ± 0.93	-6.55 ± 1.78
BOGT	May 25, 2008	Co-seismic displacement	1.68 ± 1.21	-0.08 ± 1.31	3.44 ± 5.10

In order to analyze the possible impact of the inclusion of offsets in the time series and therefore in the velocities estimation, some stations were taken as examples, associated with factors such as changes due to receiver change, (Trimble NetRS receiver to Trimble NetR9); firmware update, (4.43 to 4.47 on a Trimble NetR9 receiver); antenna reorientation at BASO station; and coseismic displacement. Offsets due to antenna changes are already well known, so they are not considered. For the time period 2008-2016 of data analysis of GPS stations in this study (until March 31, 2016), the National Seismological Network of Colombia recorded nine earthquakes of magnitude ≥ 5.5 in the Colombian territory, all with depths greater than 140 km, with the exception of the May 24, 2008, Quetame earthquake, with local magnitude 5.7 and shallow depth, with an epicenter in the eastern Colombian mountain range (4.399°N, 73.814°W), (Mora-Páez et al., 2015). The nearest GPS permanent station in operation at that time was the IGS BOGT station, located approximately 40 km northwest of the epicentral location. Table 11 shows the estimated offsets of the mentioned cases in the three components.

Table 12. Velocities estimation before and after the inclusion of offsets.

ID	VELOCITIES			OBS.
	North (mm/yr)	East (mm/yr)	Up (mm/yr)	
BASO	15.38 +/- 0.34	6.50 +/- 0.89	1.90 +/- 0.60	No offset
	15.48 +/- 0.35	6.70 +/- 0.85	1.46 +/- 0.62	Offset
BACO	8.2 +/- 1.06	13.29 +/- 0.89	-1.1 +/- 2.14	No offsets
	7.79 +/- 1.04	13.19 +/- 0.04	-0.72 +/- 2.14	Offsets
TONE	15.73 +/- 0.21	4.42 +/- 0.50	1.63 +/- 0.73	No offsets
	15.53 +/- 0.21	4.25 +/- 0.47	2.57 +/- 0.56	Offsets
BOGT	15.45 +/- 0.31	-0.38 +/- 0.25	-35.32 +/- 0.97	No offsets
	15.14 +/- 0.22	-0.41 +/- 0.25	-35.22 +/- 0.99	Offsets

Table 12 shows the velocities estimation before and after the inclusion of the estimated offsets. It is possible to conclude that in all these cases, the velocity changes are

not significant compared with the estimation errors, so these offsets do not affect the velocity estimate significantly.

6.1.2. Velocity uncertainties

The noise in the GPS observations can be described by means of several models, proposed by different authors (e.g. Zhang et al., 1997; Mao et al., 1999; Langbein, 2004; Williams et al., 2004; Davis et al., 2012) with different approaches. For this study, using the Hector software (Bos et al., 2013), three types of noise models, namely: White, PowerLawApprox, and Combined Power law + White, were tested.

White noise is a random signal with a constant power spectral density. It is a simple case of a stochastic process where the values are independent and identically distributed over time with zero mean and equal variance, that is, they are random without temporal correlation. White noise is independent of frequency and is usually associated with hardware noise or measurement errors. The white noise contains little or no geodetic information, but it is useful to get a good understanding of the white noise statistics to enable efficient filtering, and the estimation of the uncertainties of velocities (Montillet et al., 2013). Mao et al. (1999) concluded that if pure white noise is assumed, the velocity error in the GNSS time series could be underestimated by factors in the range of 5-11.

Power Law Noise is the noise that follows a power law. In Hector software, the "PowerLawApprox" noise model is implemented by using a Toeplitz approach (Bos et al., 2013). In the Toeplitz approximation, the covariance matrix is approximated by a Toeplitz matrix that has a constant value at each diagonal and the inverse can be easily calculated, reducing processing time when large number of observations are required.

For this dissertation, only the horizontal components were considered for conservative reasons. Estimation of vertical velocities and their associated uncertainties will be made in another study. The values contained in Appendix E are used to generate the histograms of the uncertainties in the estimation of the velocity components for each station, using the three different noise models, which are presented in Figure 51.

Figure 51 shows the histograms of the uncertainties of the horizontal velocity components obtained in the GPS stations used in this study: White, PowerLaw, and PowerLaw + White noise models. On the Y axis, the percentage of stations that are within the respective ranges of the uncertainties is represented, and on the X axis the values of the uncertainties. The histograms obtained are skewed right or positively skewed, which means that the tail extended to the right represents the highest uncertainty values in the velocity estimation.

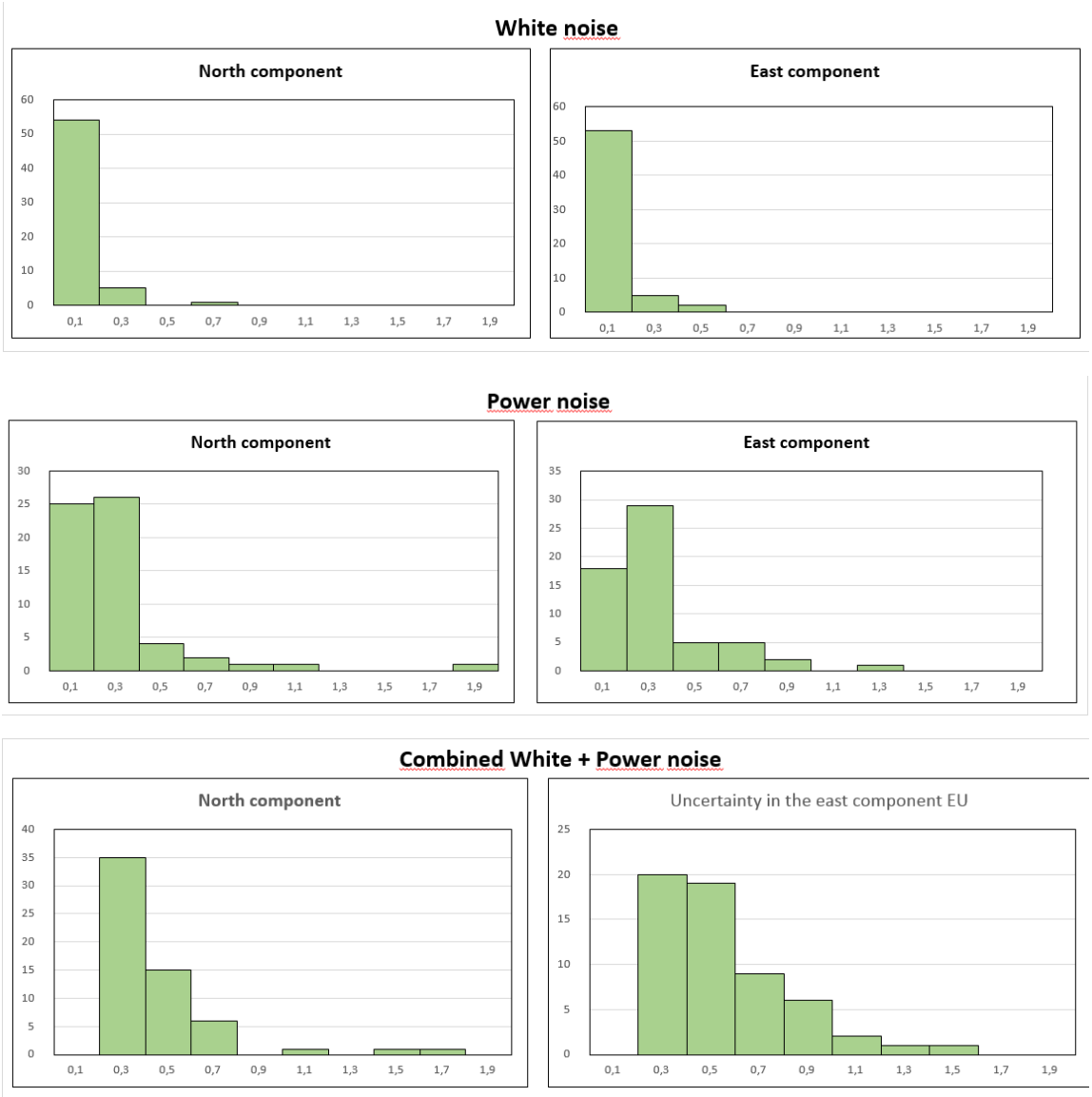

Figure 51. Histogram of the horizontal uncertainties of velocity for each noise model.

Table 13 shows the velocities and uncertaintities obtained the three GPS stations, ALPA, MALO and MITU, using the White, PowerLaw and Combined PowerLaw + White Noise models. As expected, the uncertainties in the velocities observed in the histograms and also at the three stations used as an example, are larger in the combined model than in the other two types of noise model. An important aspect in the reliable estimation of geodetic velocities and their uncertainties is the use of appropriate noise models. Several authors, (e.g. Johnson and Agnew, 1995; Zhang et al., 1997; Mao et al. 1999; Williams et al., 2004) have demonstrated that uncertainties in the estimation of geodetic velocity have been underestimated by a factor of 2 to 11 when only white noise is taken into account in the analysis of noise in the time series. Langbein (2008) and Goudarzi et al. (2015) concluded that white noise is probably more associated with the noise of GNSS instruments as well as the measurement errors. He et al. (2017) consider that in general, geodetic time series should be described as a combination of white noise and colored noise. Therefore, it is widely suggested, in order to be able to make a better description of the geodetic time series, to use a combination of white noise model plus time-correlated colored noise, Kall et al. (2019). Thus, among several possible combinations, the combined model of white noise and power law is suitable for analyzing noise levels in the data.

Table 13. Velocities and uncertaintities in three geodetic stations using different noise models.

ID	White noise		PowerLawApprox noise		PowerLaw + White noise	
	North component	East component	North component	East component	North component	East component
ALPA	13.3 ± 0.1	8.2 ± 0.1	13.4 ± 0.3	8.5 ± 0.3	13.6 ± 0.6	8.4 ± 0.9
MALO	13.6 ± 0.1	48.4 ± 0.1	13.6 ± 0.2	48.3 ± 0.3	13.6 ± 0.3	48.3 ± 0.6
MITU	11.7 ± 0.1	-4.6 ± 0.1	11.6 ± 0.2	-4.7 ± 0.3	11.5 ± 0.3	-4.7 ± 0.4

6.1.3. GeoRED network implementation and data quality

The GPS time series and the estimation of the velocities of the 60 stations presented in this dissertation make it possible to establish, for the observation period over 2.5 years, the obtaining of good results that guarantees that the GeoRED network allows to make a significant contribution to the study and understanding of the geodynamics in the northwestern corner of South America. The GeoRED project is a growing network in number of stations, and some of them already have several years of observation, and the

fundamental aim is to continue with the densification of stations improving the spatial coverage of the network.

In order to be able to generate reliable GPS time series as well as their respective velocities, several essential aspects in the implementation process have been kept in mind in order to guarantee good quality continuity of the data as follows:

a) With a fundamental objective of obtaining high-quality GPS data, which is reflected in the time series and velocities estimates, site selection has been done through an interdisciplinary work of geologists and geodesists. In the selection, high tectonic and geological complexity in the northwestern corner of South America was taken into account though a preliminary division of the territory into sub-blocks as a working hypothesis, delimited by geological features based on existing bibliographic information.

b) With this same purpose, the best practices in the construction of the stations have been considered. The construction guarantees that the signal received on the geodetic antenna responds to the tectonic activity prevailing in the study region. Thus, sequentially in time, several types of construction were used: reinforced concrete pillar, shallow-drilled braced, shallow braced (non-drilled), and deep-drilled braced monuments, the latter modified from UNAVCO, which in some cases corresponds to drilling depth more than 20 m.

c) Colombia is located in the vicinity of the terrestrial equator, corresponding to the tropical weather conditions with two prevailing dry and wet periods. These factors are taken into account for the installation of the stations, protection of the equipment and guarantee of solar energy for the supply of photovoltaic systems.

d) Colombia territory is characterized by a variety of topography with three mountain ranges, valleys, islands and coasts in two oceans. GPS stations are located at different heights and frequent maintenance visits are necessary to ensure the continuity of the data. Different conditions of temperature, humidity and salinity in several places generate special conditions in some GPS sites that implies changes of geodetic equipment, antennas, receivers or both, which causes an impact on the time series. Along with this, the

different degrees of difficulty in accessing remote sites must be taken into account, which implies that the response time to solve problems is delayed much longer than expected, so there are data gaps in some stations which implies discontinuity in the time series.

f) Data transmission networks in Colombia have coverage limitations, which in addition to the problems of transmission equipment, which occur frequently, affect the timely reception of the data at the gathering and processing center in Bogotá. This also generates an impact on the time series due to data loss, or in some cases, wait until the visit is made and proceed to the manual download. As in the previous case, the solution of this problem depends on the access conditions.

These aspects were taken into account for the optimal interpretation of results, understanding that it corresponds to a process of geodetic innovation to gain knowledge in order to establish the current deformation of the earth's crust in Colombia.

6.2. Tectonic features in the northwestern corner of South America

The northwestern corner of South America and southeastern Central America is characterized by the interaction of four lithospheric plates, South America, Nazca, Caribbean and Cocos, which have been defined by seismicity, active volcanoes and spreading ridges (Molnar and Sykes, 1969; Pennington, 1981).

Thus, the velocity field in the northwestern corner of South America can be described by the following main tectonic issues:

a) motion of the North Andean Block
b) subduction of the Nazca plate beneath South America plate;
c) motion of the South America plate;
d) subduction of the Caribbean plate;
e) Panama Arc-North Andes Collision

6.2.1. Motion of the North Andean Block

The North Andean Block (NAB) has been described by several authors (e.g. Pennington, 1981; Kellogg et al., 1985; Freymueller et al., 1993; Taboada et al., 2000; Audemard, 2001, 2003, 2014; Audemard and Audemard, 2002; Collot et al., 2002; Bird, 2003). Thus, from previous studies, NAB is defined as follows: to the west, the Colombia-Ecuador Trench and the Panamá Block; to the south, the megathrust of Dolores-Guayaquil; to the east and northeast, the East Frontal Fault System which includes the Pallatacanga fault in Ecuador; Algeciras, Guaicáramo and Yopal faults in Colombia, and Boconó fault in Venezuela; and to the north, the South Caribbean Deformed Belt-SCDB, which extends west-east from the Gulf of Urabá, on the border between Colombia and Panama, up to Los Roques canyon (Figure 52).

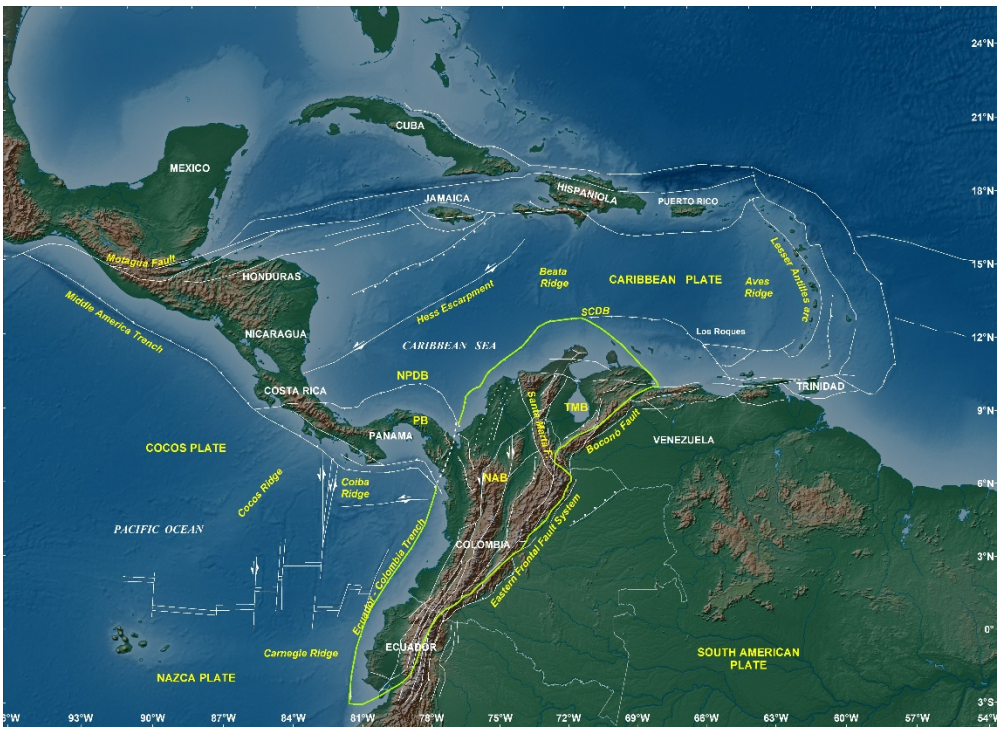

Figure 52. Map that depicts the North Andean Block – NAB.
PB: Panama Block; SCDB: South Caribbean Deformed Belt; NPDB: North Panama Deformed Belt; TMB: Triangulated Maracaibo Block; after Audemard (2014). NAB is delineated.

The determination of the North Andean block motion in this dissertation is based on the estimation of a new Euler pole from 12 stations selected by trial and error tests. These stations, located south of latitude 7.5N °, would represent the rigid motion of the

NAB in the central region of Colombia and southwestern part of Ecuador. Since it has been established in this dissertation the effect of the collision of the Panama block with the NAB as well as the convergence of the Caribbean plate with South American plate, it is possible to conclude that the Euler pole estimated here would not represent the rigid motion of the NAB in its northern zone. This permits to consider the segmentation of NAB in two blocks, based on geodetic results. This consideration must be taken into account in subsequent studies mainly related to the subduction of the Caribbean plate beneath the South America plate, which has not been the main objective of this dissertation.

An important aspect to consider regarding the NAB is the mechanisms that are responsible for its tectonic escape. Proposed mechanisms can be summarized as follows:

a) Carnegie Ridge collision (Pennington, 1981; Gutscher et al., 1999; Spikings et al., 2001; 2005; 2010; Witt et al., 2006; Egbue and Kellogg, 2010);
b) rapid oblique convergence to the Colombia-Ecuador margin between the Nazca and South America plates, (Ego et al., 1996; Kellogg and Mohriak, 2001; Alvarado et al., 2016);
c) high coupling at the interface of the subduction plate, (Egbue & Kellogg, 2010; Witt and Bourgois, 2010; Chlieh et al., 2014.

The Nazca Plate transports the Carnegie Ridge, a volcanic ridge of 2 km height, ~200 km wide, with an E-W trend, as a result of the interaction between the Galapagos Hot Spot and the Cocos-Nazca Spreading Center (Sallares and Charvis, 2003; Yepes et al., 2016). The Carnegie ridge enters the subduction of the Nazca plate beneath South America plate between 2°S and 1°N of latitude. Along the collision zone of the Carnegie ridge with the trench, the Ecuadorian continental margin is currently uplifting (Lonsdale and Klitgord, 1978). The general orientation of the trench changes at the end of the Carnegie Ridge in the

northern sector, taking a direction of 33° azimuth. Gutscher (1999) proposes a prolongation of the Carnegie Ridge larger than 110 km beyond the trench, supported by four evidences: coastal morphology, regional topography, seismic patterns and volcanic arc.

The morphology in Colombia, Ecuador and Venezuela is a result of geodynamic history of the North Andean Block driven by the oblique convergence of the Nazca plate accompanied by the accretion of oceanic terraces in the Ecuador and Colombia subduction zone. The North Andean Block, bounded to the south by a transpressive right-lateral fault system in Ecuador that continues in Colombia as the Algeciras fault, that is part of the Eastern Frontal Fault System, which constitutes the boundary with the South American plate, is being pushed toward to the northeast (Egbue and Kellogg, 2010; Nocquet et al., 2014; Alvarado et al., 2016, Yepes et al., 2016). Clear evidence of the oblique convergence of the Nazca plate subducting beneath South America is supported by the velocity vectors with respect to SOAM obtained in this dissertation for the GPS permanent stations installed on the Malpelo (MALO) and Galapagos (GLPS) islands, both located on the Nazca plate.

6.2.1.1.The Caldas Tear

Vargas and Mann (2013) proposed an ~240 km long east–west-striking slab tear, named the Caldas tear, obtained from mapping of earthquake-defined Benioff zones combined with tomographic imaging, that separate two distinct subducted slabs in the Colombia region. The slab offset has been interpreted as a tear in the subducting Nazca slab (e.g., Corredor, 2003; Syracuse et al., 2016) or the southern edge of the subducted Caribbean flat slab (e.g., Taboada et al., 2000; Yarce et al., 2014). Vargas and Mann (2013) suggest decreasing eastward movement by comparing BOGO station motion, located in Bogota at the south of the proposed Caldas tear, with respect to other stations in the result of Trenkamp et al. (2002). They estimated, considering BOGO station and CHEP station, located on the Panama indenter, an active displacement of ~24 mm/year across the Caldas tear. The stations used by Vargas and Mann (2013) correspond mainly to GPS field stations occupied under episodic campaigns during the execution of the GPS CASA Project previously mentioned.

It is not appropriate to consider that the displacement observed between the two stations used by Vargas and Mann (2013), BOGO and CHEP, to represent the Caldas tear.

The velocity vectors of the stations in Panama are substantially larger than the velocity vector at the BASO station. This station, located on the Pacific coast, represents the North Andean block motion motion, although there is a small effect due to the subduction of the Nazca plate and/or collision of the Panama block, according to the results obtained following the methodology of Duong et al. (2013).

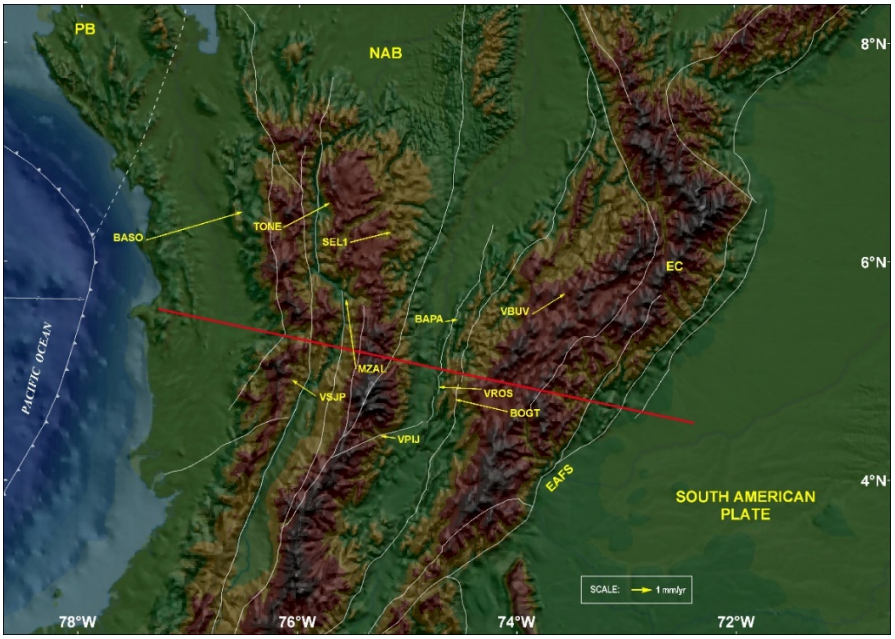

Figure 53. Residual of the velocity vectors wrt.
NAB and location of the proposed Caldas Tear (red line) by Vargas and Mann, (2013).

Velocity vectors at the stations located both north and south of the proposed Caldas tear zone at 4.5-5.5°N show different directions. The vectors to the north have a general northeast direction, while the stations that are to the south have a general direction to the west, with the exception of the MZAL station, which may be affected by the activity of Nevado del Ruiz volcano. Caldas tear has no surficial expression. It is not possible to establish, according to the residuals of the vectors with respect to NAB showed in the Figure 53, that these correspond to the effect of the proposed Caldas tear by Vargas and Mann, (2013).

It is possible to consider that the named Caldas "tear" is not actually a tear, but rather the southern edge of the Caribbean plate. Wagner et al. (2017) states that the understanding of the evolution of plate boundaries in the Colombian region is limited by the uncertainty that exists about the modern geometry of subducted slabs and vice versa,

and consider that the best evidence for the presence of slab material at depth is observed in the location of two different, abruptly offset dipping planes of seismicity, known as Wadati Benioff Zones. They also pointed out that the proposed Caldas tear by Vargas and Mann (2013) corresponding to the Wadati Benioff Zone offset coincides with the location of the subducting inactive expansion center known as Sandra Ridge.

Kellog et al. (2019), consider that there are two possible interpretations, following several authors, regarding the shallow dipping "Bucaramanga slab". The first model corresponds to a recently flattened Nazca lithosphere, which would allow interpreting the offset of 250 km in the Wadatti-Benioff seismic zone as the proposed Caldas tear in the Nazca plate with normal subduction to the south and flat slab subduction to the north. The second model corresponds to considering the 250 km offset of the proposed Caldas tear as the southern limit of the subducent flat Caribbean plate overlying the Nazca slab that is steeper dipping. Kellogg et al. (2019), using a comprehensive data set of more than 1000 volcanic radiometric ages, reviewed the Boschman plate model (2014), mainly for the Northern Andes and on a smaller scale for the Caribbean. Combining with seismicity and the location of the quaternary arc volcanoes, they state that the proposed Caldas tear is actually the southern edge of the Caribbean plate (Figure 54).

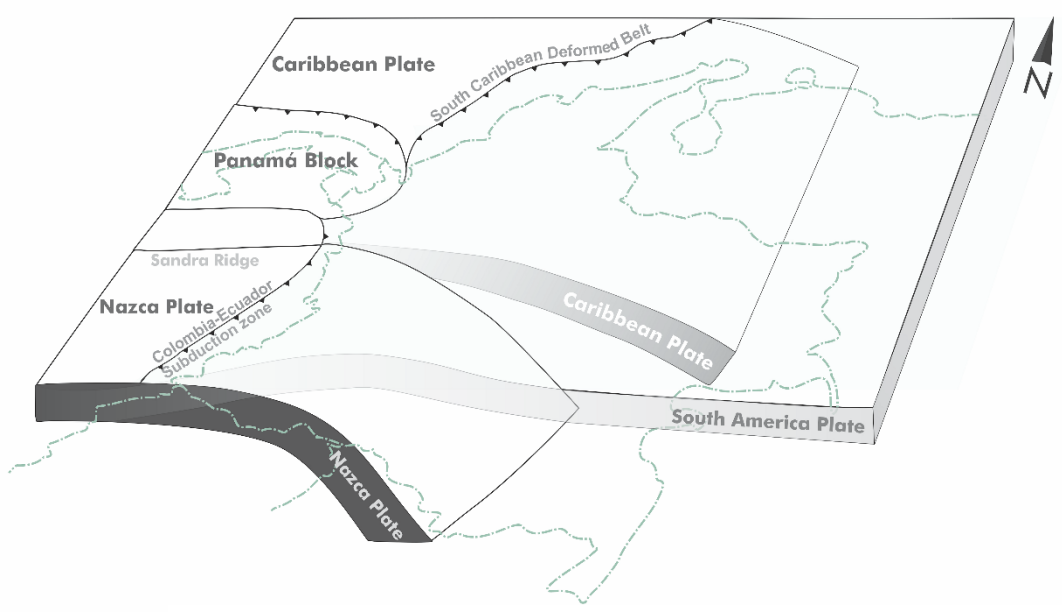

Figure 54. 3D scheme of northwestern South America, and subduction of the Caribbean and Nazca tectonic plates.
Modified from Taboada, 2000; Corredor, 2003; Vargas and Mann, 2013, Wagner, 2017; Idárraga-García et al, 2016

6.2.2. Subduction of the Nazca plate beneath South America plate

The GPS station located on the Galapagos Island, Ecuador (GLPS), installed in 2002 has several years of observation, and is part of the IGS global network. In this study, data from the permanent station located on the Malpelo Island, Colombia, (MALO), owned by the Colombian Geological Survey, installed in 2009 by the GeoRED project, are used. The northern zone of the Nazca plate does not have sites for the installation of GPS stations, and therefore there is not enough number of stations that allow the generation of an appropriate model of the Nazca plate motion. Therefore, the main contribution of this dissertation and the GeoRED project is the estimation of a reliable velocity, obtained from the GPS data with several years of observation at MALO station, and that have not yet been distributed to the geodetic community.

The velocity estimation of the GPS stations GLPS and MALO located on the Nazca plate, and used in this study, as well as the magnitude and eastward direction of the vectors of these stations clearly indicate the oblique subduction of the Nazca plate beneath South America plate. The GPS GLPS station (0.743°S, 90.3W) subducts eastward in Ecuador beneath the South American plate at a rate of 51.7 mm/yr with an azimuth of 78.6° with respect to ITRF2008, and 54.8 mm/yr and azimuth 87.8° with respect to SOAM. The GPS MALO station (4.003, 81.606W) moves towards the east, indicating a subduction of 50.2 mm/yr and azimuth of 74.3° with respect to ITRF2008, and 53.3 mm/yr with an azimuth of 85.5° with respect to SOAM. At the latitude of the Galapagos Island, the general azimuth of the trench is 17°. The stations located on the coast of the Pacific Ocean show velocity vectors greater than most of other vectors in Colombia, which means the accumulated strain in the Nazca subduction zone.

6.2.2.1. Interplate coupling along the Nazca subduction zone in Colombia and Ecuador

Different studies permit to conclude that there is high coupling at the interface of the subducting Nazca plate (Gailler et al., 2007; Egbue and Kellogg, 2010; Witt and Bourgois, 2010; Yepes et al. 2016). Guscher (1999) pointed out that the Carnegie Ridge collision may have affected the coupling between the Nazca and South America plates,

emphasizing four major earthquakes that occurred in this area in the last century. He also affirms that none of these earthquakes ruptured across the ridge itself.

Sagiya and Mora-Páez (2019) presented the first estimate of the interplate coupling along the Pacific coast of Colombia using GPS data. Based on the relative movement between the Nazca plate and the North Andean Block of 54.4 mm/yr, a maximum accumulated slip deficit of 4 m was estimated for the source region of big earthquakes in 1942 and 2016 over 74 years between the two earthquakes. Using the horizontal velocity vectors with respect to SOAM obtained in this dissertation, Chlieh et al. (2014) had obtained similar results, identifying strongly locked patches in three zones, although estimates off southwestern Colombia are different. The result of Sagiya and Mora-Páez (2019) indicated that the interplate coupling on the plate boundary off southewestern Colombia, where a M8 earthquake occurred in 1906 and 1979, is lower than that off Ecuador. The result suggests a possibility that the 1979 earthquake may not be a simple partial repetition of the M8.8 rupture in 1906. These new geodetic results implies that the coupling condition on the plate interface and earthquake occurrences there may not be so simple as was expected in a classical theory of earthquake cycle. This estimation was still preliminary because the spatial coverage of the stations used for this study is not yet sufficient. However, given the conditions of the area covered by tropical jungle, in addition to security conditions, it is required to start considering two alternatives for refining the coupling model: performing field campaigns to collect data on benchmarks in this area, or venturing into the application of techniques associated to the concept of seafloor geodesy.

6.2.2.2. Viscoelastic relaxation associated to 1979, Colombia, subduction earthquake

Making a comparison with previous studies, it is observed that the values of the east components of the velocities with respect to South America as well as with respect to NAB at the ESMR, TUCO, GUAP and BUGT stations, decrease as the position of the stations moves away from the equator. White et al. (2003), using a subset of GPS data gathered during the CASA project in Colombia and Ecuador, interpreted the reduction in apparent locking in southwest Colombia relative to northern Ecuador as a result of viscoelastic relaxation in the lower crust following the 1979 M_w 8.2 subduction earthquake. At stations inland and north of GUAP station, the velocities obtained in this dissertation have a

substantially higher eastward component than those in the 1990s as was reported by Trenkamp et al. (2002). Although no data from GUAP site were available at that time, the model of White et al. (2003) predicted a substantially smaller velocity than the velocity at Tumaco.

In order to evaluate the effect of the viscoelastic relaxation associated with the December 12, 1979, (Mw 8.2) earthquake, post-seismic deformation due to this event is calculated using the viscoelastic-gravitational dislocation theory through the use of the PSGRN/PSCMP software (Wang et al., 2006). The earthquake parameters used are strike 31°, dip 20° and rake angle of 126° (Kanamori and MacNally, 1982) and other complementary information from White et al. (2003) for comparison purposes. For the model estimation, a two-layer half-space model similar to the one used by Wang et al. (2006) is assumed. The elastic layer thickness is assumed to be 55 km and the asthenospheric viscosity values in the range of 10^{18} to 10^{20} Pa-s are tested.

Observed and calculated velocities are compared in Figure 55 for 4 sequential periods of 10 years. It should be noted that observations were available only for the second (1989-1999) and the last (2009-2019) periods. Calculated vectors from viscoelastic relaxation model are in the WNW direction and their amplitude gradually decrease with time. At the stations near the Colombia-Ecuador border (stations 1 and 2), postseismic effects are not significant compared with the observed velocities, which mainly reflect elastic deformation due to interplate coupling (Sagiya and Mora, 2019). On the other hand, at the northern stations (stations 3 ~ 6), we identify significant velocity changes between the 1990's and the 2010's. Viscoelastic calculation demonstrates that postseismic northwestward motion attenuates between these time periods from about 5 mm/yr to 1-2 mm/year. This change is roughly consistent with the observational velocity changes. Although the fitting between the observed and calculated changes are not perfect, we expect to reproduce the observation by optimizing the fault model parameters for the 1979 earthquake and the rheological model parameters.

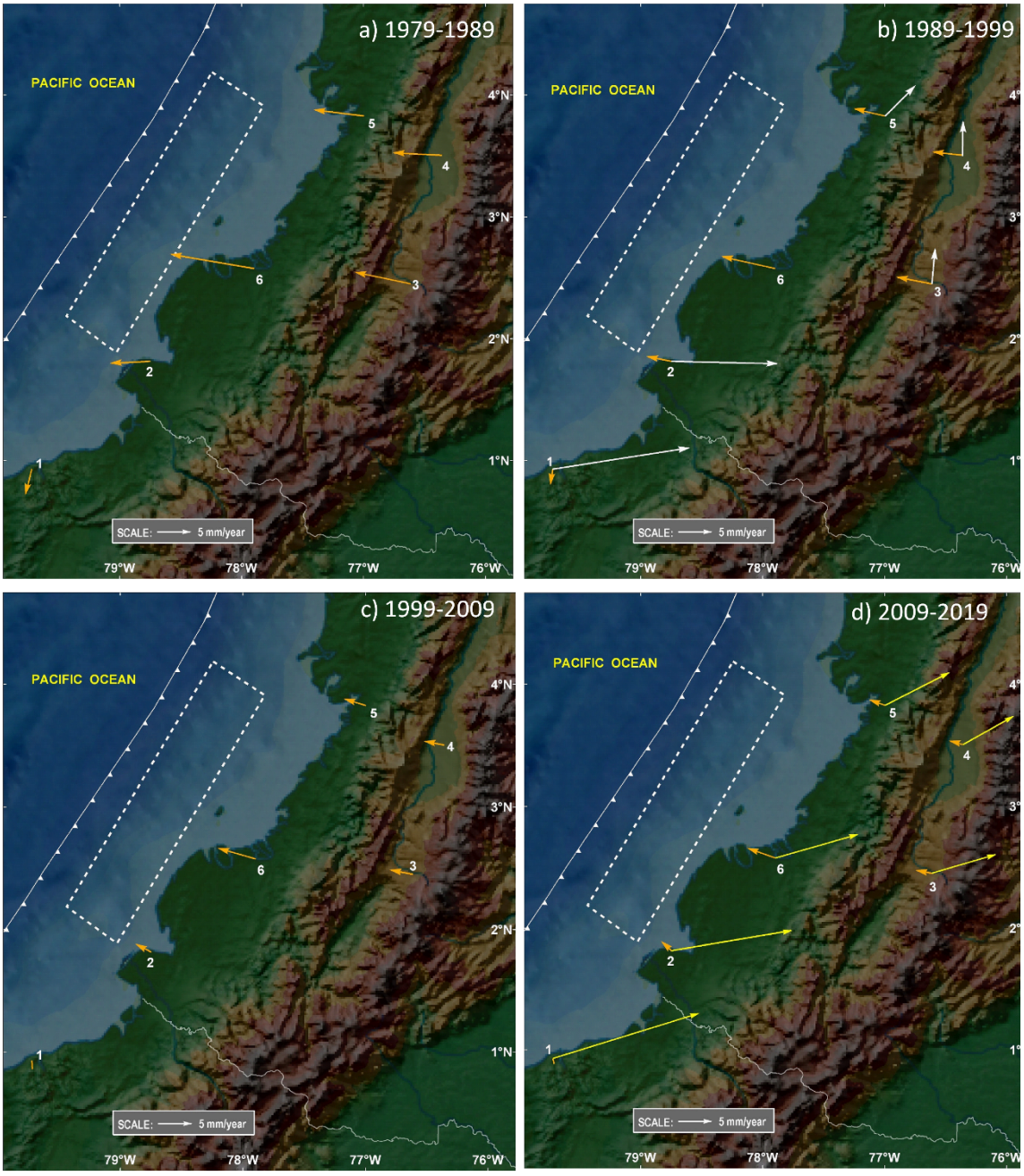

Figure 55.Viscoelastic relaxation related to the 1979 Nazca subduction zone earthquake. Viscoelastic estimation is represented by orange arrows. Time of calculation: a) 1979-1989; b) 1989-1999; c) 1999-2009; d) 2009-2019. White vectors correspond to results of GPS campaign data from the CASA Project, and yellow vectors are the result of this dissertation, based on GPS data from permanent stations.

6.2.3. Caribbean subduction

The convergence of the Caribbean plate with South America is represented in this study by the velocity of the GPS SAN0 and CN35 stations, installed on the islands of San Andres and Providencia respectively, on the Caribbean plate. The velocities in these stations correspond to an oblique convergence of 18.4 mm/yr and azimuth of 97.5° in SAN0, and 17.2 mm/yr with azimuth of 99.7° in CN35. These results are consistent with the predictions of northwest-southeast convergence in the South Caribbean Deformed Belt of 19 ± 3 mm/yr (Kellogg and Bonini, 1982) and 17 mm/yr (Kellogg and Bonini, 1985), and also with the estimate of Pérez et al. (2018) of 19.6 ± 2 mm/yr.

Although it is not the main purpose in this dissertation, the motion of the Caribbean plate has been estimated using the Euler's poles derived from the MORVEL global model (DeMets et al. 2010) and from the regional model of Symithe et al. (2015), in order to compare the velocities obtained with these models and those obtained in this study at CN35 and SAN0 stations, both located on the Caribbean plate.

Table 14 shows the velocity values in the east and north components of these stations and the uncertainties. It is observed that the velocities do not differ substantially from each other; however, it can be observed that the velocities of this study are closer to the generation of a pole that probably represents better the Caribbean plate motion. Upcoming studies, with a greater number of stations, will surely allow the refining of this model. In fact, the GeoRED project has installed three additional permanent stations in other Colombian islands.

Table 14. Comparison of velocities on the Caribben plate using different Euler poles.

Source	ID	Vel (E) mm/yr	Vel(N) mm/yr	sig (E)	sig (N)
DeMets et al.. (2010)	CN35	-1.7	-2.2	0.8	0.6
	SAN0	-0.8	-1.6	0.4	0.3
Symithe et al.. (2015)	CN35	-1.7	-1.0	0.8	0.6
	SAN0	-0.8	-0.4	0.4	0.3
This study	CN35	-0.9	0.0	0.4	0.4
	SAN0	-0.7	0.3	0.6	0.4

The seismicity in northern Colombia and western Venezuela is diffuse and shallow, Malave and Suárez, (1995); Benz et al. (2011). However, with the densification of seismological stations, especially in Colombia, moderate and small earthquakes have been recorded, and also has permitted to improve the earthquakes locations. Perez et al. (2018) reviewed the seismicity of the region based in the ISC revised catalogs (mb $\geq$ 4.5) for the period 1980-2013, micro-earthquakes locations between 2.5 and 4.5 mb reported by the National Seismological Network of the Colombian Geological Survey, and by the Venezuelan Foundation for Seismological Research-FUNVISIS for the period 2003-2012, being able to illustrate the northeast strike and southeast dip of the zone of Benniof that permits to define the subduction of the Caribbean slab beneath South America plate.

The results of the GPS measurements in the subduction zone of the Caribbean plate make it possible to establish motions in the position of each station, which, however, are characterized by the absence of earthquakes associated with these displacements. Therefore, it is possible to conclude that the region is aseismic and that the relative plate motion is probably accommodated by aseismic creeping at the plate interface. The SCDB would then be considered as its surface expression.

CHAPTER 7

PANAMÁ ARC-NORTH ANDES COLLISION, IMPLICATION FOR MOUNTAIN BUILDING AND SHORTENING

This chapter presents the results obtained from GPS processing to explain several phenomena that occur in the northwestern corner of South America such as the collision of the Panama arc with the North Andean block and its impact on mountain building and shortening on the Eastern Cordillera.

7.1. GPS observation

GPS analysis in this study provided an estimate of a margin-normal shortening of the Eastern Cordillera of Colombia less than 4.1 mm/year, which is consistent with the previous estimate of 3.7 ± 0.3 mm/yr by Mora-Paez et al. (2016). In addition to the margin-normal shortening, significant right-lateral shear is identified at the east and the west of the Eastern Cordillera. As for the vertical component, although the GPS vertical velocities have not been used in this study, the values of the vertical component for 4 permanent stations located in the Eastern cordillera are considered here: BAME: 3.4 ± 1.2 mm/yr; UWAS: 2.9 ± 0.5 mm/yr; VBUV: 0.9 ± 0.9 mm/yr, and VROS: 1.1 ± 1.1 mm/yr. The mean uplift rate of these four stations is 2.0 ± 0.9 mm/year.

7.2. Collision of Panama Isthmus

Collision of the Isthmus of Panama against South America is an important geological event that may affect the tectonic framework of the study area. About the timing of the Panama-Chocó arc-North Andes collision, there have been many studies with different estimates. Coates et al. (2004) considered that the beginning of the Panama-Chocó arc-North Andes collision occurred at much younger age, around 12 Ma. Barat et al. (2014) estimated the first contact between Panama and South America started at 38-40 Ma. Montes et al. (2012, 2015), based on ages of magma cooling, rotations of paleomagnetic poles, U/Pb dating, and anomalies of the Atlantic sea-floor, proposed that the closure of the Isthmus of Panama occurred around 15 Ma, without space for the trans-isthmian marine

passages. O'Dea et al., (2016), consider that the Panama arc, initially underwater, collided with South America about 24 million years ago and thus has continued to the present. Also, Osborne et al. (2014) and Sepulcher et al. (2014), based on paleoceanographic studies, indicated a decrease in the transport of deep and intermediate waters from the Pacific to the Caribbean between 10 to 11 Ma, probably related to a closure of the Central American Seaway. On the other hand, changes recorded in the salinity of the water of the Caribbean Sea (Haug et al., 2001) and the Great American Biotic Interchange (Marshall et al., 1982) did not occur until 4.2 Ma and 3.5 Ma.

7.3. Uplift of Eastern Cordillera

The eastern mountain range of Colombia has become an important source of sediments around 12-15 Ma (Gregory-Wodzicki, 2000; Mora et al., 2014). Wijninga (1996) and Gregory-Wodzicki (2000) indicated that most of the uplift in the central and eastern flank of the Eastern Cordillera occurred in the last 12 Ma based on paleobotanical studies and apatite fission-track dating (Mora et al., 2008; Mora et al., 2010b). Anderson et al. (2016), based on an integrated analysis of paleoprecipitation data in the Upper Magdalena Valley and new apatite fission track dating of the Garzon Massif, established that an early exhumation may have begun 12.5 Ma ago, but only a substantial orographic barrier was established between 6-3 Ma when the exhumed material was greater than 1 km/Ma. These studies suggested a change of deformation style and subsequent accelerated uplift during 6-3 Ma around the Eastern Cordillera. The accelerated tectonic uplift during the last 6 Ma is supported by the Neogene exhumation based on apatite fission track data and low temperature thermochronology (Mora et al. 2008; Parra et al. 2009). Mora et al (2010a), using apatite fission data, estimated that the exhumation rates in the range of 1-1.5 mm/yr for compressive structures in the eastern foothills of the Eastern mountain range over the last 3 Ma. Wittmann et al. (2011), using the geochronological analysis with cosmogenic nuclide, estimated denudation rates of 0.49–1.2 mm/year for the Ecuadorian Andes.

Based on various geologic information, Egbue et al (2014) reconstructed the tectonic uplift from the present-day total uplift and paleoelevation data as shown in Figure 56a. The paleo-elevations estimated from paleobotanical and geomorphological data are shown by the black line with squares (Wijninga, 1996 and Gregory-Wodzicki, 2000), which are consistent with the present mean elevation value over 3 km. The tectonic uplift curves

estimated from a current total structural relief (10 km) and assumed erosion rates of 0.5 and 1.0 mm/a are shown by thin black lines. Figure 56b shows shortening rates estimated from uplift rates.

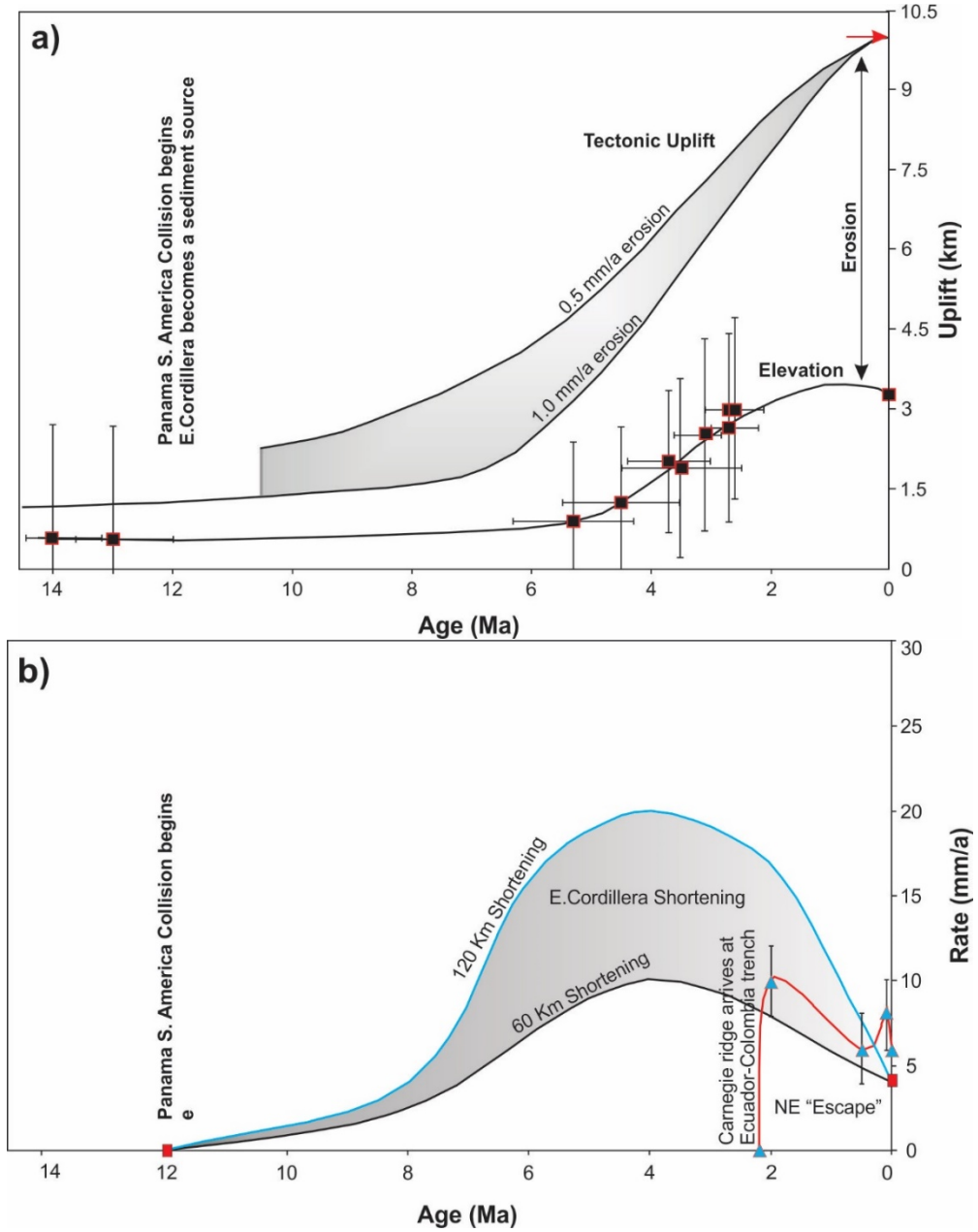

Figure 56. Uplift and shortening of the Eastern Cordillera in Colombia.
a) Uplift history 12 Ma to Present estimated from total tectonic uplift (10 km) and paleoelevation data (black squares with error bars after Wijninga, 1996; Gregory-Wodzicki, 2000) for erosion rates of 0.5 and 1.0 mm/yr. GPS uplift rate (0.0 ± 1.0 mm/a, red lines) can be compared to our estimated uplift rate (slope of tectonic uplift curve) (After Egbue et al., 2014). b) Shortening rates for 60 and 120 km shortening are estimated from uplift rates. The red square at time 0 represents the range-normal shortening GPS estimate from this study. The red line and black squares with error bars are northeastward geologically measured "escape" rates compiled by Egbue and Kellogg (2010) (Mora et al., 2019, modified from Egbue et al., 2014).

7.4. Crustal thickening associated with shortening

Two geodynamic processes, crustal thickening and removal of mantle lithosphere, are possibly responsible for a high terrain. Horizontal shortening of the crust in a state of isostatic equilibrium accounts for the high terrain of most mountain belts (Molnar, 2018) whereby excess mass of the high terrain is compensated by a deficit of mass in a crustal root (Airy isostasy). The time required for the high terrain to develop by this process obviously scales with the rate of horizontal crustal shortening. Alternatively, many high plateaus are underlain by hot material in the upper mantle in case the mantle lithosphere is removed, either by peeling away from the crust as delamination (Bird, 1978, 1979) or by sinking as blobs of dense material during growth of convective instability (e.g., England and Houseman, 1989). The speed with which such removal can occur remains controversial, but current ignorance allows for removal of mantle lithosphere in periods as short as a few Ma (e.g., Houseman et al., 1981; Houseman and Molnar, 1997). Amounts of surface uplift that might isostatically balance the replacement of cold mantle lithosphere by hot asthenosphere, however, probably do not exceed 1000–2000 m.

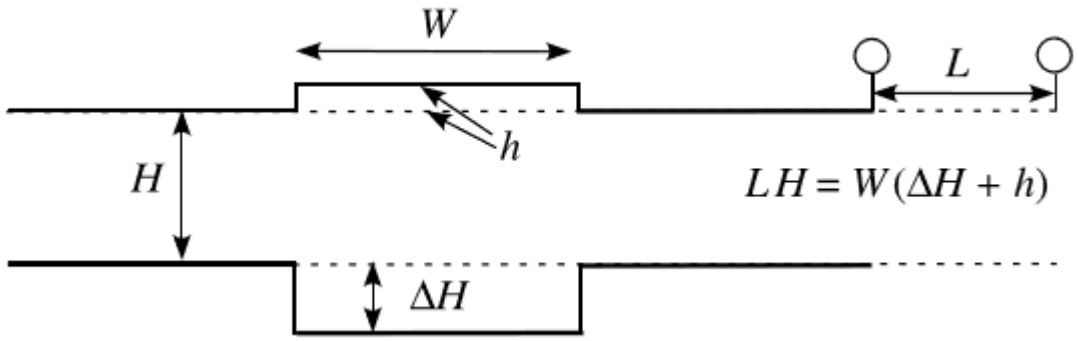

Figure 57. Cartoon showing budget of crust.

Estimates of crustal thickness can be used to estimate amounts of crustal shortening. If a high mountain range of mean height h is isostatically compensated by a crustal root of excess thickness ΔH, then crust beneath the range is thicker by $\Delta H + h$ than the surrounding crust (Figure 57). Suppose that crust of thickness H is shortened horizontally to build a range with crustal thickness $\Delta H + H + h$ over a width W, That extra cross-sectional area presumably was built by horizontal shortening of L, so that

$$L * H = W * (\Delta H + H + h) \qquad (7.1)$$

By assuming the Airy isostacy, the thickness of the crustal root is given by

$$\Delta H = \frac{\rho_c}{\rho_m - \rho_c} h \qquad (7.2)$$

And because the crust is thicker by $\Delta H + h$, the thickness of crust beneath the high terrain is greater than beneath lowlands by

$$\Delta H + h = \frac{\rho_m}{\rho_m - \rho_c} h \quad (7.3)$$

Also, the ratio between the horizontal shortening can be written as follows.

$$L = \left(1 + \frac{\Delta H + h}{H}\right) W \quad (7.4)$$

By assuming $\rho_c = 2.8 \times 10^3\ kg/m^3$, $\rho_c - \rho_m = 0.4 \pm 0.1 \times 10^3\ kg/m^3$, we can evaluate the amount of isostatic uplift for the excess thickness ΔH. For the cases with $\Delta H = 15, 20, or\ 25\ km$, it is inferred that $h = 2.1 \pm 0.7\ km,\ 2.9 \pm 0.9\ km, or\ 3.6 \pm 1.2\ km$, respectively. With an observed mean height of the cordillera as ~2.7 km, clearly a crustal root as thick as 15–25 km is plausible. Also the excess crustal thickness $\Delta H + h$ will be 18 to 28 km.

There is abundant evidence of crustal shortening on the flanks of the Eastern Cordillera (e.g., Bayona et al., 2008; Cediel et al., 2003; Colletta et al., 1990; Cortés et al., 2006; Dengo and Covey, 1993; Egbue and Kellogg, 2012; Mora et al., 2008, 2010a, 2010b, 2010c, 2014). Therefore, the high terrain is, at least in part, a result of crustal thickening and isostatic balance. This crustal shortening has occurred, at least in part, on structures that initially developed during a Mesozoic stage of crustal extension when grabens and normal faults formed (e.g., Cediel et al., 2003; Jimenez et al., 2013; Moreno et al., 2013; Roeder and Chamberlain, 1995; Roure et al., 1997; Sarmiento-Rojas et al., 2006; Tesón et al., 2013). Attempts to balance cross sections across the entire Cordillera have led to differing results. For example, Colletta et al. (1990) estimated more than 100 km of shortening, Bayona et al. (2008) estimated 110 km, Dengo and Covey (1993) suggested

150km, and Roeder and Chamberlain (1995) inferred 170 km, but Cooper et al. (1995) argued for only 68 km and Teixell et al. (2015) for 82 km. Additionally, Cortés et al. (2006) argued for 70 km in the southern, relatively narrow part of the cordillera. For the eastern side of the Cordillera, Mora et al. (2008) inferred 58 km of shortening. Tesón et al. (2013) estimated between 62 and 80 km for four cross sections, and they concluded that shortening of the entire Eastern Cordillera must be less than 25%. Moreover, Tesón et al. (2013) argued that because the normal faults have been reactivated in oblique crustal shortening, amounts of shortening was less than the common values of 100–150 km. It is possible to argue that the opposite should hold, given that crust was thinned during the Mesozoic phase of crustal shortening. Veloza et al. (2012) notes that some shortening is concentrated in the southeast margin, where geological data show active faulting and localized convergence at 2.1 ± 1.2 (2σ) mm/yr.

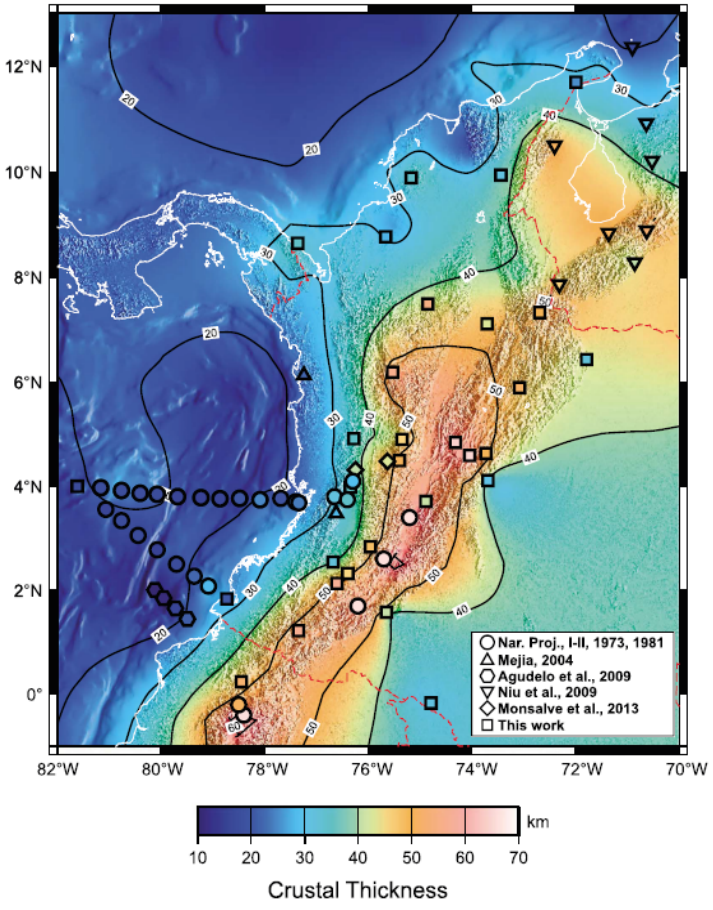

Figure 58.Map of topography of the Eastern Cordillera and adjacent regions.
The location of seismograph stations and estimates of crustal thickness (Poveda et al., 2015).

Poveda et al. (2015), using receiver functions, estimated crustal thicknesses of ~25–35 km beneath the low area to the east of the Eastern Cordillera and thicknesses of 45–58 km beneath the high terrain of the Cordillera (Figure 58). Thus, the crust beneath the Eastern Cordillera is 15–25 km thicker than that beneath surrounding regions, which is consistent with the model calculation. If the crust were initially as thin as 30 km as the evidence of Mesozoic graben formation implies (e.g., Roeder and Chamberlain, 1995), the current thickness of 45–58 km means 50% to nearly 100% shortening and the original width of 150–300 km is necessary. Tesón et al. (2013) also inferred that the resulting thickening of 7.5 ± 1.25 km would account for 1 ~ 1.5 km of the current elevations.

Shortening and elevation change are related in compressional margins. If we assume that shortening rate of the Eastern Cordillera $\boldsymbol{v}$ is proportional to the tectonic uplift rate $\boldsymbol{u}$, then, the relationship can be simplified with a constant. Thus,

$$\boldsymbol{v} = k\boldsymbol{u}, \qquad (7.5)$$

where k is a dimensionless proportionality constant. It should be noted that there is a maximum limit on elevation related to equilibrium for compressional stresses and vertical gravity forces.

The maximum and minimum estimation of shortening in the Eastern Cordillera for the last 12 Ma were 150 km (Dengo and Covey, 1993) and 68 km (Cooper et al, 1995). Egbue and Kellogg (2012) estimated that about 80% of the shortening occurred in the last 12 Ma. Therefore, the maximum/minimum shortening in the last 12 Ma is about 120 km and 54 km, corresponding to the uplift u of 6.7 km (Figure 57a). The proportional constant k is 18 and around 8, respectively. By assuming this proportionality, we can estimate time depdendence of crustal shortening rate as shown in Figure 57b based on the uplift history in Figure 57a. In the shortening history of Eastern Cordillera shorwn in Figure 57b, crustal shortening was the fastest (10~20 mm/yr) around 4 Ma and decreased to the current value of around 4 mm/yr. Mountain building scenarios for the Eastern Cordillera should be consistent with such temporal variation of crustal shortening.

7.5.Apparent discrepancy between geologic and geodetic data

Some authors, relying on young cooling ages of exhumed rock or evidence of more recent folding and faulting on the flanks of the Eastern Cordillera, have inferred that Plio-Quaternary deformation has played a key role in the construction of the high terrain (e.g., Campbell and Bürgl, 1965; Gómez et al., 2003, 2005a; Horton et al., 2010; Mora et al., 2008, 2010a, 2010b). Most, however, suggest that crustal shortening responsible for the Eastern Cordillera began earlier. Some have concluded that initiation of important shortening began in Middle Miocene (e.g., Bayona et al., 2008; Colletta et al., 1990; Cooper et al., 1995; Dengo and Covey, 1993; Gómez et al., 2005b; Hoorn, 1993; Hoorn et al., 1995; Mora et al., 2014), but a consensus suggests that a nonnegligible amount of shortening occurred earlier in Cenozoic time (e.g., Babault et al., 2013; Bande et al., 2012; Bayona et al., 2013; Caballero et al., 2013; Campos and Mann, 2015; Cediel et al., 2003; Egbue and Kellogg, 2012; Gómez et al., 2003; Hoorn et al., 2010; Horton et al., 2010; Martinez, 2006; Mora et al., 2010b, 2010c; Ochoa et al., 2012; Parra et al., 2009a, 2009b, 2012; Sánchez et al., 2012; Saylor et al., 2011, 2012; Villamil, 1999).

Thus, the apparently recent surface uplift of the Eastern Cordillera inferred from paleobotanical observations offers a test about possible processes that can build mountain belts rapidly. If these inferences of rapid uplift are applied to the entire Eastern Cordillera, they would require that the current low rate of shortening apply only to the past few million years, and hence would indicate a remarkably abrupt recent change in rate. It is important to consider that there is a relatively low convergence rate. If the entire Eastern Cordillera rose in the past few million years, and it was due by thickening of the crust, that would require a much higher convergence rate than what GPS results show, and the GPS rate cannot be applied for a geological time scale.

At the same time, however, because most mountain ranges have not been built in such a short period, the apparent youth of the Eastern Cordillera itself makes it exceptional among mountain ranges around the world. Alternatively, such rapid surface uplift might refer only to the outer edges of the Cordillera where outward growth is taking place. Molnar (2018) pointed out that although continued convergence could mean greater thickening and greater mountain range, it is more likely to mean a growth in the width of the mountain range.

7.6. Scenarios of mountaing building

Mora-Páez et al. (2016) interpreted that the small value of the shortening observed in the GPS results is an evidence of slow formation of the Eastern Colombian mountain range over a period of 40 Ma. They interpreted that the paleobotanical evidence for recent rapid uplift may correspond to local elevation change or may have been affected by climate change or by invasive species from North America.

The apparent dichotomy of the rapid shortening of the Eastern cordillera in the Miocene and the very slow current normal shortening range, confirmed with the GPS results, can be explained by the proposal of a broken indenter model. This model is based on the following considerations:

a) The collision of the Panama-Chocó arc with the South America plate began around 12-15 Ma ago (Figure 59a).
b) The reconstruction of the arc performed by Coates et al. (2004) indicates that in the post-collision phase, at 6 Ma, the Panama-Chocó block deforms internally and has become widely emergent.
c) The collision of the Panama-Chocó arc with the Northern Andes can be modeled mechanically as a rigid indenter (Figure 59b).
d) Subsequently, the Choco arc broke off from the indentor and was accreted to the North Andean Block (Figure 59c).

The present GPS velocities of 15-18 mm/yr relative to the North Andes at the stations located on the Panama Block probably represents the rigid collision of Panama-Chocó with the North Andes, that produced rapid permanent deformation in the North Andes, mainly after the closure of the Central American Seaway and the formation of the land bridge in the last 10 Ma. During the last 2 Ma, the indenter associated with the Panama collision was broken and mechanically decoupled from the Panama block. Then the deformation front moved westward from the Eastern Cordillera to the current collision zone. As a result of this change, the shortening as well as the uplift rate at the Eastern Cordillera dramatically decreased to the current value as observed by GPS.

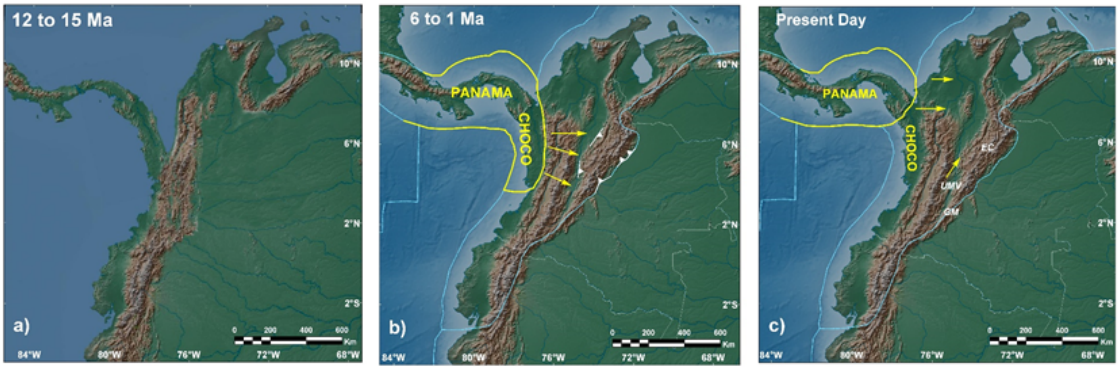

Figure 59. Schematic evolution of Panama - North Andes.
a) 12-15 Ma. initial collision of Panama-Choco arc and North Andes. b) 6 to 1 Ma. Panama-Choco-North Andes collision. Permanent shortening and rapid uplift of Eastern Cordillera. Upper Magdalena Valley (UMV), Eastern Cordillera (EC), Garzón Massif (GM). c) Present. Choco arc is accreted to the North Andes

The second alternative explanation is related to paleobotanical evidences. Most authors, such as van der Hammen et al. (1973), Hooghiemstra, (1984); Kroonenberg et al. (1990); Wijninga and Kuhry, (1990); Andriessen et al. (1993); Helmens and Van der Hammen, (1994); Wijninga, (1996); Hooghiemstra and Van der Hammen, (1998); Hooghiemstra et al, (2006), have carried out studies of fossil pollen in high terrain areas above 2500 m in the Eastern Cordillera of Colombia, suggesting that vegetation similar to what currently exists characterizes the low tropical areas adjacent to this mountain range 6 to 3 Ma. This similarity, together with the difference that exists between the plants that live in the lowlands and highlands today, permits to deduce that the Sabana de Bogotá and probably the entire Eastern Cordillera rose since ~3 Ma from low elevations less than 1000 meters to its present-day elevation. Several authors (e.g. Van der Hammen et al., 1973; Wijninga, 1996, Van der Hammen and Hooghiemstra, 1997; Hooghiemstra et al., 2006; Torres et al., 2013) have argued for 1500 ±500 m since 4 Ma, and 2000 m from some time before.

Other studies related to the cooling ages of the rocks exhumed along the eastern flank of the Eastern mountain range indicated an unexpected acceleration in cooling, that suggest rapid exhumation since ~3 Ma and again, with the inference that the Eastern cordillera rose substantially since around ~3 Ma (Mora et al., 2008, 2014). Mora et al. (2010a, 2010b), using fission track data, estimated exhumation rates in the range of 1-1.5 mm/a for compression structures in the eastern foothills of the Eastern Cordillera over the last 3 Ma.

These inferences of large, Pliocene or Quaternary surface uplift differ from most such inferences elsewhere, because the global cooling since ~3 Ma and resultant accelerated erosion due to increased glaciation in elevated terrain offer explanations for the apparent increases in surface elevations. However, it is necessary to emphasize the meaning of the "apparent" increase in surface elevation. So far, globally, inferences have been made about the recent rapid uplift of mountain ranges of 1-3 km during 1-3 Ma. This uplift is suggested based on the fossil plants found in high elevation that live only at lower elevation today. Therefore, it was inferred that when the surface, the earth cooled. Additionally, glaciers were much rarer before ~3 Ma, but they have shaped the landscape in high mountains. Therefore, some have assumed a recent uplift because of this erosion. The Eastern Cordillera is special in its climate change, from warmer before ~3 Ma to cooler with glaciers later, which affected the mid- and high-latitudes, but not the tropics (e.g., Molnar and England, 1990; Zhang et al., 2001; Molnar et al., 2018). Climate changes in the tropics since 3–5 Ma, however, do not seem to have been large, and certainly not large enough (~9–12°C) to account for the paleobotany-based 1500–2500 m differences between present-day and inferred past elevations, (Molnar and England, 1990). Much evidence showed that temperatures at high latitudes have varied enormously over the past 100 Ma, but with little change in the tropics (Zachos et al., 1994).

Thus, we should reconsider the implications of paleobotanical observations, which include: (1) that vegetation currently living at high elevations of 2500–4000 m differs from that inferred from fossil plant organs at 3–6 Ma and, (2) that 4–6 Ma fossil plant organs resemble those of plants currently living below ~1500 ± 500m (e.g., Hooghiemstra et al., 2006). The recent work by Anderson et al. (2015) suggested that the rise of the Sabana de Bogotá may have been slower than that inferred from fossil pollens. As an important point, the paleobotanical evidence comes from only a small part of the Eastern Cordillera. Thus, changes in elevations of that region ought not be generalized to the entire Cordillera. In particular, the oldest site of paleobotanical finds, Tequendama, with an age between ~6 and ~15 Ma (Wijninga, 1996), lies along the southwest end of the Eastern Cordillera, and it could have risen to its present-day elevation as the southwest margin of the Cordillera rose, without any concurrent surface uplift of the rest of the range. Finally, many of the plants that dominate high elevations today are immigrants from North America since ~3Ma:

Myrica at ~3Ma, Juglans (walnut) at ~2.4Ma, Alnus (alder) at ~1 Ma, and Quercus (oak) at ~400ka (Andriessen et al., 1993; Torres et al., 2013; van der Hammen and Cleef, 1983; Van der Hammen and Hooghiemstra, 1997). Perhaps we ought not to ignore the possibility that the differences in present-day floral assemblages from fossil assemblages are due less to recent uplift and more to invasive species from North America, which entered Colombia since 3–6 Ma, out-competed plants that had lived at high elevations and limited their habitats to lowlands.

With respect the strike-slip component, although most discussions of the Eastern Cordillera have focused on the shortening across the belt, Montes et al. (2005) showed geological evidence for substantial right-lateral shear of the Eastern Cordillera; this evidence includes not only slip on strike-slip faults but also penetrative strain of cobbles in conglomerate layers. Thus, the shear that they found is distributed, not localized on one or a few major faults. This observation is consistent with the mapping of active faults in Colombia by Veloza et al. (2012). Although they showed relatively rapid right-lateral shear farther south, they depict no active strike-slip faults within the Eastern Cordillera in Colombia.

7.7. Summary

The different tectonic features that explain the velocity field obtained in this study have been described. Important contribution of this dissertation is the reliable estimation of the velocity of the Nazca plate, that is possible using GPS data, with several years of observation at MALO station, owned by the Colombian Geological Survey, located on the Malpelo Island, the only island that exists in the northern part of the Nazca plate.

It is concluded that after 40 years of the occurrence of the 1979 subduction earthquake, it is possible to observe that the viscoelastic relaxation is a process that still continues to control the post-seismic deformation induced by the earthquake in this area.

The horizontal velocity field presented in this study highlights the increase in deformation of the North Andean block north of 7.5°N of latitude related to the present-day convergence of Panama-North Andean block. Based on this interpretation, the rupture

in the Panama-Chocó indentor and the Choco accretion to the NAB must have occurred very recently, probably in the last 1-2 Ma, to explain the rapid Late Miocene-Pliocene shortening and uplift, and the equally rapid deceleration in the margin-normal shortening rate.

Two alternatives of interpretation of results related to the mountain building as well as shortening in the Eastern Cordillera of Colombia are presented. The first one is based in a proposed "broken indenter" model for the Panama-Choco arc that consider that the Choco arc has been recently accreted to the NAB, and the second one, based on the comparison of GPS data with paleobotanical results, that suggest rapid uplift (7 km) and shortening (120 km) in the last 10 Ma.

CHAPTER 8

CONCLUSIONS

The dissertation contains a generalized description of the tectonic framework of the study area, and the limits of the so-called North Andean Block were illustrated in the most detailed way possible from the existing literature.

The analysis of the time series and the estimation of the velocities in the 60 stations used in this dissertation are based on a minimum observation time of 2.5 years in each station. Using data from GPS permanent stations installed under the GeoRED Project in Colombia as well as from stations located in Ecuador and Panama, which are used by data exchange with ESPONA from Quito, Ecuador, as well as from the COCONET project, a new velocity field for northwestern South America and southeastern Central America has been estimated.

A new comprehensive model of the North Andean Block motion is presented in this study. Previous estimates made by other authors were based on data from stations located over a very small area, mainly in Ecuador and two sites in Colombia, which is not appropriate to extrapolate to the north. For the new model, stations located in both Ecuador and Colombia, distant from the Nazca subduction zone were selected. Also, stations located to the west of the NAB eastern boundary with South America are considered. No sites north of 7.5°N latitude is selected. The selected stations represent the rigid motion of the block; this selection is based on trial and error tests. The predicted motions of the NAB are almost in the same direction across the block, with a motion of 8.6 mm/yr with respect to South America in a N60°E direction. Emphasis is placed on the mechanisms that are considered responsible for the tectonic escape of the NAB, proposed by several authors, such as the collision of the Carnegie ridge, the rapid oblique convergence of the Nazca plate along the Colombia-Ecuador trench, and the high coupling at the Nazca-NAB subduction plate interface, the last two clearly demonstrated with GPS results.

The obtained velocity field allows to confirm the oblique subduction of the Nazca plate with respect to the South America plate, based on the geodetic observations made at the GPS stations located on the islands of Malpelo (Colombia) and Galapagos (Ecuador), both located on the Nazca plate. GPS costal stations on the Pacific Ocean show velocity vectors with magnitude greater than most of other velocity vectors in Colombia, which can be interpreted as accumulated strain in the Nazca subduction zone.

Comparisons of the results of this dissertation are made with those obtained in a previous study conducted by Trenkamp et al. (2002). The velocity vectors in the stations used for this analysis indicate that the measurements and the results obtained in both studies are consistent and stable for the time at which the measurements were made, and each of the measurements responds to the state-of-the-art in the development of the reference frame used in each case. An essential aspect to consider was to analyze the impact on the use of different reference frames in the two solutions. With this purpose, and considering that Trenkamp et al. (2002) did not include vertical velocities in their solutions, a transformation of the station velocities from ITRF2008 to ITRF96 was carried out. As a result of this analysis, it was established that the impact on using two different reference frames is -0.3 mm/year in the annual velocity of the east component and 3.2 mm/year in the annual velocity of the north component. It is important to consider that the results obtained in this study are based on data from permanent stations, which are more robust, while those from previous studies were based on data from field stations, obtained under the modality of field campaigns with intervals of data collection between 2 and 3 years. The effect of the 1979 M_w 8.2 subduction earthquake was discussed based on the comparison of GPS velocities in different time periods. Thus, a modeling of viscoelastic relaxation was performed. The results of this analysis permit to conclude that the observations at the CASA project field stations, corresponding to the study by Trenkamp et al. (2002) for the period 1988-1998, were significantly affected by the postseismic deformation of the earthquake, which allows explain the differences found with the estimated velocities in this dissertation. It can even be concluded that viscoelastic relaxation associated at this earthquake is a process that still persists.

The Colombia section of the Nazca-NAB trench continues to pose a high risk of a great mega-subduction earthquake in southern Colombia. The 1942, 1958, 1979, and 2016

trench earthquakes have only released a fraction of the energy accumulated in the Ecuador-Colombia trench since the great 1906 earthquake. Interseismic strain is accumulating rapidly in the overriding plate at least as far north as Tumaco. Southern Colombian coastal sites are moving more rapidly inland as the viscoelastic mantle flow effects of the 1979 earthquake gradually decay. Residual motions within the NAB have important implications for Nazca and Caribbean subduction earthquake cycles as well as for mountain building in the Eastern Cordillera of Colombia.

From the estimation of the velocity field of this dissertation, a margin-normal shortening can be established at least of 4.1 mm/yr in the Eastern Cordillera of Colombia. Two alternatives are presented regarding mountain building and shortening in the Eastern Cordillera of Colombia due to the collision of the Panama block. The first one is based in a proposed "broken indenter" model for the Panama-Choco arc that consider that the Choco arc has been recently accreted to the NAB. The "broken indenter" model allows to explain, from the GPS results of this dissertation, the accretion of the Chocó arc to the NAB, as well as to consider the collision of the Panama-Choco arc with the NAB as the mechanism that could explain the shortening and uplifting of the eastern Colombian mountain range. The second one, from GPS data compared with paleobotanical results from the range suggest rapid uplift (7 km) and shortening (120 km) in the last 10 Ma. This would imply an average shortening rate of about 12 mm/yr for the last 10 Ma or about 3 times the GPS values obtained. It is important to consider that an extrapolation of GPS rates is being done, finding some differences with those that indicate the elevation process in the range estimated by the paleovegetation studies. It is probably a daring presumption because it corresponds to make inferences toward the past, as it is also complicated to specify the uplift and main deformation phase because probably is not a constant process since when it started. Thus, more studies are required, for example those that specify when the collision of Panama arc began, or for example, the application of new techniques that allow a better definition of ages in paleovegetation analysis.

In order to confirm the accretion of the Choco arc to the NAB, additional GNSS stations and measurements are needed. The Panama arc is rapidly colliding eastward with the NAB. The Panama-Choco collision was likely responsible for much of the uplift of the Eastern Cordillera. The present on-going collision poses a major earthquake hazard from

the Panama border to Medellin city in Colombia, the larger urban center located at the northwestern zone of the country.

The velocity vectors obtained in this dissertation suggest deformation associated with the subduction of the Caribbean plate beneath the NAB. Although significant motion to the east of the NAB with respect to SOAM has been estimated, the Caribbean coastal stations still show large motions with respect to NAB. However, there is still a debate, not yet resolved, if there is subduction in this boundary. Most of the deformation in the northwestern of Colombia is caused by the motion of the Caribbean plate, so it is important to consider that the Panama block also contributes to such deformation, which requires performing more analyzes that allow determining the contribution of each one of the two deformation sources, responsible for the existence of a high tectonic complexity region.

It is important to consider that the current spatial density of coastal sites in Colombia does not allow for a detailed image of elastic strain accumulation; however, maturing time series of new sites will allow for a more detailed study in the future.

It is also important to mention that the objectives established in the GeoRED project proposal in 2006 have been fulfilled, which has allowed obtaining results corresponding to a first phase of the implementation of the GNSS space geodesy technology in Colombia. Therefore, new objectives and challenges are being conceived, emphasizing the use of complementary tools for the study of the crustal deformation, for example InSAR. My efforts are being addressed to have a high-quality GNSS infrastructure that will serve as an essential framework for the study of crustal and atmospheric dynamics of the entire Colombian territory, and, at the same time, sharing data and research results with neighboring countries.

BIBLIOGRAPHY

Acosta J., F. Velandia, J. Osorio, L. Lonergan and H. Mora, (2007). Strike-slip deformation within the Colombian Andes, In: Deformation of the Continental Crust: The Legacy of Mike Coward, Ries A C., Butler, R. W. H. & Graham, R. H. (eds), Geological Society, London, Special Publications, 272, 303–319.

Adamek, S., C. Frohlich, W. D. Pennington, (1988). Seismicity of the Caribbean–Nazca boundary; Constraints on microplate tectonics of the Panama region, J. Geophys. Res. 93: 2053-2075.

Adams D. K., S. I. Gutman, K. L. Holub and D. S. Pereira, (2013), GNSS observations of deep convective time scales in the Amazon. Geophysical Research Letters 40: 2818–2823. DOI: 10.1002/grl.50573

Adriano B., M. Arcila, R. Sanchez, E. Mas, S. Koshimura, P. Arreaga and N. Pulido, (2017), Estimation of the tsunami source of the 1979 great Tumaco earthquake using numerical modeling, 16th. World Conference on Earthquake, Conference Paper

Agnew, D. C., Burke, K., Cazenave, A., Dixon, T., Hager, B. H., Heirtzler, J. R., Jordan, T. H., Minster, J. B., McNutt, M. K., Royden, L. H., Sandwell, D. T., and Turcotte, D. L., (1988). Long term dynamics of the solid Earth, in Lecture Notes in Earth Sciences, 22. The Interdisciplinary Role of Space Geodesy, I. Mueller and S. Zerbini, Eds., Springer-Verlag.

Allen, R. M., and A. Ziv, (2011), Application of real-time GPS to earthquake early warning, Geophys. Res. Lett., 38, L16310, doi:10.1029/2011GL047947.

Allmendinger, R. A., Loveless, J. P., Pritchard, M. E., and Meade, B., (2009). From decades to epochs: Spanning the gap between geodesy and structural geology of active mountain belts: Journal of Structural Geology, doi: 10.1016/j.jsg.2009.08.008.

Altamimi, Z., X. Collilieux, and L. Métivier (2011). ITRF2008: An improved solution of the International Terrestrial Reference Frame, J. Geod., 85(8), 457–473, doi:10.1007/s00190-011-0444-4

Altamimi Z., L. Métivier, and X. Collilieux (2012). ITRF2008 plate motion model, J. Geophys. Res., 117, B07402, doi:10.1029/2011JB008930

Alvarado A., L. Audin, J. M. Nocquet, E. Jaillard, P. Mothes, P. Jarrin, M. Segovia, F. Rolandone, and D. Cisneros (2016), Partitioning of oblique convergence in the Northern Andes subduction zone: Migration history and the present-day boundary of the North Andean Sliver in Ecuador, Tectonics, 35 : 1048–1065. doi:10.1002/2016TC004117.

Anderson, V. J., Horton, B. K., Saylor, J. E., Mora, A., Tesón, E., Breecker, D. O., and Ketcham, R. A., (2016). Andean topographic growth and basement uplift in southern Colombia: Implications for the evolution of the Magdalena, Orinoco, and Amazon river systems: Geosphere, v. 12, no. 4, p. 1235–1256, doi:10.1130/GES01294.1.

Andrei, C.-O., S. Lahtinen, M. Nordman, J. Näränen, H. Koivula, M. Poutanen and J. Hyyppä, (2018), GPS Time Series Analysis from Aboa the Finnish Antarctic Research Station. *Remote Sens. 10*, 1937.

Andriessen, P. A. M., K. F. Helmens, H. Hooghiemstra, P. A. Riezobos, and T. Van der Hammen (1993), Absolute chronology of the Pliocene-Quaternary sediment sequence of the Bogotá area, Colombia, Quat. Sci. Rev., 12, 483–503.

Argus, D. F., R. G. Gordon, and C. DeMets, (2011), Geologically current motion of 56 plates relative to the no-net-rotation reference frame, Geochemistry, Geophysics, Geosystems 12 (11), doi:10.1029/2011GC003751

Argus D. F., R. G. Gordon, M. B. Heflin, C. Ma, R. J. Eanes, P. Willis, W. R. Peltier and S. Owen (2010), The angular velocities of the plates and the velocity of Earth's centre from space geodesy, Geophys. J. Int. (2010) 180, 913–960 doi: 10.1111/j.1365-246X.2009.04463.x

Argus, D. F. and R. G. Gordon, (1991), No-net-rotation model of current plate velocities incorporating plate motion model NUVEL-1, Geophys. Res. Lett., 18, 2039-2042,doi:10.1029/91GL01532.

Assumpcao, M., (1992). The Regional Intraplate Stress Field in South America. J. Geophys. Res. 97, 11889-11903. Doi: 10.1029/91JB01590

Audemard, F. A. (1993). Néotectonique, Sismotectonique et Aléa Sismique du Nord-ouest du Vénézuéla (Système de failles d'Oca–Ancón). PhD thesis, Université Montpellier II, France, 369 pp + appendix.

Audemard, F. A. (2001). Quaternary tectonics and stress tensor of the northern inverted Falcón Basin, northwestern Venezuela. Journal of Structural Geology, Special Memorial Issue to Paul Hancock, 23(2-3): 431-453. doi: 10.1016/S0191-8141(00)00116-4

Audemard F. E. and F. A. Audemard, (2002), Structure of the Mérida Andes, Venezuela: relations with the South America-Caribbean geodynamic interaction. Tectonophysics, 345 (1–4): 299–327.

Audemard, F. A. (2002). Ruptura de los grandes sismos históricos venezolanos de los siglos XIX y XX, revelados por la sismicidad instrumental contemporánea. XI Congreso Venezolano de Geofísica, Caracas, Venezuela, Nov. 17-20, 2002 (8pp; Extended Abstract in CD).

Audemard F., M. Machette, J. Cox, R. Dart, K. Heller, (2000). Map and Database of Quaternary Faults and Folds in Venezuela and its Offsohre Regions. USGS Open-File Report, 00-1018 (accessible from USGS webpage; open file reports ofr-00-0018).

Audemard, F. A. (2003). Geomorphic and geologic evidence of ongoing uplift and deformation in the Mérida Andes, Venezuela. Quaternary International, 101-102C: 43-65. doi: 10.1016/S1040-6182(02)00128-3

Audemard, F. A. (2009). Key issues on the post-Mesozoic southern Caribbean plate boundary. In: James, K.H., Lorente, M.A. and Pindell, J., (eds) Origin and Evolution of the Caribbean Plate, Geological Society, London, Special Publications, 328: 567-584. doi: 10.1144/SP328.23

Audemard F., (2014). Active block tectonics in and around the Caribbean: a review. In: The Northeastern Limit of the South American Plate – Lithosperic Structures from Surface to the Mantle, M. Schmitz, F. Audemard, F. Urbani (Eds), Fac. Ing. Univ. Central de Venezuela y FUNVISIS, ISBN 978-980-00-2800-1, 29-77

Banks N., C. Carvajal, H. Mora and E. Tryggvasson (1990), Deformation monitoring at Nevado del Ruiz, Colombia - October 1985 - March 1988, J. Volcanology and Geothermal Research 41: 269-295, https://doi.org/10.1016/0377-0273(90)90092-T

Barat, F., de Lépinay B. M., Sosson M., Müller C., Baumgartner P. O., Baumgartner-Mora C., (2014). Transition from the Farallon Plate subduction to the collision

between South and Central America: Geological evolution of the Panama Isthmus, Tectonophysics 622, 145-167, doi.org/10.1016/j.tecto.2014.03.008.
Barka A. and R. Reilinger, (1997), Active tectonics of the Eastern Mediterranean region: deduced from GPS, neotectonics and seismicity data, Annali di Geofisica Vol XL (3), 587-610
Bartel B., (2014), Stability of PBO GPS Monument Types, Earth Scope, Project Highlight, http://www.earthscope.org/articles/PBO_GPS_monument, (accessed on June 18, 2018)
Bastos L., M. Bos and R. M. Fernandes (2010), Deformation and Tectonics: Contribution of GPS Measurements to Plate Tectonics – Overview and Recent Developments, In: Sciences of Geodesy G. Xu (Ed), 10.1007/978-3-642-11741-1_5
Bawden, G.W., W. Thatcher, R. S. Stein, K. W. Hudnut, G. and Peltzer, (2001). Tectonic contraction across Los Angeles after removal of groundwater pumping effects: Nature, v. 412, p. 812-815.
Bayona G., A. Cardona, C. Jaramillo, A. Mora, C. Montes, V. Caballero, H. Mahecha, F. Lamus, O. Montenegro, G. Jiménez, A. Mesa and V. Valencia, (2013). Onset of fault reactivation in the Eastern Cordillera of Colombia and proximal Llanos Basin; response to Caribbean–South American convergence in early Palaeogene time. Geological Society, London, Special Publications published online March 8, 2013 as doi: 10.1144/SP377.5
Benz, H. M., A. C. Tarr, G. P. Hayes, A. Villaseñor, K. P. Furlong, R. L. Dart, and S. Rhea, (2011), Seismicity of the Earth 1900–2010, Caribbean plate and vicinity, U.S. Geological Survey Open-File Report 2010–1083-A, scale 1:8,000,000.
Bernal-Olaya, R., P. Mann, C.A. Vargas, (2015). Earthquake, tomographic, seismic reflection, and gravity evidence for a shallowly dipping subduction zone beneath the Caribbean margin of northwestern Colombia, in C. Bartolini and P. Mann eds, Petroleum Geology and Potential of the Colombian Caribbean Margin, AAPG Memoir 108, ISBN 13: 978-0-89181-388-0, 247-270.
Bertiger W., S. Desai, B. Haines, N. Harvey, A. Moore, S. Owen, J. Weiss., (2010). Single Receiver Phase Ambiguity Resolution with GPS Data. Journal of Geodesy. DOI: 10.1007/s00190-010-0371-9.
Bevis M., S. Businger, T. A. Herring, C. Rocken, R. A. Anthes y R. H. Ware, (1992), GPS Meteorology: Remote Sensing of Atmospheric Water Vapor Using the Global Positioning System, Journal of Geophysical Research 97: 15787–15801, DOI: 10.1029/92JD01517
Bevis M., J. Bedford and D. Caccamise II, (2020), The Art and Science of Trajectory Modelling, In Geodetic Time Series Analysis in Earth Sciences, J.-P. Montillet and M. S. Bos (eds)., Springer Geophysics, Springer Nature Switzerland AG 2020, 1-27, https://doi.org/10.1007/978-3-030-21718-1_1
Bezada, M. J., A. Levander, and B. Schmandt (2010), Subduction in the southern Caribbean: Images from finite frequency P wave tomography, J. Geophys. Res., 115, B12333, doi:10.1029/2010JB007682.
Bilek, S. L., and Lay, T., 2018, Subduction zone megathrust earthquakes: Geosphere 14 (4): 1468–1500, https:// doi .org /10 .1130 /GES01608.1
Bilham R., R. S. Yeats, S. Zerbini, S., (1989). Space geodesy and global forecast of earthquakes, EOS Transactions, Am. Geophys. Un. 70, 65-73.
Blewitt G., W. C. Hammond, and C. Kreemer, (2009, Geodetic observation of contemporary deformation in the northern Walker Lane: 1. Semipermanent GPS

strategy, in Oldow, J. S., and Cashman, P.H., eds., Late Cenozoic Structure and Evolution of the Great Basin–Sierra Nevada Transition: Geological Society of America Special Paper 447, p. 1–15, doi: 10.1130/2009.2447(01).

Blewitt G., (2009), GPS and Space-Based Geodetic Methods, In: Treatise on Geophysics: Geodesy, Vol 3, G. Schubert (Ed), Elsevier, Amsterdam, 351-390

Blewitt G., Lavallée D., (2002). Bias in Geodetic Site Velocity due to Annual Signals: Theory and Assessment, in: Ádám J., Schwarz KP. (Eds.), Vistas for Geodesy in the New Millennium. International Association of Geodesy Symposia. 125. Springer, Berlin, Heidelberg.

Blewitt G., and D. Lavallée (2002), Effect of annual signals on geodetic velocity, J. Geophys. Res., 107(B7), B72145, doi:10.1029/2001JB000570.

Blewitt G., (1990), An Automatic Editing Algorithm for GPS Data, Geophys. Res. Lett. 17(3), 199-202, doi.org/10.1029/GL017i003p00199

Blume F., H. Berglund, K. Feaux, K. Austin, T. Dittman, C. Walls, H. Mattioli and T. Herring, (2013), Stability of GNSS Monumentation: Analysis of co-located monuments in the Plate Bpundary Observatory, AGU Fall Meeting, G5IB-04

Boehm, J., B. Werl, and H. Schuh (2006), Troposphere mapping functions for GPS and very long baseline interferometry from European Centre for Medium-Range Weather Forecasts operational analysis data, J. Geophys. Res., 111, B02406, doi:10.1029/2005JB003629.

Bogusz J., S. Rosat, A. Klos and A. Lenczuk (2018), On the noise characteristics of time series recorded with nearby located GPS receivers and superconducting gravity meters, Acta Geod Geophys (2018) 53:201–220, doi.org/10.1007/s40328-018-0212-5

Bos M. S., J.-P. Montillet, S.D.P. Williams and R.M.S. Fernandes (2020), Introduction to Geodetic Time Series Analysis, In Geodetic Time Series Analysis in Earth Sciences, J.-P. Montillet and M. S. Bos (eds)., Springer Geophysics, Springer Nature Switzerland AG 2020, 29-52, doi.org/10.1007/978-3-030-21718-1_2

Bos M. and R. Fernandes, (2016). Hector User Manual, version 1.6, 31 p.

Bos M. S., R.M.S. Fernandes, S.D.P. Williams and L. Bastos, (2013). Fast Error Analysis of Continuous GNSS Observations with Missing Data. J. Geod., Vol 87 (4), 351-360, doi:10.1007/s00190-012-0605-0.

Bos M. S, Bastos L, Fernandes R.M.S., 2010. The influence of seasonal signals on the estimation of the tectonic motion in short continuous GPS time-series", Journal of Geodynamics, Vol. 49(3-4), 205– 209, doi:10.1016/j.jog.2009.10.005.

Boschman, L.M., D. J. J. van Hinsbergen, T. H. Torsvik, W. Spakman, J. L. Pindell, (2014). Kinematic reconstruction of the Caribbean region since the Early Jurassic, Earth-Science Reviews 138, 102-136, doi.org/10.1016/j.earscirev.2014.08.007.

Box G., G. Jenkins and G. Reinsel, (2005), Time Series Analysis: Forecasting and Control, Wiley & Sons, New Jersey, 4th. Ed., 746 p.

Braun J., Mattioli G., Calais E., Carlson D., Dixon T. H., Jackson M., Kursinski R., Mora-Paez H., Miller M., Pandya R-. Robertson R., and Wang G., (2012). Focused Study of Interweaving Hazards Across the Caribbean, Eos, Vol. 93, No. 9: 89-90

Buttkus B. (2000), Spectral Analysis and Filter Theory in Applied Geophysics, Springer-Verlag Berlin, Heidelberg, 667 p.

Cannavo F. Nad M. Palano (2016), Defining Geodetic Reference Frame using Matlab: PlatEMotion 2.0, Pure Appl. Geophysi. 173:937-944

Cannavo and Palano (2011), PlatEmotion: A Matlab tool for Geodetic Reference Frame, Istituto Nazionale di Geofisica e Vulcanologia, Rapporti Tecnici 201, 13 p.

Case, J. E., and W. D. MacDonald, (1973), Regional gravity anomalies and crustal structure in northern Colombia, Geol, Soc. Am. Bull, 84: 2905-2916.

Case, J.E., S. Duran, R. A. Lopez and W. R. Moore (1971). Tectonic investigations in western Colombia and eastern Panama, Geol. Soc. Am. Bull. 82, 2685–2712.

Cediel, F., R.P. Shaw and C. Cáceres (2003). Tectonic assembly of the Northern Andean Block, in TheCircum-Gulf of Mexico and the Caribbean: Hydrocarbon habitats, basin formation, and plate tectonics C.Bartolini, R.T.Buffler and J. Blickwede, (editors) AAPG Memoir 79, 815–848.

Chlieh M., P.A. Mothes, J.M. Nocquet, P. Jarrin, P. Charvis, D. Cisneros, Y. Font, J. Y. Collot, J.C. Villegas-Lanza, F. Rolandone, M. Vallée, M. Regnier, M. Segovia, X. Martin and H. Yepes (2014). Distribution of discrete seismic asperities and aseismic slip along the Ecuadorian megathrust, Earth and Planetary Science Letters 400: 292–301

Coates, A. G., Collins, L.S., Aubry, M-P., Berggren, W. A., (2004). The geology of the Darien, Panama, and the late Miocene-Pliocene collision of the Panama arc with northwestern South America, Geological Society of America Bulletin, v. 116, p. 1327-1344., doi: 10.1130/B25275.1

Coates. A., Stallard R., (2013).How old is the Isthmus of Panama? Bulletin of Marine Science, 89(4), 801-813

Colleta, B., F. Hebrard, J. Letouzey, P. Werner, P., and J. L. Rudkiewicz, (1990), Tectonic style and crustal structure of the Eastern Cordillera, Colombia from a balanced cross - 121 - 7. References section, in Letouzey, J., ed., Petroleum and Tectonics in Mobile Belts: Paris, Editions Technip, pp 81-100.

Collot, J.-Y., P. Charvis, M.-A. Gutscher, and S. Operto, (2002), Exploring the Ecuador-Colombia active margin and interplate seismogenic zone, Eos Trans. AGU, 83, 185–190, 2002.

Combrinck W. L. and M. Schmidt, (1998), Physical Site Specifications: Geodetic Site Monumentation, Position Paper, IGS Network Systems Workshop
November 2-5, 1998 Annapolis, (accessed on June 18, 2018, http://www.hartrao.ac.za/geodesy/site_mon.htm)

Cooper, M.A., Addison, F. T., Alvarez, Coral, R. M., Graham, R. H, Hayward, A. B., Howe, S., Martinez, J., Naar, J., Peñ as, R., Pulham, A. J., Taborda, A., (1995). Basin development and tectonic history of the Llanos basin, Eastern Cordillera, and Middle Magdalena Valley, Colombia. AAPG Bulletin 79 (10), 1421-1443.

Corredor F., (2003). Seismic strain rates and distributed continental deformation in the northern Andes and three-dimensional seismotectonics of northwestern South America, Tectonophysics 372 (3–4), 147-166

Cortes, M. and J. Angelier, (2005). Current states of stress in the northern Andes as indicated by focal mechanism of earthquakes. Tectonophysics 403:29-58.

Cox A. and R. B. Hart, (2009). Plate Tectonics. How it Works. John Wiley & Sons, New York, NY, 392 p.

Crespo, E., K. K. Nyman, T. D. O'Rourke, (1987). Ecuadorean Earthquakes of March 5, 1987, Earthquake Engineering Research Institute, Special Earthquake Report 4

Davis J. L., Y. Fialko, W. E. Holt, M. M. Miller, S. E. Owen, and M. E. Pritchard (Eds.) (2012), A Foundation for Innovation: Grand Challenges in Geodesy, Report

from the Long-Range Science Goals for Geodesy Community Workshop, UNAVCO, Boulder, Colorado, 79 pp.
DeMets, C., Gordon, R. G., Argus, D. F., and Stein, S., (1990). Current plate motions: Geophysical Journal International, v. 101, p. 425-478.
DeMets, C., R. G. Gordon, D. F. Argus, (2010). Geologically current plate motions. Geophysical Journal International, 181: 1–80. doi: 10.1111/j.1365-246X.2009.04491.x
DeMets, C., R. G. Gordon, D.F. Argus, and S. Stein, (1994). Effect of recent revisions to the geomagnetic reversal time scale on estimates of current plate motions. Geophys. Res. Lett., 21: 2191–2194. doi:10.1029/94GL02118
Dengo, C., Covey, M., (1993). Structure of the Eastern Cordillera of Colombia: implications for trap styles and regional tectonics. AAPG Bulletin 77 (8), 1315-1337.
DesRoches R., M. Comerio, M. Eberhard, W. Mooney, G. J. Rix, (2011) Overview of the 2010 Haiti Earthquake. Earthquake Spectra: October 2011, Vol. 27 (S1), S1-S21. https://doi.org/10.1193/1.3630129
Dewey, J. W., (1972). Seismicity and tectonics of western Venezuela, Bull. Seismol. Soc. Am., 62, 1711-1751.
Dixon T. H., M. P. Golombek, and C. L. Thornton, (1985), Constraints on Pacific plate kinematics and dynamics with Global Positioning System measurements, IEEE Trans. Geosci. & Remote Sensing GE-23, 491-50
Dixon T. H. and S. K. Wolf, (1990a).Some Tests of Wet Tropospheric Calibration for the CASA UNO Global Positioning System experiment, Geophys. Res. Lett. 17 (3), 203-206.
Dixon, T. H., D. M. Tralli, G. Blewitt, and J.P. Dawson, (1990b), Geodetic baselines across the Gulf of California using the Global Positioning System, in Gulf and Peninsular Province of the Californias, edited by J.P. Dauphin, Memoir 47, American Association of Petroleum Geologists, Tulsa, Okla.
Dixon, T. H., G. Gonzalez, E. Katsigris, and S. M. Lichten, (1991a), First epoch geodetic measurements with the Global Positioning System (GPS) across the northern Caribbean plate boundary, J. Geophys. Res. 96 (B2): 2397-2415, doi.org/10.1029/90JB02003
Dixon, T.H., (1991b), An introduction to the Global Positioning System and some geological applications, Rev. Geophys., 29, No. 2, pp. 249-276.
Dixon T., R. Robertson, J. Braun, E. Calais, D. Carlson, M. Jackson, R. Kursinski, G. Mattioli, M. M. Miller, H. Mora-Paez, R. Pandya and G. Wang, (2011), Report on the activities of the COCONet Workshop for Community Science, Station Siting, and Capacity Building, February 2-4, 2011, San Juan, Puerto Rico
Dixon, T. H., (1993). GPS measurement of relative motion of the Cocos and Caribbean plates and strain accumulation across the Middle America trench: Geophysical Res. Letters 20, 2167-2170.
Dixon, T. H., G. Gonzalez, S. M. Lichten, and E. Katsigris, (1991). First epoch geodetic measurements with the Global Positioning System across the Northern Caribbean Plate Boundary Zone, J. Geophys. Res., 96(B2), 2397–2415, doi:10.1029/90JB02003.
Dockter, S., D. Elliot, F. Wyatt, J. Galetzka, K. Hudnut, SCIGN Short Drilled-Braced Geodetic Monument, https://www.scign.org/arch/sdb_monument.htm, (accessed on June 8, 2018)

Doglioni C. and F. Riguzzi (2017), The space geodesy revolution for plate tectonics and earthquake studies, Satellite Positioning for Geosciences Conference, Rend. Fis. Acc. Lincei, DOI 10.1007/s12210-017-0639-6

Duong N. A., T. Sagiya, F. Kimata, T. D. To, V. Q. Hai, D. C. Cong, N. X. Binh and N. D. Xuyen (2013), Contemporary horizontal crustal movement estimation for northwestern Vietnam inferred from repeated GPS measurements, Earth Planets Sp 65: 1399-1410, https://doi.org/10.5047/eps.2013.09.010

Duque-Caro H., (1979), Major structural elements and evolution of northwestern Colombia, in Watkins, J. S., and others, eds., Geological and Geophysical investigations of continental margins: American Association of Petroleum Geologists Memoir 29: 329-351.

EarthScope (2018), EarthScope: Exploring the Structure and Evolution of the North American Continent, http://www.earthscope.org (accessed on June 19, 2018)

ECMWF (2018), European Centre for Medium-Range Weather Forecasts, https://www.ecmwf.int (accessed on June 10, 2018)

Egbue O., and J. Kellogg (2010). Pleistocene to Present North Andean "escape", Tectonophysics, 489 (1-4), 248-257, doi:http://dx.doi.org/10.1016/j.tecto.2010.04.021.

Egbue O., and Kellogg, J., (2010). Pleistocene to Present North Andean "escape": Tectonophysics, v. 489, p. 248–257, doi: 10.1016/j.tecto.2010.04.021.

Egbue O., and Kellogg, J., (2012). Three-dimensional structural evolution and kinematics of the Piedemonte Llanero, Central Llanos foothills, Eastern Cordillera, Colombia, Journal of South American Earth Sciences, doi:10.1016/j.jsames.2012.04.012

Egbue O., J. Kellogg, H. Aguirre and C. Torres (2014). Evolution of the stress and strain fields in the Eastern Cordillera, Colombia. J. Structural Geology, 58, 8-21.

Ego F., M. Sebried, A. Lavenu, H. Yepez and A. Eguez (1993). A new geodynamical model for the northern Ecuador Andes, EUG VII, 4-8 April 1933, Terra abstract 5 (1), 203.

Ego F., M. Sebrier, A. Lavenu, H. Yepes, and A. Egues, (1996). Quaternary state of stress in the Northern Andes and the restraining bend model of the Ecuadorian Andes. Tectonophysics 259,101–116.

Elliot J. R., R. J. Walters and T. J. Wright (2016), The role of space-based observation in understanding and responding to active tectonics and earthquakes, Nat. Commun. 7: 13844, doi: 10.1038/ncomms13844.

England P. and D. McKenzie (1982), A thin viscous sheet model for continental deformation, Geophys. J. R. astr. Soc. 70, 295-321

Estey L. H. and C. M. Meertens, (1999), TEQC: The Multi-Purpose Toolkit for GPS/GLONASS Data, L. H. Estey and C. M. Meertens, GPS Solutions 3 (1) 42-49, John Wiley & Sons, doi:10.1007/PL00012778

Fernandes R. M. S. , H. Mora-Páez, P. LaFemina, M. Bos, (2016), Present-day GPS velocity field of South America, Proceedings IASPEI Regional Assembly Latin-American Seismological Comission-LACSC, Seismology for Science and Science for Society, Abstract O190, p. 118, San José de Costa Rica, June 20-22, 2016

Fernandes R. M. S., pers. comm.

Fernandes R. M. S., M. Bos, A. Alothman, H. Mora-Páez, (2017), Comparing Global and Dedicated Plate Angular Velocity Models: the cases of Arabia and South

America, Abstract G04-4-02, IAG Symposia » G04. Earth rotation and geodynamics, IAG-IASPEI Joint Meeting, Kobe International Center, Kobe, Japan, July30-August 4, 2017

Förste, C., Bruinsma, S. L., Abrikosov, O., Lemoine, J.-M., Marty, J. C., Flechtner, F., Balmino, G., Barthelmes, F., Biancale, R. (2014): EIGEN-6C4 The latest combined global gravity field model including GOCE data up to degree and order 2190 of GFZ Potsdam and GRGS Toulouse. DOI: http://doi.org/10.5880/ICGEM.2015.1

Freymueller, J.T. and J.N. Kellogg, (1990). The extended tracking network and indications of baseline precision and accuracy in the North Andes, CASA UNO Special Issue, Geophysical Research Letters, 17, 207-210.

Freymueller, J.T., J. N. Kellogg, and V. Vega (1993). Plate Motions in the North Andean region, J. Geophys. Res. 98 (B12), 21853-21863.

Gailler A., P. Charvis and E. Flueh (2007), Segmentation of the Nazca and South American plates along the Ecuador subduction zone from wide angle seismic profiles, Earth and Planetary Science Letters 260:444–464, DOI: 10.1016/j.epsl.2007.05.045

GeoNet, (2018), Geological Hazard Information for New Zealand, https://www.geonet.org.nz/about, (accessed on December 8, 2018).

GGOS, 2018, GGOS Atmosphere Project, http://ggosatm.hg.tuwien.ac.at, (accessed on June 10, 2018)

Goudarzi M.A., M. Cocard, R. Santerre (2015), Noise behavior in CGPS position time-series: The eastern North America case study. J. Geod. Sci. 5 (1), doi.org/10.1515/jogs-2015-0013

Goudarzi M.A., M. Cocard, R. Santerre (2014), EPC: Matlab software to estimate Euler pole parameters, GPS Solut. 18:153–162, DOI 10.1007/s10291-013-0354-4

Gregory-Wodzicki, K.M., (2000). Andean paleoelevation estimates: A review and critique. GSA Bulletin 112, 1091-1105.

GSI, (2018), Geodetic Survey, http://www.gsi.go.jp/ENGLISH/page_e30030.html (accessed on December 8, 2018)

Gutscher, M. A., Malavieille, J., Lallemand, S., Collot, J. Y., (1999). Tectonic segmentation of the North Andean margin; impact of the Carnegie Ridge collision. Earth Planet. Sci. Lett. 168, 255-270.

Hackl M., R. Malservisi, U. Hugentobler, and R. Wonnacott (2011), Estimation of velocity uncertainties from GPS time series: Examples from the analysis of the South African TrigNet network, J. Geophys. Res., 116, B11404, doi:10.1029/2010JB008142.

Hatanaka, Y. (2008), A Compression Format and Tools for GNSS Observation Data, Bulletin of the Geographical Survey Institute, 55, 21-30 http://www.gsi.go.jp/common/000045517.pdf

Haug, G., Tiedemann R., Zahn R., Ravelo A. C., (2001). Role of the Panama uplift on oceanic freshwater balance, Geology 29, 207–210, doi.org/10.1130/0091-7613(2001)029<0207:ROPUOO>2.0CO;2

Hayes G., (2018), Slab2, A Comprehensive Subduction Zone Geometry Model: U.S. Geological Survey data release, https://doi.org/10.5066/F7PV6JNV.

Helmens, K. F., and T. Van der Hammen (1994), The Pliocene and Quaternary of the high plain of Bogotá (Colombia): A history of tectonic uplift, basic development and climatic change, Quat. Int., 21, 41–61.

Herd D., (1986), The 1985 Ruiz Volcano Disaster, EOS Transactions 67 (19), 457-460, AGU, https://doi.org/10.1029/EO067i019p00457-03
Hermelin, M. (2005). Desastres de Origen Natural en Colombia 1979–2004. Medellín, Colombia. Ed. Fondo editorial Universidad EAFIT, 247. ISBN: 958-8173-89-2.
Herring, T. A., T. I. Melbourne, M. H. Murray, M. A. Floyd, W. M. Szeliga, R. W. King, D. A. Phillips, C. M. Puskas, M. Santillan, and L. Wang (2016), Plate Boundary Observatory and related networks: GPS data analysis methods and geodetic products, Rev. Geophys., 54, 759–808, doi:10.1002/2016RG000529.
He X., J-P. Montilletc, R. Fernandesd, M. Bos, K. Yu, X. Hua, W. Jiang, (2017), Review of current GPS methodologies for producing accurate time series and their error sources, J. Geodynamics 106: 12–29, doi:10.1016/j.jog.2017.01.004
Hey, R., (1977). Tectonic evolution of the Cocos–Nazca spreading center, Geol. Soc. Am. Bull., 88: 1404-1420
Hudnut K. W., Y. Bock, J. E. Galetzka, F. H. Webb and W. Young (2002), The Southern California Integrated GPS Network (SCIGN), In: Seismotectonics in Convergente Plate Boundary, Eds. Y. Fujinawa and A. Yoshida, TerraPub, Tokyo, 166-189.
ICSM, (2014), Guideline for Continuously Operating Reference Stations Special Publication 1, version 2.1, Intergovernmental Committee on Survey and Mapping (ICSM) Permanent Committee on Geodesy (PCG), Australia, 43 p.
Idárraga-García, J., J.-M. Kendall, and C. A. Vargas (2016), Shear wave anisotropy in northwestern South America and its link to the Caribbean and Nazca subduction geodynamics, Geochem. Geophys. Geosyst., 17, doi:10.1002/2016GC006323.
IGS, (2018), Strategic Plan 2017, WDS-IUGG-GOGOS, 44 p.
IGS, (2017), Current IGS Site Guidelines, International GNSS Service, https://kb.igs.org/hc/en-us/articles/202011433-Current-IGS-Site-Guidelines, (accessed on June 18, 2018)
IRIS, (2016), Magnitude 7.8 near the coast of Ecuador, 11 p.
Isacks, Bryan, Jack Oliver, and Lynn R. Sykes, 1968. Seismology and the new global tectonics. J. Geophys. Res. 73 (18):5855-5899. ISSN 2156-2202. doi: 10.1029/JB073i018p05855.
Johnson H.O. and D.C. Agnew, (1995), Monument motion and measurements of crustal velocities. Geophys Res Letters 22(21):2905–2908, DOI 10.1029/95GL02661
Jordan, T. H., (1975), The present-day motions of the Caribbean plate, J. Geophys. Res., 80: 4433-4439.
Julivert, M., (1970), Cover and basement tectonics in the Cordillera oriental of Colombia, South America, and a comparison with some other folded chains, GSA Bulletin 81 (12): 3623-3646, https://doi.org/10.1130/0016-7606(1970)81[3623:CABTIT]2.0.CO;2
Kall T., T. Oja, K. Kollo and A. Liibusk (2019), The Noise Properties and Velocities from a Time-Series of Estonian Permanent GNSS Stations, Geosciences 9, 233, doi:10.3390/geosciences9050233
Kanamori H. and K. C. McNally (1982), Variable rupture mode of the subduction zone along the Ecuador-Colombia coast, Bull. Seism. Soc. A, 72, 1241-1253
Kanamori, H., (1983). Magnitude scale and quantification of earthquakes, Tectonophysics 93:185-199
Kellogg J. N. and W. E. Bonini, (1982), Subduction of the Caribbean Plate and basement uplifts in the overriding South America plate. Tectonics 1(3): 251-276.

Kellogg, J. N. & Bonini, W. E. (1985). Reply to comment on "Subduction of the Caribbean plate and basement uplifts in the overriding South American plate". Tectonics, 4 (7): 785-790.

Kellogg J. N. (1984). Cenozoic tectonic history of the Sierra de Perijá, Venezuela–Colombia, and adjacent basins, in W. Bonini, R. Hargraves, and R. Shagam, eds., The Caribbean–South American plate boundary and regional tectonics: GSA Memoir 162: 239–261.

Kellogg J. N., I. J. Ogujioford, D. R. Kansakar, (1985). Cenozoic tectonics of the Panama and North Andes blocks. Memorias Congreso Latinoamericano de Geología 6: 34-49, INGEOMINAS, Bogotá.

Kellogg J. N., and T.H. Dixon (1990), Central and South America GPS Geodesy - CASA UNO. Geophys. Res. Lett. 17 (3): 195–198, doi:10.1029/GL017i003 p00195.

Kellogg J. N., J. T. Freymueller, T. H. Dixon, R. E. Neilan, C. Ropain U., S. Camargo M., B. Fernandez C., J. L. Stowell, A. Salazar, J. Mora. V., L. Espin, V. Perdue, L. Leos, (1990). First GPS baseline results from the North Andes, Geophys. Res. Lett. 17:211-214.

Kellogg J., V. Vega V., (1995). Tectonic development of Panama, Costa Rica, and the Colombian Andes: Constraints from Global Positioning System geodesy studies and gravity., in Mann P. ed., Geologic and Tectonic Development of the Caribbean Plate Boundary in Southern Central America: Boulder, Colorado, Geological Society of America Special Paper 295

Kellogg J. N. and W. Mohriak (2001), Tectonic and geological environment of coastal South America. In: Seeliger, U. and Kjerfve, B. (eds.) Coastal Marine Ecosystems of Latin America: Ecological Studies, 144: 1-16.

Kellogg J. N. and H. Mora-Páez, (2016), Panama Arc-North Andes collision: Broken indenter model from new GPS velocity field, IASPEI - Regional Assembly (Latin-American and Caribbean Seismological Commission - LACSC), San José, Costa Rica.

Kellogg, J. N, G. B. Franco and H. Mora-Páez, (2019), Cenozoic tectonic evolution of the North Andes with constraints from volcanic ages, seismic reflection, and satellite geodesy, In “Andean Tectonics” (eds. B. K. Horton and A. Folguera), 69-102, Elsevier.

Kobayashi D., P. LaFemina, H. Geirsson, E. Chichaco, A. Abrego, H. Mora and E. Camacho, (2014). Kinematics of the Western Caribbean: Collision of the Cocos Ridge and Upper Plate Deformation, Geochem. Geophys. Geosyst. 15, 1671-1683, doi:10.1002/2014GC005234.

Kroehler M., P. Mann, A. Escalona and G. L. Christeson (2011), Late Cretaceous-Miocene diachronous onset of back thrustingalong the South Caribbean deformed belt and its importancefor understanding processes of arc collision and crustal growth, Tectonics 30, TC6003, doi:10.1029/2011TC002918

Ladd, J. W., M. Truchan, M. Talwani, P. L. Stoffa, P. Buhl, R. Houtz, A. Mauffret, G. K. Westbrook, (1984). Seismic reflection profiles across the southern margin of the Caribbean, Bonini, W. E. (editor), R. B. Shagam, R. (Eds), The Caribbean-South American plate boundary and regional tectonics, Memoir - Geological Society of America, 153-159.

Langbein, J., F. Wyatt, H. Johnson, D. Hamann, and P. Zimmer, (1995), Improved stability of a deeply anchored geodetic monument for deformation monitoring, Geophys. Res. Lett., 22, 3533–3536

Langbein J. (2004), Noise in two-color electronic distance meter measurements revisited. J Geophys Res 109:B04406, DOI 10.1029/2003JB002819
Langbein, J. (2008), Noise in GPS displacement measurements from Southern California and Southern Nevada, J. Geophys. Res., 113, B05405, doi:10.1029/2007JB005247.
Langley R., (2018), Innovation: The International GNSS Service, GPS World, https://www.gpsworld.com/the-international-gnss-service-25-years-on-the-path-to-multi-gnss/ (accessed on January 20, 2019)
Li X., X. Zhang and B. Guo, (2013), Application of collocated GPS and seismic sensors to earthquake monitoring and early warning. Sensors (Basel, Switzerland), 13(11), 14261-76. doi:10.3390/s131114261
Londoño J. M., S. Quintero, K. Vallejo, F. Muñoz and J. Romero (2019), Seismicity of Valle Medio del Magdalena basin, Colombia, Journal of South American Earth Sciences 92 (2019) 565–585, https://doi.org/10.1016/j.jsames.2019.04.003
Lonsdale P., and K. D. Klitgord, (1978). Structure and tectonic history of the eastern Panama Basin. GSA. Bulletin 89, 981–999.
Lundgren, P., M. Protti, A. Donnellan, M. Heflin, E. Hernandez, D. Jefferson, (1999). Seismic cycle and plate margin deformation in Costa Rica: GPS observations from 1994 to 1997, J. Geophys. Res., 104(B12): 28,915-28,926.
Manaker D. M., E. Calais, A. M. Freed, S. T. Ali, P. Przybylski, G. Mattioli, P. Jansma, C. Prépetit, J. B. De Chabalier (2008). Interseismic Plate coupling and strain partitioning in the Northeastern Caribbean, Geophys. J. Int. 174 (3), 889–903, doi: 10.1111/j.1365-246X.2008.03819.x
Mann, P. and R. A. Kolarsky, (1995). East Panama deformed belt; structure, age, and neotectonic significance. In: Mann P. (ed.) Geologic and Tectonic Development of the Caribbean Plate Boundary in Southern Central America, Geol. Soc. Am. Special Paper, 295: 111-130.
Mantilla-Pimiento A. M., G. Jentzsch, J. Kley and C. Alfonso-Pava (2009), Configuration of the Colombian Caribbean Margin: Constraints from 2D Seismic Reflection data and Potential Fields Interpretation, In Subduction Zone Geodynamics, S. Lallemand and F. Funiciello (eds.), Frontiers in Earth Sciences, Springer-Verlag Berlin Heidelberg, DOI 10.1007/978-3-540-87974-9
Marshall, L. G., S. D. Webb, J. J. Sepkoski and D. M. Raup, (1982). Mammalian evolution and the Great American Interchange, Science, 215(4538), 1351–1357.
Masters T. G and P. M. Shearer (1995), Seismic Models of the Earth: Elastic and Anelastic, In: Global Earth Physics: A Handbook of Physical Constants, AGU Reference Shelf, T. Aherens (Ed.), 88-103, https://doi.org/10.1029/RF001p0088
McCaffrey, R., (1996). Estimates of modern arc-parallel strain rates in fore arcs. Geology 24, 27-30.
McCaffrey, R., (2002). Crustal block rotations and plate coupling. In: Stein, S., Freymueller, J. (Eds.), Plate Boundary Zones. AGU Geodynamics Series 30, 101-122.
McCaffrey, R., (2005). Block kinematics of the Pacific - North America plate boundary in the southwestern US from inversion of GPS, seismological, and geologic data, Journal of Geophysical Research 110, B07401, doi:10.1029/2004JB003307
Meilano I., H. Abidin, Andreas, I. Gumilar, Sarsito, R. Hanifa, Rino, Harjono, T. Kato, Kimata, and Y. Fukuda, 2012,"Slip Rate Estimation of the Lembang Fault West Java from Geodetic Observation," J. Disaster Res., Vol.7, No.1, pp. 12-18

Mégard, F., (1987), Cordilleran Andes and Marginal Andes: A review of Andean geology north of the Arica Elbow (18°S), In: Circum-Pacific Orogenic Belts and Evolution of the Pacific Ocean Basin, J. W. H. Monger and J. Francheteau (Eds), AGU Geodynamics Series 18: 71-95, Washington, USA

Meyer, R. P., W. D. Mooney, A. L. Hales, C. Helsley, G. P. Woollard, D. M. Hussong, L. W. Kroenke, J. E. Ramirez (1976), Project Nariño III: Refraction Observation Across a Leading Edge, Malpelo Island to the Colombian Cordillera Occidental. The geophysics of the Pacific Ocean Basin and its margin, 105-132. 10.1029/GM019p0105.

Molnar P. and L. Sykes, (1969). Tectonics of the Caribbean and Middle America Regions from Focal Mechanism and Seismicity. GSA Bull. 80: 1639-1684

Molnar P., (2018), Molnar, P. (2018), Simple concepts underlying the structure, support and growth of mountain ranges, high plateaus and other high terrain, in Mountains, Climate, and Biodiversity, edited by C. Hoorn, A. Perrigo, and A. Antonelli, Wiley, 17-36.

Montes, C., Cardona A., Jaramillo C., Pardo A., Silva J.C., Valencia V., Ayala C., Perez-Angel L.C., Rodriguez-Parra L.A., Ramirez V., Nino H., (2015). Middle Miocene closure of the Central American Seaway, Science, v. 348, 6231, 226-229.

Montes, C., G. Bayona, A. Cardona, D.M Buchs, C. A. Silva, S. Morón, N. Hoyos, D. A. Ramírez, C. A. Jaramillo, V. Valencia, (2012). Arc-continent collision and orocline formation: Closing of the Central American seaway, Journal of Geophysical Research, v. 117, B04105, doi:10.1029/2011JB008959, 2012.

Montillet J.-P., P. Tregoning, S. McClusky and K. Yu., (2013), Extracting white noise statistics in GPS coordinate time series, IEED Geoscience and Remote Sensing Letters 10 (3): 563-567.

Mora A., Ketcham R.A., Higuera-Diaz I. C., Bookhagen B., Jimenez L., Rubiano, (2014). Formation of passive-roof duplexes in the Colombian Subandes and Peru, Lithosphere 6 no. 6, 456 – 472.

Mora Páez H., S. López., N. Acero, J. Ramírez C., E. Salcedo y R. Trenkamp, (2015), Análisis geodésico y deformación sismotectónica asociada al sismo de Quetame, Colombia, 24 de mayo de 2008. Boletín Geológico 43: 7-22, Bogotá ISSN 0120-1425

Mora-Páez H., (1994), Centro de Investigaciones y Procesamiento GPS, Fase 1, Propuesta de Proyecto, (in spanish, submitted to the Geophysics Sub-Directorate, internal communication).

Mora-Páez H., (1995), Central and South America GPS Geodesy: Relative Plate Motions Determined From 1991 and 1994 Measurements in Colombia, Costa Rica, Ecuador, Panama and Venezuela, M.S. Thesis, University of South Carolina, Columbia, 94 p.

Mora-Páez H., (2001), Geodesia aplicada: Geodesia Tectónica y Volcánica, Plan de Trabajo 1.0, (in Spanish), Submitted to the Geophysics Sub-Directorate, internal communication, April 24, 2001.

Mora-Páez H., (2002), The Nationwide Permanent GPS Array in Colombia, South America, for Geodynamics and Disasters Prevention Purposes, 13 p.

Mora-Páez H., (2006). National GPS Network for Geodynamics Research, BPIN document and supplementary information, Project Proposal, (in Spanish), submitted to the National Planning Department, Colombia, INGEOMINAS, 63 p. + 5 modules

Mora-Páez H., (2013), Utilizing Space Geodetic Techniques (GPS/GNSS) to Observe and Model Crustal Deformation in South America, Regional Model of Seismic Hazard in South America, SARA Project Workshop, GEM (Global Earthquake Model), Topic 5: Crustal Deformation from GPS/GNSS in S.A., Bogota, Colombian Geological Survey, December 4-6, 2013

Mora-Páez H., D. J. Mencin, P. Molnar, H. Diederix, L. Cardona-Piedrahita, J.-R. Peláez-Gaviria and Y. Corchuelo-Cuervo, (2016). GPS velocities and the construction of the Eastern Cordillera of the Colombian Andes, Geophys. Res. Lett., 43, 8407-8416, doi:10.1002/2016GL069795

Mora-Páez H., J.-R. Peláez-Gaviria, H. Diederix, O. Bohórquez-Orozco, L. Cardona-Piedrahita, Y. Corchuelo-Cuervo, J. Ramírez-Cadena and F. Díaz-Mila, (2018). Space Geodesy Infrastructure in Colombia, Seismological Research Letters, Early Edition, Focus Section on Geophysical Networks and Related Developments in Latin America Published Online 14 February, 2018

Mora-Páez, H., J. N. Kellogg, J. T. Freymueller, D. Mencin, R. M. S. Fernandes, H. Diederix, P. LaFemina , L. Cardona-Piedrahita, S. Lizarazo, J.-R. Peláez-Gaviria, F. Díaz-Mila, O. Bohórquez-Orozco, L. Giraldo-Londoño,Y. Corchuelo-Cuervo, (2017). Crustal deformation in the northern Andes – Space geodesy velocity field, Submitted to Tectonophysics

Mora, A., Parra M., Strecker M.R., Sobel E. R., Hooghiemstra H., Torres V., Vallejo Jaramillo J., (2008). Climatic forcing of asymmetric orogenic evolution in the Eastern Cordillera of Colombia, GSA Bulletin, v. 120, no. 7/8, p. 930-949.

Mora, A., Horton, B. K., Mesa, A., Rubiano, J., Ketcham, R. A., Parra, M., Blanco, V., Garcia, D., Stockli, D. F., (2010a). Migration of Cenozoic deformation in the Eastern Cordillera of Colombia interpreted from fission track results and structural relationships: Implications for petroleum systems, AAPG Bulletin, v. 94, no. 10, 1543-1580, doi:10.1306/01051009111.

Mora A., Parra, M., Strecker, M. R., Sobel, E. R., Zeilinger, G., Jaramillo, C., Da Silva, S., and Blanco, M., (2010b). The eastern foothills of the Eastern Cordillera of Colombia: An example of multiple factors controlling structural styles and active tectonics: Geological Society of America Bulletin, v. 112, p. 1846-1864, doi:10.1130/B30033.1

Morell, K. D. (2016), Seamount, ridge, and transform subduction in southern Central America, Tectonics, 35, 357–385, doi:10.1002/2015TC003950

Mothes P. A., F. Rolandone, J.-M. Nocquet, P. Jarrin, A. P. Alvarado, M. C. Ruiz, D. Cisneros, H. Mora-Páez & M. Segovia, (2017). Coseismic Surface Slip Recorded by Continuous and High Rate GPS during the 2016 Pedernales Mw 7.8 Earthquake, Northern Andes, Ecuador-Colombia, Seismological Research Letters, Early Edition, Focus Section on Geophysical Networks and Related Developments in Latin America Published Online 14 February, 2018

Mukul M., Sridevi J., Ansari K., Matin A. and Joshi V., (2018). Structural insights from geodetic Global Positioning System measurements in the Darjiling-Sikkim Himalaya. Journal of Structural Geology. 10.1016/j.jsg.2018.03.007.

Muller, R. and M. Seton (2014), Plate Motion. In Harff, J., Meschede, M., Petersen, S., Thiede, J. (Eds.), Encyclopedia of Marine Geosciences, 669-676. Netherlands: Springer Netherlands. http://dx.doi.org/10.1007/978-94-007-6644-0_131-1"

Muntendam-Bos, A. G., M. H. P. Kleuskens, M. Bakr, G. de Lange, and P. A. Fokker, (2009). Unraveling shallow causes of subsidence: Geophysical Research Letters, v. 36.

NASA (1991). Major Emphasis Areas for Solid Earth Science in the 1990s : Report of the NASA Coolfont Workshop, NASA Technical Memorandum 4256.

Neilan, R.E., T.H. Dixon, T.K. Meehan, W. G. Melbourne, J. A. Scheid, J. N. Kellogg, J. L. Stowell, (1989). Operational aspects of CASA UNO'88 – The first large scale international GPS Geodetic Network, IEEE Transactions on Instrumentation and Measurement, 38, no. 2, 648-651.

Nilsson, T., J. Böhm, D. D. Wijaya, A. Tresch, V. Nafisi, H. Schuh (2013). Path Delays in the Neutral Atmosphere. In: Böhm J., Schuh H. (editors): Atmospheric Effects in Space Geodesy. Springer Verlag, ISBN: 978-3-642-36931-5

Nishenko, S. P., (1989). Circum-Pacific Seismic Potential 1989-1999, Open File Report 89-89, US Geological Survey, 121 p.

Nistor S. and A. S. Buda (2016), The influence of different types of noise on the velocity uncertainties in GPS time series analysis, Acta Geodyn. Geomater. 13, No. 4 (184), 387–394, DOI: 10.13168/AGG.2016.0021

Nocquet, J., J.C. Villegas-Lanza, M. Chlieh, P. A. Mothes, F. Rolandone, P. Jarrin, D. Cisneros, A. Alvarado, L. Audin, F. Bondoux, X. Martin, Y. Font, M. Régier, M. Vallée, T. Tran, C. Beauval, J. M. Maguiña Mendoza, W. Martinez, H. Tavera, H. Yepes, (2014). Motion of continental slivers and creeping subduction in the Northern Andes, Nat. Geosci., 7 (4), 287–291, doi:10.1038/NGEO2099.

Nocquet, J.M., P. Jarrin, m. Vallée, P. A. Mothes, R. Grandin, F. Rolandone, B. Delouis, H. Yepes, Y. C. Font, D. Fuentes, M. Régnier, A. Laurendeau, D. Cisneros, S. Hernandez, A. Sladen, J. C. Singaucho, H. Mora, J. Gomez, L. Monte, P. Charvis, (2017). Supercycle at the Ecuadorian subduction zone revealed after the 2016 Pedernales earthquake. Nature Geoscience. 10, 145–149. doi:10.1038/ngeo2864.

Nocquet J.-M., (2008), Analysis of Geodetic Velocity Fields, Géosciences Azur, 14 p.

Norabuena E., T. Dixon, S. Stein and C. Harrison, (1999), Decelerating Nazca-South America and Nazca-Pacific Plate motions, Geophy. Res. Lett. 26 (22), 3405-3408-AGU, https://doi.org/10.1029/1999GL005394

Nugroho H., R. Harris, A. W. Lestariya, and B. Maruf, 2009, Plate boundary reorganization in the active Banda Arc–continent collision: insights from new GPS measurements. Tectonophysics 479, 52–65. https://doi.org/10.1016/j.tecto.2009.01.026.

O'Dea A., H. A. Lessios, A. G. Coates, R. I. Eytan, S. A. Restrepo-Moreno, A. L. Cione, L. S. Collins, A. de Queiroz, D. W. Farris, R. D. Norris, R. F. Stallard, M. O. Woodburne, O. Aguilera, M.-P. Aubry, W. A. Berggren, A. F. Budd, M. A. Cozzuol, S. E. Coppard, H. Duque-Caro, S. Finnegan, G. M. Gasparini, E. L. Grossman, K. G. Johnson, L. D. Keigwin, N. Knowlton, E. G. Leigh, J. S. Leonard-Pingel, P. B. Marko, N. D. Pyenson, P. G. Rachello-Dolmen, E. Soibelzon, L. Soibelzon, J. A. Todd, G. J. Vermeij, J. B. C. Jackson, (2016), Formation of the Isthmus of Panama, Sci. Adv. 2, e1600883

Ojeda J. and L. Donelly, (2006). Landslides in Colombia and their impact on towns and cities, In: 10th IAEG International Congress Proceedings, IAEG2006, Paper number 112, The Geological Society of London

OSO, (2018), Onsala Space Observatory, Chalmers University of Technology, http://holt.oso.chalmers.se/loading/tidemodels.html, (accessed on June 11, 2018)

Papamiditriou E., (1993). Long-term Earthquake Prediction along the Western Coast of South and Central America Based on a Time Predictable Model, Pure and Applied Geophysics 140 (2), 301-316 doi: 10.1007/BF00879409

Parra, M., Mora A., Jaramillo C., Strecker M. R., Sobel E. R., (2007). Cenozoic exhumation history in the northeastern Andes: New data based on low-T thermochronology and basin analysis in the Eastern Cordillera of Colombia, Geophys. Res. Abstr., 9, 07197.

Parra, M., Mora A., Sobel E.R., Strecker M.R., González R., (2009). Episodic orogenic-front migration in the northern Andes: Constraints from low-temperature thermochronology in the Eastern Cordillera, Colombia: Tectonics, v. 28, p. TC4004, doi:10.1029/2008TC002423.

Pennington, W.D., (1981).Subduction of the Eastern Panama Basin and Seismotectonics of Northwestern South America. J. Geophys. Res. 86 (B11), 10753–10770.

Pérez, O. J., Bilham R., Bendick R., Velandia J. R., Hernández N., Moncayo C., Hoyer M., and Kozuch M., (2001). Velocity field across the Southern Caribbean plate boundary and estimates of Caribbean/South-American plate motion using GPS geodesy 1994–2000, Geophys. Res. Lett., 28(15), 2987–2990.

Pindell, J. L., R. Higgsand, J. F. Dewey (1998). Cenozoic palinspastic reconstruction, paleogeographic evolution, and hydrocarbon setting of the northern margin of South America, In Paleogeographic Evolution and Non-glacial Eustasy, Northern South America, Pindell, J. L.and C. L. Drake (editors), Society for Sedimentary Geology, Tulsa, Oklahoma, 45–86

Pindell J. and L. Kennan, (2009), Tectonic evolution of the Gulf of Mexico, Caribbean and northern South America in the mantle reference frame: An update, Geological Society London Special Publications 328(1):1-55, http://dx.doi.org/10.1144/SP328.1

PNUD-CEPAL, (1999). El terremoto de enero de 1999 en Colombia: Impacto socioeconómico del desastre en la zona del Eje Cafetero, Programa de las Naciones Unidas para el Desarrollo–Colombia, Comisión Económica para América Latina y el Caribe – Sede Subregional en México, 18 p.

Poli P., G.A. Prieto, C. Q. Yu, M. Florez, H. Agurto-Detzel, T.D. Mikesell, G. Chen, V. Dionicio and P. Pedraza, (2015). Complex rupture of the M6.3 2015 March 10 Bucaramanga earthquake: evidence of strong weakening process, Geophys. J. Int. (2016) 205, 988–994 doi: 10.1093/gji/ggw065

Poveda, E., G. Monsalve and C. A. Vargas, (2015). Receiver functions and crustal structure of the northwestern Andean region, Colombia. Journal of Geophysical Research: Solid Earth, 120, 2408–2425. https://doi.org/10.1002/2014JB011304

Poveda, E., J. Julià, M. Schimmel and N. Perez-Garcia, (2018). Upper and middle crustal velocity structure of the Colombian Andes from ambient noise tomography: Investigating subductionrelated magmatism in the overriding plate. Journal of Geophysical Research: Solid Earth, 123. https://doi.org/10.1002/ 2017JB014688

Prieto, G.A., Beroza, G.C., Barrett, S.A., Lopez, G.A. & Florez, M., (2012). Earthquake nests as natural laboratories for the study of intermediate depth earthquake mechanics, Tectonophysics, 570, 42–56.

Pulido N., (2003). Seismotectonics of the Northern Andes (Colombia) and the Development of Seismic Networks, IISE Bulletin, 2003 Special Edition: 69-76.

Rockwell, T. K., R. A. Bennett, E. Gath, and P. Franceschi, (2010). Unhinging an indenter: A new tectonic model for the internal deformation of Panama, Tectonics, 29, TC4027, doi:10.1029/2009TC002571.

Rossello E., and S. P. Cossey (2012), What is the evidence for subduction in the Caribbean margin of Colombia?, XI Simposio Bolivariano: PETROLEUM EXPLORATION IN SUBANDEAN BASINS "Knowledge Integration - The key to success", Cartagena de Indias, Colombia, August 29th to September 1st, 2012, 8 p.

Rossello E., D. Barrero, J A. Osorio and J. F. Martinez (2015), El margen caribeño colombiano: es un análogo subexplorado del productor margen septentrional de Borneo (Malasia, Brunei)?, Memorias XV Congreso Colombiano de Geología 2015, "Innovar en Sinergia con el Medio Ambiente", Bucaramanga, Colombia, Agosto 31 – Septiembre 5, 2015, p. 305-310.

Rohm W., (2013), The ground GNSS tomography - unconstrained approach. Advances in Space Research 51: 501–513, DOI: 10.1016/j.asr.2012.09.021

Romero J., E. Castellanos, H. Alvarado, F. Muñoz, Y. Rodríguez, A. Amaya, D. León, D. Navarrete, A. Melo, C. Pava, R. Rodríguez, J. López, J. García (2017). Mapa de Unidades Tectónicas de Colombia, Servicio Geológico Colombiano, (spanish, in prep.).

Rudenko S, N. Schön, M. Uhlemann , and G. Gendt, (2013). Reprocessed height time series for GPS stations, Solid Earth 4: 23–41, doi:10.5194/se-4-23-2013

Ruhl, C. J., D. Melgar, R. Grapenthin, and R. M. Allen, (2017), The value of real-time GNSS to earthquake early warning, Geophys. Res. Lett., 44, 8311–8319, doi:10.1002/2017GL074502.

Ruegg J. C., Rudloff A., C. Vigny, R. Madariaga, de Chabalier J. B., J. Campos, E. Kausel, S. Barrientos, D. Dimitrov (2009), Interseismic strain accumulation Measured by GPS in the seismic gap between Constitución and Concepción in Chile, Physics. Earth and Planet. Int. 175: 78–85

Sagiya T., S. Miyazaki and T. Tada (2000), Continuos GPS Array and Present-day Crustal Deformation of Japan, Pure Appl. Geophys. 157:2303-23-22

Sagiya T., Nishimura T., Iio Y. and Tada T., (2002), Crustal deformation around the northern and central Itoigawa-Shizuoka Tectonic Line, EPS, 54, 1059–1063

Sagiya T., Nishimura T. and Iio Y., (2004), Heterogeneous crustal deformation along the central-northern Itoigawa-Shizuoka Tectonic Line Fault system, Central Japan, EPS 56, 1247–1252

Sagiya T., H. Kanamori, Y. Yagi, M. Yamada, and J. Mori, (2011), Rebuilding seismology, Nature, 473, 146–148, doi:10.1038/473146a

Sallares V. and P. Charvis, (2003), Crustal thickness constraints on the geodynamic evolution of the Galapagos volcanic province, Earth Planet. Sci .Lett. 214 (3–4), 545–559.

Santamaría-Gómez A., M.-N. Bouin, X. Collilieux, and G. Wöppelmann (2011), Correlated errors in GPS position time series: Implications for velocity estimates, J. Geophys. Res., 116, B01405, doi:10.1029/2010JB007701.

Saylor, J., Horton, B., Stockli, D., Mora, A., Corredor, J., (2012). Structural and thermochronological evidence for Paleogene basement-involved shortening in the axial Eastern Cordillera, Colombia: Journal of South American Earth Sciences, v. 39, p. 202-215.

Schubert, C., (1984). Basin formation along the Boconó-Morón-E1Pilar Fault System, Venezuela, J. Geophys. Res., 89: 5711-5718.

Schuster R., (1991). Introduction, In: The March 5, 1987, Ecuador Earthquakes: Mass Wasting and Socioeconomic Effects, Natural Disaster Studies, Volume 5, National Academy of Sciences, 184 p., ISBN 978-0-309-04444-8, doi:10.17226/1857

Schutz B. E., C. S. Ho, P. A. M. Abusali and B. D. Tapley (1990), CASA UNO GPS Orbit and Bseline experiments, Geophysical Research Letters, 17 (5): 643-646

Sepulchre, P., Arsouze T., Donnadieu Y., Dutay J.-C., Jaramillo C., Le Bras J., Martin E., C. Montes, and Waite A. J., (2014). Consequences of shoaling of the Central American Seaway determined from modeling Nd isotopes, Paleoceanography, 29, 176–189, doi:10.1002/2013PA002501.

Segall P., (2010), Earthquake and volcano deformation, Princeton Univ. Press, Princeton NJ.

Saeid E., K. B. Bakioglu, J. Kellogg, A. Leier, J. A. Martinez and E. Guerreo, (2017), Garzón Massif basement tectonics: Structural control on evolution of petroleum systems in upper Magdalena and Putumayo basins, Colombia, Marine and Petroleun Geology 88:381-401, http://dx.doi.org/10.1016/j.marpetgeo.2017.08.035

Sella G., T. H. Dixon and A. Mao (2002), REVEL: A model for Recent plate velocities from space geodesy, JGR 107 (B4) 2081, doi: 10.1029/2000JB000033, 2002

Servicio Geológico Colombiano, (2008). El sismo de Quetame del 24 de Mayo de 2008, Aspectos sismológicos y evaluación preliminar de daños, Informe preliminar No. 2, Bogotá, Junio de 2008, Red Sismológica Nacional (in spanish), 90 p.

Servicio Geológico Colombiano, (2015). El Sismo de la frontera Colombia-Panamá del 28 de Julio de 2015, Aspectos sismológicos y movimiento fuerte, Red Sismológica Nacional (in spanish), 17 p.

Servicio Geológico Colombiano, (2015), Mapa geológico de Colombia, Escala 1:1.000.000, Compilado por J. Gómez, N. Montes, A. Nivia y H. Diederix, (in spanish), 2 hojas, Bogotá, Colombia.

Silver, E. A., D. L. Reed, J. E. Tagudin, D. J. Heil, (1990). Implications of the north and south Panama thrust belts for the origin of the Panama orocline, Tectonics, 9(2): 261-281.

Silver, E. A., J. E. Case, H. J. MacGillavry, (1975). Geophysical study of the Venezuelan borderland, Geol. Soc. Am. Bull., 86, 213-226.

Spikings, R. A., W. Winkler, D. Seward and R. Handler (2001), Along-strike variations in the thermal and tectonic response of the continental Ecuadorian Andes to the collision with heterogeneous oceanic crust. Earth and Planetary Science Letters, 186: 57-73

Spikings, R., W. Winkler, R. Hughes, and R. Handler, R. (2005). Thermochronology of allochthonous terranes in Ecuador: Unravelling the accretionary and post-accretionary history of the Northern Andes, Tectonophysics, 399, 195-220.

Spikings, R. A., P. V. Crowhurst, W. Winkler, and D. Villagomez, (2010), Syn- and postaccretionary cooling history of the Ecuadorian Andes constrained by their in-situ and detrital thermochronometric record. Journal of South American Earth Sciences 30: 121-133

Stein, S. and Sella, G., (2002). Plate Boundary Zones: Concepts and Approaches, in Plate Boundary Zones, S. Stein, and J. Freymueller, eds, Geodynamics Series 30, American Geophysical Union, Washington, D.C., p. 1-26, 10.1029/030GD01.

Suter, F., M. Sartori, R. Neuwerth, G. Gorin, G., (2008). Structural imprints at the front of the Chocó–Panama indenter: Field data from the North Cauca Basin, central Colombia, Tectonophysics 460, 134-157.

Symithe, S., Calais E., de Chabalier J. B., Robertson R., and Higgins M., (2015). Current block motions and strain accumulation on active faults in the Caribbean, J. Geophys. Res. Solid Earth, 120, 3748–3774, doi:10.1002/2014JB011779.

Taboada, A., L. A. Rivera, A. Fuenzalida, A. Cisternas, P. Hervé, B. Harmen, J. Olaya, and C. Rivera, (2000). Geodynamics of the northern Andes: Subductions and intracontinental deformation (Colombia), Tectonics, 19, 787–813.

Teixell A., E. Teson, J. C. Ruiz and A. Mora, (2015), The structure of an inverted back-arc rift: Insights from a transect across the Eastern Cordillera of Colombia near Bogota, in C. Bartolini and P. Mann, eds., Petroleum geology and potential of the Colombian Caribbean Margin: AAPG Memoir 108, p. 499–516.

Tesón, E., et al. (2013), Relationship of Mesozoic graben development, stress, shortening magnitude, and structural style in the Eastern Cordillera of the Colombian Andes, Geol. Soc. London Spec. Publ., 377, 257–283.

Thatcher W., (1995). Microplate versus continuum descriptions of active deformation. Journal of Geophysical Research. 100. 3885-3894. 10.1029/94JB03064.

Thatcher W., (2009). How the Continents Deform: The Evidence from Tectonic Geodesy, Annu. Rev. Earth Planet. Sci. 2009.37:237-262. doi: 10.1146/annurev.earth.031208.100035

Thouret J.C., (1990), Effects of the November 13, 1985 eruption on the snow pack and ice cap of Nevado del Ruiz volcano, Colombia, J. Volcanology and Geothermal Research 41: 177-201, https://doi.org/10.1016/0377-0273(90)90088-W

Toto E. A. and J. N. Kellogg (1992), Structure of the Sinu-San Jacinto fold belt. An active accretionary prism in northern Colombia, Journal of South American Earth Sciences 5 (2), 211-222.

Trenkamp R., H. Mora, E. Salcedo y J. Kellogg, (2004). Possible Rapid Strain Accumulation Rates near Cali, Colombia, determined from GPS Measurements (1996-2003), Earth Sciences Res. J. 8 (1), ISSN 1794-6190, 25-33.

Trenkamp R., J. Kellogg, J. Freymueller and H. Mora, (2002). "Wide plate margin deformation, southern Central America and northwestern South America, CASA GPS observations", Journal of South American Earth Sciences 15, Elsevier, Pergamon Press, 157-171.

Turner J. F., J. C. Iliffe , M. K. Ziebart and C. Jones, (2013), Global Ocean Tide Models: Assessment and Use within a Surface Model of Lowest Astronomical Tide, Marine Geodesy, 36:2, 123-137, doi: 10.1080/01490419.2013.771717

UNAVCO, (2016), UNAVCO Resources: GNSS Station Monumentation, http://kb.unavco.org/kb/article/unavco-resources-gnss-station-monumentation-104.htm, (accessed on June 18, 2018)

UNAVCO, (2017), EarthScope - Plate Boundary Observatory (PBO), https://www.unavco.org/projects/major-projects/pbo/pbo.html (accessed on June 19, 2018)

UNAVCO, (2018), Plate Boundary Observatory, http://pboweb.unavco.org/, (accessed on December 8, 2018).

UNAVCO, (2018), COCONet, https://coconet.unavco.org/coconet.html, (accessed on December 8, 2018).

USGS, National Earthquake Information Center, The April 16, (2016). Ecuador M 7.8 earthquake,

https://earthquake.usgs.gov/earthquakes/eventpage/us20005j32#executive, (accessed on December 17, 2017)
USGS, National Earthquake Information Center, The February 9, (1967). M 7.0 Colombia earthquake, https://earthquake.usgs.gov/earthquakes/eventpage/iscgem838623#executive (accessed on December 17, 2017)
USGS, National Earthquake Information Center, The January 12, (1956). Ecuador M 7.0 earthquake, https://earthquake.usgs.gov/earthquakes/eventpage/iscgem887842#executive (accessed on December 17, 2017)
USGS, National Earthquake Information Center, The November 15, (2004). M 7.2 earthquake near the west coast of Colombia, https://earthquake.usgs.gov/earthquakes/eventpage/usp000d8gx#executive (accessed on December 17, 2017)
USGS, National Earthquake Information Center, The November 19, (1991). M 7.2 earthquake near the west coast of Colombia, https://earthquake.usgs.gov/earthquakes/eventpage/usp0004zbt#region-info, (accessed on December 17, 2017)
USGS, National Earthquake Information Center, The September 14, (2016). Mutata, Colombia, M 6 Earthquake, https://earthquake.usgs.gov/earthquakes/eventpage/us10006pdp#executive (accessed on November 7, 2017).
Vallée M., Nocquet J.-M., Battaglia J., Font Y., Segovia M., Réhnier M., Mothes P., Jarrin P., Cisneros D., Vaca S., Yepes H., Martin X., Béthoux N., Chlieh M., (2013). Intense interface seismicity triggered by a shallow slip event in the Central Ecuador subduction zone, J. Geophys. Res. Solid Earth, 118, 2965-2981, doi:10.1002/jgrb.50216
van Benthem, S. A. C., and R. Govers (2010). The Caribbean plate: Pulled, pushed, or dragged?, J. Geophys. Res., 115, B10409, doi:10.1029/2009JB006950.
van Benthem, S. A. C., R. Govers, W. Spakman, M. J. R. Wortel, (2013). Tectonic evolution and the mantle structure under the Caribbean region, J. Geophys. Res. Solid Earth, 118, 3019–3036, doi:10.1002/jgrb.50235.
van der Hammen T., J. H. Werner, and H. van Dommelen, (1973). Palynological record of the upheaval of the Northern Andes: a study of the Pliocene and Lower Quaternary of the Colombian Eastern Cordillera and the early evolution of its High-Andean biota. Palaeobot. and Palynol. 16:1-122.
van der Hilst, R. and P. Mann (1994). Tectonic implications of tomographic images subducted lithosphere beneath northwestern South America, Geology 22, pp. 451-454.
Vargas C. A., A. Caneva, H. Monsalve, F. Salcedo and H. Mora, (2018), Geophysical Networks in Colombia, Seismological Research Letters, Early Edition, Focus Section on Geophysical Networks and Related Developments in Latin America Published Online 14 February, 2018
Vaughan, S., R. J. Bailey, and D. G. Smith, (2011), Detecting cycles in stratigraphic data: Spectral analysis in the presence of red noise, Paleoceanography, 26, PA4211, doi:10.1029/2011PA002195.
Velandia F., Acosta, J., Terraza, R., Villegas, H., (2005). The current tectonic motion of the Northern Andes along the Algeciras Fault System in SW Colombia. Tectonophysics 399 (1-4), 313-329.

Veloza G., M. Taylor, A. Mora, and J. Gosse (2015), Active mountain building along the eastern Colombian Subandes: A folding history from deformed terraces across the Tame anticline, Llanos Basin, GSA Bulletin 127 (9-10): 1155–1173, doi: https://doi.org/10.1130/B31168.1

Wallace T. C., S. L. Beck, 1993, The Oct. 17-18, (1992). Colombian earthquakes; slip partitioning or faulting complexity, Seismol. Res. Lett., 64, 29.

Wallace L.M., C. Stevens, E. Silver, R. McCaffrey, W. Loratung, S. Hasiata, R. Stanaway, R. Curley, R. Rosa, j. Taugaloidi, 2004, GPS and seismological constraints on active tectonics and arc-continent collision in Papua New Guinea: implications for mechanics of microplate rotations in a plate boundary zone. J. Geophys. Res. 109, B05404. https://doi.org/10.1029/2003JB002481.

Wallace L. M., R. McCaffrey, J. Beavan, and S. Ellis (2005), Rapid microplate rotations and backarc rifting at the transition between collision and subduction, Geology, 33, 857-860.

Wallace, L. M., S. Ellis, K. Miyao, S. Miura, J. Beavan, and J. Goto (2009), Enigmatic, highly active left-lateral shear zone in southwest Japan explained by aseismic ridge collision, Geology, 37, 143-146, https://doi.org/10.1130/G25221A.1

Wallace L.M., Barnes P., Beavan R.J., Van Dissen R.J., Litchfield N.J., Mountjoy J., Langridge R.M., Lamarche G., Pondard N., (2012), The kinematics of a transition from subduction to strike-slip: an example from the central New Zealand plate boundary. JGR, Solid Earth, Online doi:10.1029/2011JB008640

Wang R., F. Lorenzo-Martin and F. Roth (2006), PSGRN/PSCMP, a new code for calculating co- and post-seismic deformation, geoid and gravity changes based on viscoelastic-gravitational dislocation theory, Computer & Geosciences 32, 527-541.

Weber, J. C., Dixon, T. H., DeMets, C., Ambeh, W. B., Jansma, P., Mattioli, G., Saleh, J., Sella, G., Bilham, R., Pérez, O., (2001). GPS estimate of relative motion between the Caribbean and South American plates, and geological implications for Trinidad and Venezuela, Geology, 29, 75-78.

Westbrook, G. K., N. C. Hardt, R. Heath, ,(1995). Structure and tectonics of the Panama-Nazca boundary. In: Mann P. (ed) Geologic and Tectonic Development of the Caribbean Plate Boundary in Southern Central America, Geol. Soc. Am. Special Paper, 295: 91-109.

White, S. M., Trenkamp, R., J. N. Kellogg, (2003). Recent crustal deformation and the earthquake cycle along Ecuador-Colombia subduction zone, Earth and Planetary Science Letters 216, 231-242.

Wijninga V., (1996). Paleobotany and palynology of Neogene sediments from the high plain of Bogotá, (Colombia). PhD Thesis, University of Amsterdam, Amsterdam, 370 pp.

Wijninga V. M. (1996). Neogene ecology of the Salto de Tequendama site (2475 m altitude, Cordillera Oriental, Colombia): the paleobotanical record of montane and lowland forests, Review of Palaeobotany and Palynology, 92, 97-156.

Williams S. D. P. (2003a), The effect of coloured noise on the uncertainties of rates from geodetic time series. J Geodesy 76(9-10):483–494, DOI 10.1007/s00190-002-0283-4

Williams S. D. P. (2003b), Offsets in Global Positioning System time series, J. Geophys. Res. 108 (B6) 2310, doi:10.1029/2003JB002156

Witt C., J. Bourgois, F. Michaud, M. Ordoñez, N. Jimenez and M. Sosson (2006), Development of the Golfo de Guayaquil (Ecuador) as an effect of the North

Andean block tectonic escape since the Lower Pleistocene. Tectonics 25, TC3017. doi: 10.1029/2004TC001723.

Witt C. and J. Bourgois (2010), Forearc basin formation in the tectonic wake of a collision-driven, coastwise migrating crustal block: The example of the North Andean block and the extensional Gulf of Guayaquil-Tumbes Basin (Ecuador-Peru border area). GSA Bulletin, 122(1/2): 89-108; doi: 10.1130/B26386.1

Wittmann, H., von Blanckenburg, F., Guyot, J. L., Laraque, A., Bernal, C., and Kubik, P.W., (2011). Sediment production and transport from in situ-produced cosmogenic 10Be and river loads in the Napo River basin, an upper Amazon tributary of Ecuador and Peru: Journal of South American Earth Sciences, v. 31, no. 1, p. 45-53, doi:10.1016/j.jsames.2010.09.004.

Xiaoxing H, J-P. Montillet, R. Fernandes, M. Bos, K. Yu, X. Hua, W. Jiang, (2017). Review of current GPS methodologies for producing accurate time series and their error sources, Journal of Geodynamics 106 (2017) 12–29 http://dx.doi.org/10.1016/j.jog.2017.01.004

Ye L., Kanamori H., Avouac, Jean-Philippe, Li, L., Cheung, K.F., Lay, T., (2016). The 16 April 2016, Mw 7.8 (M_s 7.5) Ecuador earthquake: a quasi-repeat of the 1942 Ms 7.5 earthquake and partial re-rupture of the 1906 M_s 8.6 Colombia-Ecuador earthquake. Earth Planet. Sci. Lett. 454, 248-258, doi.org/10.1016/j.epsl.2016.09.006.

Yepes H., Audin, L., Alvarado, A., Beauval, C., Aguilar, J., Font, Y., Cotton, F. (2016): A new view for the geodynamics of Ecuador: implication in seismogenic sources definition and seismic hazard assessment, Tectonics, 35, 5, pp. 1249—1279. http://doi.org/10.1002/2015TC003941

Yoshimoto M., et al. (2017). Depth-dependent rupture mode along the Ecuador-Colombia subduction zone, Geophys. Res. Lett., 44, 2203–2210, doi:10.1002/2016GL071929.

Zheng G., H. Wang, T. J. Wright, Y. Lou, R. Zhang, W. Zhang, C. Chuang, H. Jinfang, W. NA (2017), Crustal deformation in the India-Eurasia collision zone from 25 years of GPS measurements. JGR: Solid Earth, 122, 9290–9312. https://doi.org/10.1002/2017JB014465

Zumberge J. F., M. B. Heflin, D. C. Jefferson, M. M. Watkins, F. H. Webb, (1997). Precise point positioning for the efficient and robust analysis of GPS data from large networks. Journal of Geophysical Research 102: doi: 10.1029/96JB03860. ISSN: 0148-0227.

APPENDIXES

Appendix A

Recent seismicity in Colombia

Colombia is a country that frequently experiences earthquakes, although they are not of great magnitude. However, some of them have been destructive throughout the history of the country. A general review of the seismicity that has occurred recently in Colombia is presented in chronological order, and some maps of seismogenic zones are showed using earthquake epicenters obtained in both the NEIC (National Earthquake Information Center) of the USGS and the National Seismological Network of Colombia run by the Colombian Geological Survey.

An important earthquake that is necessary to take in account for seismotectonics studies in Colombia is the February 9, 1967, M 7 earthquake (2.849°N, 74.798°W, 55.0 km depth), (USGS), associated with the Algeciras-Balsillas sector of the Algeciras Fault System, that destroyed the village of El Paraiso and caused damages in other towns of the region, and also affecting the city of Bogotá. The Algeciras Fault system is classified as a right-lateral strike-slip complex structure, with an important vertical component in which sedimentary cover and basement rocks are involved (Acosta et al., 2007). The Algeciras Fault system occurs in the central part of the Eastern Cordillera in SW Colombia and continues southward for more than 800 km into Ecuador and the Gulf of Guayaquil. This fault is a zone of simple shear, caused by the oblique convergence between the Nazca Plate and the Northern Andes. It marks the boundary of the neotectonic transpressive regime in the Northern Andes which begins in Ecuador and continues into Colombia and Venezuela (Velandia et al., 2005).

On November 19, 1991, a M 7.2 earthquake occurred near the west coast of Colombia (4.554°N, 77.442°W, 21.3 km depth). This area was the epicenter of a similar earthquake (M 7.2) occurred on November 15, 2004, (4.695°N, 77.508°W, 15.0 km depth). This event, named Pizarro earthquake, was felt in most of the country and affected mainly the city of Cali, one of the large cities in the country. These two earthquakes are located north of the Buenaventura city, and are completely separated from the source of the other

earthquakes that have occurred on the Colombia-Ecuador trench. Figure A1 shows the epicenter of the main earthquakes occurred on the Nazca-South America subduction zone.

Several earthquakes have occurred in northwestern Colombia that could be associated with on-going Panama/North Andes collision. On October 17, 1992, a large earthquake (Ms 6.7) struck northern Colombia; about 31 hours later, (October 18), a stronger earthquake (Ms 7.3) occurred in the same region. The focal mechanisms are consistent with compression normal to the Panama-Andes suture (Freymueller et al, 1993). These events caused one death and 50 injuries and at least 70% of the buildings in Murindó village were destroyed. Additionally, it caused damage in Medellín, the capital city of the Department of Antioquia, and in Apartadó village. These events apparently are linked to the eruption of a mud volcano that killed 10 people in the San Pedro de Urabá area (INGEOMINAS, 1994).

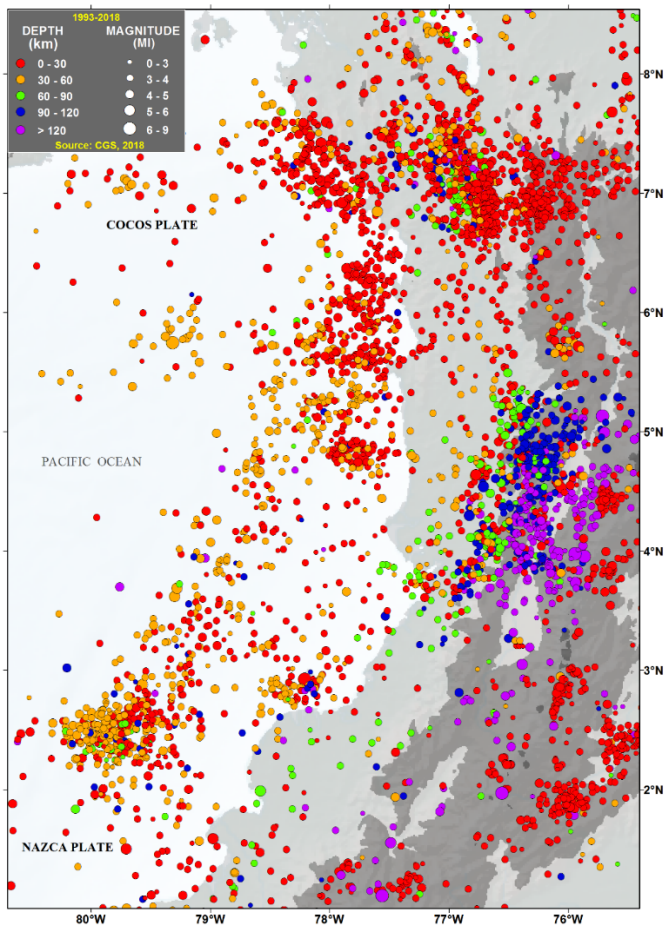

Figure A1. Earthquake epicenters in the western zone of Colombia.

Li and Toksoz (1993) compared the source properties of the 1992 sequence to those of the previous large earthquakes in Colombia, especially to the great 1979 event. Taking into consideration this event, they indicated that the October 18 mainshock was also a complex rupture process along a thrust fault plane consisting of two rupture patches, with the moment release of the second one being 7 times larger than that of the first patch. The change of the focal mechanisms for the different mainshocks indicate a complex tectonic process in the area. The 1979 event was associated with the subduction of the Nazca plate beneath South America, but the 1992 earthquakes may be related to Panama -North Andes collision. On July 28, 2015, an earthquake occurred in the boundary with Panama, (8.15°N, 77.4°W), (Mw 6.1, depth 2.5 km), (Servicio Geológico Colombiano, 2017), that affected 40 houses.

A recent earthquake occurred in this region on September 14, 2016, in the Mutatá region, Colombia, (7.37°N, 76.17°W), (Mw 6.0, depth 18 km) with a focal mechanism consistent with northwest-southeast compression (USGS National Earthquake Information Center, 2017). Figure A2 shows the earthquake epicenters in the western zone of Colombia, including the Nazca subduction zone.

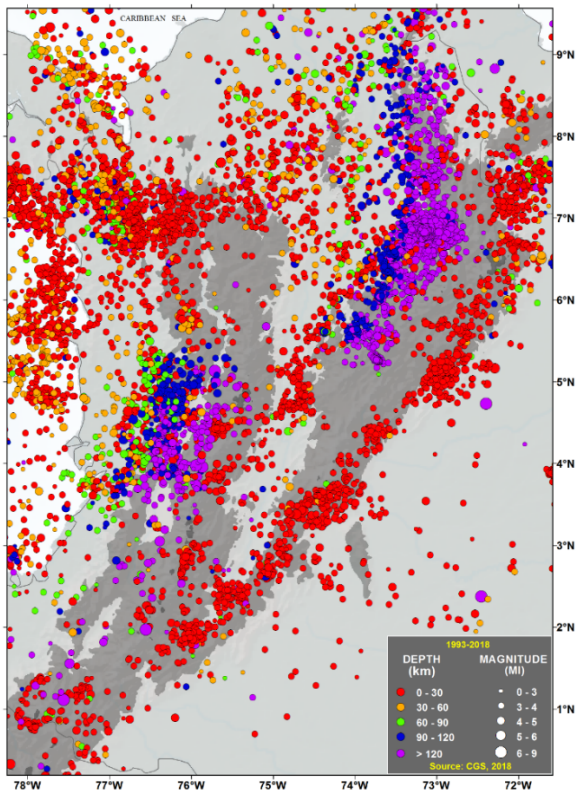

Figure A2. Earthquake epicenters in the northwestern and central zones of Colombia

In 1994, three earthquakes greater than magnitude 5.5 occurred. The first one, on May 31, (Mb 6.3) was located on northern Colombia, and was felt at Arauca, Bogotá, Bucaramanga, Manizales, Cúcuta, Sincelejo cities and even Caracas city in Venezuela. One person was injured and there was some damage in the epicentral region. The second one, on June 6, (Mb 6.4), was located along the Cordillera Central axis, 10 km southwest of Huila volcano, the largest and highest volcano in Colombia. At least 400 people were killed, 1,000 missing, and 13,000 homeless. Severe damage was caused to houses, highways and bridges by the earthquake and ensuing landslides in Cauca, Huila, Tolima and Valle departments. An avalanche from the Nevado del Huila volcano blocked the Páez river causing severe flooding at Belalcázar town and Neiva city, and landslides and mudflows along the river, destroying the town of Páez. The quake was felt in much of west-central Colombia from Tunja to Pasto cities. The third earthquake, on September 13 (Mb 6.5), did not cause injuries but its location is the same as the earthquakes mentioned above which occurred in 1992. A Mb 5.2 earthquake occurred on May 6, 1994. Figure A3 show the epicenters in the northwestern and central zones of Colombia, including the seismicity along the Eastern Frontal Fault, the boundary between the South American plate and the North Andean Block.

In 1995, two strong earthquakes occurred. The first one, on January 19, (Mb 6.5), was located under the piedmont of the Eastern Cordillera, about 30 kilometers from the largest oil field in Colombia, Cusiana. Five people were killed, several injured and at least 20 major buildings damaged in the Santafé de Bogotá area. One person was also killed at Manizales city and another at Miraflores village. More than 500 houses were damaged or destroyed in Boyacá department; 10 others were destroyed in Casanare department. Landslides blocked several rivers and streams in Colombia. This earthquake was felt throughout much of Colombia and western Venezuela. The second one, on February 8, an earthquake measuring Mb 6.4 was located in southwestern Colombia, about 60 kilometers north of Cali, in the Cauca Valley. At least 40 people were killed and there were more than 250 injuries in the Pereira area. The earthquake was strong enough to cause buildings to collapse over a wide area, especially in the city of Pereira.

On January 25, 1999, two earthquakes, the most destructive shallow crustal events in Colombia history occurred in the Central Region of Colombia, near the city of Armenia,

named the Coffee Growers Region. At least 1,185 were killed, more than 8,000 injuries, and more than 250,000 homeless, (PNUD-CEPAL, 1999). The Figure A3 shows the epicentral location of earthquakes in this region of the country, including the seismic events mentioned.

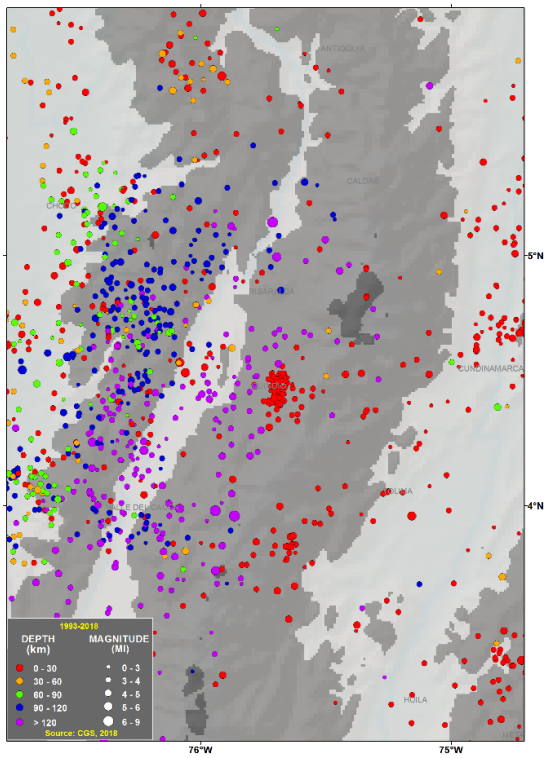

Figure A3. Seismicity in the Coffee Growers Region.

On May 24, 2008, at 14:20 hours local time, 21 stations of the National Seismic Network of Colombia – RSNC recorded a seismic event. The epicenter was located on the Eastern Cordillera, 8.6 km north from the urban area of the Quetame Municipality (Cundinamarca department), 40 km south west from Bogota, the capital city of the country, and 35 km northwest from Villavicencio city, with coordinates 4,399° N in latitude and 73,814° W in longitude, shallow depth and a Richter Scale local magnitude of 5.7, computed from the maximum amplitude of the record according to the RSNC report. The Seismology Group of the Harvard University reported this earthquake with a Mw 5.9, (Servicio Geológico Colombiano, 2008). The earthquake was felt in most of the country, and there were 11 fatalities and 4,181 injured, and several houses collapsed in the Quetame town. In Bogota, a building was affected with minor damage.

Although not responsible for much damage or numbers of deaths, the major source of numbers of seismic events is the Bucaramanga Nest, that represents the highest concentration of intermediate-depth (160 km) seismicity in the world (Prieto et al, 2012). Located in the northeastern of Colombia, near the border with Venezuela and near the city of Bucaramanga, Colombia, the nest generates events daily, with approximately one M4.7 earthquake per month, in which energy is released from a small located volume; several models have been proposed to explain it. The greater earthquake that occurred recently was on March 10, 2015, (6.83°N, 73.13°W), (Mw 6.3, depth 156 km), and was felt in most of the Colombian territory, and also in some area of Venezuela. Some damages were reported in towns of Santander, Norte de Santander, Antioquia, Cundinamarca y Boyacá departments. Poli et al., (2016), with respect to this earthquake, infer a complex rupture process with two distinct stages, characterized by different rupture velocities possibly controlled by the evolution of strength on the fault, Figure A4.

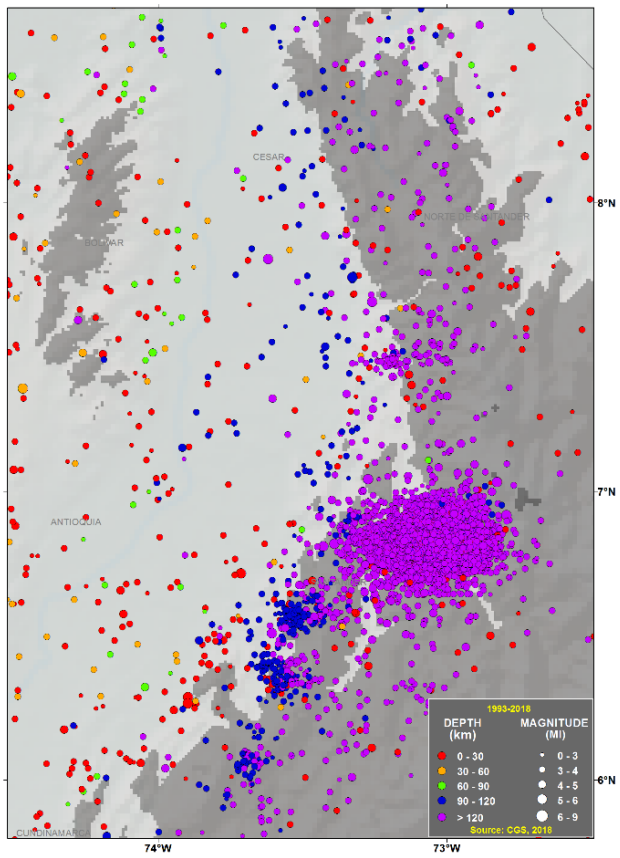

Figure A4. The Bucaramanga seismic nest

The northern zone of Colombia, including the border with Venezuela and the Caribbean region, also presents seismicity, as shown in Figure A5.

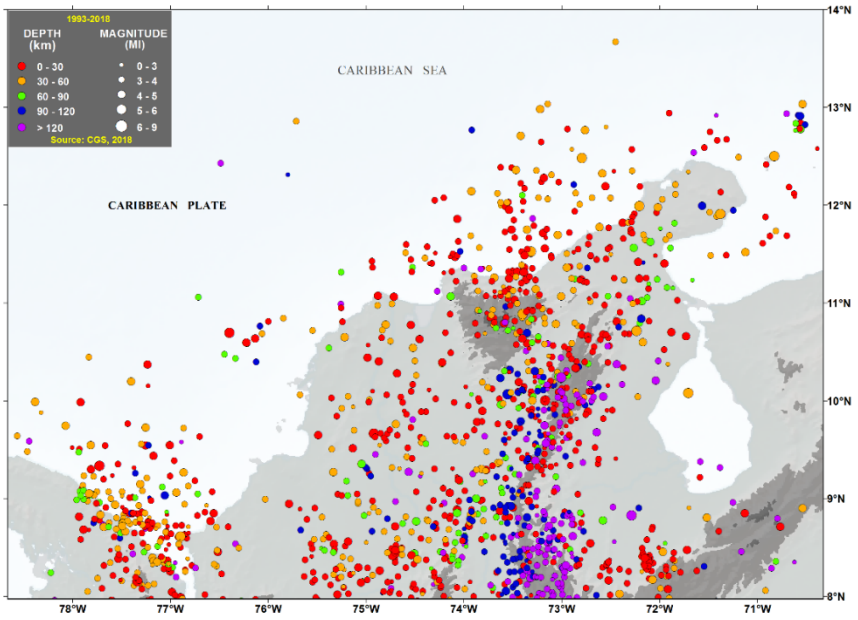

Figure A5. Epicenter location in the northern zone of Colombia

Appendix B

Evolution of the GNSS CORS GeoRED Network

The following maps illustrate the evolution of the GNSS GeoRED network of Colombia conceived for geodynamics research, (Mora-Páez, 2006; Mora-Páez at al., 2018).

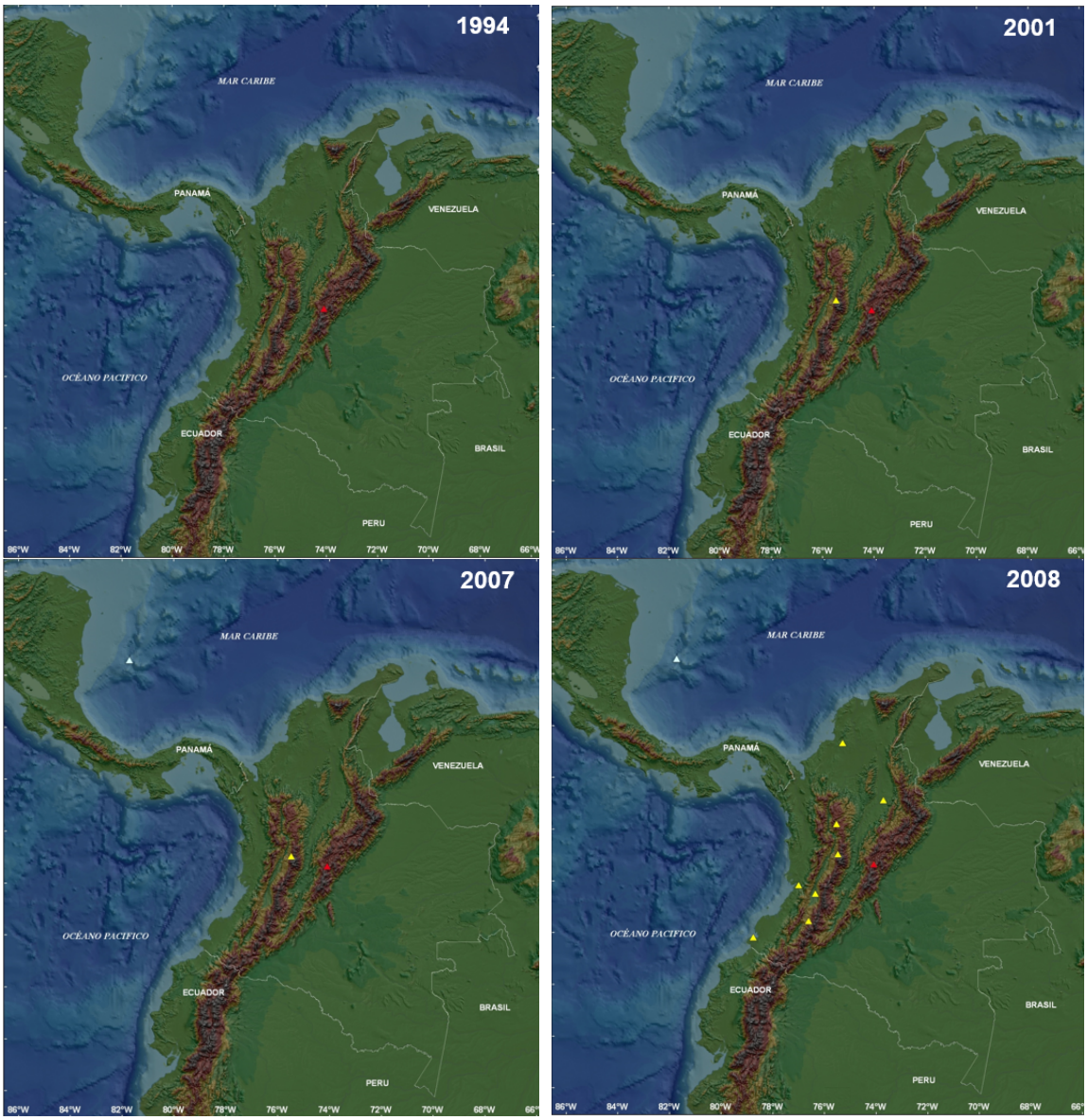

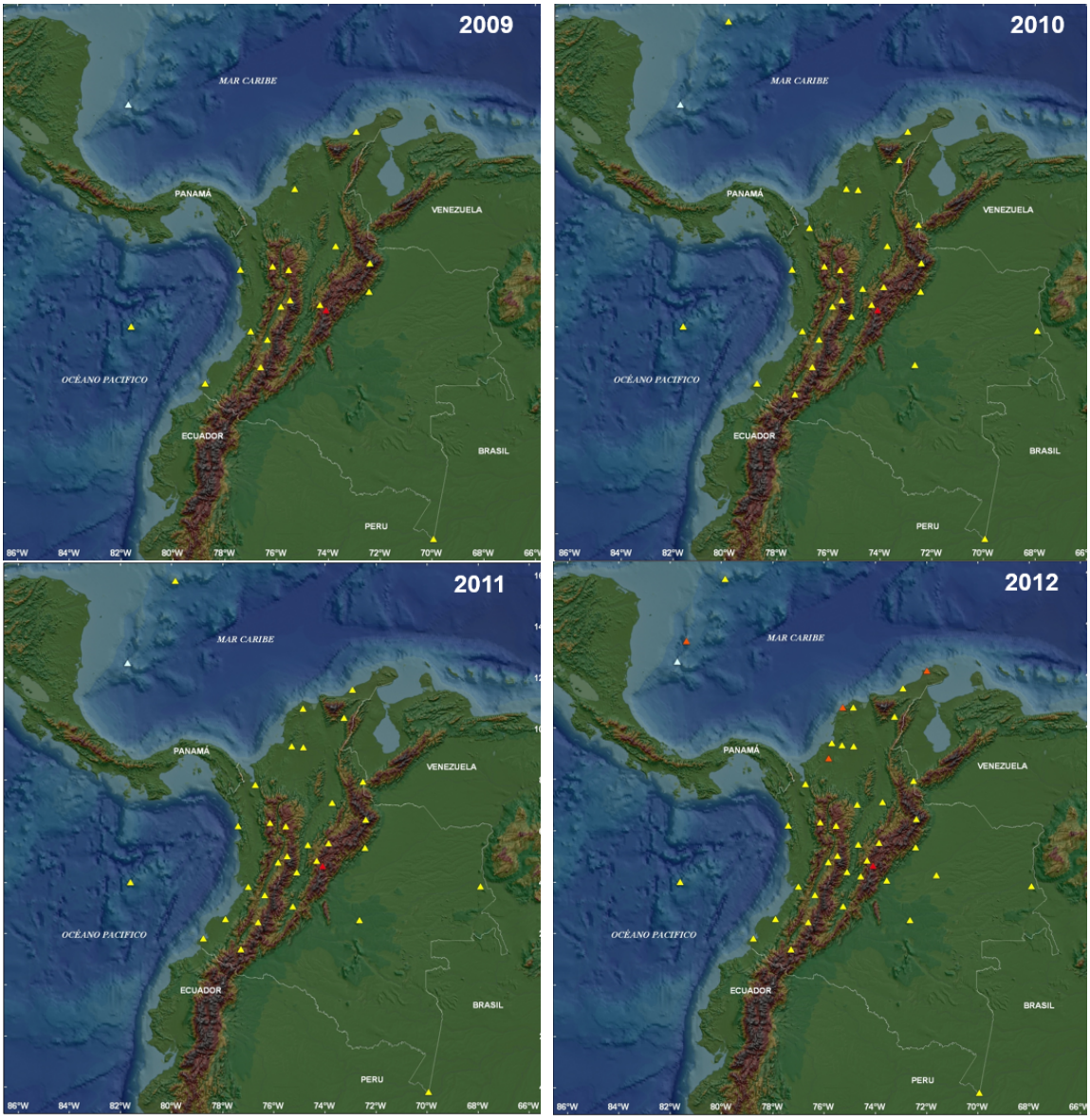
2009
2010
2011
2012
MAR CARIBE
PANAMÁ
VENEZUELA
OCÉANO PACIFICO
ECUADOR
BRASIL
PERU
86°W
84°W
82°W
80°W
78°W
76°W
74°W
72°W
70°W
68°W
66°W

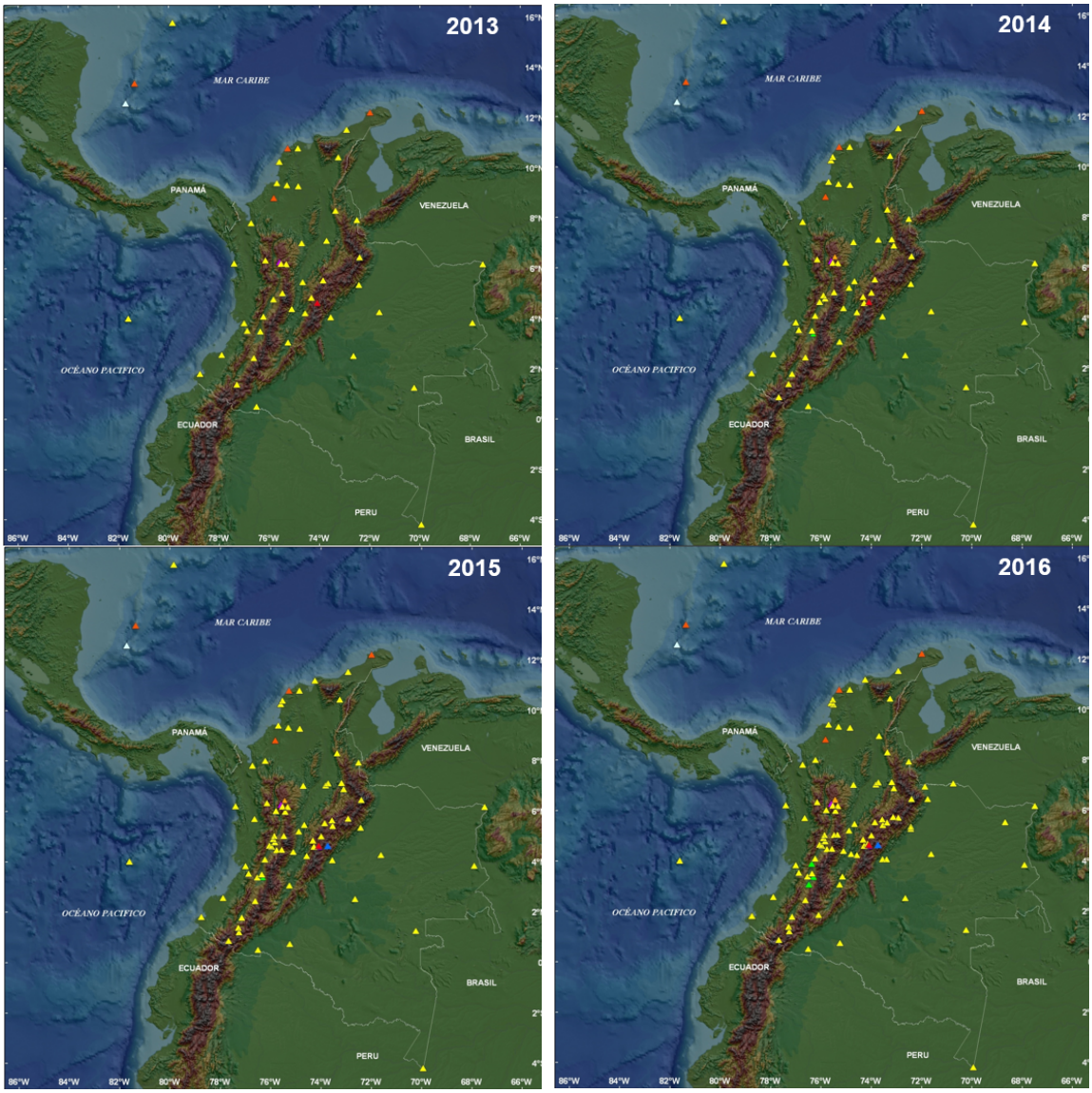
2013
2014
2015
2016
MAR CARIBE
PANAMÁ
VENEZUELA
OCÉANO PACIFICO
ECUADOR
BRASIL
PERU

GNSS/GPS
ESTACIONES PERMANENTES

- GeoRED - NASA
- GeoRED
- GeoRED - UCAR
- GeoRED - COCONET
- GeoRED - Universidad Nacional
- GeoRED - CENICAÑA
- GeoRED - Area Metropolitana Valle de Aburrá
- GeoRED - EAAB

Appendix C

GPS time series

This appendix contains the GPS time series plots of the stations used in this dissertation.

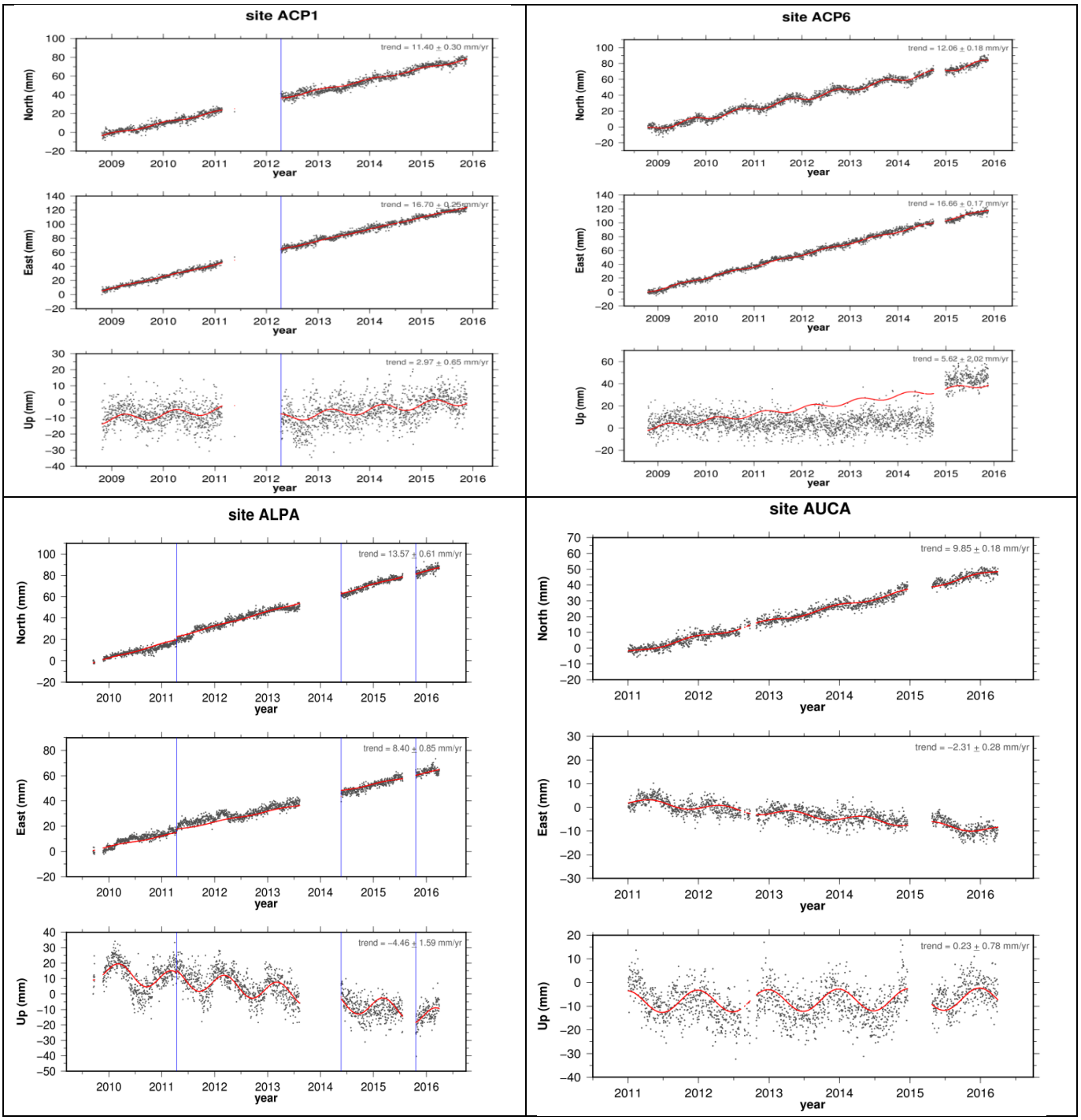

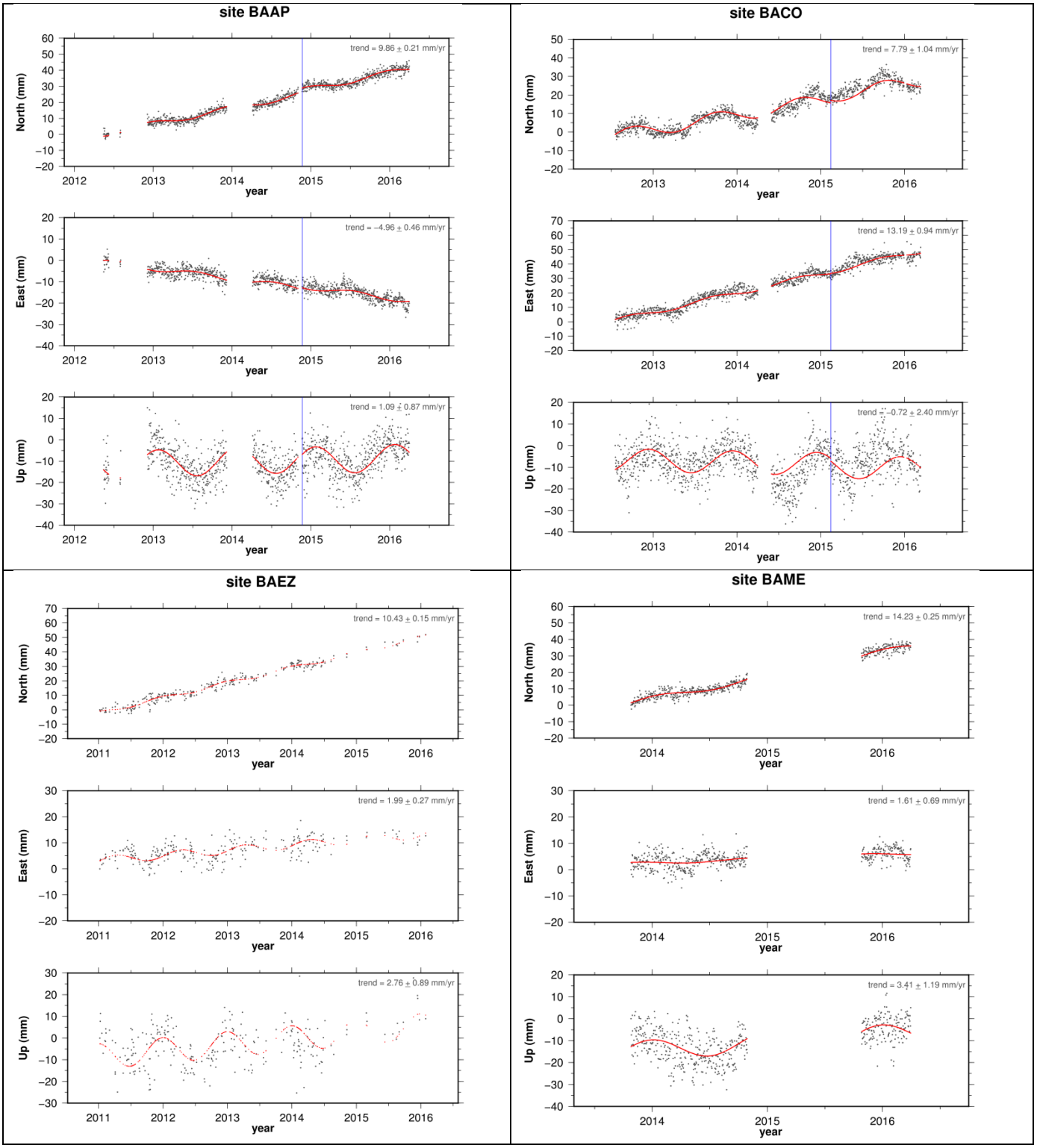
site BAAP
trend = 9.86 ± 0.21 mm/yr
North (mm)
trend = −4.96 ± 0.46 mm/yr
East (mm)
trend = 1.09 ± 0.87 mm/yr
Up (mm)
year
site BACO
trend = 7.79 ± 1.04 mm/yr
North (mm)
trend = 13.19 ± 0.94 mm/yr
East (mm)
trend = −0.72 ± 2.40 mm/yr
Up (mm)
year
site BAEZ
trend = 10.43 ± 0.15 mm/yr
North (mm)
trend = 1.99 ± 0.27 mm/yr
East (mm)
trend = 2.76 ± 0.89 mm/yr
Up (mm)
year
site BAME
trend = 14.23 ± 0.25 mm/yr
North (mm)
trend = 1.61 ± 0.69 mm/yr
East (mm)
trend = 3.41 ± 1.19 mm/yr
Up (mm)
year

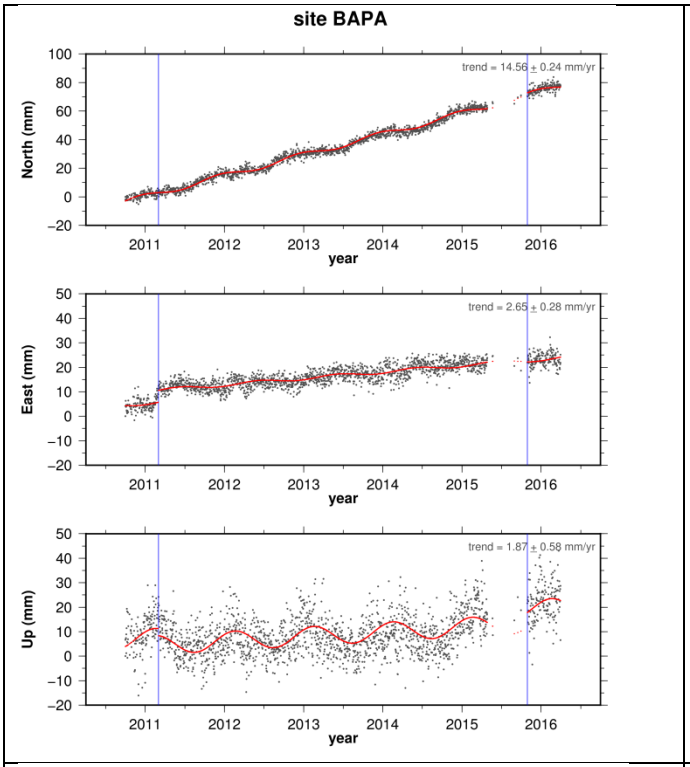
site BAPA
North (mm)
trend = 14.56 ± 0.24 mm/yr
East (mm)
trend = 2.65 ± 0.28 mm/yr
Up (mm)
trend = 1.87 ± 0.58 mm/yr
year

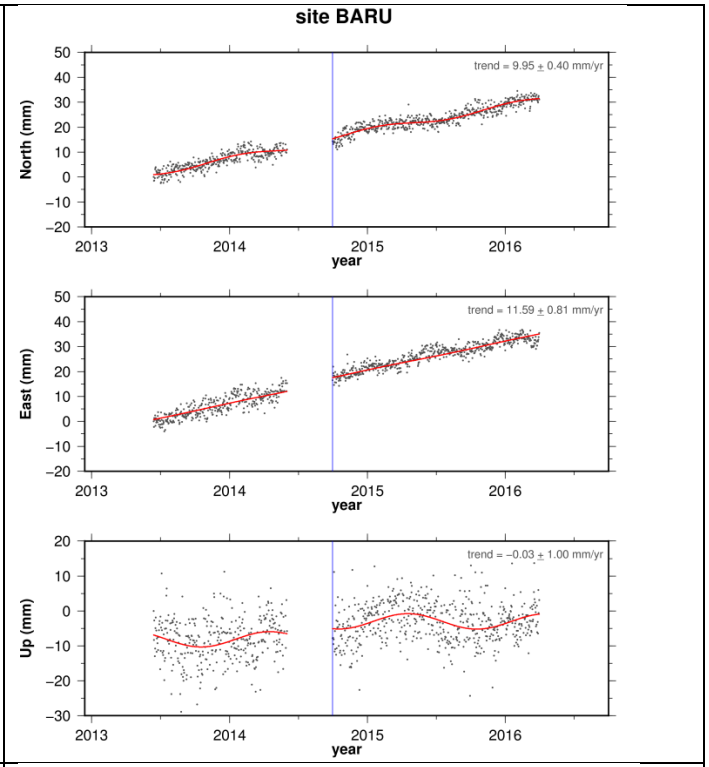
site BARU
North (mm)
trend = 9.95 ± 0.40 mm/yr
East (mm)
trend = 11.59 ± 0.81 mm/yr
Up (mm)
trend = −0.03 ± 1.00 mm/yr
year

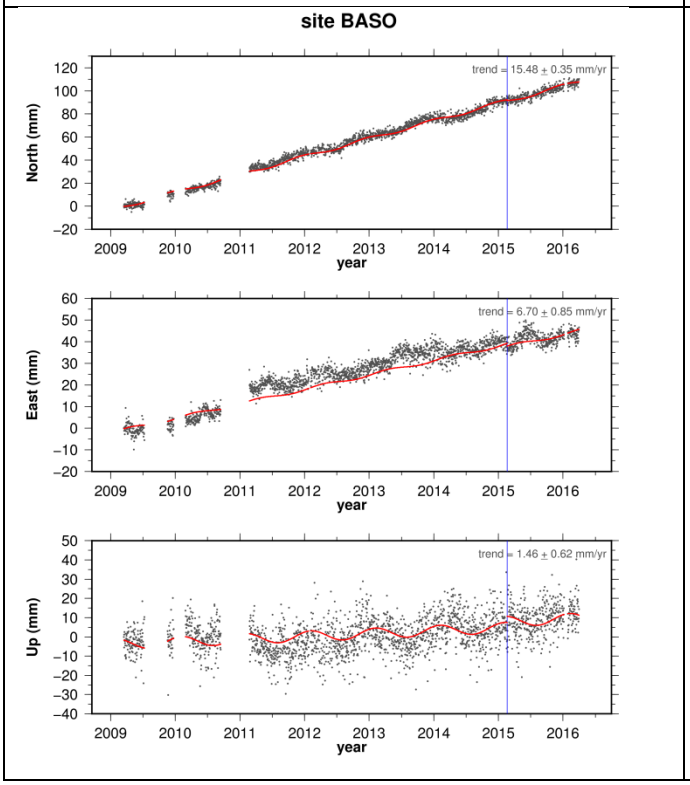
site BASO
North (mm)
trend = 15.48 ± 0.35 mm/yr
East (mm)
trend = 6.70 ± 0.85 mm/yr
Up (mm)
trend = 1.46 ± 0.62 mm/yr
year

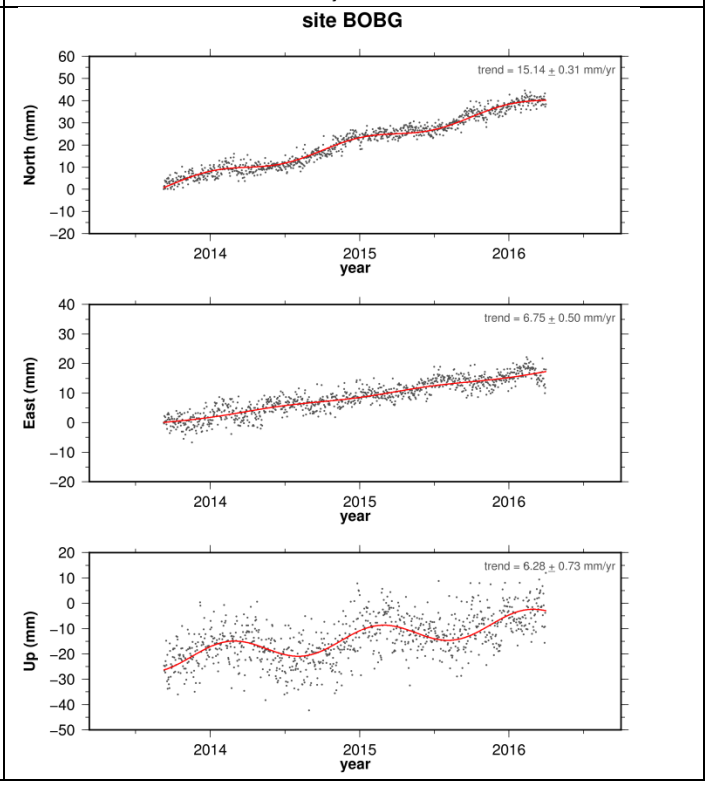
site BOBG
North (mm)
trend = 15.14 ± 0.31 mm/yr
East (mm)
trend = 6.75 ± 0.50 mm/yr
Up (mm)
trend = 6.28 ± 0.73 mm/yr
year

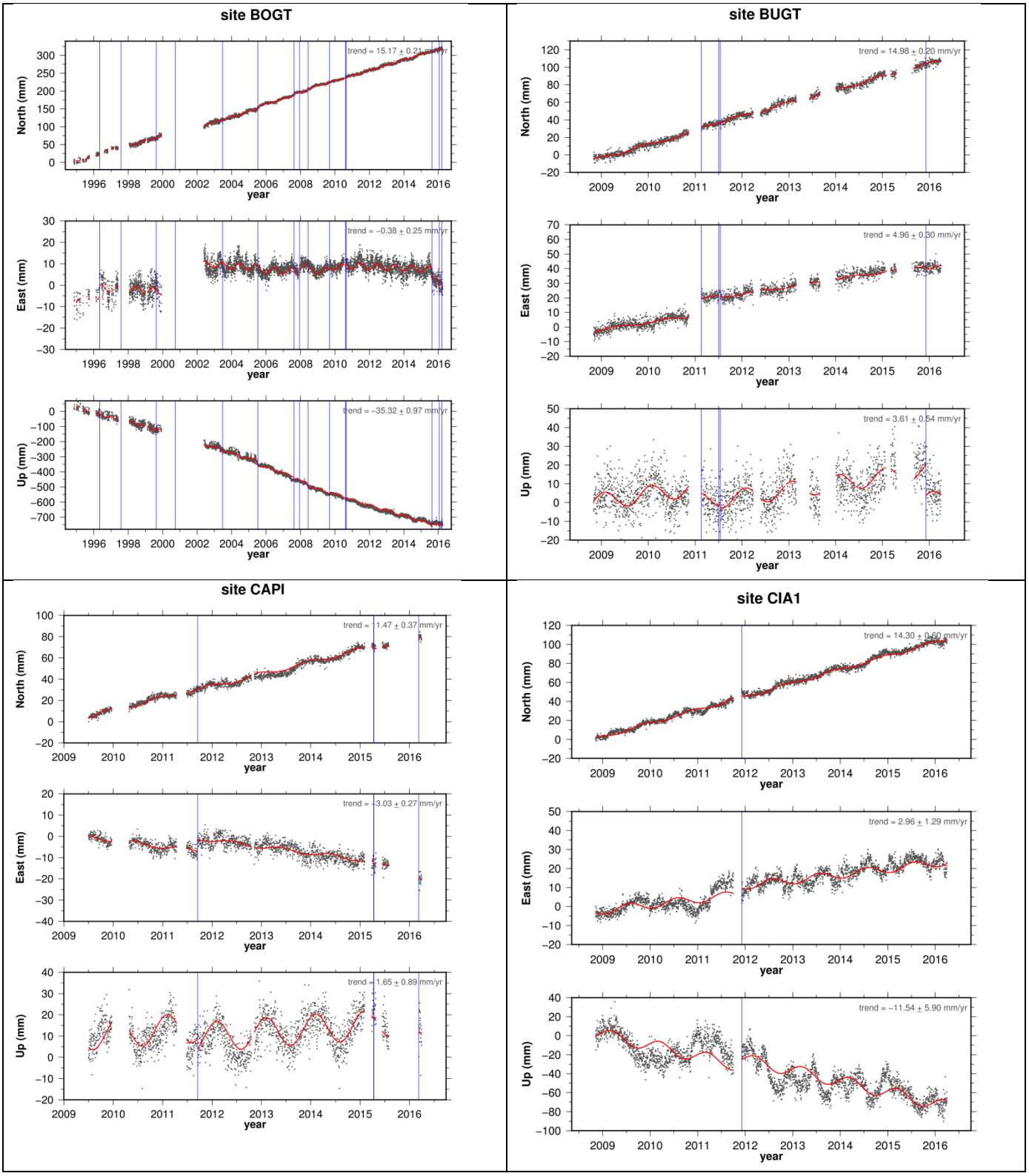
site BOGT
North (mm)
trend = 15.17 ± 0.21 mm/yr
East (mm)
trend = −0.38 ± 0.25 mm/yr
Up (mm)
trend = −35.32 ± 0.97 mm/yr
year
site BUGT
North (mm)
trend = 14.98 ± 0.20 mm/yr
East (mm)
trend = 4.96 ± 0.30 mm/yr
Up (mm)
trend = 3.61 ± 0.54 mm/yr
year
site CAPI
North (mm)
trend = 1.47 ± 0.37 mm/yr
East (mm)
trend = −3.03 ± 0.27 mm/yr
Up (mm)
trend = 1.65 ± 0.89 mm/yr
year
site CIA1
North (mm)
trend = 14.30 ± 0.60 mm/yr
East (mm)
trend = 2.96 ± 1.29 mm/yr
Up (mm)
trend = −11.54 ± 5.90 mm/yr
year

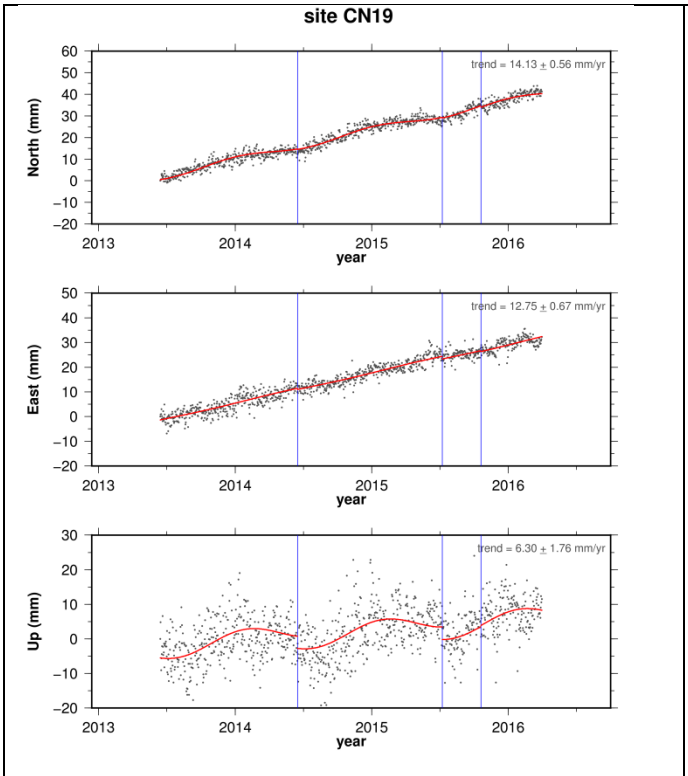
site CN19
North (mm)
trend = 14.13 ± 0.56 mm/yr
East (mm)
trend = 12.75 ± 0.67 mm/yr
Up (mm)
trend = 6.30 ± 1.76 mm/yr
year

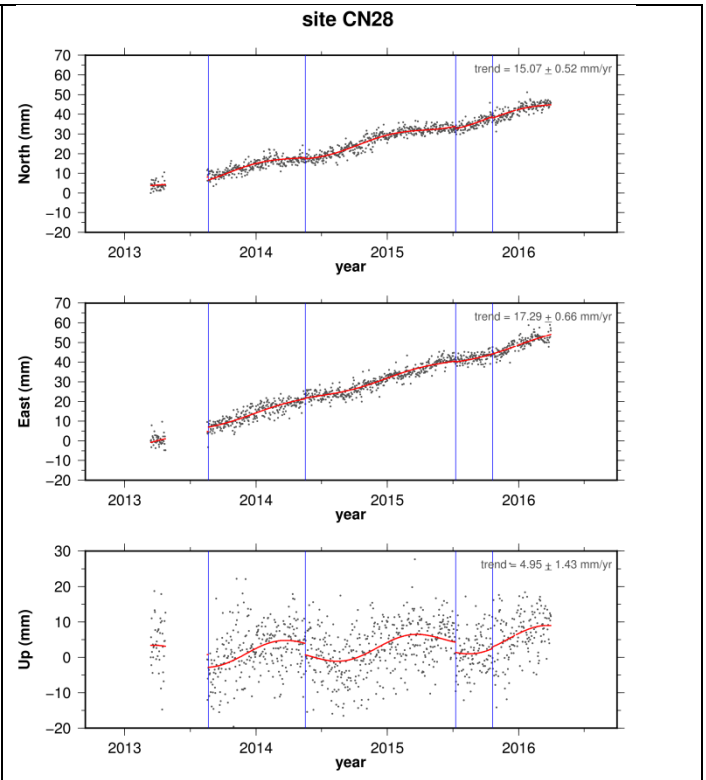
site CN28
North (mm)
trend = 15.07 ± 0.52 mm/yr
East (mm)
trend = 17.29 ± 0.66 mm/yr
Up (mm)
trend = 4.95 ± 1.43 mm/yr
year

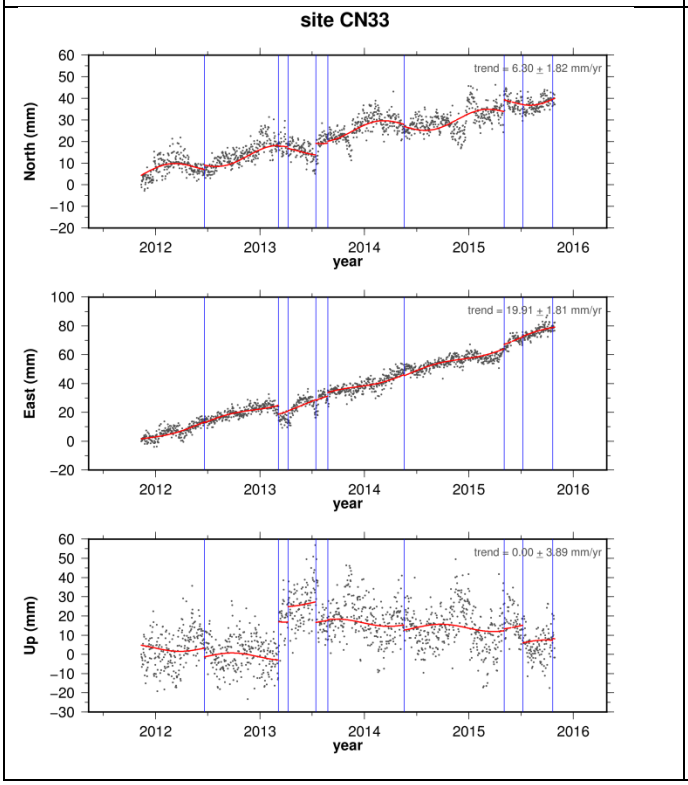
site CN33
North (mm)
trend = 6.30 ± 1.82 mm/yr
East (mm)
trend = 19.91 ± 1.81 mm/yr
Up (mm)
trend = 0.00 ± 3.89 mm/yr
year

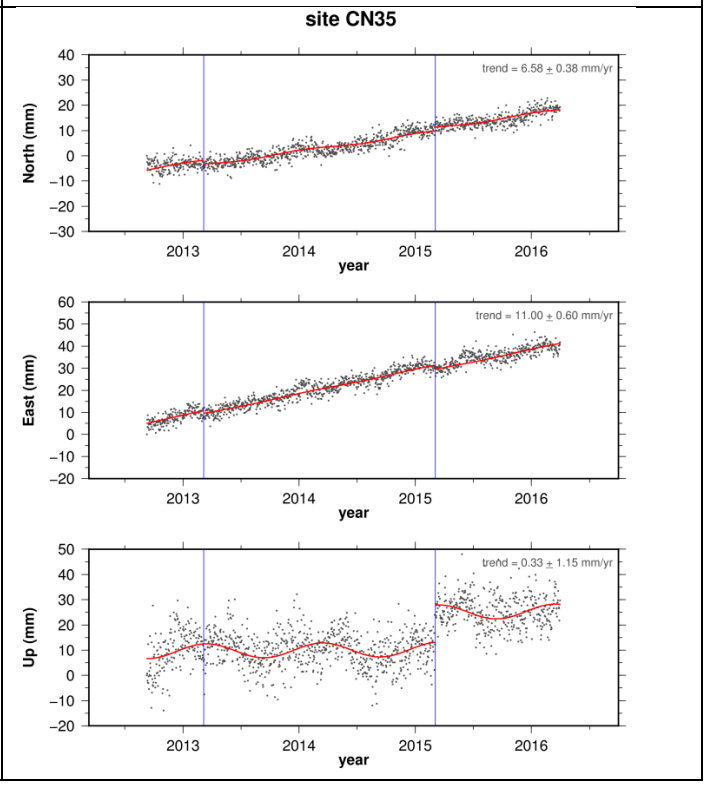
site CN35
North (mm)
trend = 6.58 ± 0.38 mm/yr
East (mm)
trend = 11.00 ± 0.60 mm/yr
Up (mm)
trend = 0.33 ± 1.15 mm/yr
year

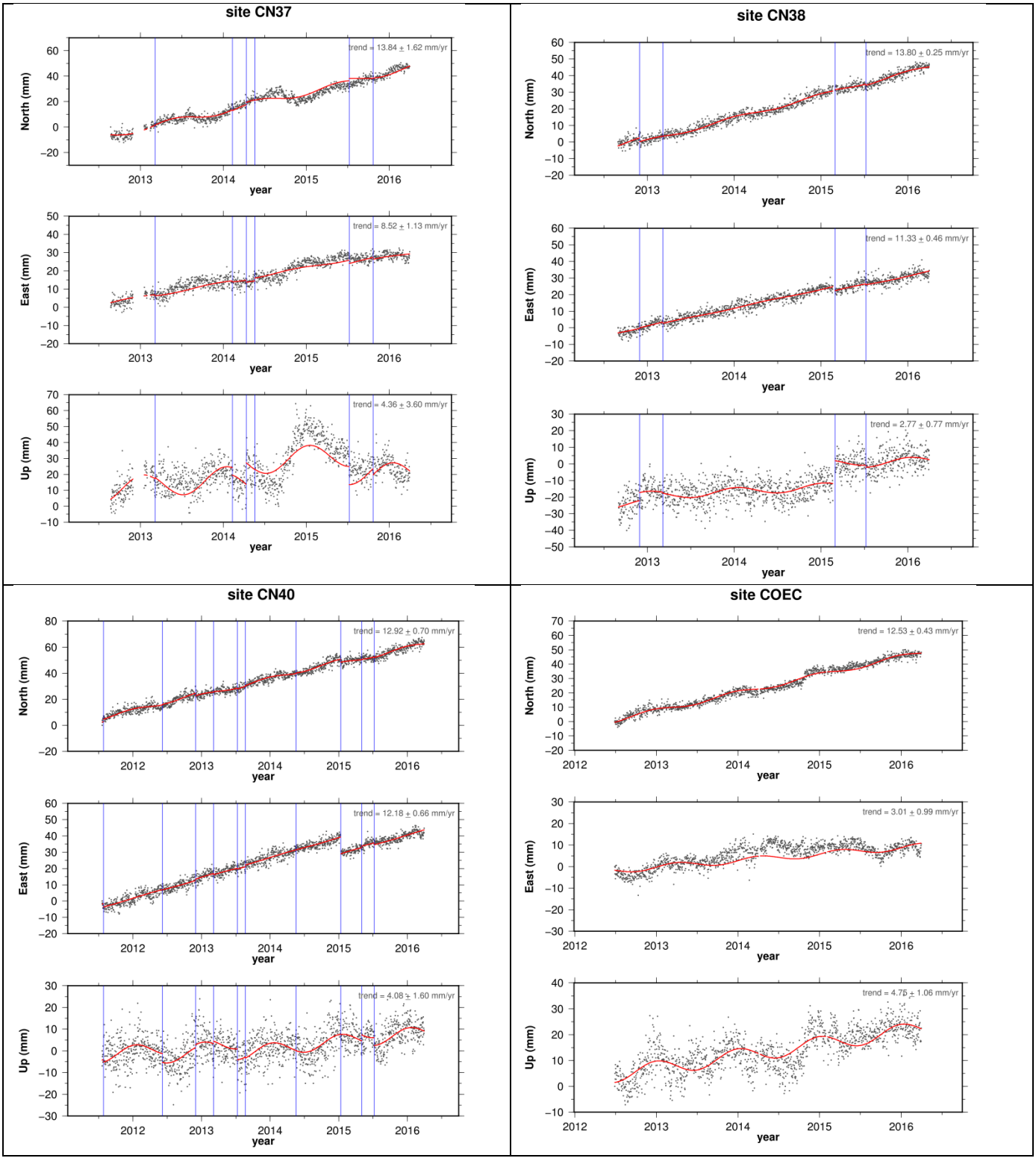
site CN37
North (mm)
trend = 13.84 ± 1.62 mm/yr
East (mm)
trend = 8.52 ± 1.13 mm/yr
Up (mm)
trend = 4.36 ± 3.60 mm/yr
year
site CN38
North (mm)
trend = 13.80 ± 0.25 mm/yr
East (mm)
trend = 11.33 ± 0.46 mm/yr
Up (mm)
trend = 2.77 ± 0.77 mm/yr
year
site CN40
North (mm)
trend = 12.92 ± 0.70 mm/yr
East (mm)
trend = 12.18 ± 0.66 mm/yr
Up (mm)
trend = 4.08 ± 1.60 mm/yr
year
site COEC
North (mm)
trend = 12.53 ± 0.43 mm/yr
East (mm)
trend = 3.01 ± 0.99 mm/yr
Up (mm)
trend = 4.75 ± 1.06 mm/yr
year

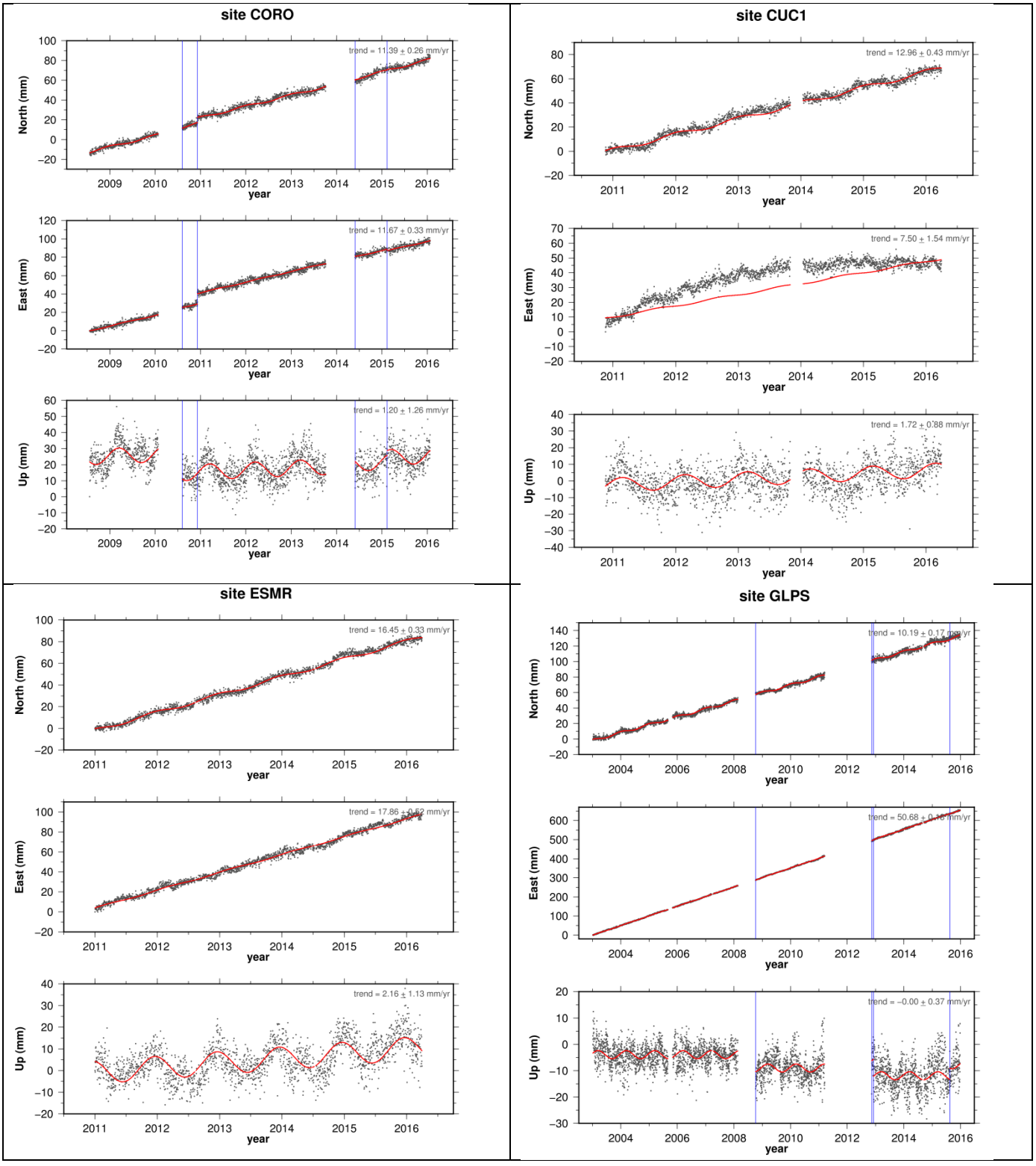
site CORO
North (mm)
trend = 11.39 ± 0.26 mm/yr
East (mm)
trend = 11.67 ± 0.33 mm/yr
Up (mm)
trend = 1.20 ± 1.26 mm/yr
year
site CUC1
North (mm)
trend = 12.96 ± 0.43 mm/yr
East (mm)
trend = 7.50 ± 1.54 mm/yr
Up (mm)
trend = 1.72 ± 0.88 mm/yr
year
site ESMR
North (mm)
trend = 16.45 ± 0.33 mm/yr
East (mm)
trend = 17.86 ± 0.62 mm/yr
Up (mm)
trend = 2.16 ± 1.13 mm/yr
year
site GLPS
North (mm)
trend = 10.19 ± 0.17 mm/yr
East (mm)
trend = 50.68 ± 0.16 mm/yr
Up (mm)
trend = −0.00 ± 0.37 mm/yr
year

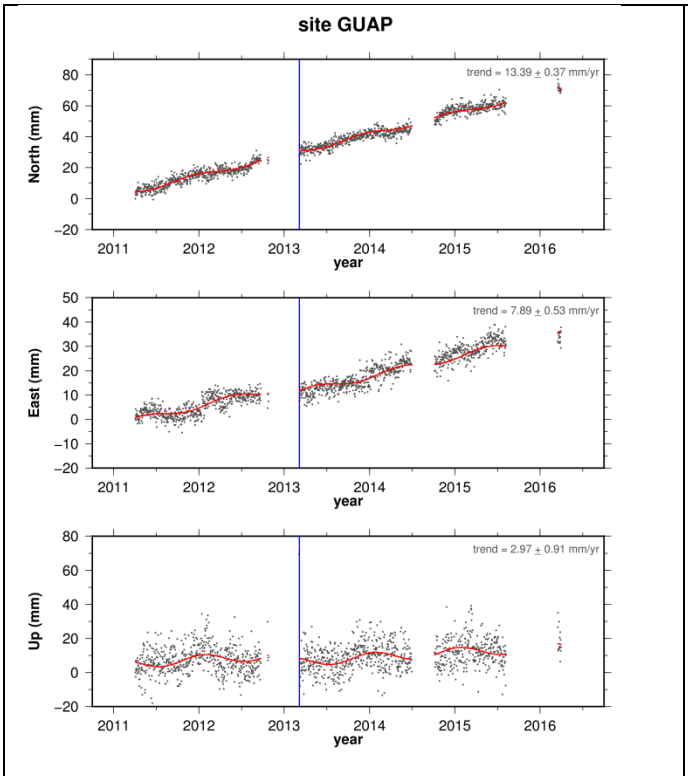
site GUAP
North (mm)
trend = 13.39 ± 0.37 mm/yr
East (mm)
trend = 7.89 ± 0.53 mm/yr
Up (mm)
trend = 2.97 ± 0.91 mm/yr
year

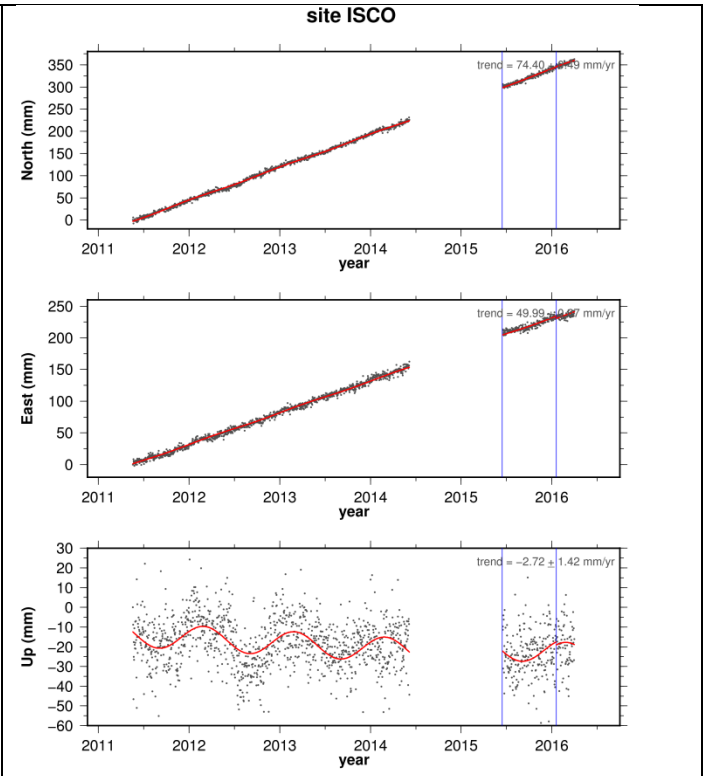
site ISCO
North (mm)
trend = 74.40
East (mm)
trend = 49.99
Up (mm)
trend = −2.72 ± 1.42 mm/yr
year

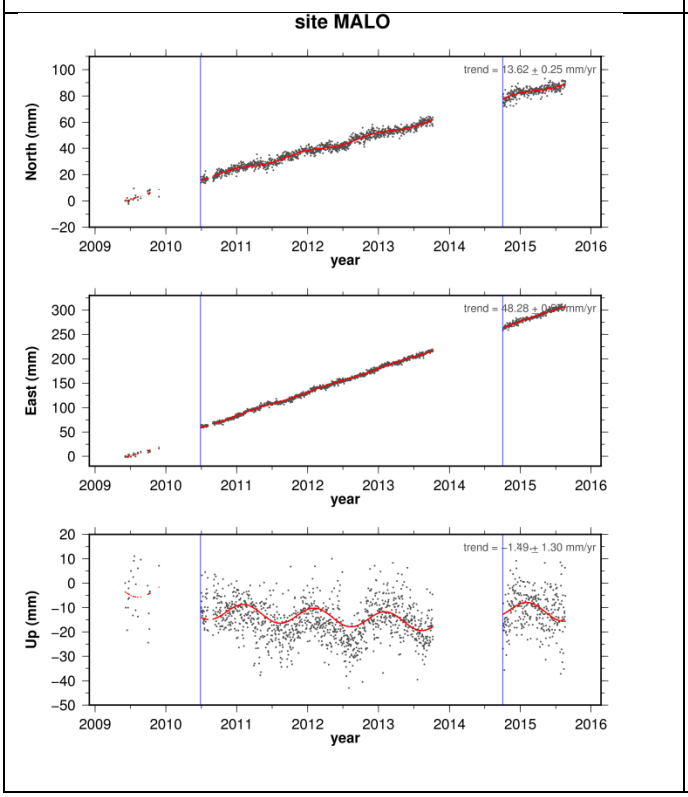
site MALO
North (mm)
trend = 13.62 ± 0.25 mm/yr
East (mm)
trend = 48.28
Up (mm)
trend = −1.49 ± 1.30 mm/yr
year

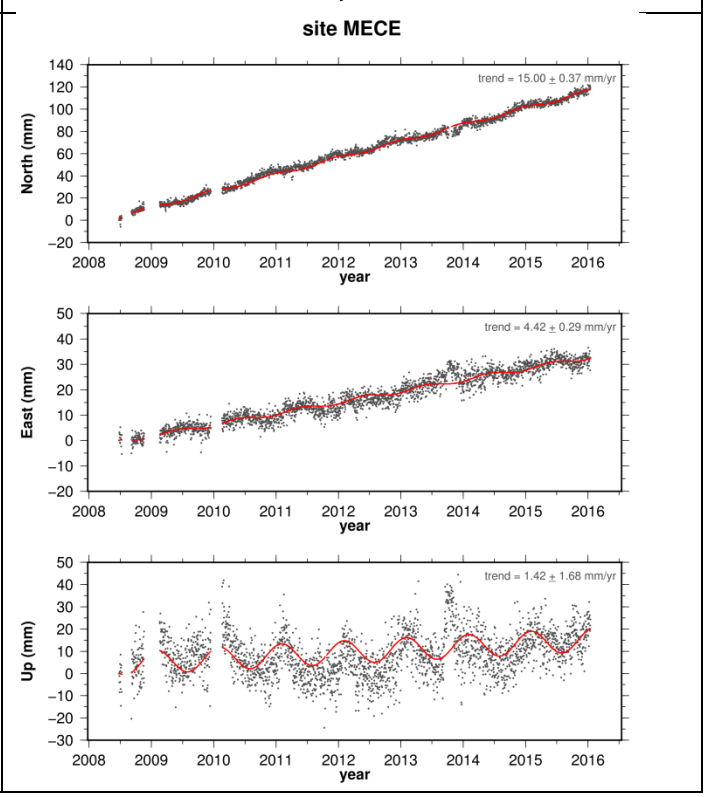
site MECE
North (mm)
trend = 15.00 ± 0.37 mm/yr
East (mm)
trend = 4.42 ± 0.29 mm/yr
Up (mm)
trend = 1.42 ± 1.68 mm/yr
year

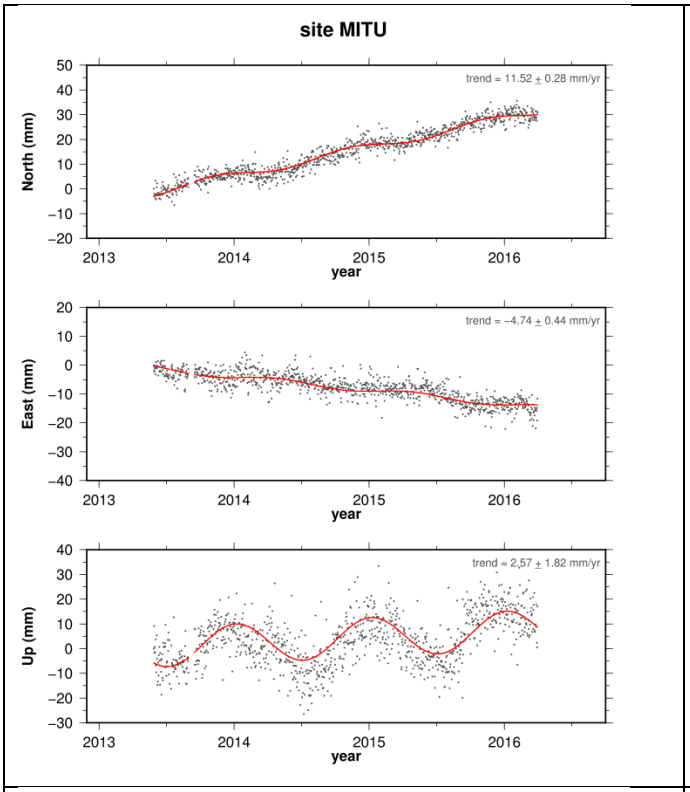
site MITU
North (mm)
trend = 11.52 ± 0.28 mm/yr
East (mm)
trend = −4.74 ± 0.44 mm/yr
Up (mm)
trend = 2.57 ± 1.82 mm/yr
year

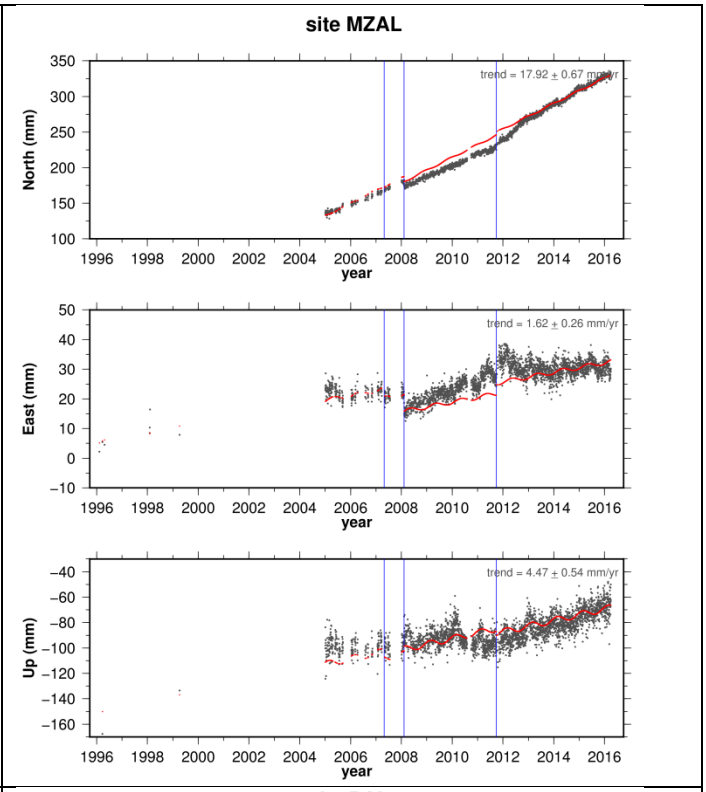
site MZAL
North (mm)
trend = 17.92 ± 0.67 mm/yr
East (mm)
trend = 1.62 ± 0.26 mm/yr
Up (mm)
trend = 4.47 ± 0.54 mm/yr
year

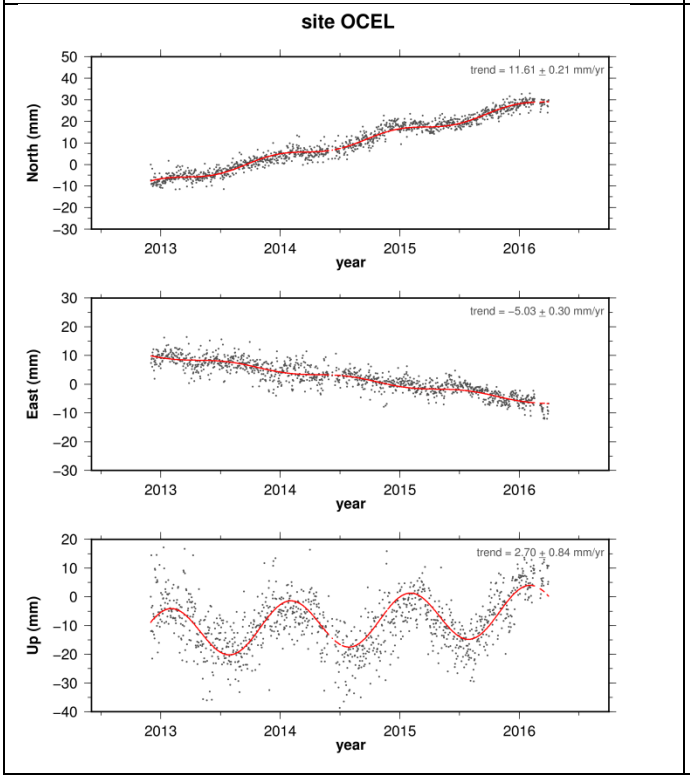
site OCEL
North (mm)
trend = 11.61 ± 0.21 mm/yr
East (mm)
trend = −5.03 ± 0.30 mm/yr
Up (mm)
trend = 2.70 ± 0.84 mm/yr
year

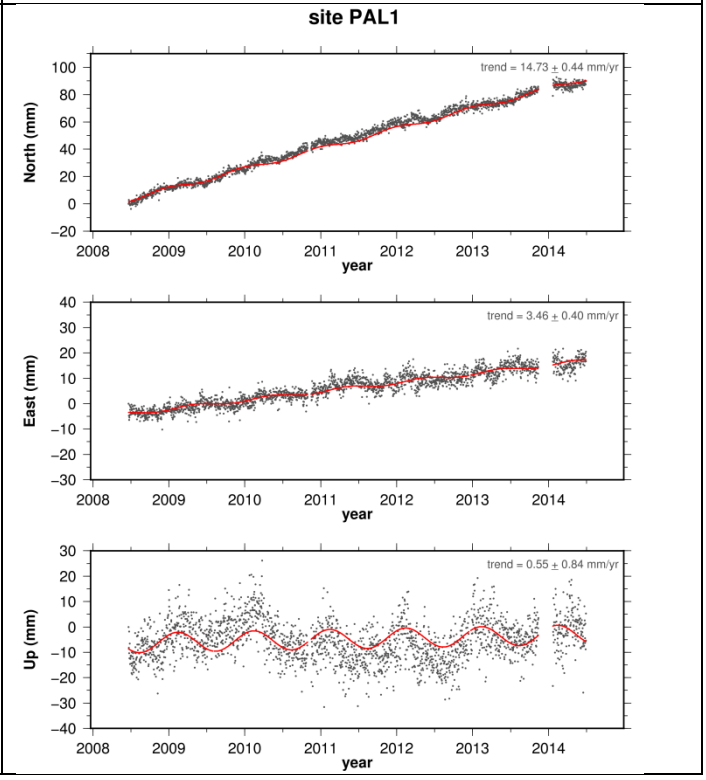
site PAL1
North (mm)
trend = 14.73 ± 0.44 mm/yr
East (mm)
trend = 3.46 ± 0.40 mm/yr
Up (mm)
trend = 0.55 ± 0.84 mm/yr
year

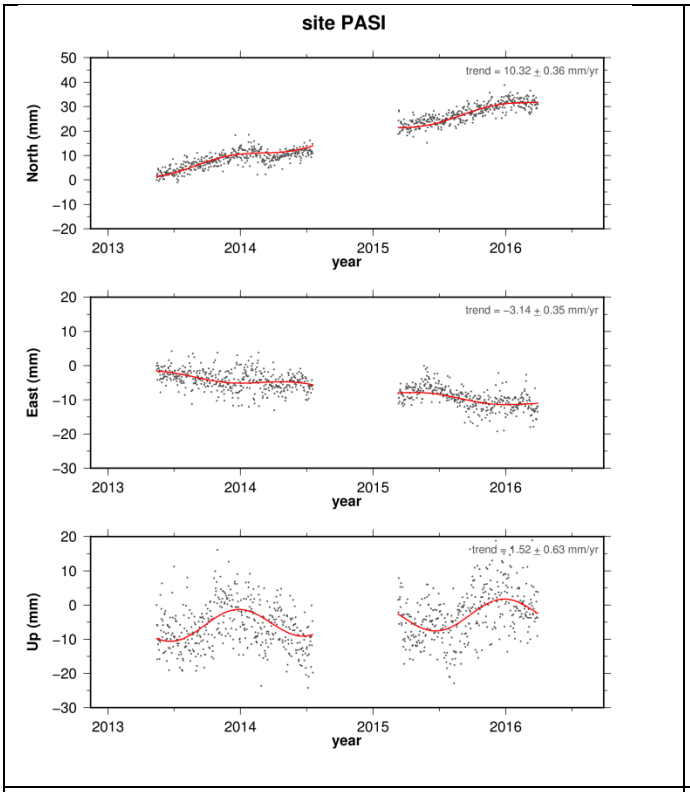
site PASI
North (mm)
trend = 10.32 ± 0.36 mm/yr
East (mm)
trend = −3.14 ± 0.35 mm/yr
Up (mm)
trend = 1.52 ± 0.63 mm/yr
year

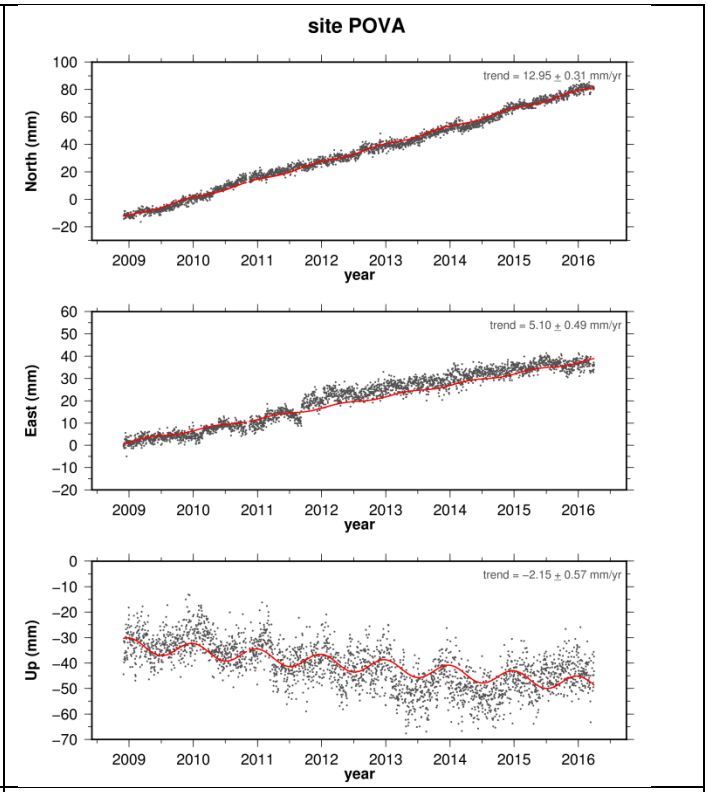
site POVA
North (mm)
trend = 12.95 ± 0.31 mm/yr
East (mm)
trend = 5.10 ± 0.49 mm/yr
Up (mm)
trend = −2.15 ± 0.57 mm/yr
year

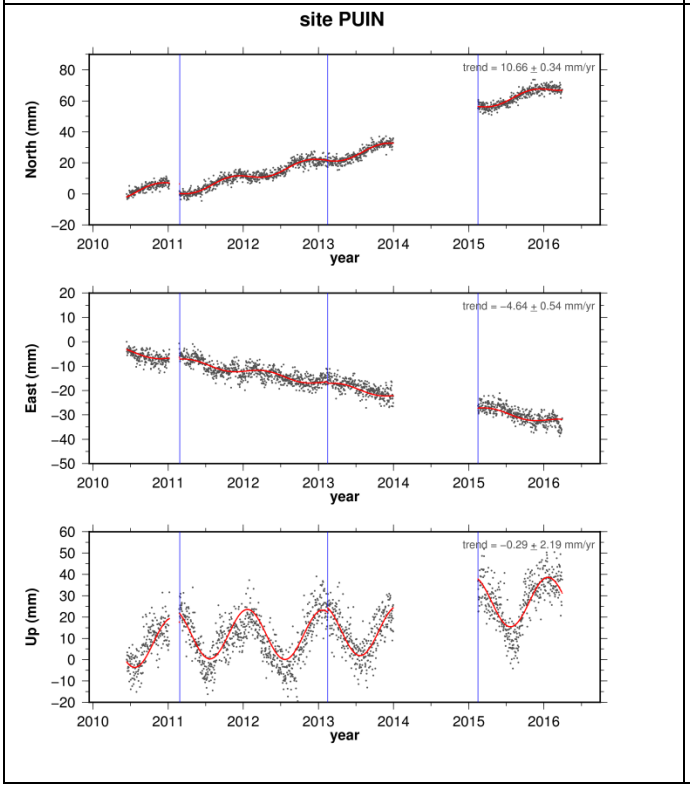
site PUIN
North (mm)
trend = 10.66 ± 0.34 mm/yr
East (mm)
trend = −4.64 ± 0.54 mm/yr
Up (mm)
trend = −0.29 ± 2.19 mm/yr
year

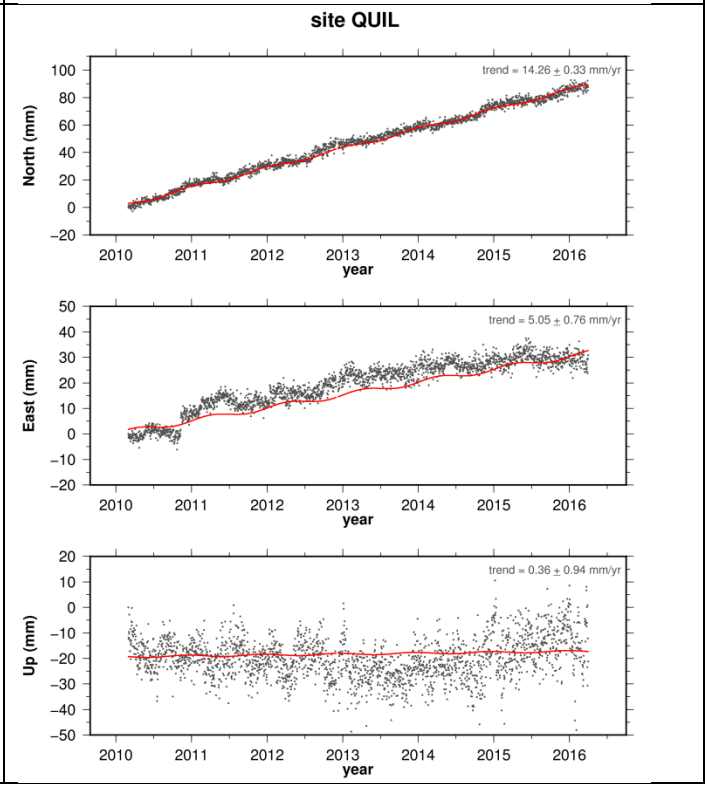
site QUIL
North (mm)
trend = 14.26 ± 0.33 mm/yr
East (mm)
trend = 5.05 ± 0.76 mm/yr
Up (mm)
trend = 0.36 ± 0.94 mm/yr
year

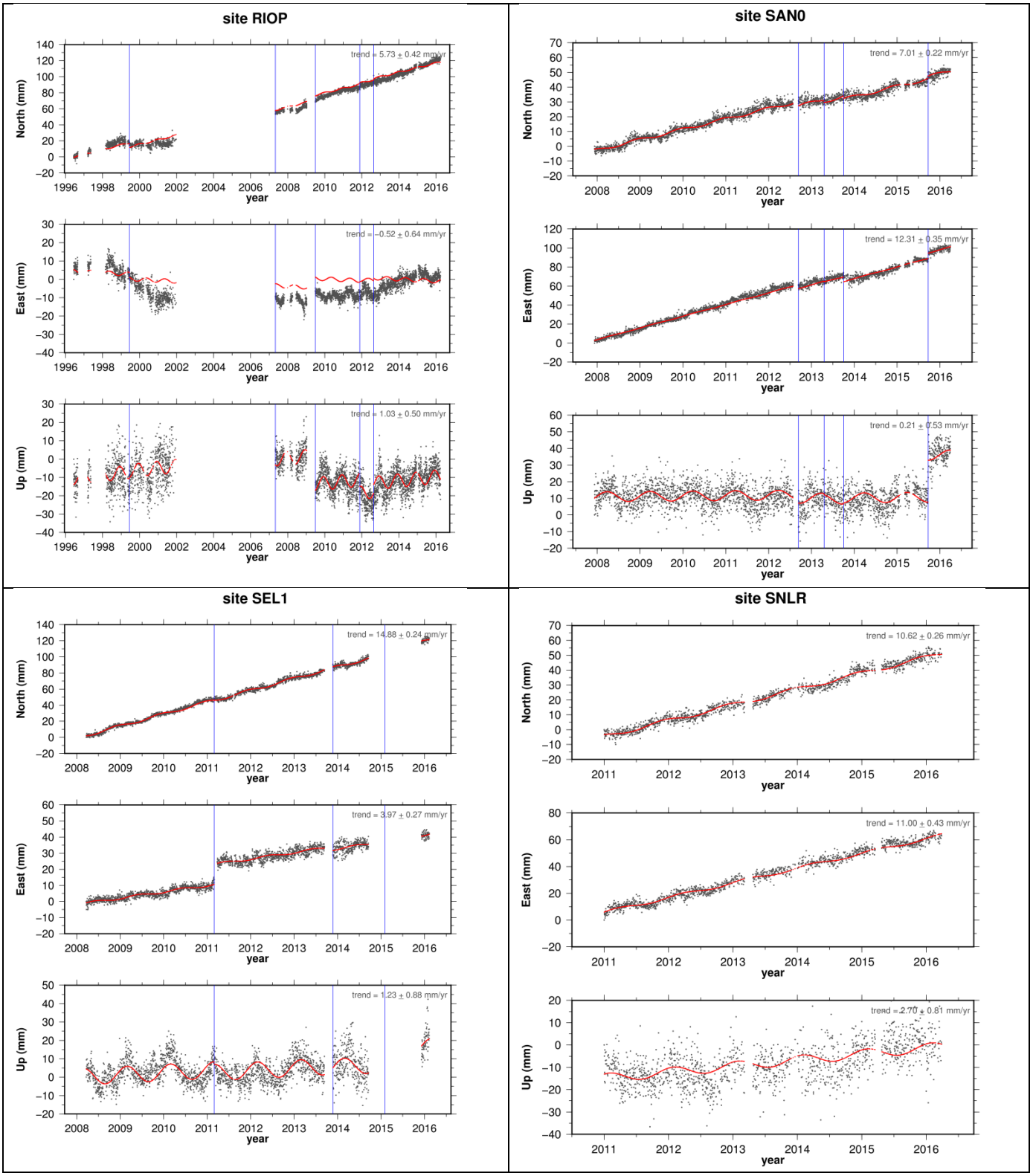
site RIOP
North (mm)
trend = 5.73 ± 0.42 mm/yr
East (mm)
trend = −0.52 ± 0.64 mm/yr
Up (mm)
trend = 1.03 ± 0.50 mm/yr
year
site SAN0
North (mm)
trend = 7.01 ± 0.22 mm/yr
East (mm)
trend = 12.31 ± 0.35 mm/yr
Up (mm)
trend = 0.21 ± 0.53 mm/yr
year
site SEL1
North (mm)
trend = 14.88 ± 0.24 mm/yr
East (mm)
trend = 3.97 ± 0.27 mm/yr
Up (mm)
trend = 1.23 ± 0.88 mm/yr
year
site SNLR
North (mm)
trend = 10.62 ± 0.26 mm/yr
East (mm)
trend = 11.00 ± 0.43 mm/yr
Up (mm)
trend = 2.70 ± 0.81 mm/yr
year

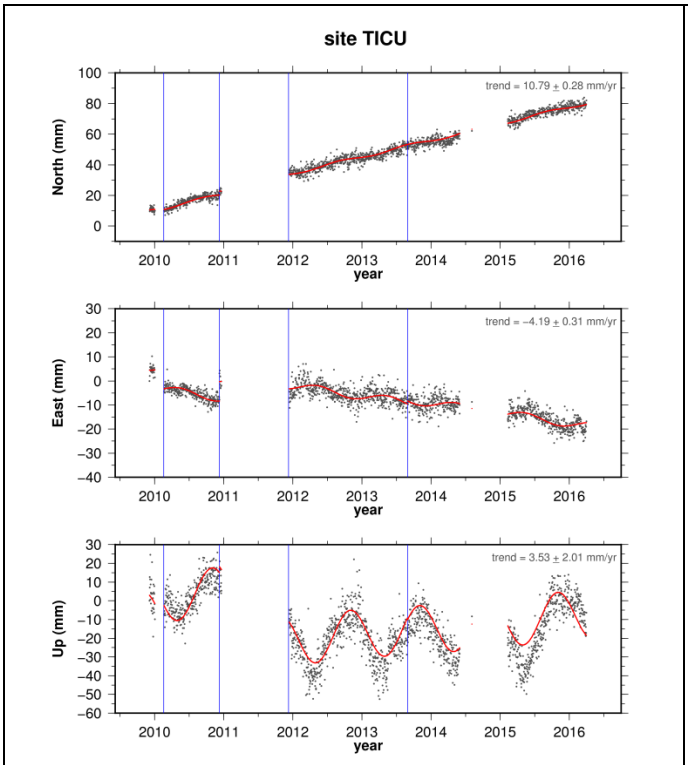
site TICU
North (mm)
trend = 10.79 ± 0.28 mm/yr
East (mm)
trend = −4.19 ± 0.31 mm/yr
Up (mm)
trend = 3.53 ± 2.01 mm/yr
year

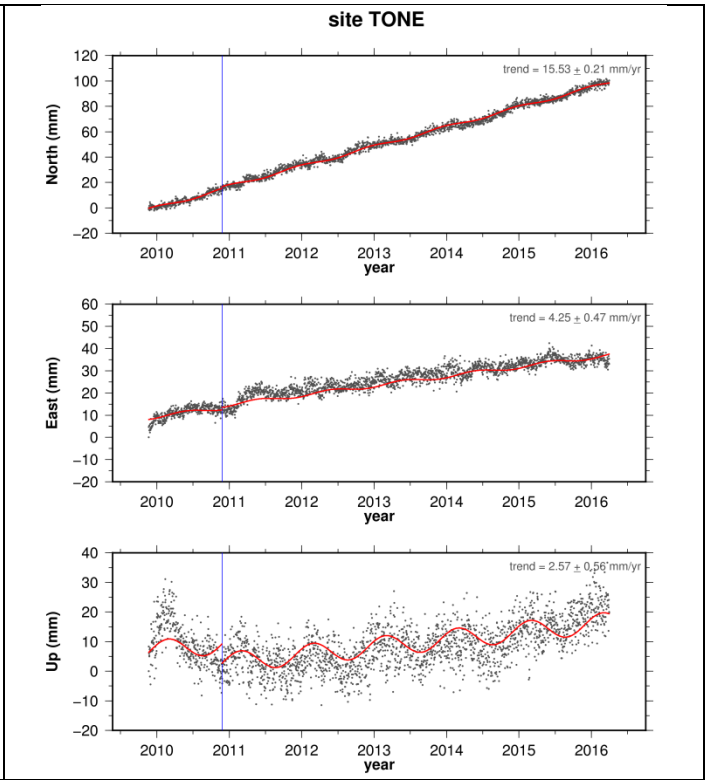
site TONE
North (mm)
trend = 15.53 ± 0.21 mm/yr
East (mm)
trend = 4.25 ± 0.47 mm/yr
Up (mm)
trend = 2.57 ± 0.56 mm/yr
year

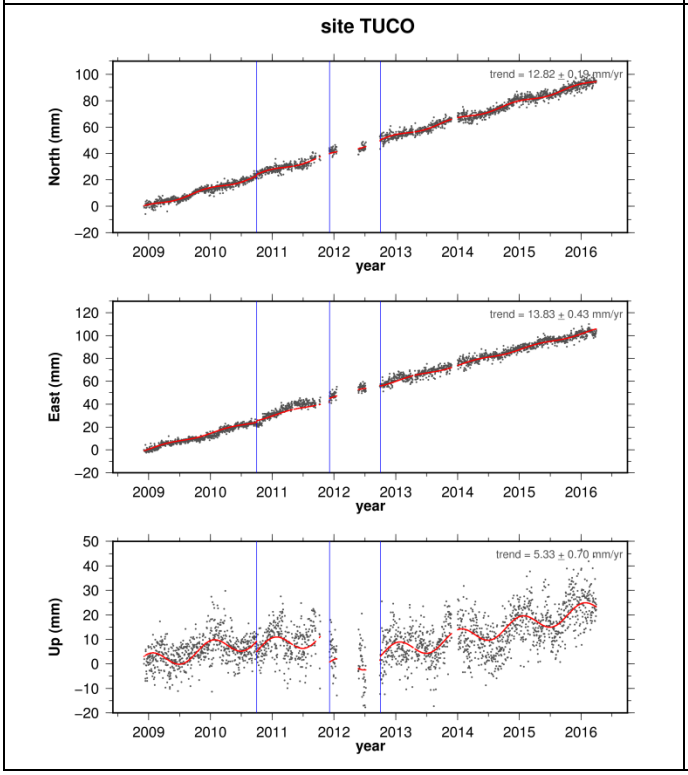
site TUCO
North (mm)
trend = 12.82 ± 0.19 mm/yr
East (mm)
trend = 13.83 ± 0.43 mm/yr
Up (mm)
trend = 5.33 ± 0.70 mm/yr
year

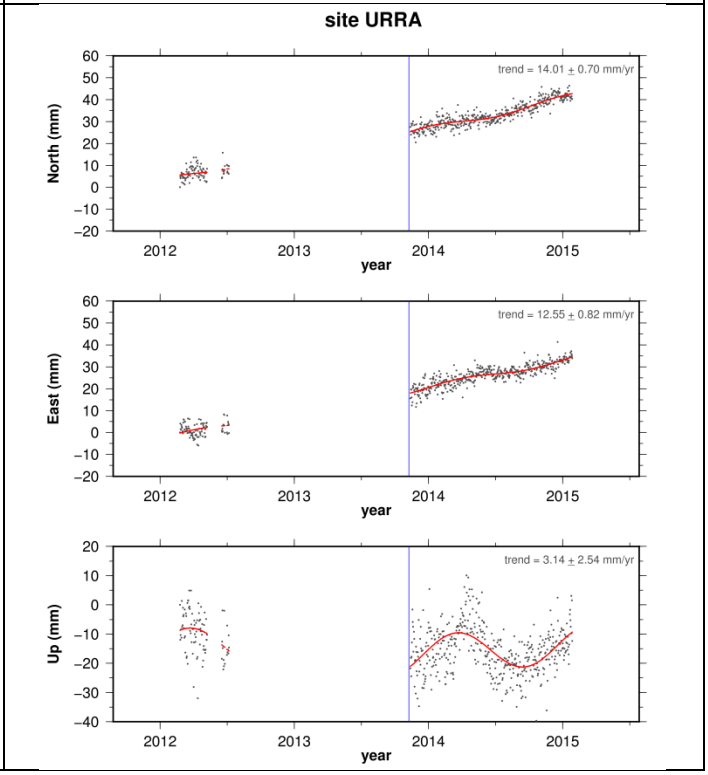
site URRA
North (mm)
trend = 14.01 ± 0.70 mm/yr
East (mm)
trend = 12.55 ± 0.82 mm/yr
Up (mm)
trend = 3.14 ± 2.54 mm/yr
year

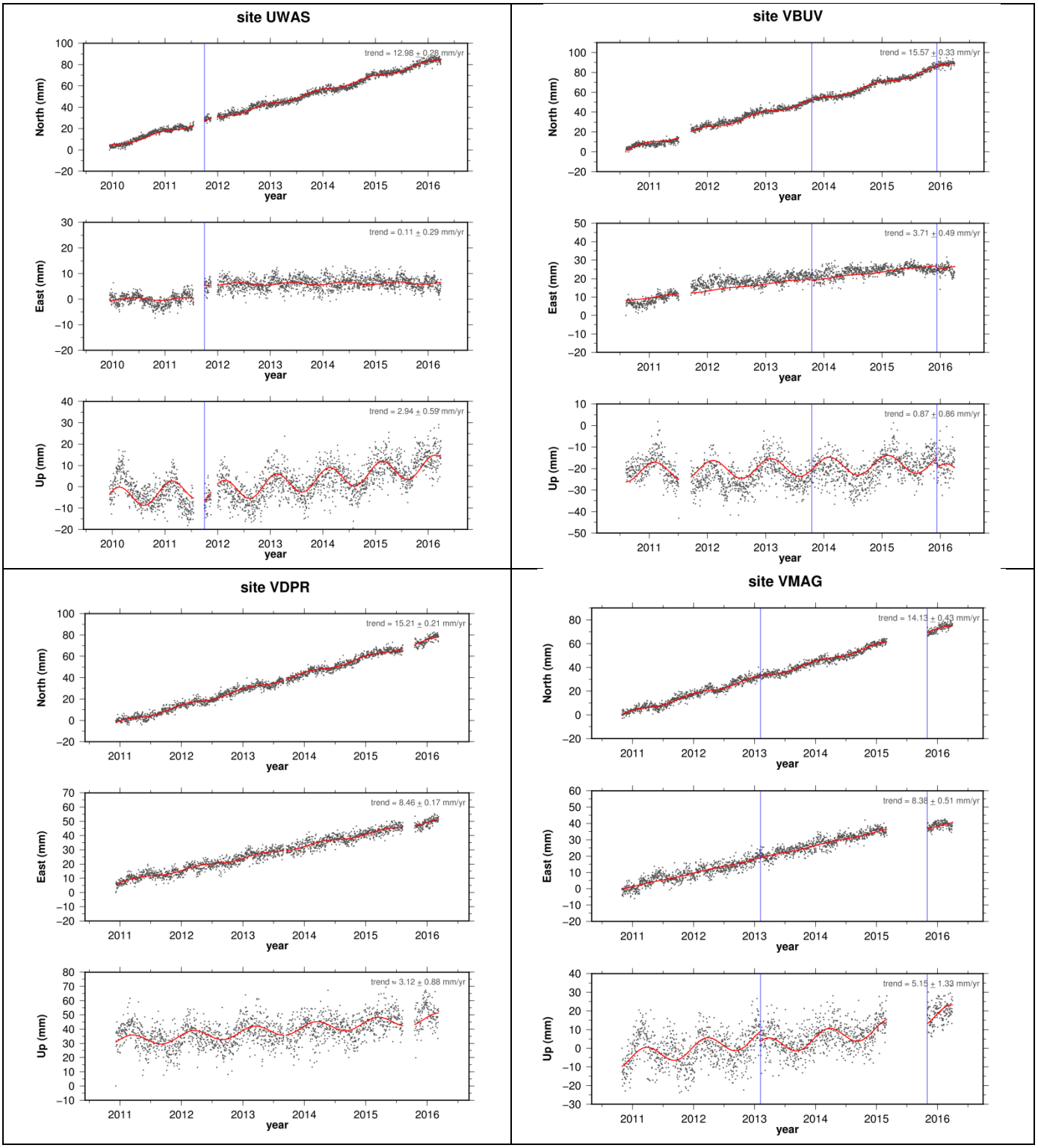
site UWAS
trend = 12.98 ± 0.28 mm/yr
North (mm)
trend = 0.11 ± 0.29 mm/yr
East (mm)
trend = 2.94 ± 0.59 mm/yr
Up (mm)
year
site VBUV
trend = 15.57 ± 0.33 mm/yr
North (mm)
trend = 3.71 ± 0.49 mm/yr
East (mm)
trend = 0.87 ± 0.86 mm/yr
Up (mm)
year
site VDPR
trend = 15.21 ± 0.21 mm/yr
North (mm)
trend = 8.46 ± 0.17 mm/yr
East (mm)
trend = 3.12 ± 0.88 mm/yr
Up (mm)
year
site VMAG
trend = 14.13 ± 0.43 mm/yr
North (mm)
trend = 8.38 ± 0.51 mm/yr
East (mm)
trend = 5.15 ± 1.33 mm/yr
Up (mm)
year

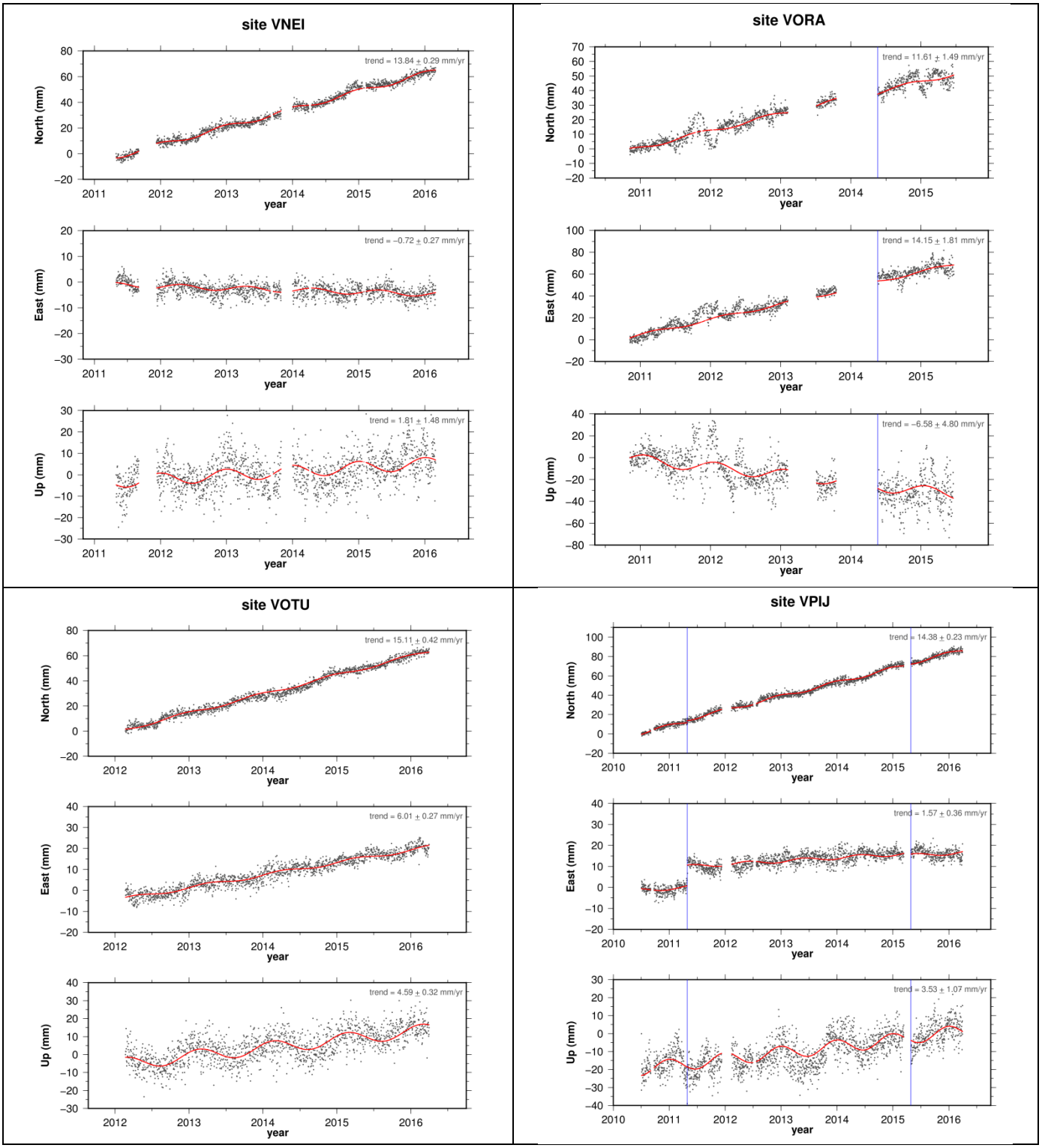
site VNEI
North (mm)
trend = 13.84 ± 0.29 mm/yr
East (mm)
trend = −0.72 ± 0.27 mm/yr
Up (mm)
trend = 1.81 ± 1.48 mm/yr
year
site VORA
North (mm)
trend = 11.61 ± 1.49 mm/yr
East (mm)
trend = 14.15 ± 1.81 mm/yr
Up (mm)
trend = −6.58 ± 4.80 mm/yr
year
site VOTU
North (mm)
trend = 15.11 ± 0.42 mm/yr
East (mm)
trend = 6.01 ± 0.27 mm/yr
Up (mm)
trend = 4.59 ± 0.32 mm/yr
year
site VPIJ
North (mm)
trend = 14.38 ± 0.23 mm/yr
East (mm)
trend = 1.57 ± 0.36 mm/yr
Up (mm)
trend = 3.53 ± 1.07 mm/yr
year

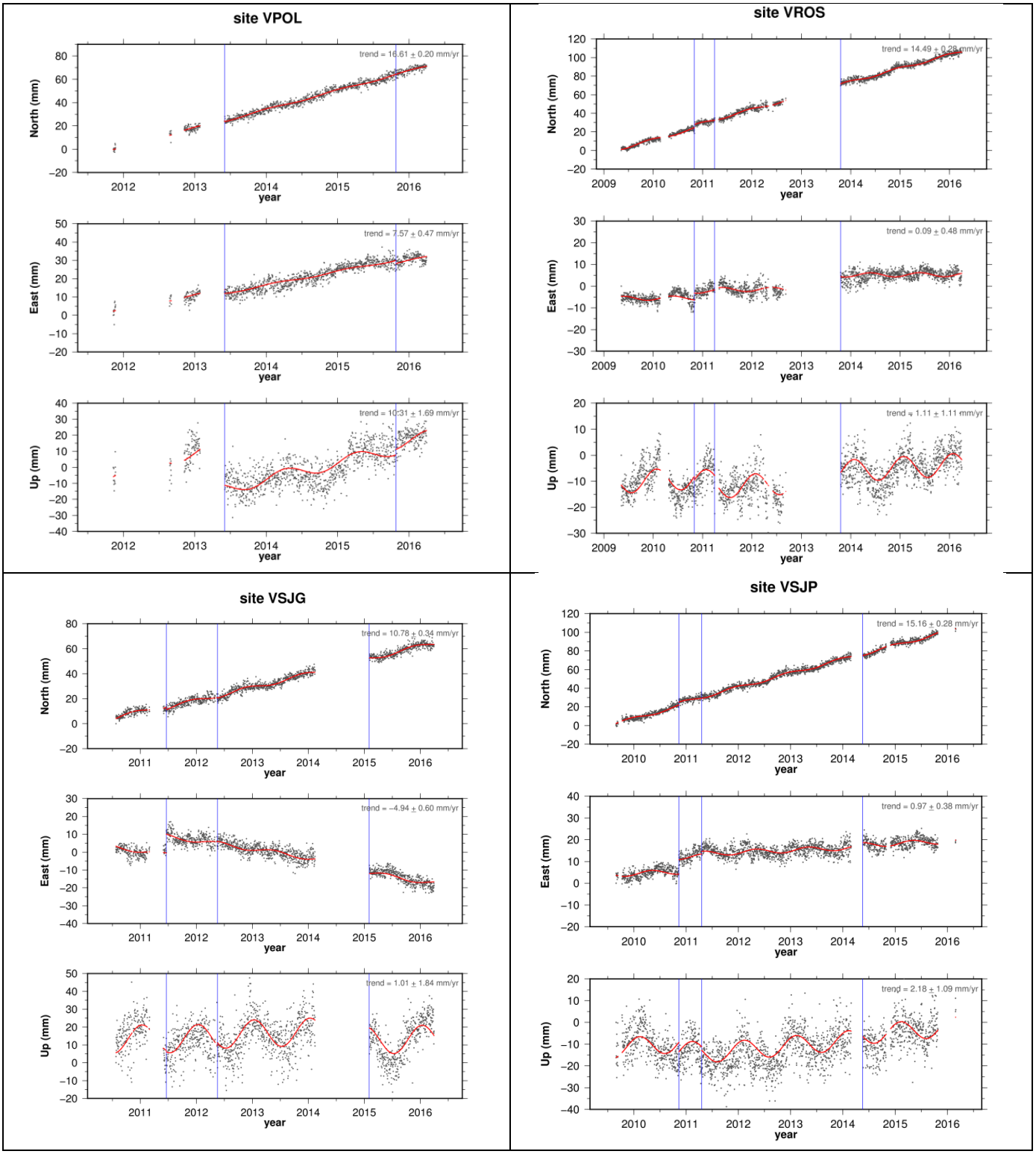
site VPOL
North (mm)
East (mm)
Up (mm)
year
site VROS
North (mm)
East (mm)
Up (mm)
year
site VSJG
North (mm)
East (mm)
Up (mm)
year
site VSJP
North (mm)
East (mm)
Up (mm)
year

Appendix D

PSD components

North component

ID	Obser. number	Gaps (%)	Data points (n)	Data used (N)	Segments number (K)	Segments Lenght (L)	U	dt	G scale (Amp)	Total variance in signal (time domain)	Total variance in signal (spectrum)	freq0	freq1	Standar deviation of the driving noise	Fraction for model Powerlaw	Fraction for model white	Powerlaw: value of fractional difference (d)
ACP1	2582	18.2	2580	2580	7	645	0.9608	8.64e+04	0.1894	6.331	5.756	1,79E-04	5,78E-02	217.603	0.39875	0.60125	0.4055
ACP6	2591	6175	2588	2588	7	647	0.9609	8.64e+04	0.1891	8.898	8.315	1,79E-04	5,78E-02	261.050	0.99999	0.00001	0.3126
ALPA	2390	18.28	2388	2388	7	597	0.9619	8.64e+04	0.1969	5.784	5.129	1,94E-04	5,78E-02	169.031	0.18324	0.81676	0.6338
AUCA	1916	10.8	1916	1916	7	479	0.9634	8.64e+04	0.2198	4.101	3.739	2,42E-04	5,78E-02	183.181	0.47299	0.52701	0.3751
BAAP	1417	22.58	1416	1416	7	354	0.968	8.64e+04	0.2557	3.109	2.441	3,27E-04	5,79E-02	171.162	0.99999	0.00001	0.1789
BACO	1332	6682	1332	1332	7	333	0.9656	8.64e+04	0.2637	8.784	8.453	3,48E-04	5,77E-02	204.612	0.28404	0.71596	0.6016
BAEZ	1848	86.42	1848	1848	7	462	0.9642	8.64e+04	0.2238	4.979	0	2,51E-04	5,79E-02	215.949	100000	0.00000	0.1672
BAME	888	41.22	888	888	7	222	0.9727	8.64e+04	0.3229	3.889	3.179	5,21E-04	5,79E-02	192.180	100000	0.00000	0.1790
BAPA	2009	9955	2008	2008	7	502	0.9636	8.64e+04	0.2147	4.538	4.147	2,31E-04	5,79E-02	187.478	0.46212	0.53788	0.3867
BARU	1022	12.52	1020	1020	7	255	0.9688	8.64e+04	0.3013	3.511	3.067	4,54E-04	5,76E-02	180.586	0.99999	0.00001	0.1926
BASO	2572	16.6	2572	2572	7	643	0.9606	8.64e+04	0.1897	7.608	6.554	1,80E-04	5,78E-02	215.778	0.15508	0.84492	0.5658
BOBG	935	0.107	932	932	7	233	0.9697	8.64e+04	0.3152	4.552	4.607	4,97E-04	5,76E-02	200.579	0.60401	0.39599	0.2809
BOGT	7815	27.98	7812	7812	7	1953	0.9585	8.64e+04	0.1089	5.629	4.121	5,93E-05	5,78E-02	197.040	0.66951	0.33049	0.4095
BUGT	2708	22.86	2708	2708	7	677	0.9614	8.64e+04	0.1849	6.062	4.578	1,71E-04	5,78E-02	227.883	0.31597	0.68403	0.3774
CAP1	2463	22.17	2460	2460	7	615	0.9617	8.64e+04	0.194	5.282	5.065	1,88E-04	5,78E-02	167.187	0.18664	0.81336	0.5711
CIA1	2701	2518	2700	2700	7	675	0.9612	8.64e+04	0.1852	5.509	5.477	1,71E-04	5,78E-02	166.627	0.22721	0.77279	0.6579
CN19	1021	0.3918	1020	1020	7	255	0.9688	8.64e+04	0.3013	3.13	3.21	4,54E-04	5,76E-02	166.700	100000	0.00000	0.2284
CN28	1114	11.13	1112	1112	7	278	0.9718	8.64e+04	0.2886	4.204	3.964	4,16E-04	5,79E-02	200.267	0.99020	0.00980	0.1511
CN33	1447	0.6911	1444	1444	7	361	0.9634	8.64e+04	0.2532	16.09	16.5	3,21E-04	5,77E-02	310.558	0.99999	0.00001	0.4398
CN35	1300	0.2308	1300	1300	7	325	0.9647	8.64e+04	0.2669	4.455	4.253	3,56E-04	5,77E-02	194.967	0.88497	0.11503	0.2653
CN37	1317	4935	1316	1316	7	329	0.9652	8.64e+04	0.2653	9.14	9.241	3,52E-04	5,77E-02	192.094	0.20038	0.79962	0.6845
CN38	1310	0.8397	1308	1308	7	327	0.9649	8.64e+04	0.2661	3.479	3.335	3,54E-04	5,77E-02	181.860	0.99990	0.00010	0.1560
CN40	1716	0.1748	1716	1716	7	429	0.9631	8.64e+04	0.2323	4.547	4.548	2,70E-04	5,77E-02	197.177	0.73951	0.26049	0.2922
COEC	1373	2258	1372	1372	7	343	0.964	8.64e+04	0.2598	4.154	4.165	3,37E-04	5,77E-02	160.933	0.38074	0.61926	0.4907
CORO	2742	17.72	2740	2740	7	685	0.9605	8.64e+04	0.1838	4.043	3.353	1,69E-04	5,78E-02	183.892	0.50622	0.49378	0.3488
CUC1	1961	4233	1960	1960	7	490	0.9645	8.64e+04	0.2174	7.189	6.991	2,36E-04	5,79E-02	204.301	0.22566	0.77434	0.5497
ESMR	1917	1878	1916	1916	7	479	0.9634	8.64e+04	0.2198	4.809	4.863	2,42E-04	5,78E-02	178.485	0.23477	0.76523	0.5265
GLPS	4739	21.92	4736	4736	7	1184	0.9599	8.64e+04	0.1398	3.269	2.467	9,78E-05	5,79E-02	146.472	0.74470	0.25530	0.3956
GUAP	1824	26.81	1824	1824	7	456	0.9656	8.64e+04	0.2253	6.411	5.019	2,54E-04	5,79E-02	233.035	0.23905	0.76095	0.4180
ISCO	1778	21.32	1776	1776	7	444	0.9647	8.64e+04	0.2283	8.323	7.123	2,61E-04	5,79E-02	262.231	0.28456	0.71544	0.4221
MALO	2269	34.33	2268	2268	7	567	0.9615	8.64e+04	0.2021	4.957	3.973	2,04E-04	5,78E-02	209.682	0.41095	0.58905	0.3292
MECE	2760	9746	2760	2760	7	690	0.9623	8.64e+04	0.1832	6.778	6.35	1,68E-04	5,79E-02	196.076	0.19996	0.80004	0.5852
MITU	1038	2119	1036	1036	7	259	0.9693	8.64e+04	0.299	5.351	5.327	4,47E-04	5,76E-02	219.094	0.36038	0.63962	0.3107
MZAL	4106	28.23	4104	4104	7	1026	0.9604	8.64e+04	0.1502	76.98	83.12	1,13E-04	5,79E-02	181.025	0.11723	0.88277	0.7435
OCEL	1217	4601	1216	1216	7	304	0.9685	8.64e+04	0.2759	4.753	4.491	3,81E-04	5,79E-02	206.658	0.55542	0.44458	0.2682
PAL1	2201	4771	2200	2200	7	550	0.9636	8.64e+04	0.2052	7.085	7.068	2,10E-04	5,79E-02	173.662	0.17455	0.82545	0.6093
PASI	1051	22.93	1048	1048	7	262	0.9701	8.64e+04	0.2972	5.153	4.915	4,42E-04	5,79E-02	206.090	0.32464	0.67536	0.3835
POVA	2678	1083	2676	2676	7	669	0.9609	8.64e+04	0.186	5.783	5.803	1,73E-04	5,78E-02	175.222	0.18858	0.81142	0.5786
PUIN	2118	21.86	2116	2116	7	529	0.9619	8.64e+04	0.2092	4.193	3.961	2,19E-04	5,78E-02	193.841	0.32533	0.67467	0.3378
QUIL	2222	0.9901	2220	2220	7	555	0.9622	8.64e+04	0.2042	5.766	5.9	2,09E-04	5,78E-02	182.190	0.21208	0.78792	0.5495
RIOP	7235	46.72	7232	7232	7	1808	0.959	8.64e+04	0.1132	18.95	13.34	6,40E-05	5,79E-02	181.286	0.19593	0.80407	0.6441
SAN0	3037	4379	3036	3036	7	759	0.961	8.64e+04	0.1746	4.284	4.22	1,52E-04	5,78E-02	179.092	0.30941	0.69059	0.4468
SEL1	2883	18.94	2880	2880	7	720	0.9615	8.64e+04	0.1793	3.395	3.126	1,61E-04	5,79E-02	156.323	0.45028	0.54972	0.4290
SNLR	1915	28.77	1912	1912	7	478	0.9654	8.64e+04	0.2201	5.385	3.745	2,42E-04	5,79E-02	206.938	0.24099	0.75901	0.4614
TICU	2308	28.86	2308	2308	7	577	0.9621	8.64e+04	0.2003	4.862	3.842	2,01E-04	5,78E-02	200.863	0.32518	0.67482	0.3848
TONE	2323	0.1722	2320	2320	7	580	0.9626	8.64e+04	0.1998	4.162	4.324	2,00E-04	5,79E-02	171.300	0.46554	0.53446	0.4255
TUCO	2675	13.72	2672	2672	7	668	0.9623	8.64e+04	0.1862	4.216	3.59	1,73E-04	5,79E-02	190.312	0.47454	0.52546	0.3300
URRA	1069	50.33	1068	1068	7	267	0.9669	8.64e+04	0.2944	5.339	4.295	4,33E-04	5,77E-02	224.290	0.99999	0.00001	0.1776
UWAS	2302	5169	2300	2300	7	575	0.962	8.64e+04	0.2006	4.276	4.082	2,01E-04	5,78E-02	160.038	0.49414	0.50586	0.4540
VBUV	2063	4023	2060	2060	7	515	0.9626	8.64e+04	0.212	4.705	4.525	2,25E-04	5,78E-02	168.841	0.46884	0.53116	0.4605
VDPR	1919	4534	1916	1916	7	479	0.9634	8.64e+04	0.2198	5.897	5.603	2,42E-04	5,78E-02	216.600	0.53822	0.46178	0.3641
VMAG	1980	12.58	1980	1980	7	495	0.9628	8.64e+04	0.2162	4.441	3.964	2,34E-04	5,78E-02	184.788	0.19214	0.80786	0.5309
VNEI	1765	12.12	1764	1764	7	441	0.9622	8.64e+04	0.2291	4.769	4.246	2,62E-04	5,77E-02	184.899	0.31614	0.68386	0.4640
VORA	1687	24.3	1684	1684	7	421	0.9624	8.64e+04	0.2345	15.3	14.38	2,75E-04	5,77E-02	288.783	0.70574	0.29426	0.5305
VOTU	1500	0.06667	1500	1500	7	375	0.9648	8.64e+04	0.2485	5.531	5.628	3,09E-04	5,77E-02	190.285	0.26819	0.73181	0.5071
VPIJ	2099	7384	2096	2096	7	524	0.9635	8.64e+04	0.2102	3.963	3.729	2,21E-04	5,79E-02	174.325	0.61609	0.38391	0.3523
VPOL	1603	29.57	1600	1600	7	400	0.9651	8.64e+04	0.2406	4.099	3.765	2,89E-04	5,79E-02	197.300	0.99990	0.00010	0.1545
VROS	2518	23.39	2516	2516	7	629	0.9611	8.64e+04	0.1918	3.313	2.989	1,84E-04	5,78E-02	162.361	0.81693	0.18307	0.3178
VSIG	2076	23.89	2076	2076	7	519	0.9629	8.64e+04	0.2112	4.482	4.126	2,23E-04	5,78E-02	202.209	0.82919	0.17081	0.2256
VSIP	2376	11.66	2376	2376	7	594	0.9634	8.64e+04	0.1974	4.244	3.845	1,95E-04	5,79E-02	183.853	0.51201	0.48799	0.3725

Table D2. East component

ID	Obser. number	Gaps (%)	Data points (n)	Data used (N)	Segments number (K)	Segments Lenght (L)	U	dt	G scale (Amp)	Total variance in signal (time domain)	Total variance in signal (spectrum)	freq0	freq1	Standar deviation of the driving noise	Fraction for model Powerlaw	Fraction for model white	Powerlaw: value of fractional difference (d)
ACP1	2582	18.24	2580	2580	7	645	0.9608	8.64e+04	0.1894	5.578	4.988	1,79E-04	5,78E-02	216.626	0.32675	0.67325	0.3919
ACP6	2591	6059	2588	2588	7	647	0.9609	8.64e+04	0.1891	6.37	5.995	1,79E-04	5,78E-02	213.630	0.55610	0.44390	0.3814
ALPA	2390	18.45	2388	2388	7	597	0.9619	8.64e+04	0.1969	8.65	7.314	1,94E-04	5,78E-02	170.568	0.12553	0.87447	0.7160
AUCA	1916	10.65	1916	1916	7	479	0.9634	8.64e+04	0.2198	5.616	4.944	2,42E-04	5,78E-02	203.552	0.43382	0.56618	0.4350
BAAP	1417	22.79	1416	1416	7	354	0.968	8.64e+04	0.2557	4.754	3.819	3,27E-04	5,79E-02	191.926	0.39267	0.60733	0.4266
BACO	1332	7132	1332	1332	7	333	0.9656	8.64e+04	0.2637	7.891	7.437	3,48E-04	5,77E-02	232.939	0.11321	0.88679	0.6370
BAEZ	1848	86.31	1848	1848	7	462	0.9642	8.64e+04	0.2238	9.289	0	2,51E-04	5,79E-02	281.116	0.99993	0.00007	0.2604
BAME	888	41.67	888	888	7	222	0.9727	8.64e+04	0.3229	7.355	6.163	5,21E-04	5,79E-02	241.227	0.42915	0.57085	0.4126
BAPA	2009	9955	2008	2008	7	502	0.9636	8.64e+04	0.2147	5.655	5.058	2,31E-04	5,79E-02	215.152	0.36005	0.63995	0.4105
BARU	1022	12.52	1020	1020	7	255	0.9688	8.64e+04	0.3013	5.006	4.342	4,54E-04	5,76E-02	195.904	0.52803	0.47197	0.3900
BASO	2572	16.64	2572	2572	7	643	0.9606	8.64e+04	0.1897	18.22	16.31	1,80E-04	5,78E-02	227.821	0.09616	0.90384	0.7192
BOBG	935	0.2139	932	932	7	233	0.9697	8.64e+04	0.3152	5.402	5.374	4,97E-04	5,76E-02	214.270	0.33095	0.66905	0.4120
BOGT	7811	28.15	7808	7808	7	1952	0.959	8.64e+04	0.1089	6.787	5.07	5,93E-05	5,79E-02	211.902	0.63927	0.36073	0.4353
BUGT	2708	23.01	2708	2708	7	677	0.9614	8.64e+04	0.1849	6.381	4.952	1,71E-04	5,78E-02	231.178	0.14782	0.85218	0.5051
CAPI	2463	22.13	2460	2460	7	615	0.9617	8.64e+04	0.194	4.773	4.476	1,88E-04	5,78E-02	189.314	0.52644	0.47356	0.4049
CIA1	2701	2481	2700	2700	7	675	0.9612	8.64e+04	0.1852	11.77	12.12	1,71E-04	5,78E-02	190.686	0.30640	0.69360	0.7262
CN19	1021	0.1959	1020	1020	7	255	0.9688	8.64e+04	0.3013	4.678	4.633	4,54E-04	5,76E-02	205.804	0.99988	0.00012	0.2161
CN28	1114	12.3	1112	1112	7	278	0.9718	8.64e+04	0.2886	5.892	5.265	4,16E-04	5,79E-02	235.007	0.89777	0.10223	0.1854
CN33	1447	0.2764	1444	1444	7	361	0.9634	8.64e+04	0.2532	11.06	11.52	3,21E-04	5,77E-02	256.451	0.27859	0.72141	0.6259
CN35	1300	0	1300	1300	7	325	0.9647	8.64e+04	0.2669	5.573	5.548	3,56E-04	5,77E-02	207.091	0.28819	0.71181	0.4750
CN37	1317	4784	1316	1316	7	329	0.9652	8.64e+04	0.2653	6.686	6.785	3,52E-04	5,77E-02	192.925	0.18328	0.81672	0.6145
CN38	1310	0.7634	1308	1308	7	327	0.9649	8.64e+04	0.2661	4.611	4.609	3,54E-04	5,77E-02	198.790	0.36764	0.63236	0.3701
CN40	1716	0.1166	1716	1716	7	429	0.9631	8.64e+04	0.2323	4.396	4.421	2,70E-04	5,77E-02	197.665	0.66986	0.33014	0.2760
COEC	1373	2185	1372	1372	7	343	0.964	8.64e+04	0.2598	12.25	12.84	3,37E-04	5,77E-02	196.972	0.20941	0.79059	0.6389
CORO	2743	18.05	2740	2740	7	685	0.9605	8.64e+04	0.1838	4.178	3.348	1,69E-04	5,78E-02	184.798	0.26623	0.73377	0.4621
CUC1	1961	4233	1960	1960	7	490	0.9645	8.64e+04	0.2174	82.88	88.92	2,36E-04	5,79E-02	219.091	0.12461	0.87539	0.7636
ESMR	1917	1826	1916	1916	7	479	0.9634	8.64e+04	0.2198	5.981	5.958	2,42E-04	5,78E-02	187.620	0.31515	0.68485	0.5626
GLPS	4739	22.35	4736	4736	7	1184	0.9599	8.64e+04	0.1398	2.918	2.194	9,78E-05	5,79E-02	141.777	0.44726	0.55274	0.4594
GUAP	1824	26.86	1824	1824	7	456	0.9656	8.64e+04	0.2253	7.802	6.069	2,54E-04	5,79E-02	239.956	0.30965	0.69035	0.4600
ISCO	1778	21.37	1776	1776	7	444	0.9647	8.64e+04	0.2283	11.34	9.661	2,61E-04	5,79E-02	301.210	0.25295	0.74705	0.4658
MALO	2269	34.6	2268	2268	7	567	0.9615	8.64e+04	0.2021	7.241	5.938	2,04E-04	5,78E-02	232.638	0.21836	0.78164	0.5163
MECE	2760	9167	2760	2760	7	690	0.9623	8.64e+04	0.1832	6.213	5.91	1,68E-04	5,79E-02	207.760	0.23957	0.76043	0.5327
MITU	1038	4239	1036	1036	7	259	0.9693	8.64e+04	0.299	7.181	7.004	4,47E-04	5,76E-02	248.408	0.22730	0.77270	0.4126
MZAL	7358	59.81	7356	7356	7	1839	0.9587	8.64e+04	0.1122	16.98	16.61	6,29E-05	5,78E-02	180.440	0.18988	0.81012	0.6448
OCEL	1216	6168	1216	1216	7	304	0.9685	8.64e+04	0.2759	6.096	5.699	3,81E-04	5,79E-02	229.073	0.59933	0.40067	0.3131
PAL1	2201	4907	2200	2200	7	550	0.9636	8.64e+04	0.2052	5.107	5.017	2,10E-04	5,79E-02	188.465	0.23597	0.76403	0.5625
PASI	1051	24.17	1048	1048	7	262	0.9701	8.64e+04	0.2972	7.012	6.382	4,42E-04	5,79E-02	249.087	0.44585	0.55415	0.3108
POVA	2679	1157	2676	2676	7	669	0.9609	8.64e+04	0.186	9.981	10.63	1,73E-04	5,78E-02	183.168	0.18732	0.81268	0.6366
PUIN	2118	21.77	2116	2116	7	529	0.9619	8.64e+04	0.2092	4.959	4.623	2,19E-04	5,78E-02	196.723	0.28595	0.71405	0.4647
QUIL	2222	0.9451	2220	2220	7	555	0.9622	8.64e+04	0.2042	21.11	22.63	2,09E-04	5,78E-02	195.877	0.25307	0.74693	0.6453
RIOP	7235	46.61	7232	7232	7	1808	0.959	8.64e+04	0.1132	47.2	38.26	6,40E-05	5,79E-02	193.797	0.11062	0.88938	0.7428
SAN0	3037	5.17	3036	3036	7	759	0.961	8.64e+04	0.1746	6.003	5.849	1,52E-04	5,78E-02	187.877	0.23655	0.76345	0.5446
SEL1	2883	19.91	2880	2880	7	720	0.9615	8.64e+04	0.1793	4.021	3.784	1,61E-04	5,79E-02	178.639	0.43973	0.56027	0.4118
SNLR	1915	28.72	1912	1912	7	478	0.9654	8.64e+04	0.2201	6.815	4.739	2,42E-04	5,79E-02	223.913	0.14220	0.85780	0.5668
TICU	2309	29.32	2308	2308	7	577	0.9621	8.64e+04	0.2003	6.949	5.221	2,01E-04	5,78E-02	245.602	0.49094	0.50906	0.3209
TONE	2323	0.2152	2320	2320	7	580	0.9626	8.64e+04	0.1998	7.317	7.55	2,00E-04	5,79E-02	180.349	0.28764	0.71236	0.5787
TUCO	2675	14.5	2672	2672	7	668	0.9623	8.64e+04	0.1862	6.612	5.778	1,73E-04	5,79E-02	195.930	0.30092	0.69908	0.5245
URRA	1069	50.51	1068	1068	7	267	0.9669	8.64e+04	0.2944	6.525	5.087	4,33E-04	5,77E-02	245.712	0.99998	0.00002	0.1957
UWAS	2302	5169	2300	2300	7	575	0.962	8.64e+04	0.2006	4.61	4.461	2,01E-04	5,78E-02	181.392	0.50898	0.49102	0.4340
VBUV	2063	4023	2060	2060	7	515	0.9626	8.64e+04	0.212	8.495	8.327	2,25E-04	5,78E-02	180.761	0.45256	0.54744	0.5230
VDPR	1919	4638	1916	1916	7	479	0.9634	8.64e+04	0.2198	6.504	6.447	2,42E-04	5,78E-02	237.123	0.57459	0.42541	0.3081
VMAG	1980	12.53	1980	1980	7	495	0.9628	8.64e+04	0.2162	6.392	5.58	2,34E-04	5,78E-02	220.277	0.27262	0.72738	0.4983
VNEI	1765	12.58	1764	1764	7	441	0.9622	8.64e+04	0.2291	5.58	5.117	2,62E-04	5,77E-02	210.467	0.35818	0.64182	0.4201
VORA	1687	24.13	1684	1684	7	421	0.9624	8.64e+04	0.2345	21.5	20.34	2,75E-04	5,77E-02	312.515	0.33821	0.66179	0.6124
VOTU	1500	0.3333	1500	1500	7	375	0.9648	8.64e+04	0.2485	5.108	5.052	3,09E-04	5,77E-02	208.005	0.36507	0.63493	0.3934
VPIJ	2099	7384	2096	2096	7	524	0.9635	8.64e+04	0.2102	5.138	4.771	2,21E-04	5,79E-02	191.546	0.38142	0.61858	0.4612
VPOL	1603	29.38	1600	1600	7	400	0.9651	8.64e+04	0.2406	5.615	5.273	2,89E-04	5,79E-02	209.749	0.31433	0.68567	0.4347
VROS	2518	23.23	2516	2516	7	629	0.9611	8.64e+04	0.1918	4.387	3.862	1,84E-04	5,78E-02	167.794	0.54119	0.45881	0.4608
VSJG	2076	23.89	2076	2076	7	519	0.9629	8.64e+04	0.2112	6.618	5.808	2,23E-04	5,78E-02	228.035	0.30891	0.69109	0.4478
VSJP	2376	11.66	2376	2376	7	594	0.9634	8.64e+04	0.1974	4.808	4.474	1,95E-04	5,79E-02	186.897	0.38410	0.61590	0.4599

Up component

ID	Obser. number	Gaps (%)	Data points (n)	Data used (N)	Segments number (K)	Segments Lenght (L)	U	dt	G scale (Amp)	Total variance in signal (time domain)	Total variance in signal (spectrum)	freq0	freq1	Standar deviation of the driving noise	Fraction for model Powerlaw	Fractio for mod white
ACP1	2582	18.59	2580	2580	7	645	0.9608	8.64e+04	0.1894	49.78	44.79	1,79E-04	5,78E-02	660.476	0.13828	0.8617
ACP6	2591	6021	2588	2588	7	647	0.9609	8.64e+04	0.1891	246.6	257.1	1,79E-04	5,78E-02	655.480	0.11532	0.8846
ALPA	2390	18.41	2388	2388	7	597	0.9619	8.64e+04	0.1969	46.38	39.97	1,94E-04	5,78E-02	541.115	0.25901	0.7409
AUCA	1916	10.86	1916	1916	7	479	0.9634	8.64e+04	0.2198	39.55	36.49	2,42E-04	5,78E-02	537.425	0.22650	0.7735
BAAP	1417	22.58	1416	1416	7	354	0.968	8.64e+04	0.2557	42.9	35.02	3,27E-04	5,79E-02	619.174	0.51424	0.4857
BACO	1332	6832	1332	1332	7	333	0.9656	8.64e+04	0.2637	59.72	56.01	3,48E-04	5,77E-02	621.299	0.14658	0.8534
BAEZ	1848	86.31	1848	1848	7	462	0.9642	8.64e+04	0.2238	62.58	0	2,51E-04	5,79E-02	662.085	0.99990	0.0001
BAME	888	41.1	888	888	7	222	0.9727	8.64e+04	0.3229	40.46	36.72	5,21E-04	5,79E-02	590.589	0.99997	0.0000
BAPA	2009	9955	2008	2008	7	502	0.9636	8.64e+04	0.2147	48.18	42.92	2,31E-04	5,79E-02	643.689	0.54995	0.4500
BARU	1022	12.52	1020	1020	7	255	0.9688	8.64e+04	0.3013	32.28	28.82	4,54E-04	5,76E-02	555.729	0.99999	0.0000
BASO	2572	16.8	2572	2572	7	643	0.9606	8.64e+04	0.1897	64.81	57.03	1,80E-04	5,78E-02	725.002	0.23450	0.7655
BOBG	934	0.4283	932	932	7	233	0.9697	8.64e+04	0.3152	46.29	46.72	4,97E-04	5,76E-02	659.798	0.58270	0.4173
BOGT	7814	29.63	7812	7812	7	1953	0.9585	8.64e+04	0.1089	129	99.15	5,93E-05	5,78E-02	796.462	0.76050	0.2395
BUGT	2708	23.04	2708	2708	7	677	0.9614	8.64e+04	0.1849	58.9	45.36	1,71E-04	5,78E-02	721.412	0.37919	0.6208
CAPI	2463	22.21	2460	2460	7	615	0.9617	8.64e+04	0.194	36.12	32.38	1,88E-04	5,78E-02	493.217	0.26948	0.7305
CIA1	2701	2555	2700	2700	7	675	0.9612	8.64e+04	0.1852	147.5	159.8	1,71E-04	5,78E-02	577.160	0.10405	0.8959
CN19	1021	0.09794	1020	1020	7	255	0.9688	8.64e+04	0.3013	32.06	32.7	4,54E-04	5,76E-02	534.802	0.40017	0.5998
CN28	1114	11.58	1112	1112	7	278	0.9718	8.64e+04	0.2886	40.69	37.92	4,16E-04	5,79E-02	630.906	0.99998	0.0000
CN33	1447	0.6911	1444	1444	7	361	0.9634	8.64e+04	0.2532	93.01	92.28	3,21E-04	5,77E-02	815.893	0.75941	0.2405
CN35	1300	0.1538	1300	1300	7	325	0.9647	8.64e+04	0.2669	42.18	42.59	3,56E-04	5,77E-02	609.546	0.37743	0.6225
CN37	1317	4708	1316	1316	7	329	0.9652	8.64e+04	0.2653	68.31	68.42	3,52E-04	5,77E-02	580.471	0.16336	0.8366
CN38	1309	0.6875	1308	1308	7	327	0.9649	8.64e+04	0.2661	36.49	35.86	3,54E-04	5,77E-02	593.125	0.99989	0.0001
CN40	1716	0.4079	1716	1716	7	429	0.9631	8.64e+04	0.2323	33.33	33.05	2,70E-04	5,77E-02	559.760	0.85353	0.1464
COEC	1373	2258	1372	1372	7	343	0.964	8.64e+04	0.2598	25.82	25.46	3,37E-04	5,77E-02	411.854	0.49240	0.5076
CORO	2743	17.72	2740	2740	7	685	0.9605	8.64e+04	0.1838	49.28	40.71	1,69E-04	5,78E-02	612.157	0.24676	0.7532
CUC1	1961	4284	1960	1960	7	490	0.9645	8.64e+04	0.2174	70.2	68.34	2,36E-04	5,79E-02	739.043	0.27083	0.7291
ESMR	1917	1982	1916	1916	7	479	0.9634	8.64e+04	0.2198	37.15	37.34	2,42E-04	5,78E-02	513.044	0.18829	0.8117
GLPS	4739	22.37	4736	4736	7	1184	0.9599	8.64e+04	0.1398	21.47	15.51	9,78E-05	5,79E-02	399.173	0.92822	0.0717
GUAP	1824	26.81	1824	1824	7	456	0.9656	8.64e+04	0.2253	57.62	43.98	2,54E-04	5,79E-02	717.861	0.37519	0.6248
ISCO	1778	21.26	1776	1776	7	444	0.9647	8.64e+04	0.2283	125.2	106.3	2,61E-04	5,79E-02	1.054.210	0.31755	0.6824
MALO	2269	34.55	2268	2268	7	567	0.9615	8.64e+04	0.2021	56.02	44.11	2,04E-04	5,78E-02	665.712	0.12685	0.8731
MECE	2760	8841	2760	2760	7	690	0.9623	8.64e+04	0.1832	79.45	76.66	1,68E-04	5,79E-02	676.048	0.13146	0.8685
MITU	1038	2312	1036	1036	7	259	0.9693	8.64e+04	0.299	56.21	57.06	4,47E-04	5,76E-02	675.702	0.06477	0.9352
MZAL	7313	59.61	7312	7312	7	1828	0.959	8.64e+04	0.1125	74.23	55.32	6,33E-05	5,79E-02	577.839	0.34499	0.6550
OCEL	1217	4684	1216	1216	7	304	0.9685	8.64e+04	0.2759	48.43	46.37	3,81E-04	5,79E-02	639.181	0.41949	0.5805
PAL1	2201	4771	2200	2200	7	550	0.9636	8.64e+04	0.2052	55.88	55.28	2,10E-04	5,79E-02	599.307	0.25272	0.7472
PASI	1051	23.22	1048	1048	7	262	0.9701	8.64e+04	0.2972	38.25	37.63	4,42E-04	5,79E-02	594.848	0.88375	0.1162
POVA	2678	1.12	2676	2676	7	669	0.9609	8.64e+04	0.186	46.12	46.67	1,73E-04	5,78E-02	536.465	0.43096	0.5690
PUIN	2118	21.72	2116	2116	7	529	0.9619	8.64e+04	0.2092	49.68	47.92	2,19E-04	5,78E-02	598.849	0.13393	0.8660
QUIL	2222	0.9001	2220	2220	7	555	0.9622	8.64e+04	0.2042	65.4	64.2	2,09E-04	5,78E-02	599.443	0.59978	0.4002
RIOP	7235	46.91	7232	7232	7	1808	0.959	8.64e+04	0.1132	42.18	28.55	6,40E-05	5,79E-02	565.989	0.55150	0.4485
SAN0	3037	4478	3036	3036	7	759	0.961	8.64e+04	0.1746	40.67	39.59	1,52E-04	5,78E-02	586.567	0.22474	0.7752
SEL1	2883	18.97	2880	2880	7	720	0.9615	8.64e+04	0.1793	34.75	31.08	1,61E-04	5,79E-02	478.467	0.40432	0.5956
SNLR	1915	28.83	1912	1912	7	478	0.9654	8.64e+04	0.2201	51.8	35.54	2,42E-04	5,79E-02	635.542	0.18984	0.8101
TICU	2309	28.71	2308	2308	7	577	0.9621	8.64e+04	0.2003	67.31	51.92	2,01E-04	5,78E-02	616.806	0.14247	0.8575
TONE	2323	0.1722	2320	2320	7	580	0.9626	8.64e+04	0.1998	36.37	35.94	2,00E-04	5,79E-02	502.794	0.47502	0.5249
TUCO	2675	13.98	2672	2672	7	668	0.9623	8.64e+04	0.1862	40.19	34.78	1,73E-04	5,79E-02	578.722	0.38270	0.6173
URRA	1069	50.33	1068	1068	7	267	0.9669	8.64e+04	0.2944	46.53	42.46	4,33E-04	5,77E-02	640.062	0.51266	0.4873
UWAS	2302	5256	2300	2300	7	575	0.962	8.64e+04	0.2006	32.51	30.23	2,01E-04	5,78E-02	475.662	0.69530	0.3047
VBUV	2062	4074	2060	2060	7	515	0.9626	8.64e+04	0.212	32.84	32.27	2,25E-04	5,78E-02	445.304	0.25304	0.7469
VDPR	1919	4586	1916	1916	7	479	0.9634	8.64e+04	0.2198	64.02	60.68	2,42E-04	5,78E-02	706.671	0.33891	0.6610
VMAG	1980	12.53	1980	1980	7	495	0.9628	8.64e+04	0.2162	50.74	45.89	2,34E-04	5,78E-02	629.328	0.22335	0.7766
VNEI	1765	12.18	1764	1764	7	441	0.9622	8.64e+04	0.2291	49.17	43.16	2,62E-04	5,77E-02	609.757	0.12700	0.8730
VORA	1685	24.99	1684	1684	7	421	0.9624	8.64e+04	0.2345	158.5	149.4	2,75E-04	5,77E-02	997.378	0.40311	0.5968
VOTU	1500	0.4	1500	1500	7	375	0.9648	8.64e+04	0.2485	34.6	34.45	3,09E-04	5,77E-02	572.273	0.99986	0.0001
VPIJ	2099	7432	2096	2096	7	524	0.9635	8.64e+04	0.2102	40.35	37.55	2,21E-04	5,79E-02	534.915	0.31779	0.6822
VPOL	1603	29.44	1600	1600	7	400	0.9651	8.64e+04	0.2406	51.33	48.33	2,89E-04	5,79E-02	614.534	0.16344	0.8365
VROS	2518	23.39	2516	2516	7	629	0.9611	8.64e+04	0.1918	25.22	21.96	1,84E-04	5,78E-02	405.138	0.45972	0.5402
VSJG	2076	23.99	2076	2076	7	519	0.9629	8.64e+04	0.2112	68.3	59.39	2,23E-04	5,78E-02	730.181	0.20934	0.7906
VSJP	2376	11.7	2376	2376	7	594	0.9634	8.64e+04	0.1974	44.9	40.43	1,95E-04	5,79E-02	575.689	0.20992	0.7900

Appendix E

Velocity Uncertainties

Uncertainties estimation on the three components for each station using the White, PowerLawApprox and Combined power law + white noise models respectively
N= North component in mm/yr, **Un** = uncertainty in north component in mm/yr;
E= East component in mm/yr, **Eu** = uncertainty in east component in mm/yr;
U= Up component in mm/yr, **Uu** = uncertainty in up component in mm/yr.

ID	White noise						PowerLawApprox noise						Combined power law+white noise					
	N	Un	E	Eu	U	Uu	N	Un	E	Eu	U	Uu	N	Un	E	Eu	U	Uu
ACP1	11.7	0.1	16.6	0.1	3.3	0.2	11.5	0.2	16.6	0.2	3.2	0.4	11.4	0.3	16.7	0.3	3.0	0.7
ACP6	12.0	0.0	16.7	0.0	3.9	0.1	12.1	0.2	16.7	0.1	4.9	0.7	12.1	0.2	16.7	0.2	5.6	2.0
ALPA	13.3	0.1	8.2	0.1	-6.6	0.3	13.4	0.3	8.5	0.3	-5.4	0.9	13.6	0.6	8.4	0.9	-4.5	1.6
AUCA	9.9	0.0	-2.1	0.1	1.5	0.1	9.8	0.2	-2.1	0.2	1.3	0.4	9.9	0.2	-2.3	0.3	0.2	0.8
BAAP	9.9	0.1	-4.9	0.1	1.3	0.4	9.9	0.2	-4.9	0.3	1.1	0.8	9.9	0.2	-5.0	0.5	1.1	0.9
BACO	7.5	0.1	13.5	0.1	-2.3	0.3	7.7	0.5	13.3	0.4	-1.5	1.0	7.8	1.0	13.2	0.9	-0.7	2.4
BAEZ	10.5	0.1	1.8	0.2	1.9	0.4	10.4	0.2	2.0	0.3	2.8	0.9	10.4	0.2	2.0	0.3	2.8	0.9
BAME	14.2	0.1	1.7	0.2	3.3	0.3	14.2	0.2	1.6	0.4	3.4	1.2	14.2	0.2	1.6	0.7	3.4	1.2
BAPA	14.4	0.0	2.7	0.1	1.5	0.1	14.5	0.2	2.7	0.2	1.8	0.4	14.6	0.2	2.6	0.3	1.9	0.6
BARU	9.8	0.2	11.3	0.2	-0.1	0.5	9.9	0.4	11.5	0.6	0.0	1.0	9.9	0.4	11.6	0.8	0.0	1.0
BASO	15.4	0.0	7.3	0.1	1.5	0.1	15.5	0.1	7.2	0.2	1.4	0.3	15.5	0.4	6.7	0.9	1.5	0.6
BOBG	15.3	0.1	6.9	0.1	6.4	0.3	15.2	0.3	6.8	0.3	6.3	0.6	15.1	0.3	6.7	0.5	6.3	0.7
BOGT	14.8	0.0	-0.7	0.0	-32.8	0.2	15.1	0.2	-0.4	0.2	-34.9	0.8	15.2	0.2	-0.4	0.3	-35.3	1.0
BUGT	15.0	0.1	5.2	0.1	3.7	0.2	15.0	0.1	5.1	0.1	3.7	0.4	15.0	0.2	5.0	0.3	3.6	0.5
CAPI	11.7	0.1	-3.3	0.1	2.0	0.2	11.6	0.2	-3.1	0.2	1.7	0.5	11.5	0.4	-3.0	0.3	1.7	0.9
CIA1	14.1	0.0	3.5	0.1	-8.4	0.2	14.1	0.2	3.4	0.4	-9.7	1.2	14.3	0.6	3.0	1.3	-11.5	5.9
CN19	14.2	0.3	13.0	0.4	7.5	1.0	14.1	0.6	12.8	0.7	6.6	1.6	14.1	0.6	12.8	0.7	6.3	1.8
CN28	15.2	0.3	17.5	0.4	5.1	1.0	15.1	0.5	17.3	0.7	5.0	1.4	15.1	0.5	17.3	0.7	5.0	1.4
CN33	4.8	0.7	18.8	0.6	5.6	1.7	6.3	1.8	19.9	1.2	0.4	3.7	6.3	1.8	19.9	1.8	0.0	3.9
CN35	6.8	0.1	11.2	0.2	-0.5	0.4	6.6	0.4	11.1	0.4	0.0	0.9	6.6	0.4	11.0	0.6	0.3	1.1
CN37	10.0	0.3	11.0	0.3	9.9	1.0	12.5	0.9	9.7	0.7	6.8	2.4	13.8	1.6	8.5	1.1	4.4	3.6
CN38	13.7	0.1	11.3	0.1	2.4	0.4	13.8	0.3	11.3	0.3	2.8	0.8	13.8	0.3	11.3	0.5	2.8	0.8
CN40	13.2	0.4	11.7	0.4	4.1	1.0	12.9	0.7	12.1	0.6	4.1	1.6	12.9	0.7	12.2	0.7	4.1	1.6
COEC	12.7	0.1	3.4	0.1	5.0	0.1	12.6	0.2	3.3	0.4	4.9	0.7	12.5	0.4	3.0	1.0	4.7	1.1
CORO	11.3	0.1	11.5	0.1	2.6	0.2	11.3	0.2	11.6	0.2	2.1	0.7	11.4	0.3	11.7	0.3	1.2	1.3
CUC1	13.0	0.0	6.9	0.1	1.7	0.1	13.0	0.2	7.2	0.5	1.7	0.4	13.0	0.4	7.5	1.5	1.7	0.9
ESMR	16.7	0.0	17.8	0.0	2.4	0.1	16.6	0.1	17.8	0.2	2.3	0.4	16.5	0.3	17.9	0.5	2.2	1.1
GLPS	10.2	0.0	50.6	0.0	0.0	0.1	10.2	0.1	50.7	0.1	0.0	0.4	10.2	0.2	50.7	0.2	0.0	0.4
GUAP	13.5	0.1	8.6	0.1	2.5	0.3	13.5	0.2	8.2	0.3	2.7	0.7	13.4	0.4	7.9	0.5	3.0	0.9

ISCO	74.6	0.1	50.4	0.1	-2.8	0.4	74.5	0.3	50.3	0.3	-2.8	0.9	74.4	0.5	50.0	0.7	-2.7	1.4
MALO	13.6	0.1	48.4	0.1	-1.2	0.2	13.6	0.2	48.3	0.3	-1.5	0.6	13.6	0.3	48.3	0.6	-1.5	1.3
MECE	14.8	0.0	4.5	0.0	1.2	0.1	14.9	0.1	4.5	0.1	1.2	0.4	15.0	0.4	4.4	0.3	1.4	1.7
MITU	11.7	0.1	-4.6	0.1	3.2	0.3	11.6	0.2	-4.7	0.3	3.1	0.7	11.5	0.3	-4.7	0.4	2.6	1.8
MZAL	19.4	0.1	0.9	0.0	4.2	0.1	18.4	0.3	1.5	0.1	4.3	0.4	17.9	0.7	1.6	0.3	4.5	0.5
OCEL	11.7	0.1	-4.9	0.1	2.3	0.2	11.6	0.2	-5.0	0.2	2.6	0.6	11.6	0.2	-5.0	0.3	2.7	0.8
PAL1	14.8	0.0	3.5	0.0	0.0	0.1	14.7	0.2	3.5	0.1	0.3	0.4	14.7	0.4	3.5	0.4	0.6	0.8
PASI	10.5	0.1	-3.1	0.1	1.6	0.2	10.4	0.2	-3.1	0.3	1.5	0.6	10.3	0.4	-3.1	0.3	1.5	0.6
POVA	12.8	0.0	5.5	0.0	-2.7	0.1	12.9	0.1	5.3	0.2	-2.3	0.3	13.0	0.3	5.1	0.5	-2.2	0.6
PUIN	10.9	0.1	-5.0	0.1	-1.2	0.4	10.8	0.3	-4.8	0.3	-0.7	1.1	10.7	0.3	-4.6	0.5	-0.3	2.2
QUIL	14.2	0.0	5.2	0.0	0.4	0.1	14.2	0.1	5.1	0.3	0.4	0.6	14.3	0.3	5.0	0.8	0.4	0.9
RIOP	7.0	0.1	0.6	0.1	1.6	0.1	6.0	0.2	-0.5	0.3	1.2	0.4	5.7	0.4	-0.5	0.6	1.0	0.5
SAN0	7.4	0.0	13.0	0.0	-0.3	0.1	7.3	0.1	12.8	0.2	-0.1	0.3	7.0	0.2	12.3	0.4	0.2	0.5
SEL1	15.2	0.1	3.9	0.1	1.7	0.2	15.0	0.2	3.9	0.2	1.3	0.6	14.9	0.2	4.0	0.3	1.2	0.9
SNLR	10.6	0.0	11.2	0.0	3.1	0.1	10.6	0.1	11.1	0.1	2.9	0.4	10.6	0.3	11.0	0.4	2.7	0.8
TICU	11.1	0.1	-4.2	0.1	4.7	0.3	10.9	0.2	-4.2	0.2	4.3	0.9	10.8	0.3	-4.2	0.3	3.5	2.0
TONE	15.4	0.0	3.9	0.0	3.2	0.1	15.5	0.1	4.1	0.2	2.8	0.4	15.5	0.2	4.2	0.5	2.6	0.6
TUCO	12.9	0.1	13.5	0.1	5.4	0.2	12.8	0.1	13.7	0.2	5.4	0.5	12.8	0.2	13.8	0.4	5.3	0.7
URRA	14.2	0.4	12.6	0.4	3.8	1.0	14.0	0.7	12.6	0.8	3.3	2.1	14.0	0.7	12.6	0.8	3.1	2.5
UWAS	12.9	0.0	0.2	0.0	3.5	0.1	13.0	0.2	0.1	0.2	3.1	0.5	13.0	0.3	0.1	0.3	2.9	0.6
VBUV	16.1	0.1	4.4	0.1	0.5	0.2	15.7	0.2	3.9	0.3	0.8	0.5	15.6	0.3	3.7	0.5	0.9	0.9
VDPR	15.2	0.0	8.4	0.0	3.2	0.1	15.2	0.1	8.4	0.1	3.2	0.5	15.2	0.2	8.5	0.2	3.1	0.9
VMAG	14.1	0.1	8.4	0.1	3.9	0.3	14.1	0.2	8.4	0.3	4.5	0.7	14.1	0.4	8.4	0.5	5.2	1.3
VNEI	14.0	0.0	-0.6	0.0	1.8	0.1	13.9	0.2	-0.7	0.1	1.8	0.4	13.8	0.3	-0.7	0.3	1.8	1.5
VORA	11.8	0.2	14.6	0.2	-8.4	0.5	11.7	1.1	14.5	0.9	-7.4	2.4	11.6	1.5	14.2	1.8	-6.6	4.8
VOTU	15.1	0.1	6.2	0.1	4.7	0.1	15.1	0.2	6.1	0.2	4.6	0.3	15.1	0.4	6.0	0.3	4.6	0.3
VPIJ	14.1	0.1	2.0	0.1	3.8	0.2	14.3	0.2	1.8	0.2	3.7	0.6	14.4	0.2	1.6	0.4	3.5	1.1
VPOL	16.7	0.1	8.3	0.1	10.5	0.3	16.6	0.2	8.0	0.3	10.5	0.9	16.6	0.2	7.6	0.5	10.3	1.7
VROS	14.6	0.1	0.6	0.1	1.7	0.2	14.5	0.3	0.2	0.3	1.2	0.8	14.5	0.3	0.1	0.5	1.1	1.1
VSJG	10.8	0.1	-5.4	0.2	2.4	0.6	10.8	0.3	-5.1	0.4	1.7	1.2	10.8	0.3	-4.9	0.6	1.0	1.8
VSJP	15.1	0.1	0.8	0.1	3.2	0.2	15.2	0.2	0.9	0.3	2.8	0.6	15.2	0.3	1.0	0.4	2.2	1.1